Characterization of Annular Flow Downstream of an Obstruction

by

Jason Chan

A dissertation submitted in partial fulfillment of
the requirements for the degree of

Doctor of Philosophy
(Mechanical Engineering)

at the
UNIVERSITY OF WISCONSIN-MADISON
2023

Date of final oral examination: 12/14/2023

The dissertation is approved by the following members of the Final Oral Committee:
Gregory F. Nellis, Professor, Mechanical Engineering
Arganthaël Berson, Assistant Professor, Mechanical Engineering
Allison Mahvi, Assistant Professor, Mechanical Engineering
Mark Anderson, Professor, Nuclear Engineering and Engineering Physics
Michael Corradini, Professor, Nuclear Engineering and Engineering Physics

Acknowledgements

In the past 5 years of graduate school, a group of individuals made profound effects on my growth as an engineer, researcher, and individual. A commonality between everyone here is having an outstanding attitude. You represent a variety of experiences and expertise, and also attitudes to strive for.

First and foremost, thank you to my MFVAL team. Thank you, Prof. Arganthaël Berson, for believing in me from the very beginning. Your spirited and can-do attitude helped me develop the confidence I have today to tackle problems in research and in life. For nearly 8 years, you were always there to celebrate the good and help rethink the dispiriting moments. Working on image processing and aligning laser optics with you were some of my fondest memories in graduate school. Thank you Prof. Greg Nellis, for showing your excitement every time we stumble upon a new epiphany. Your genuine and no-nonsense attitude helped me navigate through my graduate career. You're a man of few words, but every word you say made sense. Thank you Dress[1], for helping me believe that anything is possible if we find the right people and devote our minds. You're always curious and truly kind; maybe that's part of your secret to bringing everyone together. I wish I stopped by your office more often. You are sorely missed. Lastly, thank you to each member of my committee for your time and asking the tough questions.

Roman W. Morse, thank you for finally trusting me with the loop. For more times than I can count, your enthusiasm "to science" reminded me of the great value of our work. The way I see your mind firing on all cylinders during our conversations helped me get past disheartening obstacles through the years. Your conviction to resolve all your questions, and to show your discomfort with hand-wavy answers are inspiring; I hope to be more like you.

Thank you Dr. Evan Hurlburt for your unwavering support for the work that we do. I am in awe of the long time you have dedicated to the field of two-phase flow. Perhaps that is why I see your name around every corner during my literature review. Your expert insights into our experimental work have been tremendously invaluable in helping us decide our research direction, all the while encouraging us to practice autonomy in carrying out our work. To Dr. Jean-Marie Le Corre, among many things, thank you for reaching out to our team in the first place, and collaborating with us in the effort to create an opensource

[1] Dr. Kristofer M. Dressler

sub-channel analysis code. Your assistance in Roman and my job search means the world to us.

Thank you Brett Lindeman for teaching me how to build an experiment. I would still be looking for just the right thread sealant if it weren't for your wealth of working knowledge in fabrication and experiment design. By practicing yourself, you also taught me how to be patient and methodical in everything I do.

The work I did is undoubtedly built on nearly a decade-long effort of experimental work conducted by MFVAL members. Thank you Brian Fehring for making CAD work and aluminum TIG welding look easy. From the pulse generator to the electrical rework and optical design, you laid down the foundation of recent MFVAL work. Thank you to all the undergraduate researchers who taught me to be better mentors: Sydney Wagner, Daniel Roth, Simon Livingston-Jha, Madison Shipshock, Maggie Meissner, Ian Hogenkamp and Evan Ogren. Special thanks to Chris Rushmore for taking ownership of designing and fabricating the current test section; your work is a piece of art. Thank you Dr. Tim Shedd and Dr. Mark Rodarte for laying down the groundwork that made everything I did at MFVAL possible.

Thank you Heather Casterline for being a great roommate, offering an affordable living arrangement, and allowing me to use the garage as a woodworking workshop where I can de-stress at the end of the day. From our outdoor adventures and house projects, to heartfelt discussions about our disagreements and emotions, I'm grateful for your help in keeping me sane. To our dogs, Tollie and Moe, who will rather chew up this paper than read it, thank you for having the purest hearts and sweetest personalities and lifting me up daily.

Thank you, Mom and Dad, for letting me study abroad for so many years. None of this would be possible without you.

Contents

List of Tables

List of Figures

Nomenclature

Abbreviations

CHF Critical heat flux

DHF Dryout heat flux

HTC Heat transfer coefficient

LFT Liquid film thickness

MFVAL Multiphase Flow Visualization and Analysis Lab

Symbols

α Thermal diffusivity

$\Delta\rho$ Density difference

δ Film thickness

$\dot{m}$ Mass flow rate

$\dot{q}''$ Heat flux

Γ Mass flow rate per unit length [kg/m-s]

Ka Kapitza

$\mathcal{F}$ Two-phase Reynolds number ratio

μ Fluid viscosity

ν Kinematic viscosity, $\nu = \frac{\mu}{\rho}$

Nu Nusselt number

$\overline{\delta}$ Time-averaged liquid film thickness

$\overline{\delta}$ Time-averaged non-dimensionalized liquid film thickness

$\overline{\Gamma}$ Time-averaged mass flow rate per unit length [kg/m-s]

$\overline{\rho}$	Average two-phase mixture density
$\overline{w}$	Time-averaged stream-wise Velocity
Pr	Prandtl number
Re	Reynolds number
ρ	Fluid density
σ	Surface tension
τ	Shear stress
θ	Incline angle
c	Pixel size
d	Characteristic length
D_h	Hydraulic diameter
G	Mass flux [kg/m^2-s]
g	Gravitational acceleration
h	Local heat transfer coefficient
k	Thermal conductivity
L	Length
R	Radius
T	Temperature
t	Time
T_∞	Bulk/free-stream temperature
T_{sat}	Saturation temperature
T_{wall}	Temperature of the interior wall (heated surface) of the test section
u	Velocity
u_τ	Friction velocity
W	Flow channel span-wise width
w	Stream-wise Velocity
x	Vapor quality

Subscripts

crit	critical
ff	falling film
lam	laminar
pred	predicted
turb	turbulent
b	base film
c	characteristic
l	liquid phase
v	vapor phase
w	wave

Chapter 1

Introduction

The goal of this research is to characterize the heat transfer characteristics of annular flow downstream of an obstruction. Applications of two-phase heat transfer are broad and ubiquitous. From refrigerators, air conditioners and dehumidifiers, to nuclear reactors, data centers, and space exploration, engineers take advantage of the high heat transport capability of the vaporization phenomenon in a two-phase fluid. That is, heat is more efficiently removed by a saturated fluid than by a sub-cooled liquid or a super-heated vapor. Saturated flows are categorized by the two-phase flow regime that is present. Figure 1.1 shows the boiling regimes as a slightly sub-cooled liquid flows through a heated flow channel and becomes saturated.

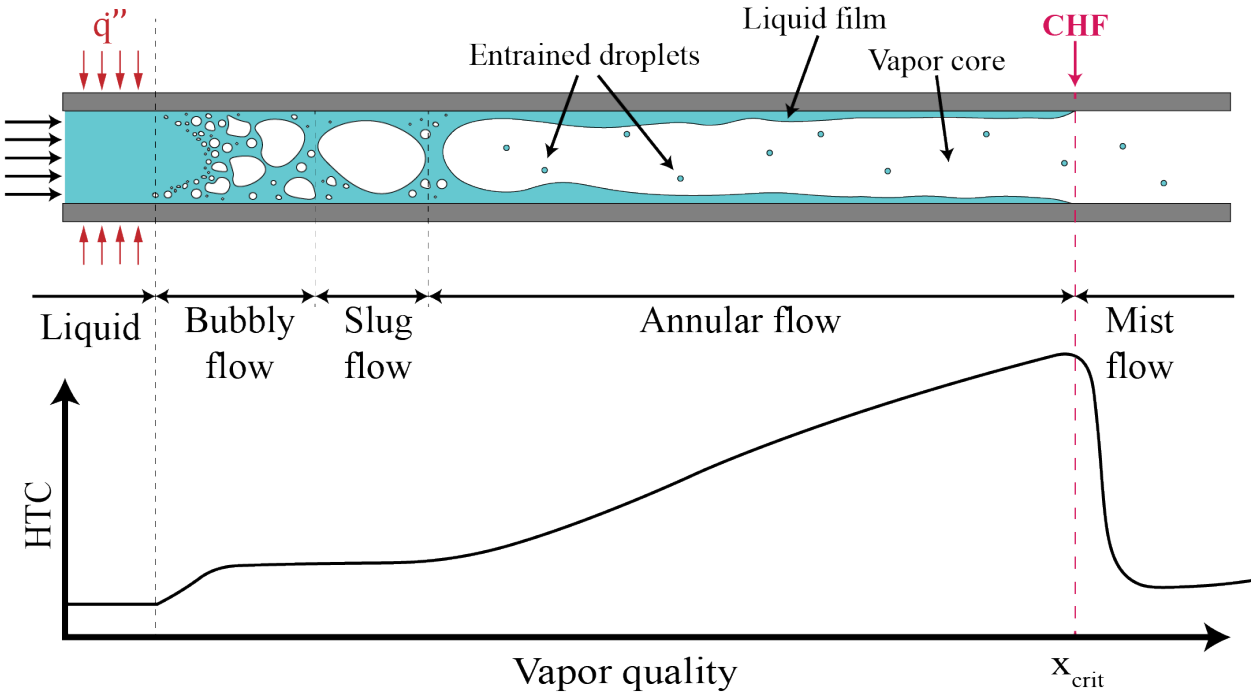

Figure 1.1: Evolution of saturated flow through two-phase flow regimes (top), and the associated HTC and vapor quality (bottom). (Morse et al., 2021)

As a slightly sub-cooled liquid enters a heated flow channel, it becomes a saturated liquid as heat transfer occurs. The amount of heat transfer between the fluid and the surrounding solid surface is quantified by the heat transfer coefficient (HTC). The HTC is the ratio of heat flux (units: W/m^2) to the temperature difference between the solid and the fluid (units: K). As the saturated liquid continues to remove heat from the wall, the flow vapor quality increases. As seen in Figure 1.1, the local vapor quality corresponds directly to an associated two-phase flow regime and HTC. Here, the vapor quality, x, is defined as,

$$x = \frac{\dot{m}_v}{\dot{m}}$$

where $\dot{m}$ is the sum of the liquid flow rate, $\dot{m}_l$, and the vapor flow rate, $\dot{m}_v$:

$$\dot{m} = \dot{m}_l + \dot{m}_v$$

In general, the HTC increases with increasing x, up to x_{crit}, the vapor quality associated with the critical heat flux, or CHF. The CHF is defined as the heat flux where the HTC reaches its maximum value. Beyond x_{crit}, the heat transfer coefficient between the heated wall to the fluid plummets, resulting in a sharp increase in the wall temperature, T_{wall}, as the thin liquid film dries out. The saturated liquid in the flow beyond x_{crit} exists mostly in the form of entrained droplets in vapor.

Of the flow regimes shown in Figure 1.1, the focus of the current study is the annular flow regime, where the greatest heat transfer occurs. Annular flows are characterized by a turbulent vapor core, liquid droplets entrained within the vapor core, and a wavy liquid film on the wall of the heated flow channel. The characterization of the wavy liquid film in vertical annular flow is of interest in this study. The study requires the development of experimental methods. Due to the complex nature of two-phase flow fields, a falling water film was used to verify these methods before applying them to an annular flow. The falling film is more accessible and therefore provides a straightforward environment for developing and validating experimental methods.

Disturbance waves play a dominant role in the mass, momentum, and energy transport of thin film flows such as falling film and annular two-phase flows (Morse et al., 2021; Moreira et al., 2020). Due to their stochastic nature, wave statistics such as wave height, frequency, and intermittency are used to characterize disturbance waves (Zeng et al., 2022). From these statistics, a deeper understanding of the flow structures can be realized.

Wave statistics can be estimated using empirical correlations based on experimentation. Empirical correlations are available for some disturbance wave characteristic in a variety of thin film flows (Henstock and Hanratty, 1976; Zhao et al., 2013; Schubring et al., 2010a), but physical models of the wave structures developed with experimental data are not as comprehensive. This work aims to contribute in this regard.

A literature review in Chapter 2.2 describes the benefits and limitations of existing liquid film thickness measurement techniques. An optical non-intrusive film thickness measurement

technique with high temporal resolution that is used in this work is then described. In Chapter 3.1, the experimental setup and validation process are presented. In Chapter 3.3, analysis of the time resolved film thickness measurements are presented, and disturbance wave shapes and velocities for a range of flow rates and conditions are calculated (Moreira et al., 2020).

In Chapter 3.4, a two-layer physical framework is used to analyze the wave characteristics. Compared to using only empirical correlations, the main benefit of developing such an analysis framework to calculate wave statistics is wider applicability to different flow conditions. Similar to the two-layer approach taken by Le Corre (2022), the two-layer characterization framework for disturbance waves in this work splits the wavy liquid film into a wave layer and a base film layer in order to more accurately describe the underlying physical phenomenon. One of the physical quantities of interest in annular flows is the liquid film flow rate (LFFR) due to its relationship to base film thickness, which has a direct impact on heat transfer (Chen, 1966). The two-layer framework provides a method of calculating the LFFR carried by the base film and waves, given time-resolved liquid film thickness (LFT) measurements.

Chapter 2

Literature review

Fundamentally, two-phase heat transfer is quantified by the local two-phase HTC, h, using Newton's law of cooling:

$$h = \frac{\dot{q}''}{T_{wall} - T_{\infty}} \tag{2.1}$$

where $\dot{q}''$ is the heat transfer rate per unit area, or heat flux, at the wall, T_{wall} is the wall temperature, and T_{∞} is the bulk temperature of the fluid. Since the fluid is saturated, the bulk fluid temperature is taken to be the fluid saturation temperature: $T_{\infty} = T_{sat}$. Eq. 2.1 can then be rewritten as

$$h = \frac{\dot{q}''}{T_{wall} - T_{sat}} \tag{2.2}$$

The consequence of this substitution is the assumption that all the heat transferred from the wall to the liquid is used for evaporation. This involves two methods of flow boiling at the two phase interfaces: nucleation boiling at the wall-liquid interface and convective boiling at the liquid-vapor interface. Nucleation boiling has been well-studied (Galloway and Mudawar, 1993; Zhang et al., 2012; Ahn et al., 2010); however, the convective boiling phenomenon is less well understood and is the focus of this study.

2.1 HTC and film thickness characteristics

The purpose of this section is to demonstrate the importance of liquid film thickness to the annular flow HTC based on previous work in the literature. One of the earliest publication in this area is by Chen (1966) who proposed a modification to the single-phase correlation by Dittus and Boelter (1930) for vertical saturated two-phase flow.

2.1.1 Chen (1966)

The Dittus and Boelter (1930) correlation predicts a Nusselt number for turbulent single-phase flows,

$$Nu_{DB} = 0.023 Re^{0.8} Pr^{0.4} \tag{2.3}$$

in terms of the Reynolds number, Re, and the Prandtl number, Pr. Re is defined as

$$Re = \frac{\rho u d}{\mu} \tag{2.4}$$

where ρ is fluid density, u is the velocity, d is a characteristic length, and μ is the fluid viscosity. Pr is defined as

$$Pr = \frac{\mu}{\rho}\frac{\rho c}{k} = \frac{\nu}{\alpha} \tag{2.5}$$

where ν is the fluid kinematic viscosity, and α is the thermal diffusivity. The Nusselt number, Nu, is defined as

$$Nu = \frac{hd}{k} \tag{2.6}$$

where h is the local HTC, d is a characteristic length, and k is the thermal conductivity of the fluid. The result of heat transfer correlations is a predicted Nusselt number, Nu_{pred}, from which an appropriate HTC, h_{pred}, can be calculated as:

$$h_{pred} = \left(\frac{k}{d}\right) Nu_{pred} \tag{2.7}$$

Applying Eq. (2.7) to Eq. (2.3), the Dittus and Boelter (1930) prediction of single-phase HTC, h_{DB}, is:

$$h_{DB} = \left(\frac{k}{D_h}\right) 0.023 Re^{0.8} Pr^{0.4} \tag{2.8}$$

where D_h is the flow channel hydraulic diameter. While the Dittus-Boelter equation works well for single-phase flow, including at the two limits of 0 and 1 vapor quality, a modification is needed to account for the interactions between the liquid and vapor phases. Chen (1966) proposed a modification function, $\mathcal{F}$, such that

$$h_{Chen} = h_{DB,l}\, \mathcal{F} \tag{2.9}$$

where $h_{DB,l}$ is the Dittus and Boelter HTC prediction using liquid-phase values. The justification for using liquid-phase value is due to the dominant effect of the liquid in a two-phase flow, as heat from the wall is transferred directly through the liquid film in annular flow. $\mathcal{F}$ is the two-phase Reynolds number ratio

$$\mathcal{F} = \left(\frac{Re}{Re_l}\right)^{0.8} \tag{2.10}$$

where Re is the two-phase Reynolds number, and Re_l is the liquid-phase Reynolds number. The liquid Reynolds number is calculated as

$$Re_l = \frac{D_h G(1-x)}{\mu_l} \tag{2.11}$$

where x is the vapor quality of the two-phase mixture, and G is the two-phase mass flux. The two-phase Reynolds number is calculated as

$$Re = \frac{\rho_l D_h}{\mu_l} \frac{G}{\overline{\rho} A_c} \tag{2.12}$$

where A_c is the cross sectional area of the flow channel, D_h is the flow channel hydraulic diameter, and $\overline{\rho}$ is the average two-phase mixture density, $\overline{\rho} = x\rho_v + (1-x)\rho_l$. The Chen (1966) modified correlation provides:

$$h_{Chen} = 0.023 Re_l^{0.8} Pr_l^{0.4} \frac{k_l}{D_h} \mathcal{F} \tag{2.13}$$

which is an estimate of the convective HTC in vertical two-phase flow that relies on the liquid film mass flow rate, $G(1-x)$. One way of obtaining this value is through the film thickness, δ, associated with the direction of heat transfer from the wall through the liquid film. In other words, the liquid film thickness is integral to the application of the Chen correlation.

One drawback of this correlation is the assumption of no entrained liquid droplets in the vapor core of annular flow. Re_l represents the liquid film mass flux in the form of $G_l = G(1-x)$, when in fact, some portions of the liquid are entrained and may contribute to the heat transfer mechanism differently than the bulk liquid film does. A liquid film measurement technique with high spatial-temporal resolution would provide a more accurate estimation for the liquid film mass flux.

2.1.2 Liquid film and waves in annular flow

Hewitt (1969) showed images of the flow field under annular flow conditions. Based on these images, Hewitt discerned two types of wave structures in the liquid film: disturbance waves and ripples. Ripples are standing-wave-like structures that occur near the base film, and between relatively large-amplitude disturbance waves. Ripples transport energy, but not mass, and are continuously regenerated despite coalescing with disturbance waves, or eventually dissipating due to viscous forces (Hewitt, 1969; Borhani et al., 2010).

Disturbance waves, on the other hand, transport mass and are the dominant wave structure in annular flow. As the high-velocity vapor flows over the liquid film surface, a stacking effect of the liquid film occurs that ultimately creates the disturbance waves. The phenomena is visually analogous to the spreading of icing on cake; as the viscous icing is sheared along its surface, the icing stacks up and creates a lump. Extending the analogy, the balance between the vapor shear force (spreading of icing) and the liquid (icing) viscous forces affect the size of the disturbance wave (stacked-up lump). The turbulent characteristics of disturbance waves were also confirmed in the images provided by Hewitt (1969). The images show the creation and dissipation of vortices, coalescence of waves, and the overall non-uniform and stochastic wave behaviors.

2.1.3 Henstock and Hanratty (1976)

A model for predicting the time-averaged liquid film thickness along a flat wall in air-water systems and free falling water films was developed by Henstock and Hanratty (1976). They described the time-averaged dimensionless liquid film thickness, $\overline{\delta}^+$, as a function of a laminar flow and a turbulent flow:

$$\overline{\delta}^+ = f(\overline{\delta}^+_{lam},\ \overline{\delta}^+_{turb}) \tag{2.14}$$

where the film thickness, $\overline{\delta}^{+}$, is non-dimensionalized

$$\overline{\delta}^{+} = \overline{\delta}\frac{u_\tau}{\nu_l} \tag{2.15}$$

by the liquid kinematic viscosity, ν_l, and the friction velocity, $u_\tau = \sqrt{\frac{\tau_c}{\rho_l}}$. τ_c is the characteristic shear stress associated with the different types of wavy flows described by Henstock and Hanratty.

For gas-liquid flow over a flat wall, $\overline{\delta}^{+}_{lam} = 0.707Re^{0.5}$ and $\overline{\delta}^{+}_{turb} = 0.0379Re^{0.9}$, which are combined by an empirical fit

$$\overline{\delta}^{+} = \left[{\overline{\delta}^{+}_{lam}}^{2.5} + {\overline{\delta}^{+}_{turb}}^{2.5}\right]^{0.4} \tag{2.16}$$

$$= \left[\left(0.707Re^{0.5}\right)^{2.5} + \left(0.0379Re^{0.9}\right)^{2.5}\right]^{0.4} \tag{2.17}$$

A similar process was carried out for a free falling film where $\overline{\delta}^{+}_{ff,lam} = 0.707Re^{0.5}$ and $\overline{\delta}^{+}_{ff,turb} = 0.031Re^{0.9}$, which are combined by an empirical fit

$$\overline{\delta}^{+}_{ff} = \left[{\overline{\delta}^{+}_{ff,lam}}^{5} + {\overline{\delta}^{+}_{ff,turb}}^{5}\right]^{0.2} \tag{2.18}$$

$$= \left[\left(0.707Re^{0.5}\right)^{5} + \left(0.031Re^{0.9}\right)^{5}\right]^{0.2} \tag{2.19}$$

All of the experimental results used for empirical fitting by Henstock and Hanratty reported no or negligible liquid entrainment in the vapor (air) phase of the flow. The work by Henstock and Hanratty allows comparison of the time-averaged film thickness mentioned in this work to previous work. From its close fit to those experimental results, this model supports the assertion that a wavy liquid film is comprised of a laminar flow and a turbulent flow. From observation, the former corresponds to the relatively smooth base film, while the latter corresponds to the non-uniform and stochastic disturbance waves. Lastly, this work shows the physical similarity in falling film flow and vapor-liquid flow. By adapting the characteristic shear stress of each respective type of flow, the same modelling approach can

be used to predict the time-averaged liquid film thickness.

2.2 Film thickness measurement methods

A wide array of liquid film thickness measurement techniques with different capabilities have been developed over the years. A comprehensive review of these methods have been presented by Clark (2002) and Tibiriçá et al. (2010). Some of the earliest work used needle contact probes (Neal and Bankoff, 1963) for point measurements, and conductance probes (Collier and Hewitt, 1964) for localized measurements. The needle contact probe measures film thickness by physically measuring the distance at which a needle tip contacts the film surface (Fujita et al., 1986; Nosoko et al., 1996). It requires access to physical space above the film surface and is suitable for external flows. Several drawbacks of this method include poor time-resolution, potential of probe bending during calibration (Hewitt et al., 1962), and film distortion due to physical contact. This technique is limited to point measurements.

Conductance probes are some of the most widely used film measurement techniques (Clark, 2002). Electrodes are arranged in and around the flow to measure the electrical conductance of liquid in a certain region. Depending on the electrode arrangement, the film thickness within a certain range can be linearly correlated to the measured electrical conductance. With an appropriately designed electrode configuration, the ease of implementation and near-instantaneous response (Pearlman, 1963) are contributing factors to their wide adoption. These probes, however, require physical contact with the flow, and can potentially disrupt the liquid film. Even in the case of flush-mounted electrodes, where the electrodes are flush with the flow channel wall, the film can be disrupted by the the change in wall material. Moreover, these measurement techniques are limited to being implemented in electrically conductive working fluids. Capacitance probes operate similarly.

Optical methods are often used to measure refrigerant films as refrigerants tend to be

dielectric (Ubara et al., 2022; Fehring, 2018). Interferometry (Jonsson and Höglund, 1993; Morales-Espejel et al., 2015) is a commonly used optical thin film measurement technique, where the optical interference pattern caused by monochromatic light passing through a thin film correlates precisely to the film thickness. Fluorescence (Schubring et al., 2010b) is another technique in which the intensity of the light emitted by a fluorescent dye mixed with the working fluid is proportional to the film thickness. The introduction of the dye can be problematic as it may alter the working fluid properties, and may be difficult to fully remove from a flow facility. Confocal chromatic displacement sensors Ubara et al. (2022) take advantage of controlled chromatic aberration to determine the distance between a target surface and a polychromatic light sensor. As with optical methods in general, implementing these measurement techniques require careful calibration and specialized optics, light sources or materials.

2.2.1 Technique used in this work

The optical film thickness measurement technique used in this work was adapted from the method introduced by Hurlburt and Newell (1996), and refined by Shedd and Newell (1998) and Moreira et al. (2020). It relies on the total internal reflection (TIR) of light past the critical angle of refraction at the liquid-vapor interface. The beam path of a laser ray through the various layers is shown in Figure 2.1. A collimated beam is directed perpendicular to the exterior glass surface. A translucent white tape is attached to this interface to diffuse the incident beam into the glass. Diffused rays then propagate into the liquid before reaching the liquid-vapor interface. Since the refractive index of vapor is lower than the liquid, a critical angle, θ_c, exists that satisfies Snell's law for TIR at this interface. Incident rays propagating at an angle lower than θ_c will mostly refract through the interface, whereas rays propagating at and above θ_c will reflect completely. The reflected light forms a circular shape resembling a light ring. The position of the reflected beam on the white tape, where an image is taken, depends on the water thickness at the point of TIR. By setting the initial incident beam

location as a reference, the radii around the light ring are measured and the associated liquid thicknesses inferred. The process of analyzing the reflected light ring images is described in Chapter 3.3.

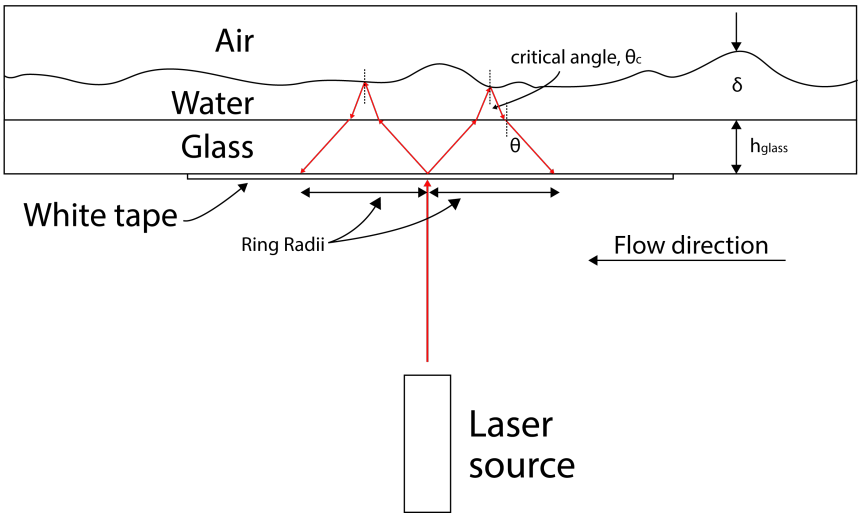

Figure 2.1: Optical schematic of the film thickness measurement technique.

Chapter 3

Falling film

3.1 Experimental setup

The validation of the optical film thickness measurement technique used in this work is performed on a falling film facility with de-ionized water as the working fluid. The facility shown in Figure 3.1 features an inclined glass pane as the flow channel. The clear glass pane is 1500 mm long, 430 mm wide, 0.7 mm thick, and allows optical measurements of the film thickness. The schematic of the facility is shown in Figure 3.2. Water is pumped from the lower tank to the upper tank using a rotary vane pump (Fluid O-Tech PA411) driven by a permanent magnet DC motor (Dayton 2M167D). The pump provides a maximum volumetric flow rate of 2 L/min. The mass flow rate is controlled using a motor control module and measured by a Coriolis flow meter (Micro Motion 2700). The incline angle can be changed from 0 to 60 degrees from horizontal.

Figure 3.1: Photograph of the falling film facility. The adjustable inclined angle is manually controlled using a rope-and-pulley system.

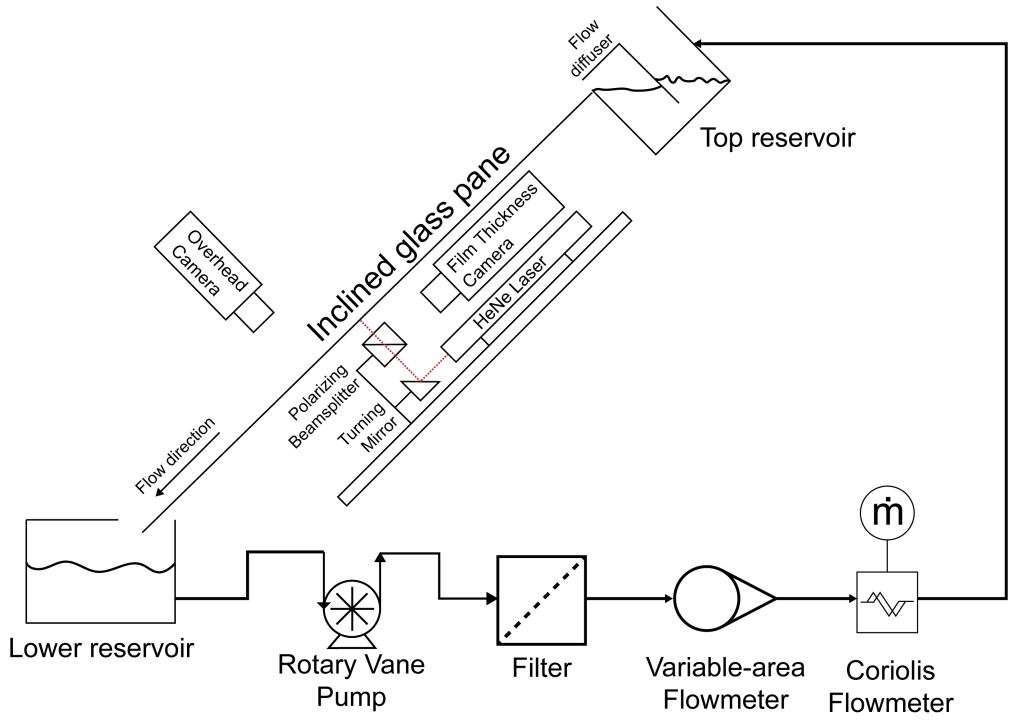

Figure 3.2: Schematic of the falling film facility.

3.1.1 Optical setup

The optical setup includes a polarized 5 mW HeNe laser, a beamsplitter, and a high-speed camera. A CAD rendering of the setup is shown in Figure 3.3. An aluminum optical breadboard was used to hold all of the optical components. Starting from the laser source, (632.8 nm, ThorLabs HNL050LB), a laser beam propagates through the 0.5 inch lens tube (ThorLabs SM05L10) to the silver turning mirror (ThorLabs CCM5-P01). The laser module is housed inside a 66-mm optical rail (ThorLabs XT66RL2) segment that also supports the high-speed camera. Various optomechanical spacers are used to evenly support the laser tube.

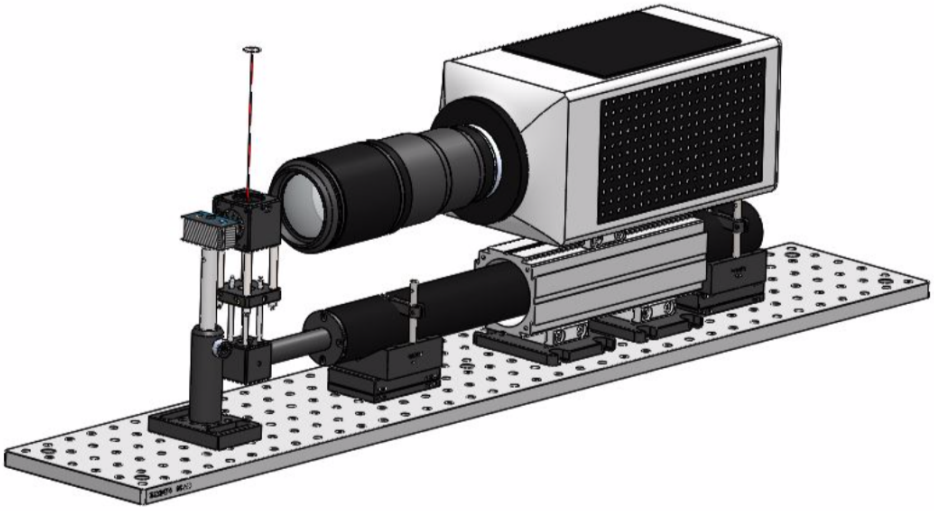

Figure 3.3: Optical setup for the film thickness measurement system.

Following the laser beam path in Figure 3.4, the laser beam is directed to a beamsplitter where the reflected is absorbed by a beam block. The transmitted light propagates to the glass pane. The reflections of the laser rays from the glass-water interface projects a light ring on a white diffusing tape. The high-speed camera (Phantom VEO 640) is mounted directly over and parallel to the laser, so that it can collect images of the reflected image in the beamsplitter.

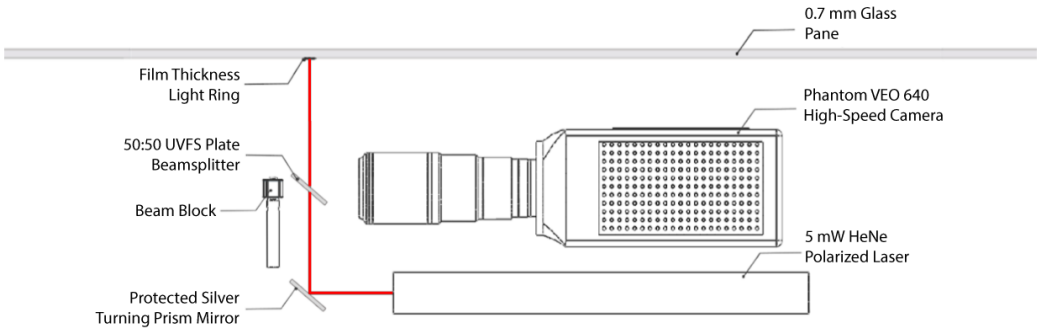

Figure 3.4: Optical setup for the film thickness measurement system.

3.2 Measurements

3.2.1 Parametric study

Two sets of parametric studies were conducted using the falling film facility in which the mass flow rate and incline angle are the independent parameters. The first study was carried out following the test matrix provided in Table 3.1, using 2000 frames per second (fps) image sampling frequency. Each data set was 5 seconds long and included approximately 20 disturbance waves. Mass flow rates were chosen such that wave features moved slowly enough that the captured images of both the ring and the film could be used to clearly discern wave structures. Incline angles were limited by the capabilities of the facility to 60 degrees from horizontal.

Table 3.1: Test conditions for 2000 fps sampling rate.

No.	Γ [kg/m-s]	$\dot{m}[g/s]$	θ [deg]
1.1	0.0120	5	20
1.2	0.0241	10	20
1.3	0.0241	10	60
1.4	0.0361	15	30
1.5	0.0361	15	60
1.6	0.0482	20	20
1.7	0.0964	40	30
1.8	0.0964	40	60
1.9	0.1446	60	30
1.10	0.1446	60	60
1.11	0.1928	80	30
1.12	0.1928	80	60
1.13	0.2892	120	30
1.14	0.2892	120	60

After analyzing images captured in the first study, a second study was conducted to fill in missing data. The first study was used to examine the variations among disturbance waves in each flow condition. By lowering the imaging frequency to 1000 fps in the second study, twice as many waves were recorded for each experiment, but with less time-resolution for each wave. The list of tests in the second study is provided in Table 3.2.

Table 3.2: Test conditions for 1000 fps sampling rate.

No.	Γ [kg/m-s]	$\dot{m}[g/s]$	θ [deg]	#	Γ [kg/m-s]	$\dot{m}[g/s]$	θ [deg]
2.1	0.0481	20	20	2.26	0.1691	70	20
2.2	0.0481	20	30	2.27	0.1691	70	30
2.3	0.0481	20	40	2.28	0.1691	70	40
2.4	0.0481	20	50	2.29	0.1691	70	50
2.5	0.0481	20	60	2.30	0.1691	70	60
2.6	0.0721	30	20	2.31	0.1931	80	20
2.7	0.0721	30	30	2.32	0.1931	80	30
2.8	0.0721	30	40	2.33	0.1931	80	40
2.9	0.0721	30	50	2.34	0.1931	80	50
2.10	0.0721	30	60	2.35	0.1931	80	60
2.11	0.0961	40	20	2.36	0.2171	90	20
2.12	0.0961	40	30	2.37	0.2171	90	30
2.13	0.0961	40	40	2.38	0.2171	90	40
2.14	0.0961	40	50	2.39	0.2171	90	50
2.15	0.0961	40	60	2.40	0.2171	90	60
2.16	0.1201	50	20	2.41	0.2411	100	20
2.17	0.1201	50	30	2.42	0.2411	100	30
2.18	0.1201	50	40	2.43	0.2411	100	40
2.19	0.1201	50	50	2.44	0.2411	100	50
2.20	0.1201	50	60	2.45	0.2411	100	60
2.21	0.1451	60	20	2.46	0.2651	110	20
2.22	0.1451	60	30	2.47	0.2651	110	30
2.23	0.1451	60	40	2.48	0.2651	110	40
2.24	0.1451	60	50	2.49	0.2651	110	50
2.25	0.1451	60	60	2.50	0.2651	110	60

3.3 Results

A time-series of light-ring images, one of which is shown in Fig. 3.5b, are first fit to ellipses. The ellipses are defined by two orthogonal radii (R_1 and R_2), a rotation (θ_{rot}) about the horizontal (x) axis, and center positions for which the corresponding local FTs can be calculated Hurlburt and Newell (1996); Schubring et al. (2010a); Fehring (2018). Hurlburt and Newell (1996) used the cross-correlated lag times of two independent FT sensors to calculate disturbance wave velocities in the flow. The sensors were a fixed distance apart and aligned in the flow direction. In this experiment, the light-ring captured from a single FT sensor is used by bisecting the ring into two halves (the upstream (top) and downstream (bottom) halves). The two radii are related to the upstream and downstream film thicknesses and can be cross-correlated in time to provide wave velocity. The physical distance in the flow direction between the two FT measurement locations are approximately 0.01 m.

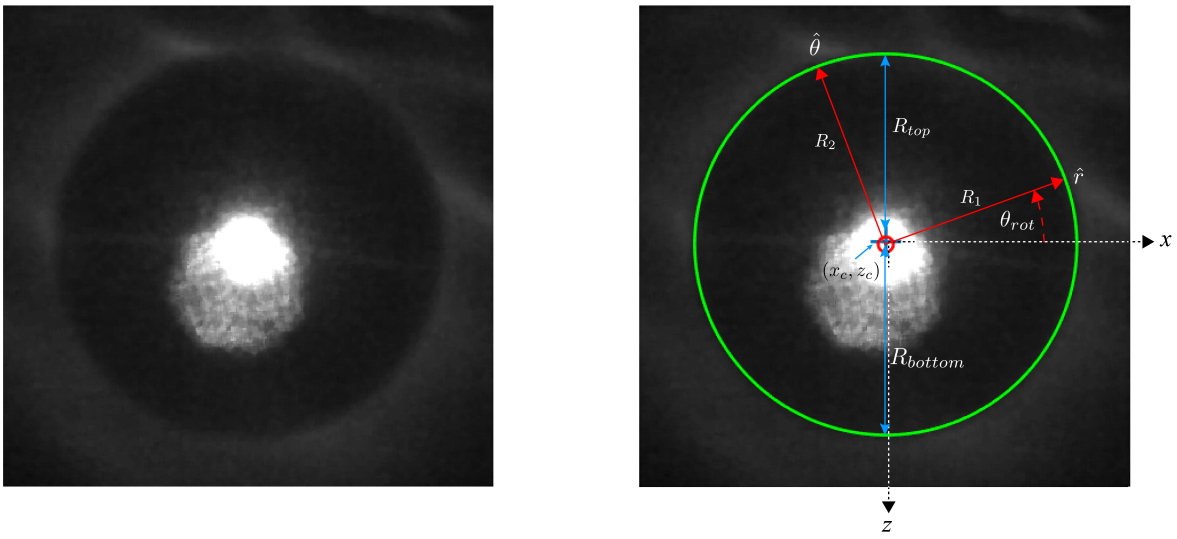

(a) (b)

Figure 3.5: (a) Sample light-ring image. (b) Illustration of ring-detection parameters and key variables. The green line is the fitted ellipse, the red lines are the radii and rotation that defines the ellipse, and the blue lines are the two radii converted into film thickness values.

The two light ring radii, (R_{up}, R_{down}), are calculated through several steps. First, a

reference center point (x_c, z_c) is defined using the center of a ring obtained from a dry calibration image. Since there is no liquid in a dry image, the center reflects the fixed point at which the laser beam is incident with the glass pane. Next, a line passing the reference center point is drawn in the flow direction. The coordinates $(x_c,\ z)$ of the intersection between the fitted ellipse and the vertical line are calculated:

$$\left(\frac{x_c \cdot \cos(\theta_{rot}) + z \cdot \sin(\theta_{rot})}{R_1}\right)^2 + \left(\frac{x_c \cdot \sin(\theta_{rot}) - z \cdot \cos(\theta_{rot})}{R_2}\right)^2 = 1 \quad . \tag{3.1}$$

Then, the distance from each intersection to the center point are recorded as the upstream and downstream radii. Finally, the corresponding film thicknesses, δ, are calculated:

$$\delta = \frac{(R - R_{dry})}{2\tan(\theta_{crit})} c_{pixel}$$

where θ_{crit} is the critical angle of light between water and air, and c_{pixel} is the pixel size, and R is the light-ring radius. The resulting film thickness time traces calculated from the upstream and downstream radii of a light-ring are shown in Fig. 3.6.

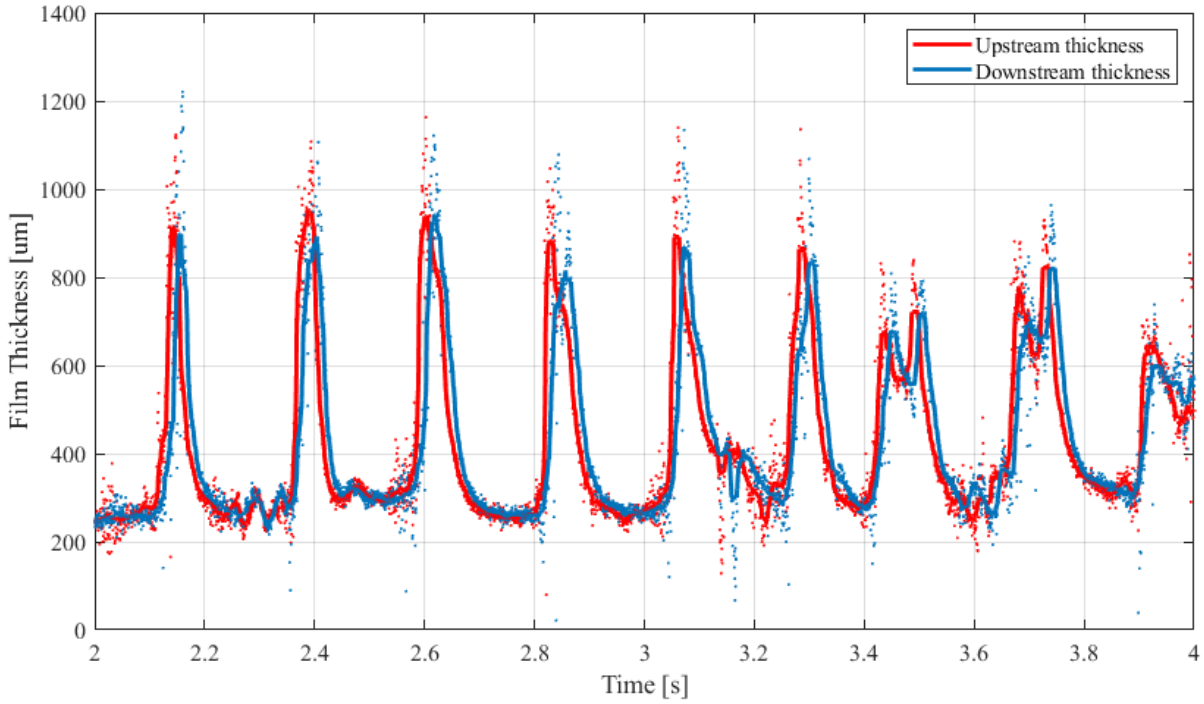

Figure 3.6: Time trace pair of film thicknesses, upstream and downstream. The raw data (shown as scatter points) are overlaid with smooth curves using a moving median filter with a filter size of 0.02 sec. Γ=0.19 kg/m-s, θ=30°

The unfiltered data is smoothed using a moving median filter with a size that contains 0.02 sec of data. At this size, the processing algorithm yields results with values of the qualities $\bar{\Gamma}_w$, $\bar{\Gamma}_b$, $\bar{w}_w$, and $\bar{\delta}_b$ that are both reasonable and insensitive to the filter size. Figure 3.7 shows the effect of the filter size on these flow characteristics. Sizes less than 0.015 sec and above 0.060 sec result in fluctuating and obviously incorrect values. Large filter sizes also remove distinctive wave shapes.

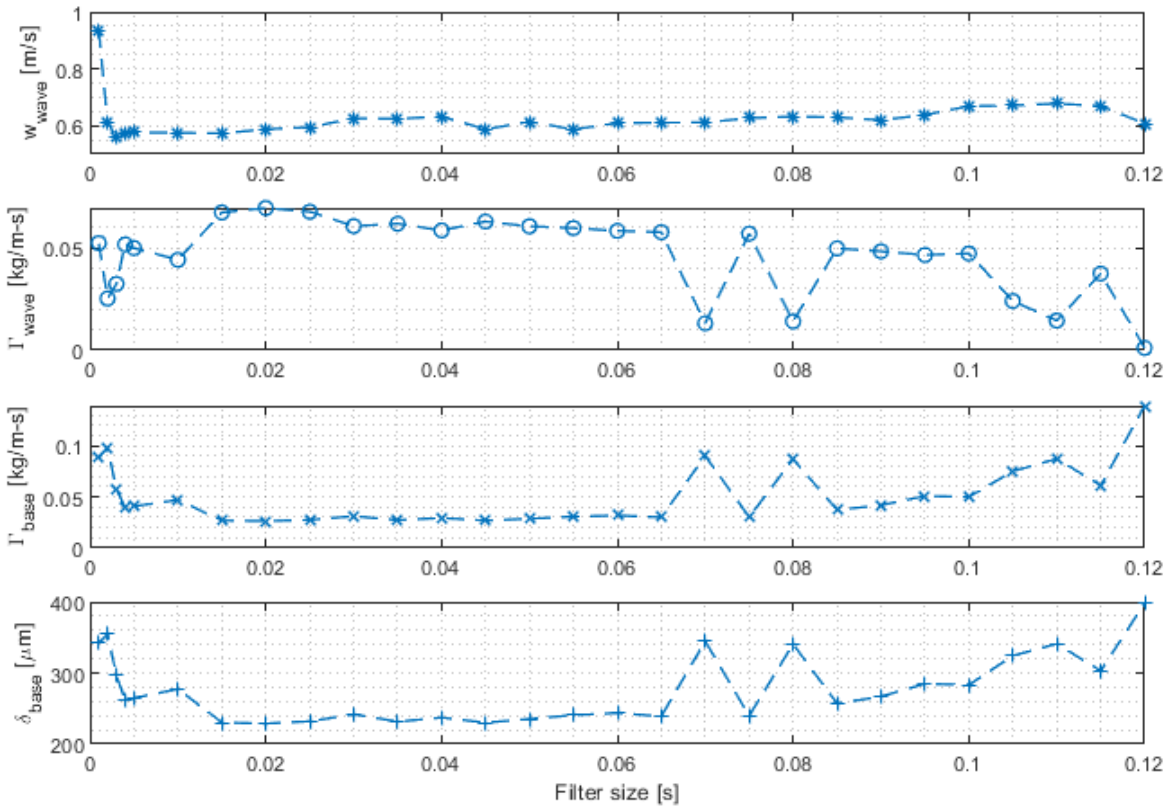

Figure 3.7: Effects of the moving median filter size on w_w, Γ_w, Γ_b, and δ_b. Γ=0.10 kg/m-s, θ=40°

3.3.1 Wave recognition

The wave recognition and velocity calculation process is based on the work by Su (2018) and Moreira et al. (2020). Figure 3.8 shows the film thickness time trace associated with three waves. The sudden increase in film thickness delineates one wave from another. These delineations are identified through an automated algorithm. The start of each wave is defined as a local minima on a rising edge in the upstream (top) thickness time trace. This rising edge traverses from a trough to a peak, and passes through specified thickness values ($\pm\sigma$) above and below the overall mean wave thickness, as shown by the horizontal lines in Fig. 3.8. The boundaries between waves that are identified using this criterion are shown in Fig. 3.8. Small ripples may create local peaks and troughs in the data, but due to their small amplitudes

they do not satisfy the recognition criteria and therefore are not identified as individual disturbance waves. Assuming that the waves are traveling at constant speed across the small distance between the top and bottom of the light ring and that their structure stays the same during this short travel, the cross-section profiles of the waves in the $z-y$ plane can be measured using this approach. Figure 3.9 shows several wave cross-sections, aligned at their peaks, for $\Gamma_{total} = 0.19$ kg/m-s and $\theta = 30^\circ$ measured with a sampling frequency of 2000 Hz. The same individual wave cross-sections (the lines) are shown individually in Fig. 3.10 overlaid with the corresponding unfiltered film thickness data (the shaded regions). The overlaid unfiltered data shows that the filter rounds out (decreases) the peak of some waves. Moreover, for the same mass flow rate, waves at 60° incline angle are less distinctive than waves at 30°, as shown in Fig 3.10b and 3.10a respectively. Time traces, overlaid wave cross sections, and individual wave cross sections of all flow conditions in this study are presented in Appendix A.1, A.2, and A.3, respectively.

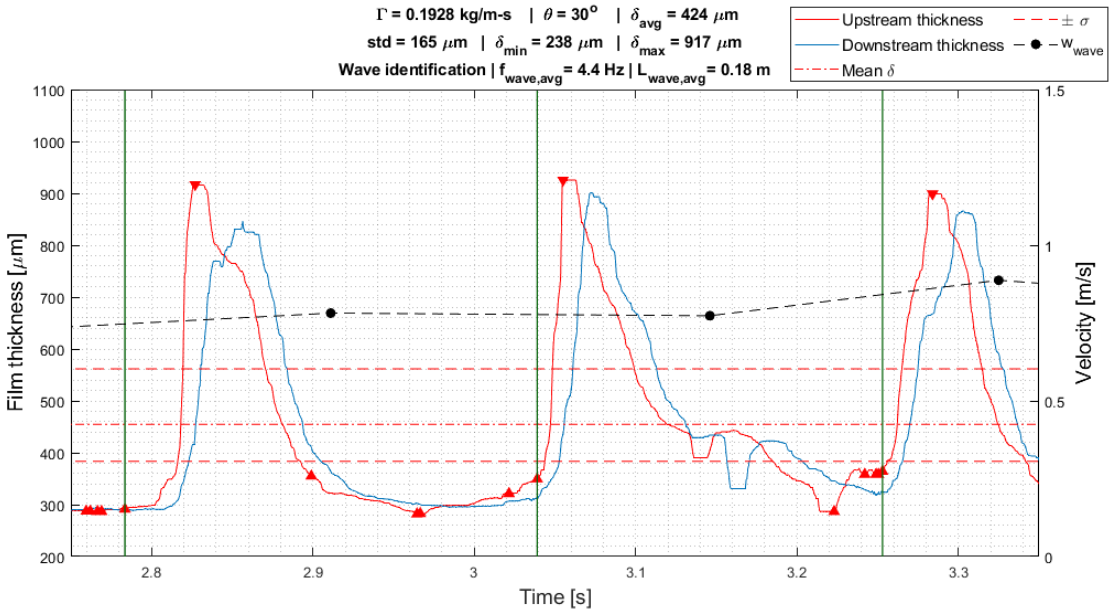

(a)

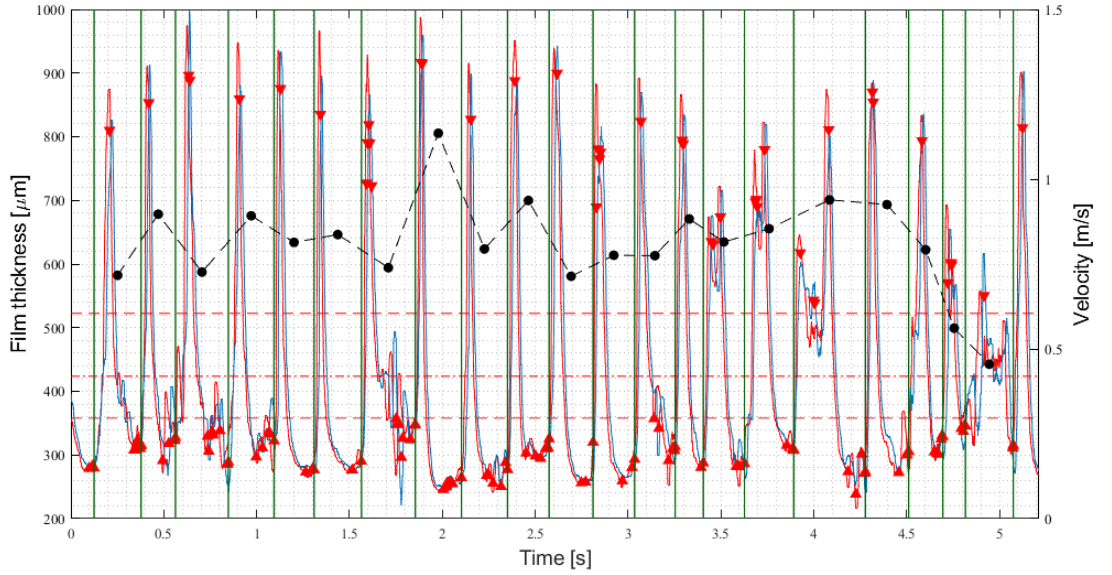

(b)

Figure 3.8: The start of each wave is defined as a point on the rising edge in the thickness data, that travels from a trough to a peak, and passes through specified values ($\pm\sigma$) above and below the overall mean wave thickness.

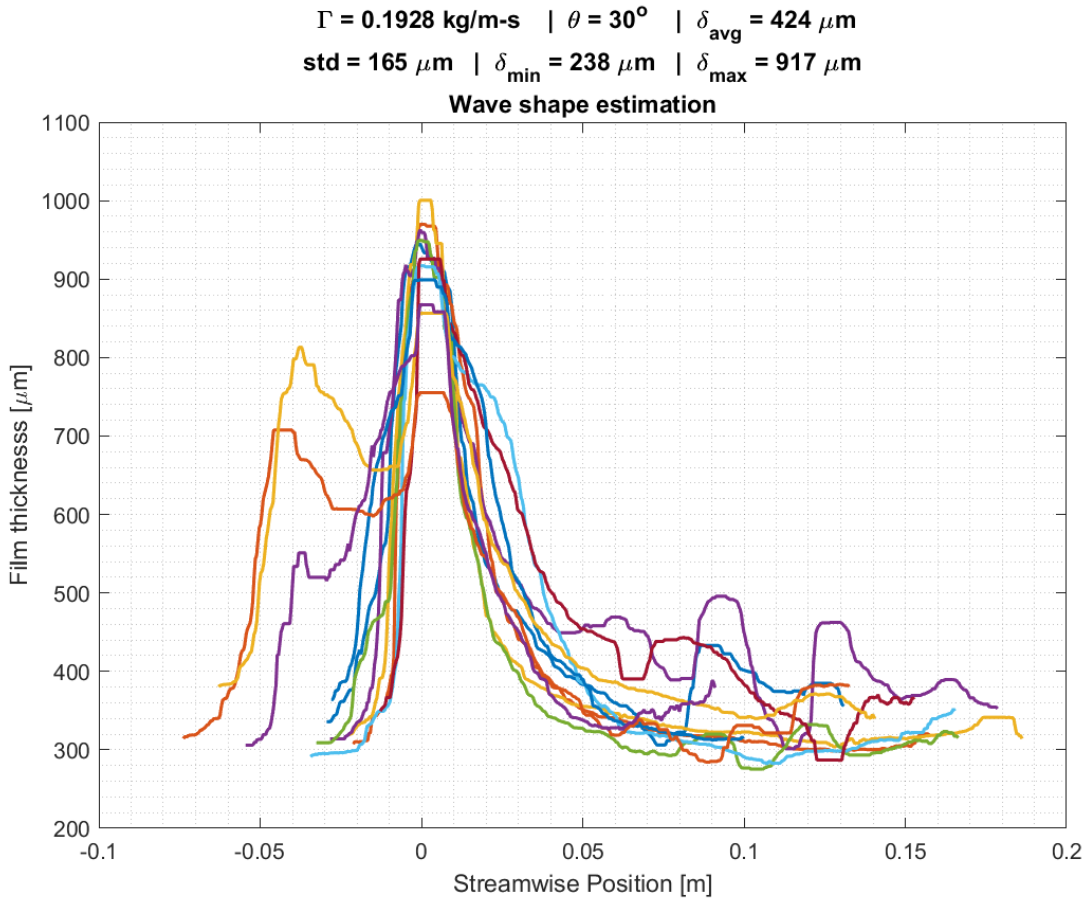

Figure 3.9: Cross-section of the waves are aligned by wave peaks. Note that there are some outliers, but the waves are generally extremely similar in both shape and size.

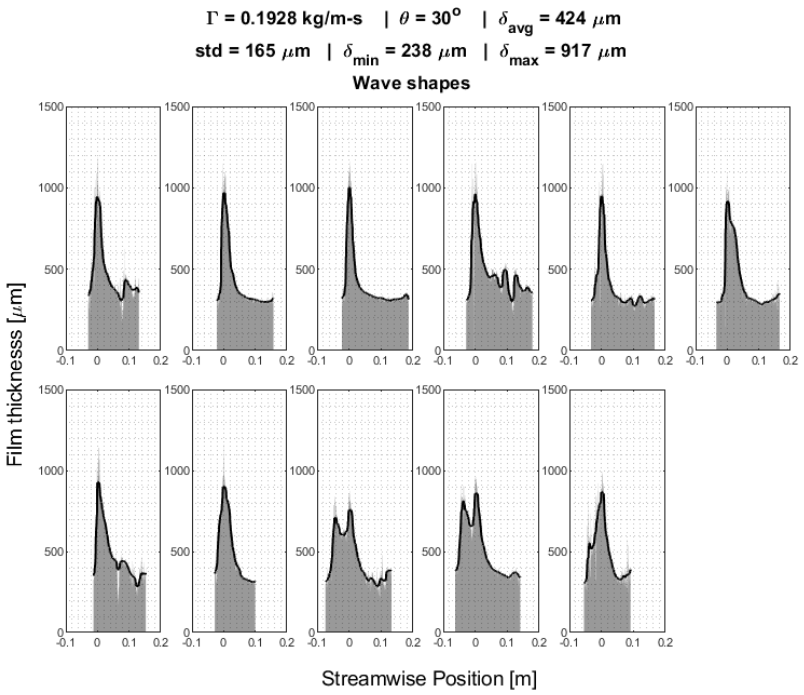

(a)

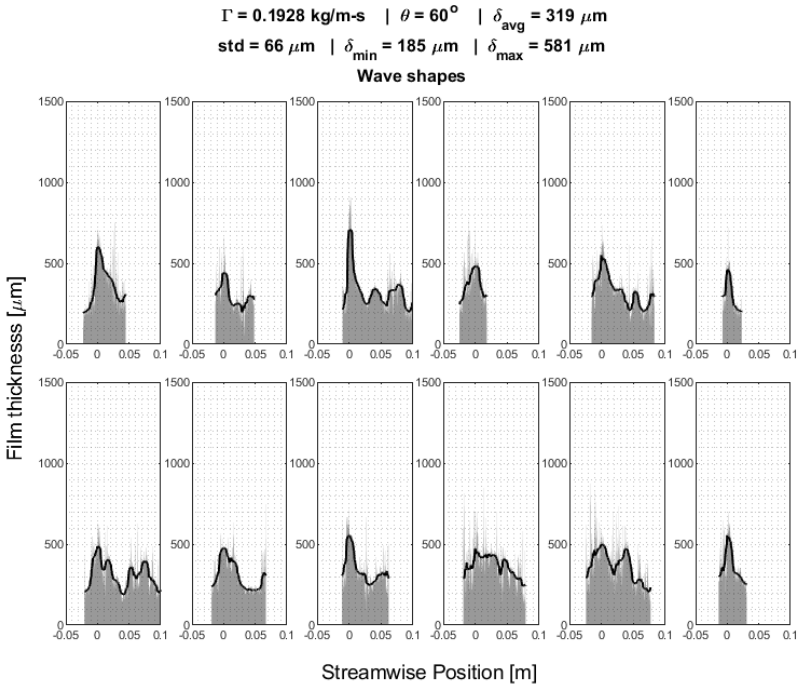

(b)

Figure 3.10: Individual cross-section of the waves from raw data (shaded) and after applying the moving median filter (line). The filter tends to round off the maximum peaks of waves.

3.3.2 Wave velocity measurement

The velocity of each wave is calculated using the most probable phase lag found by cross-correlating the top and the bottom film thickness data, as shown in Fig. 3.11a. Figure 3.11b shows the cross-correlation for different phase shifts. The phase shift corresponding to the highest cross-correlation indicates the most probable time required for the wave to travel across the light-ring. The time resolution of the cross-correlation vs. phase shift data is dependent on the sampling frequency of the film thickness data. In order to improve the time resolution, a smoothing spline is fitted to the cross-correlation curve in the region near the approximate maximum value. The maximum of the fitted curve is used as the most probably phase shift to calculate the wave velocity. This phase shift is applied to the bottom wave curve in Fig 3.11a, as shown by the dashed line, to verify that the shifted curve closely matches the top wave curve.

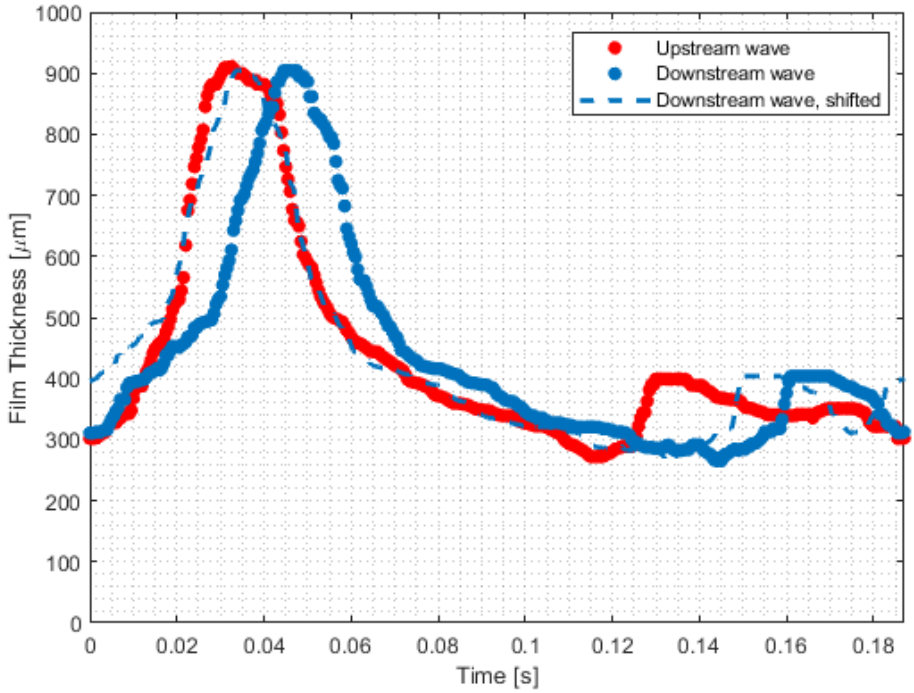

(a)

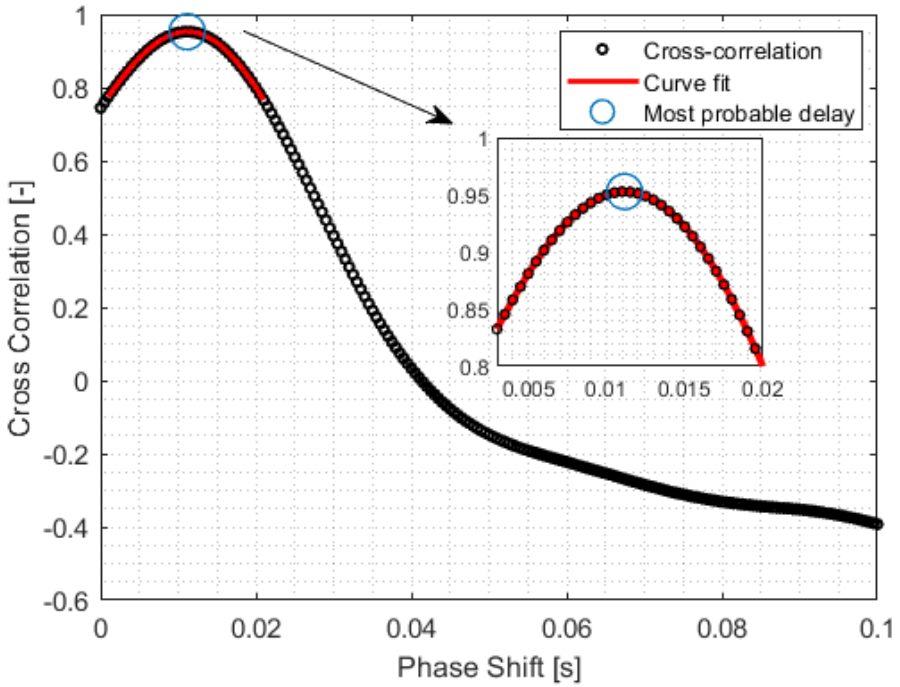

(b)

Figure 3.11: The phase shift associated with the maximum cross-correlation between the top and bottom wave FT signals is the time estimate of a wave to travel across a known small distance.

3.3.3 Validation of wave velocity measurements

The accuracy of the wave velocities calculated using the cross-correlation method was verified by comparing them with manually calculated wave velocities based on high speed video taken from above the film. The manually calculated wave velocities were calculated by measuring the time each wave took to travel a known distance in a series of wave images taken from the side. These high speed images images were taken synchronously with the light-ring images used for film thickness. Figure 3.12 shows a sample side view image with a known distance reference. The velocities calculated using the automated versus manual methods are compared in Fig. 3.13. 82% and 71% of automatically calculated velocity values are within 25% and 15% of the manually calculated values, respectively.

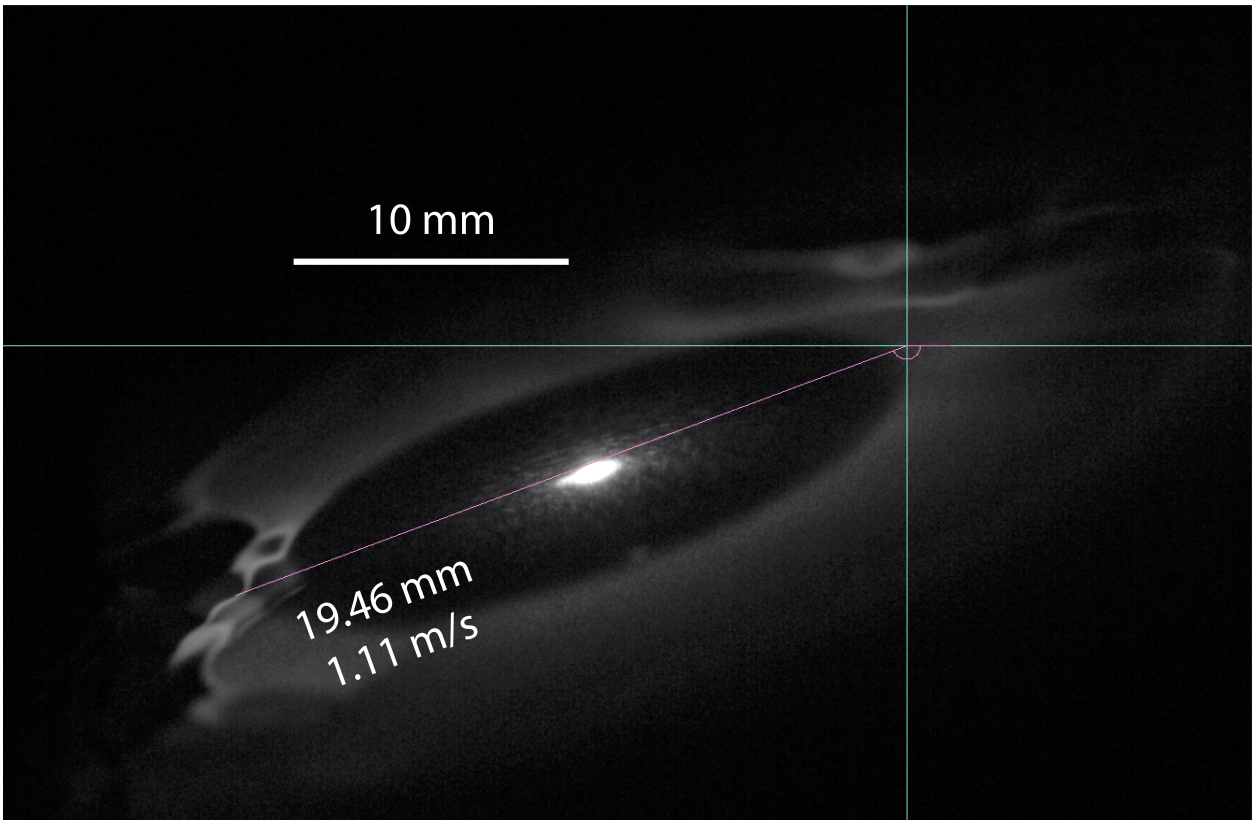

Figure 3.12: Sample image of the side view of the wavy flow. The 10-mm reference mark is used to measure the time for a wave to travel a set distance, which is used to measure its velocity.

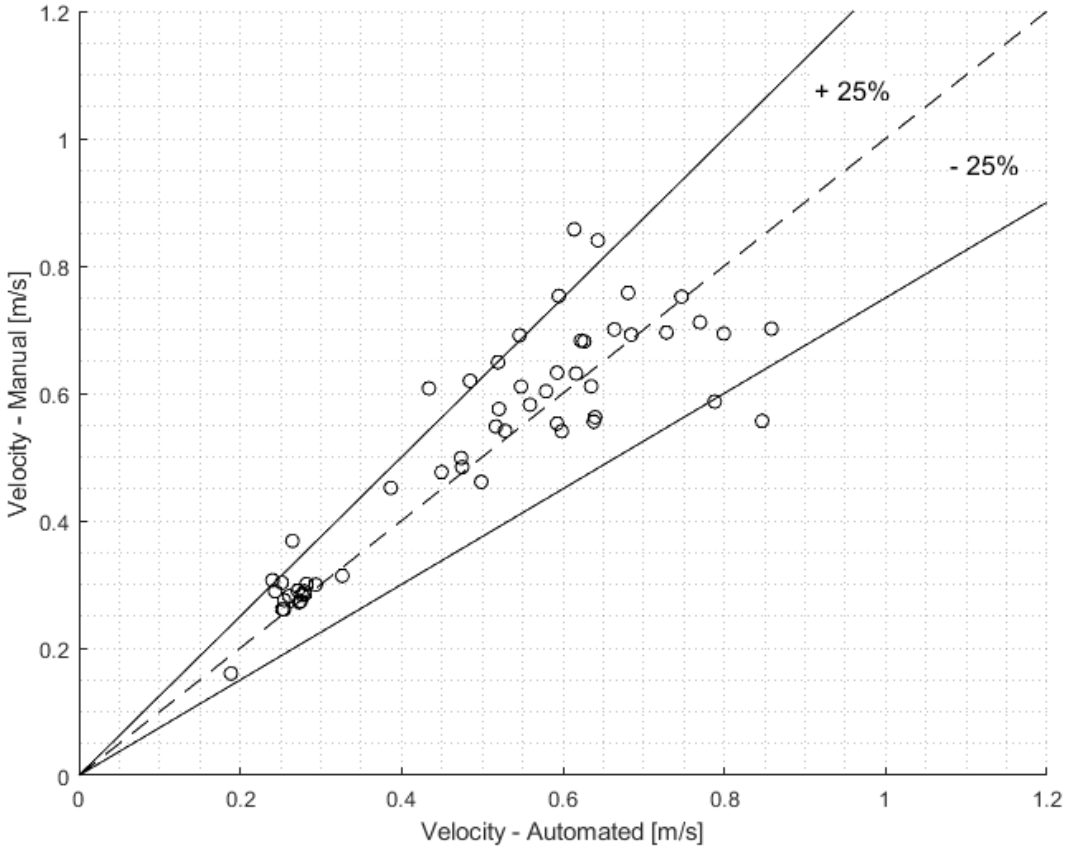

Figure 3.13: Comparison between automated versus manually measured ring velocity with a 25% margin of error.

Wave frequency as a function of the film Reynolds number, Re, and categorized by the Kapitza number, Ka, is shown in Fig. 3.14. Re is defined as,

$$Re = \frac{4\Gamma_{total}}{\mu} \quad . \tag{3.2}$$

The Kapitza number, Ka, is the ratio of surface tension force to gravitational force:

$$Ka = \frac{\sigma_l}{\rho_l (g \sin\theta)^{\frac{1}{3}} \nu_l^{\frac{4}{3}}} \quad , \tag{3.3}$$

where σ_l is the liquid surface tension, and ν_l is the liquid kinematic viscosity. The results

show that the median wave frequency is not a strong function of Re, and increases slightly with Ka. As Ka increases, the spread of wave frequency tends to decrease.

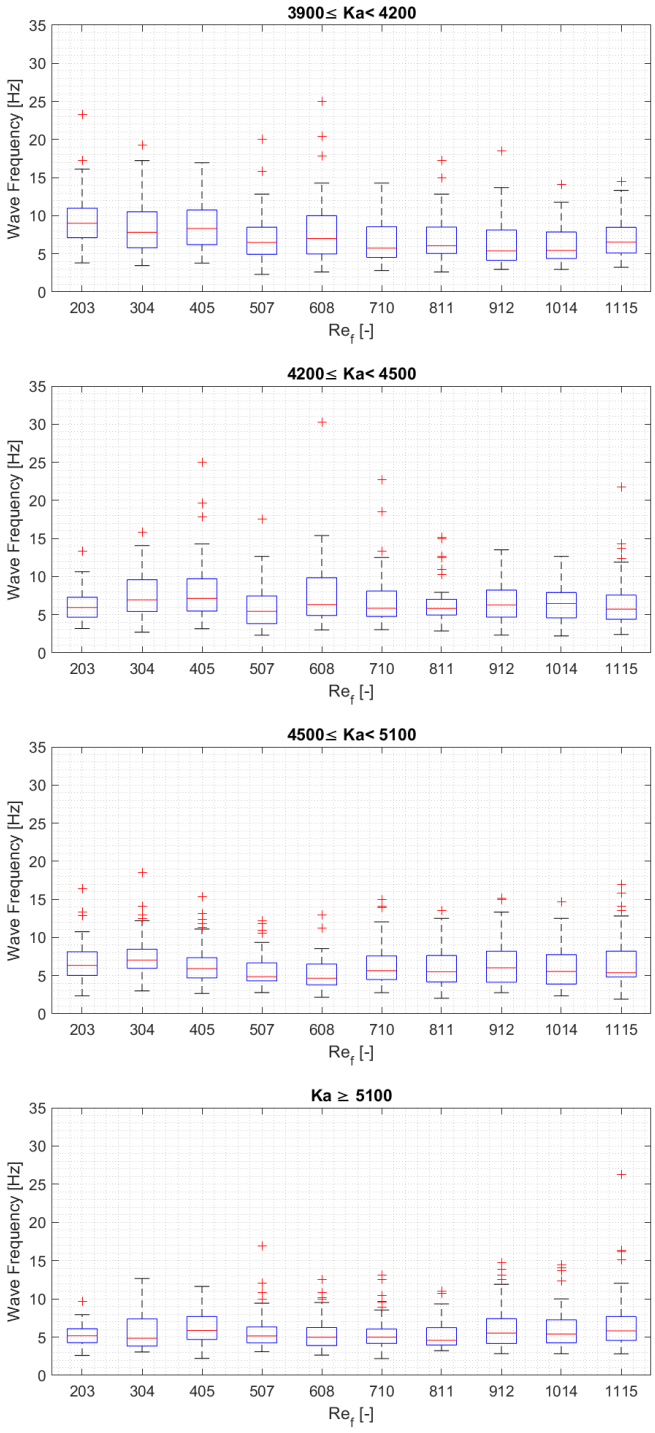

Figure 3.14: Wave frequency statistics as a function of Re. The boxes represent the 2nd and 3rd quartiles, which are separated by the median. The whiskers of the box plots represent the 1st and 4th quartiles. The crosses represent outliers that are defined as values greater than 1.5 times the interquartile range away from the bottom or top of the boxes.

3.4 Two-layer characterization framework

The experimentally observed falling liquid film suggests that the film is composed of large intermittent waves imposed on a base film layer, as illustrated in Fig. 3.15. In this situation, the total mass flow rate per unit width into the page, $\Gamma_{total,i}$, for each segment of the flow is the sum of $\Gamma_{b,i}$ in the base film and $\Gamma_{w,i}$ in the waves at any instant in time:

$$\Gamma_{total,i} = \Gamma_{b,i} + \Gamma_{w,i} \quad . \tag{3.4}$$

Time-averaging over the entire film, we obtain:

$$\overline{\Gamma}_{total} = \overline{\Gamma}_{b} + \overline{\Gamma}_{w} \quad . \tag{3.5}$$

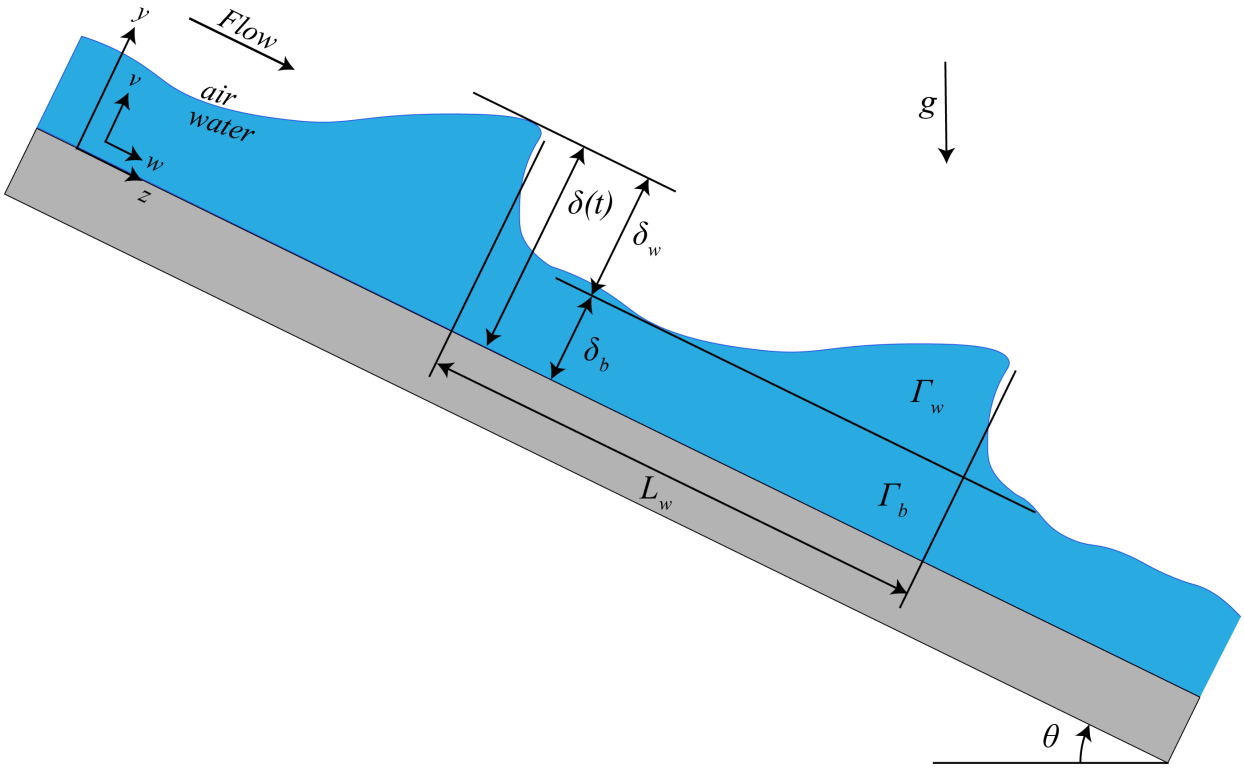

Figure 3.15: Illustration of the base-wave liquid film model for a falling liquid film on an inclined plane. The incline angle is θ with respect to horizontal. δ and Γ represents the film thickness and mass flow per span-wise width of the flow channel (into the page), respectively. Subscripts w and b are used to denote wave and and base film quantities, respectively. L_w is the stream-wise distance between waves.

In this work, the base film is defined as the underlying liquid layer with an associated $\Gamma_{b,i}$ given by:

$$\Gamma_{b,i} = \rho_l \overline{w}_b \delta_b \tag{3.6}$$

where ρ_l is the liquid density, $\overline{w}_b$ is the time-averaged base film velocity, and δ_b is the base film thickness. The base film layer in the falling film facility is assumed to be a wave-less, gravity-driven, fully-developed laminar flow, with no shear at the liquid-vapor interface. The mean velocity of such a flow is given by:

$$\overline{w}_b = \frac{\Delta\rho \, g \, \delta_b^2 \, \sin(\theta)}{3\mu_l} \tag{3.7}$$

where $\Delta\rho$ is the difference in density at the vapor-liquid interface, g is the gravitational acceleration in the downwards direction, and μ_l is the liquid viscosity (Carey, 1992). Here, the base film flow rate is assumed to be constant with time. Therefore, the time averaged base film flow is the same as the instantaneous value:

$$\overline{\Gamma}_b = \rho_l \frac{\Delta\rho g \sin(\theta)}{3\mu_l}\delta_b^3 \quad . \tag{3.8}$$

$\overline{\Gamma}_w$ is the average Γ_w associated with many (n) waves observed experimentally

$$\begin{aligned}
\overline{\Gamma}_w &= \sum_{i=1}^{n}\Big[\frac{\int_0^{L_{w,i}} \delta_{w,i}\ dz}{t_i}\Big]\frac{\rho_l}{n} \\
&= \sum_{i=1}^{n}\Big[\frac{\int_0^{L_{w,i}} (\delta_i - \delta_b)\ dz}{t_i}\Big]\frac{\rho_l}{n} \\
&= \sum_{i=1}^{n}\Big[\frac{\int_0^{L_{w,i}} (\delta_i)\ dz}{t_i}\Big]\frac{\rho_l}{n} - \overbrace{\sum_{i=1}^{n}\Big[\frac{\int_0^{L_{w,i}} dz}{t_i}\Big]\frac{\rho_l}{n}\delta_b}^{=\overline{\Gamma}_b}
\end{aligned} \tag{3.9}$$

where t_i represents the duration of time required for wave i to travel $L_{w,i}$ (the distance between two waves); t_i includes any intermittency between waves (during which $\delta_{w,i} \approx 0$). Here, the wave shape is assumed to be 2-D and constant across the width of the flow channel. Substituting Eqs. (3.6) and (3.9) into Eq. (3.5) leads to:

$$\overline{\Gamma}_{total} = \rho_l \frac{\Delta\rho g \sin(\theta)}{3\mu_l}\delta_b^3 + \sum_{i=1}^{n}\Big[\frac{\int_0^{L_{w,i}} (\delta_{w,i})\ dz}{t_i}\Big]\frac{\rho_l}{n} - \sum_{i=1}^{n}\Big[\frac{\int_0^{L_{w,i}} dz}{t_i}\Big]\frac{\rho_l}{n}\delta_b \quad . \tag{3.10}$$

Equation (3.10) represents $\overline{\Gamma}_{total}$ as a function of δ_b, the only unknown (or unmeasured) variable. All other variables are known from experimental measurements. Rearranging Eq.

(3.10) leads to:

$$\left(\rho_l \frac{\Delta\rho g \sin(\theta)}{3\mu_l}\right)\delta_b^3 - \left(\sum_{i=1}^{n}\left[\frac{\int_0^{L_{w,i}} dz}{t_i}\right]\frac{\rho_l}{n}\right)\delta_b + \left(\sum_{i=1}^{n}\left[\frac{\int_0^{L_{w,i}} (\delta_{w,i})\ dz}{t_i}\right]\frac{\rho_l}{n} - \overline{\Gamma}_{total}\right) = 0 \quad . \tag{3.11}$$

Eq. (3.11) shows that the base film thickness satisfying the two-layer wave equation is the solution to a cubic polynomial. The following sections validate this approach and describe an estimation of the base film thickness obtained from experimental data. Using the estimation, other variables in Eq. (3.11) can be solved.

3.4.1 Validation of the two-layer framework

The performance of the two-layer framework is validated using independently measured liquid-film flow rate and liquid-film thickness values. Fig. 3.16 shows that 70% of the estimated base film thickness values, obtained from Eq. 3.11, agree within 25% of the measured values. The measured base film thickness is defined as the median of the first quartile of the measured film thickness, which is related to the film thickness that exists, on average, between waves. The data points are categorized by Ka. Given a liquid film flow rate, the framework accurately predicts the base film thickness. Alternatively, given an average base film thickness, it predicts the corresponding liquid film flow rate, as shown in Fig. 3.17. The framework tends to estimate both variables more poorly when $Ka < 3900$. At these low Ka numbers, when the incline angle is steep, waves are traveling so close to one another that it is difficult to measure the base film accurately. Consequently, the measured base film is overestimated and predictions are not accurate.

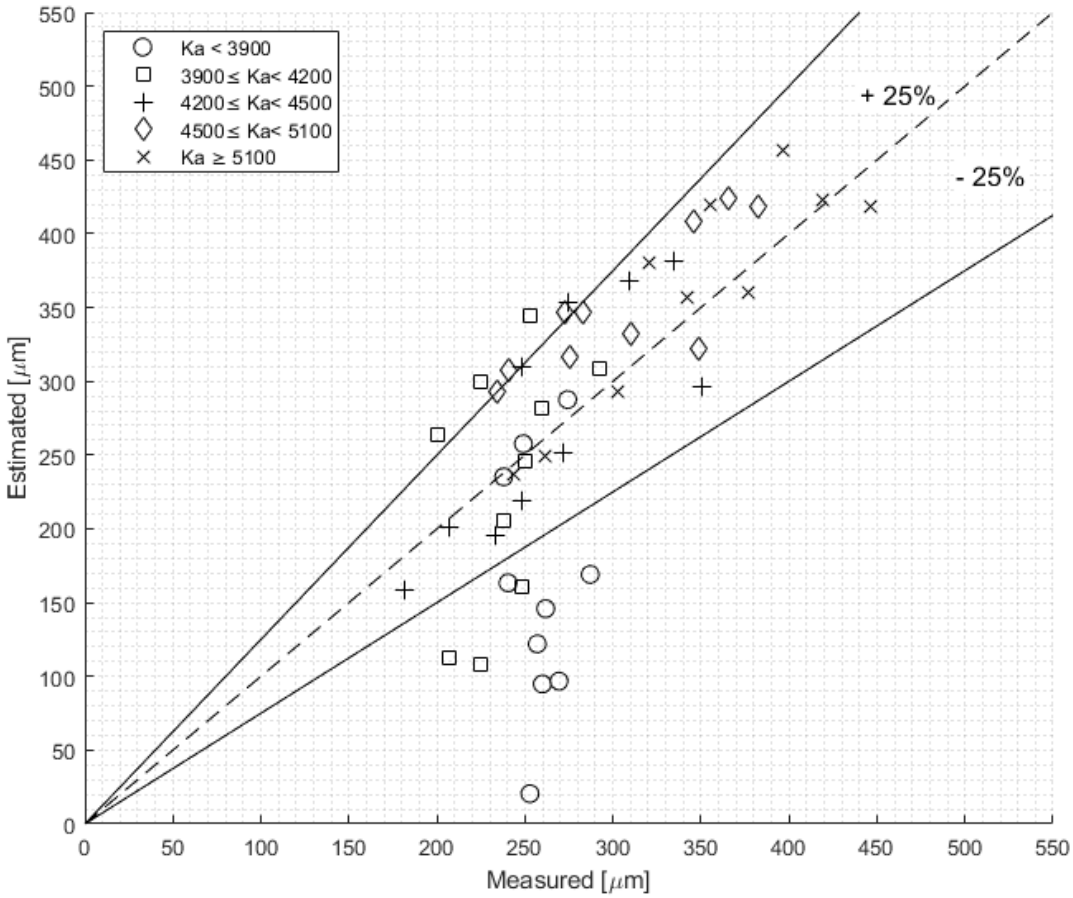

Figure 3.16: The two-layer framework generally predicts the base film thickness well when compared to the observed base film thickness for $Ka > 3900$.

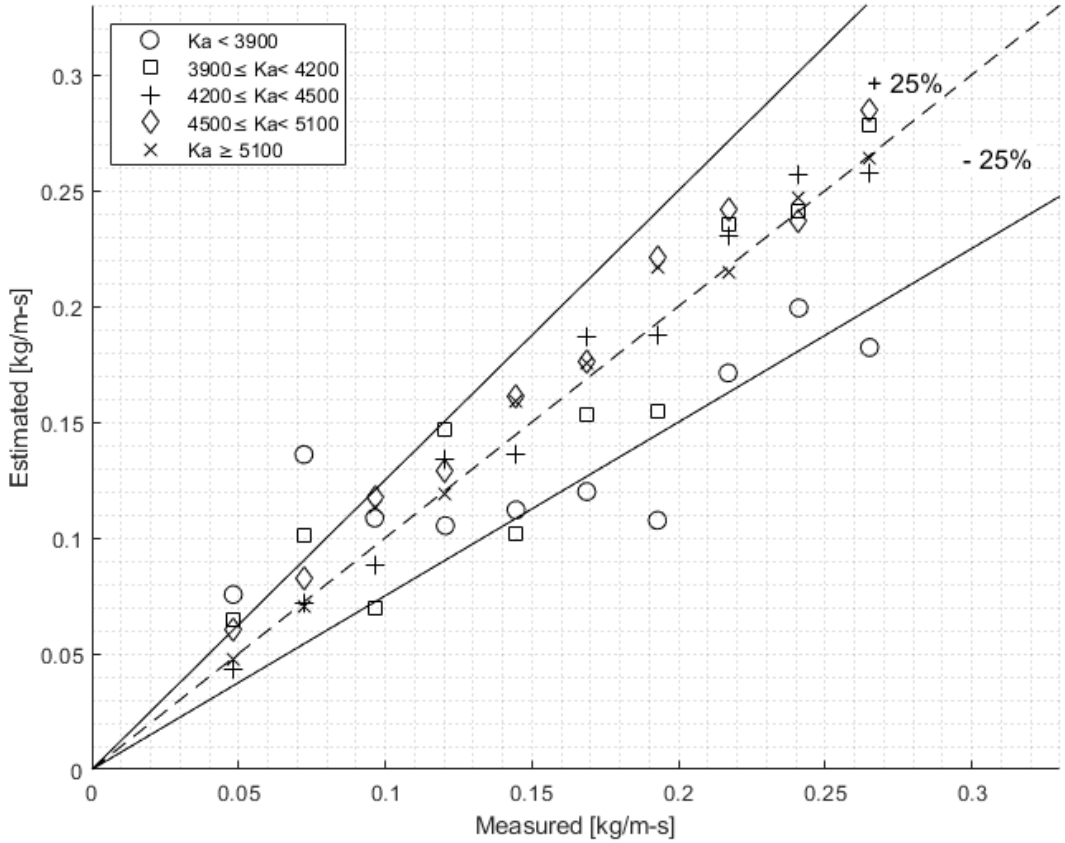

Figure 3.17: The two-layer framework predicts the liquid film flow rate well given the base film thickness.

3.4.2 Analysis using two-layer framework

The wave and base film liquid flow rates can be estimated using the two-layer framework. As shown in Fig. 3.18, most of the liquid mass is transported by the waves. The base film flow rate increases with Re, albeit at a slower rate than the wave flow rate.

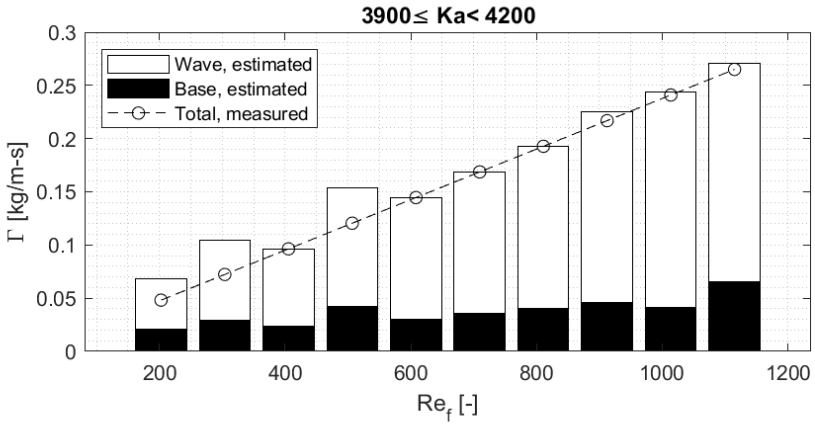
3900≤ Ka< 4200
Wave, estimated
Base, estimated
Total, measured
Γ [kg/m-s]
Re_f [-]
0
0.05
0.1
0.15
0.2
0.25
0.3
200
400
600
800
1000
1200

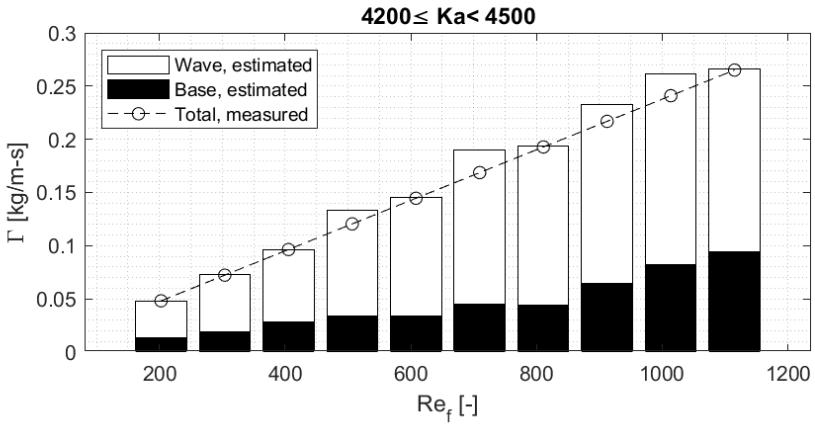
4200≤ Ka< 4500
Wave, estimated
Base, estimated
Total, measured
Γ [kg/m-s]
Re_f [-]
0
0.05
0.1
0.15
0.2
0.25
0.3
200
400
600
800
1000
1200

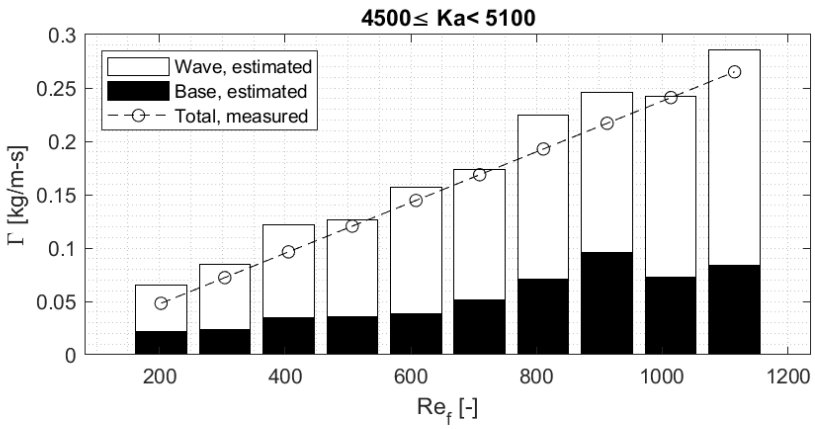
4500≤ Ka< 5100
Wave, estimated
Base, estimated
Total, measured
Γ [kg/m-s]
Re_f [-]
0
0.05
0.1
0.15
0.2
0.25
0.3
200
400
600
800
1000
1200

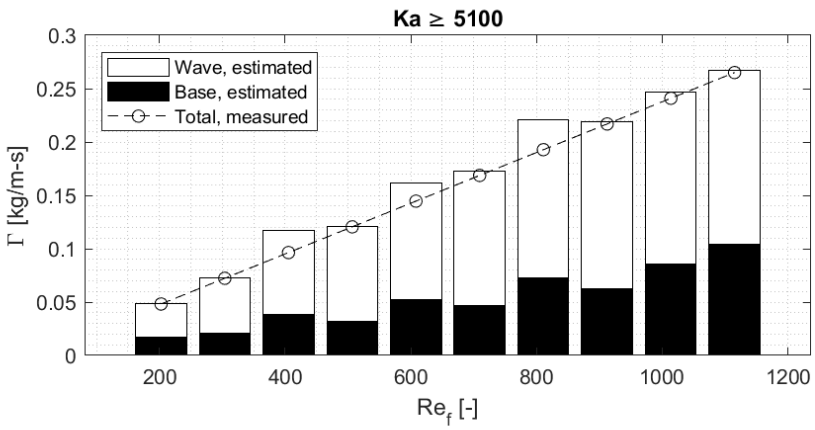
Ka ≥ 5100
Wave, estimated
Base, estimated
Total, measured
Γ [kg/m-s]
Re_f [-]
0
0.05
0.1
0.15
0.2
0.25
0.3
200
400
600
800
1000
1200

The measurements showed several trends in the wave characteristics with respect to the film Reynolds number. The characteristics are presented in wall units to be more generally comparable with other data. Figure 3.19 shows that the wave velocity (in wall units) increases with Re to approximately 1/3 power:

$$u_w^+ = 2.44 Re^{0.31} \qquad (r^2 = 0.87), \tag{3.12}$$

The wave velocity in wall units is defined as:

$$u_w^+ = \frac{u}{u_{\tau,w}}, \tag{3.13}$$

where $u_{\tau,w}$ is the friction velocity of the wave represented in terms of the wall shear stress, $\tau_{wall,w} = \rho g \bar{\delta}_w \sin\theta$, and is estimated as:

$$\begin{aligned} u_\tau &= \sqrt{\frac{\tau_{wall,w}}{\rho}} \\ &= \sqrt{g \bar{\delta}_w \sin\theta}, \end{aligned} \tag{3.14}$$

where $\bar{\delta}_w$ is the time-average wave amplitude. Fig. 3.20 shows that for $Ka > 3900$ the wave amplitude in wall units increases linearly with Re:

$$\delta_w^+ = 0.03 Re \qquad (r^2 = 0.53). \tag{3.15}$$

The wave amplitude in wall units is defined as:

$$\delta_w^+ = \frac{\bar{\delta}_w u_{\tau,w}}{\nu_l} \tag{3.16}$$

where ν_l is the liquid kinematic viscosity.

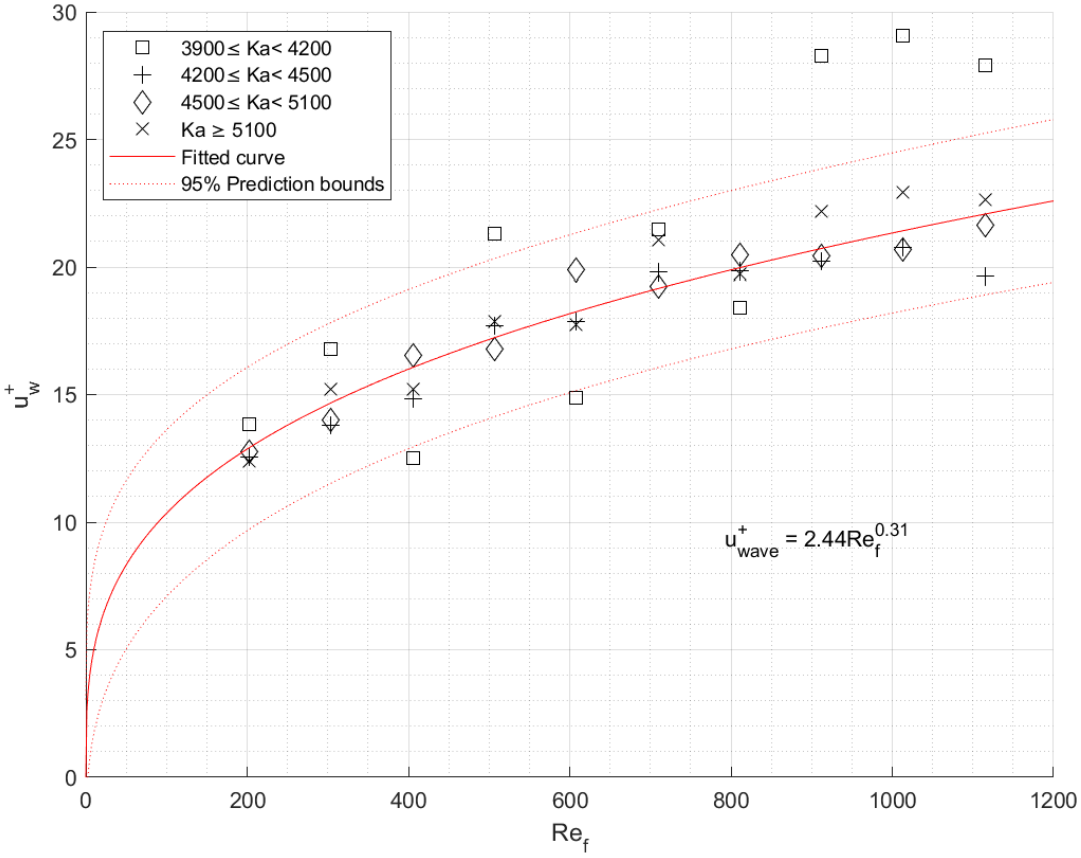

Figure 3.19: Wave velocity in wall units as a function of Re.

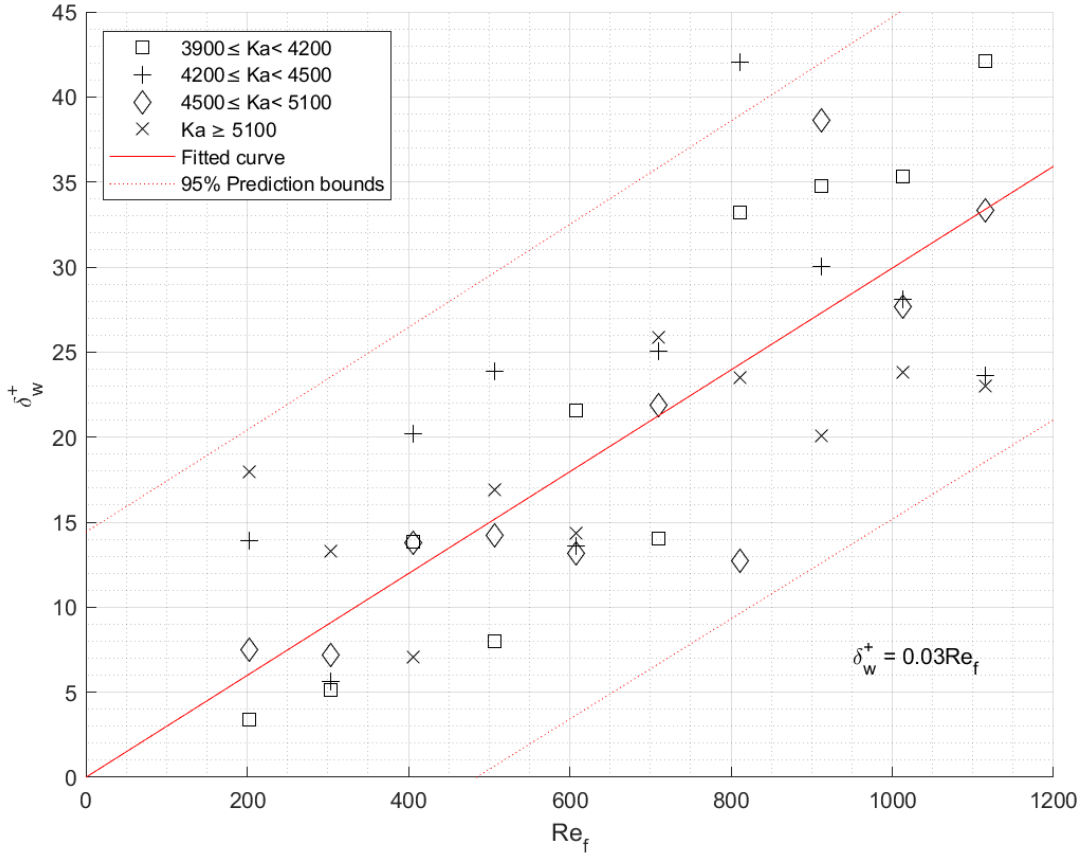

Figure 3.20: Wave amplitude in wall units as a function of Re.

Henstock and Hanratty (1976) presented similar analysis for disturbance waves in vertical annular flows, and developed an empirical fit of time-average film thickness (in wall units) to the film Reynold's number:

$$\delta_{avg}^{+} = \left[\left(0.707Re^{0.5}\right)^{2.5} + \left(0.0379Re^{0.90}\right)^{2.5}\right]^{0.40} \quad , \tag{3.17}$$

where δ_{avg}^{+} is defined as:

$$\delta_{avg}^{+} = \frac{\bar{\delta}_f u_{\tau,avg}}{\nu_l} \quad . \tag{3.18}$$

The characteristics of the liquid film in annular flow are similar to those of a falling film, although the liquid vapor interface is sheared in annular flow. Results from this work are

well predicted by the Henstock and Hanratty (1976) correlation, as shown in Fig. 3.21. This suggests that the current framework may also apply to other types of liquid film flows such as vertical annular flow.

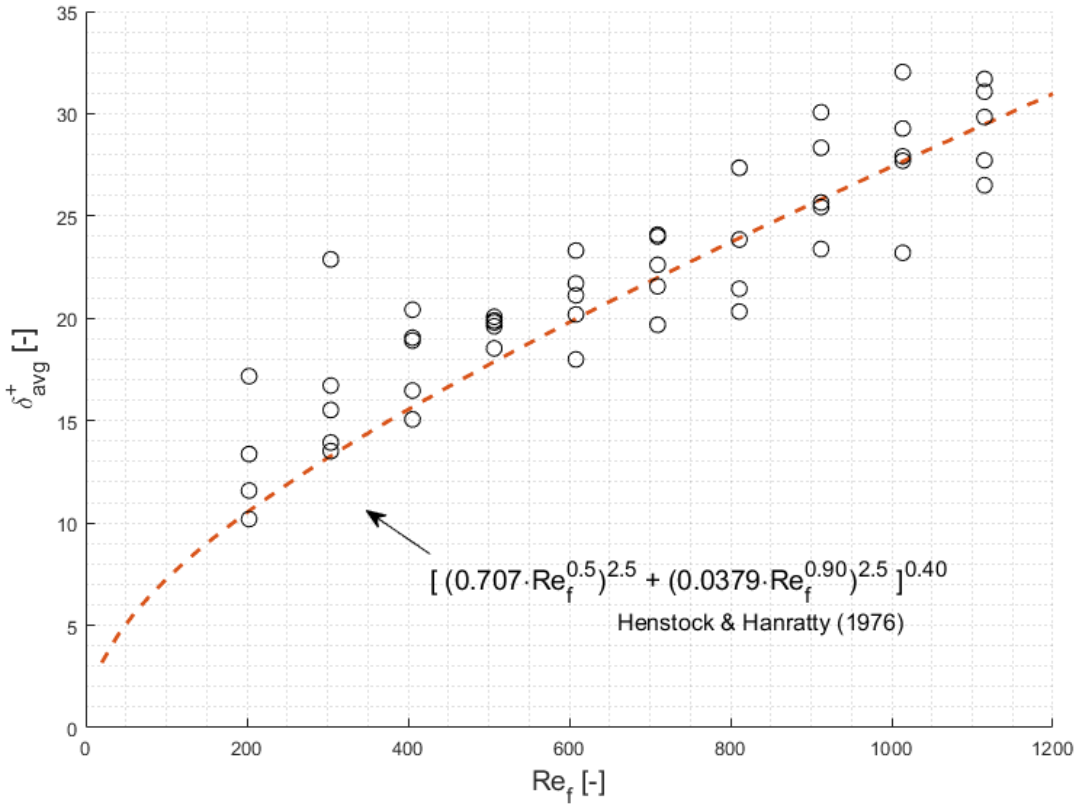

Figure 3.21: Results from the current work agree with published correlations by Henstock and Hanratty (1976)

Chapter 4

Annular flow

4.1 Facility

The Multiphase Flow Visualization and Analysis Laboratory (MFVAL) is an experimental research laboratory within the Department of Mechanical Engineering at the University of Wisconsin - Madison. The MFVAL has worked to develop a low-pressure refrigerant two-phase annular flow facility that is capable of vertical upward flows with any vapor quality, and mass flux up to 200 kg/m^2-s. The long-term goal of the laboratory is to develop a mechanistic description of the transition to dryout based on local flow and heat transfer quantities such as the local film thickness, film flow rate, wave characteristics, and local heat transfer coefficient.

For the purpose of characterizing the heat transfer of annular flow past a wall obstruction, three facility features are worth mentioning:

- **Fully instrumented, optically clear, heated test section:** The test section has large glass windows coated with a thin film of fluorine-doped tin oxide (FTO). The windows are transparent and allow optical access for measurements and flow visualization. In addition, the windows can be heated by passing a current through the FTO coating with a heat flux up to 55 kW/m^2. The test section is also fully instrumented with

pressure and temperature sensors. A schematic of the facility is shown in Figure 4.1.

- **A suite of high-speed optical measurement techniques:** The MFVAL has developed optical measurement techniques for the instantaneous, local, and non-intrusive measurements of film thickness and wall temperature (Chan et al., 2019). Coupled with high-speed videos, they allow for the time-resolved characterization of heat transfer processes during transient and cyclic events, such as the re-wetting of a surface driven by a disturbance wave. Recently, the film thickness measurement method was extended to measure wave velocity and statistics (Moreira et al., 2020). The laser optics technique used to measure wall temperature was adapted to measure the state (wet or dry) of the inner wall surface (Morse et al., 2021). The state measurement allowed for the acquisition of statistics pertaining to the duration of dryout events and time between dryout events.

- **Interchangeable wall obstruction test-section module:** The most recent upgrade to the test section is a wall-obstruction module. While single-phase flow past an obstruction has been thoroughly investigated in literature, there has been virtually no literature on two-phase flow past an emerged obstruction oriented perpendicular to the flow direction. This module allows for studies with such obstructions; it can be installed only when needed, and accepts a wide range of obstruction geometries and sizes above 1 mm in diameter. Details of this module are described in Section 4.2.

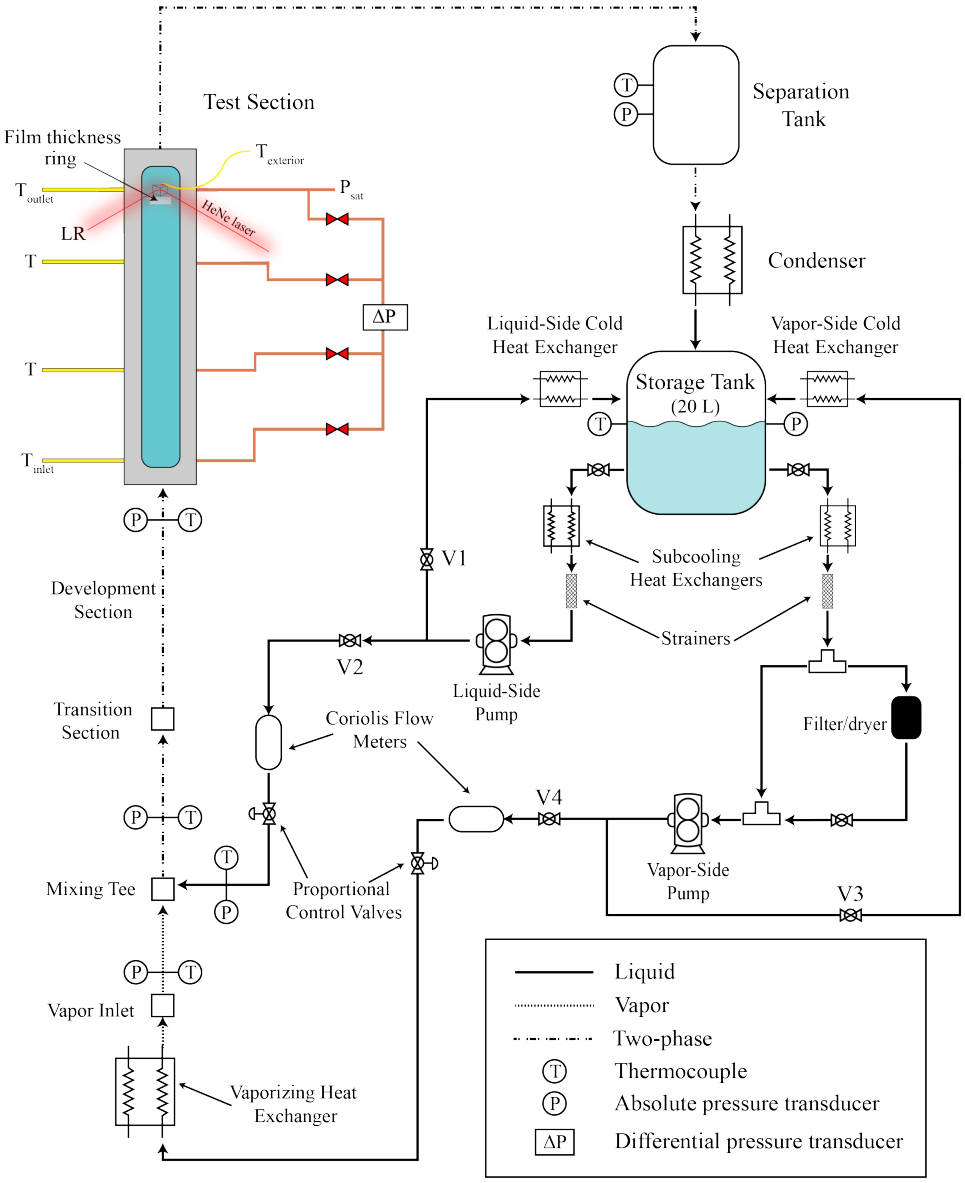

Figure 4.1: Schematic of the annular flow facility.

4.2 Test section obstruction module

The effects of a protruding obstruction on annular flow, either with or without heat flux at the flow channel wall, have not been widely investigated in publications so far. Occlusions may occur in an internal flow unintentionally, such as in the case of fouling, or intentionally,

as in the case of cooling heated rods, or inevitably, as in the case of mechanical fasteners. Regardless of the reason, these obstructions in the flow are analogous to bridge pillars in a river, where the pillars disturb the river flow. While civil engineers are interested in bridge scour avoidance[1], and have published countless papers showing its importance, that is not the focus for this task. The purpose of constructing the setup to investigate these annular flow obstructions is to better understand their effects on the liquid film thickness and, consequently, the heat transfer behavior of the flow near the obstructions.

4.2.1 Design Criteria

Several design criteria are considered for this experimental apparatus.

- **Material compatibility** The working fluid in the annular flow facility, R245fa, is known to dissolve most commonly used polymers, including acrylic, silicone and Viton. Ultem (polyetherimide) and EPDM rubbers of particular compositions are two exceptions; they are known to be compatible with R245fa from past experience. These chemically compatible polymers, stainless steel, steel, and aluminum are used to construct this apparatus.

- **Obstruction geometry** Obstructions with different geometries and sizes can be installed to the apparatus. This helps in investigating the effects of obstruction geometry on the flow field. The mechanism that holds the obstruction in place needs to prevent the obstruction from rotating about its longitudinal axis. The apparatus can accept obstructions of any size that fits within the flow channel.

- **Electrically insulated obstructions** The obstruction needs to be electrically insulated to prevent short-circuiting the electrically conductive glass wall. The channel wall surface is deposited with fluorine-doped tin oxide (FTO), a conductive metal oxide coating, that serves as an optically transparent heater, creating heat flux that is

[1]Bridge scour is the removal of sand and gravel from around bridge abutments or piers caused by fast flowing water that compromises structural integrity.

transferred to the flow. Ultem is used for the obstruction as it is electrically insulating and soft, which aids in avoiding scratching the channel wall as the obstruction is installed.

- **Thermal constraints - temperature** The temperature of the area of the heated channel wall where the obstruction makes contact can rise significantly due to the low thermal conductivity of Ultem. A thermal analysis is needed to ensure the increased wall temperature stays within the operating temperature range of the Ultem obstruction.

- **Thermal constraints - expansion** The glass wall is expected to expand as it is heated. While the magnitude of thermal expansion of glass is on the order of microns for the operating temperature range of the test section, this is sufficient for the glass to crack under a point load where the obstruction presses against the wall, or for the otherwise unsupported obstruction to lose contact with the glass and fall into the flow channel. The obstruction and its supporting mechanism need to account for the expansion of both the glass and themselves through the use of elastic materials, such as rubbers and springs. A simply rigid and fixed support is insufficient as it does not compensate for gaps between the obstruction and the glass.

- **Ease of use** The test section into which the obstruction will be installed contains many fragile components. Any damage due to installing the obstruction is highly undesirable. The obstruction module needs to be installed in a simple way to avoid damaging both the test section and the module itself. The obstruction falling into the flow channel during both installation and operation is of concern. This is because the upstream region of the flow channel (which is physically lower in the facility) is connected directly to pumps and flow adapters. Disassembling multiple components of the flow facility would increase downtime and refrigerant waste.

- **Modularity** Changing the obstruction geometry without fabricating an entirely new

obstruction module is a requirement for this design. A modular obstruction mounting mechanism is needed for parametric studies related to the impact of geometry on flow behavior. Moreover, the stream-wise position of the obstruction in the flow channel needs to be set precisely and repeatably so that the optics do not need to be re-positioned each time the obstruction is changed.

4.2.2 Current design

A CAD rendering of the module is shown in Figure 4.2. The module supports the obstruction with extendable rods that are attached to a cross bar on the top. The top bar is part of the top plate which is installed to the test section as an additional module. Figure 4.3 shows the exploded view of the assembly with descriptions to each component. Besides adding mechanical support and eliminating the risk of the obstruction falling, this design allows for fine positioning of the obstruction during installation and sufficient compensation for thermal expansion.

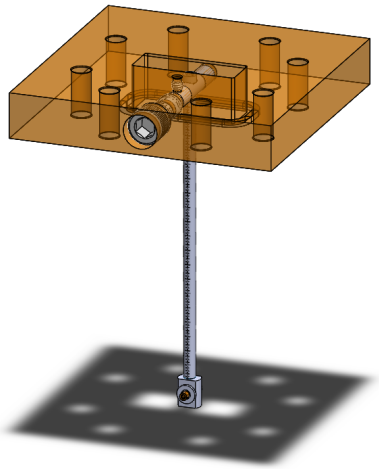

Figure 4.2: CAD rendering of the obstruction module for the annular flow facility.

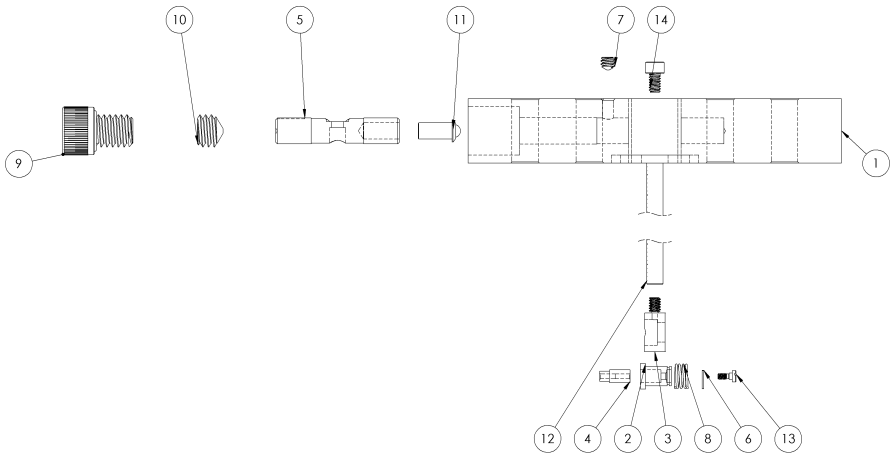

Figure 4.3: Exploded view of the improved design assembly. 1) Ultem plate attaches to the test section top plate. 2) Steel chuck holds the obstruction. 3) Steel bottom attachment holds the lower sub-assembly to the extendable rods. 4) Ultem obstruction. 5) Steel top rod. 6) Steel retaining ring. 7) Brass set screw keeps the top rod from rotating. 8) Chuck spring accounts for thermal expansion in the test section and maintains obstruction-window contact. 9) Sealing socket head screw. 10) Cone-point set screw fine tunes axial position of the top rod. 11) Spring plunger creates opposing force to the cone-point set screw. 12) Stainless steel extendable rods. 13) Precision shoulder screw draws the obstruction into the chuck. 14) Vented screw secures the extendable rod to the top rod.

A conjugate thermal and flow simulation using SolidWorks 2021 (Dassault Systemes, 2020) was performed to validate the thermal performance of the obstruction in dry-out flow conditions - the worst-case flow scenario. The vapor flow (P=120 kPa and T=45°C) is super-heated at the inlet. The mass flow rate is 60 g/s. The wall heat flux is 30 kW/m^2 and the HTC on the outer glass walls is 25 W/m^2-K at T_{amb}=25°C . The cross-sectional temperature distribution of the obstruction and surrounding walls are shown in Figure 4.4. The simulation results show the maximum temperature near the obstruction occurs in the glass wall and is approximately 140°C . The Ultem obstruction stays within its maximum operation temperature, at 59°C , as shown in Figure 4.5.

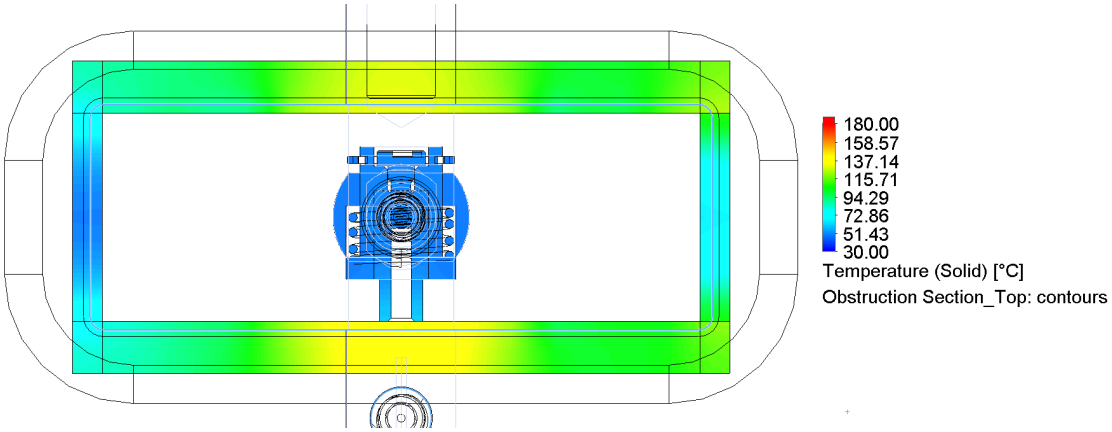

(a) Top view

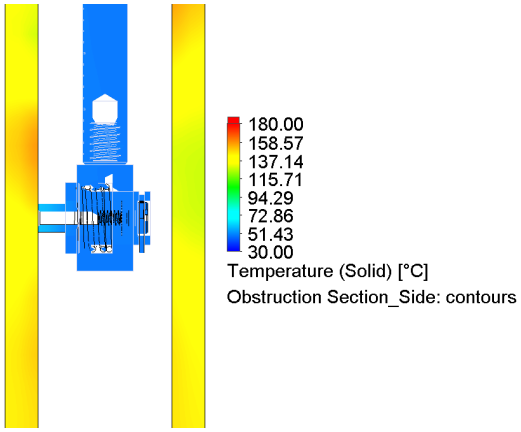

(b) Side view

Figure 4.4: Section views of the temperature distribution of the lower obstruction sub-assembly.

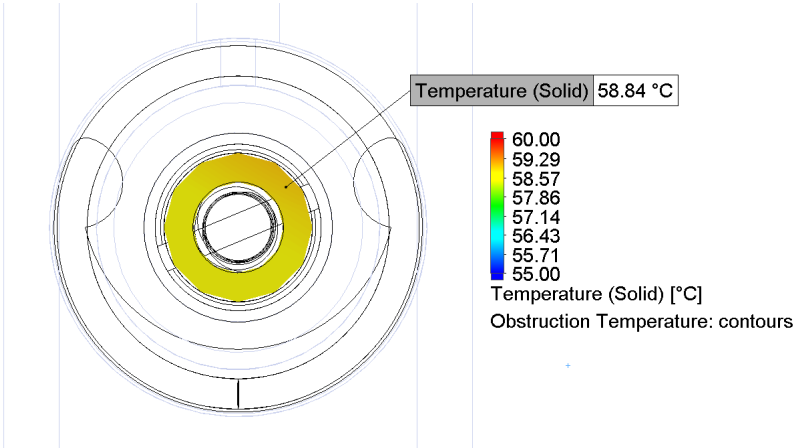

Figure 4.5: The surface of the Ultem obstruction at the glass interface reaches an estimated maximum temperature of approximately 59°C .

4.2.3 Evaluation

Qualitative and quantitative assessments of the seven design criteria identified in Section 4.2.1 were performed. Those criteria are consolidated into and reported in three groups as follows:

- Ease of use (Assembly)
- Electrical insulation
- Thermal constraints - temperature

Assembly and installation

The fully assembled obstruction module is shown in Figure 4.6. The exploded view of the parts of the polyetherimide (PEI) obstruction submodule, on the bottom-right corner of Figure 4.6 is shown in Figure 4.7a. The exploded view of the supporting structure for the obstruction submodule is shown Fig 4.7b.

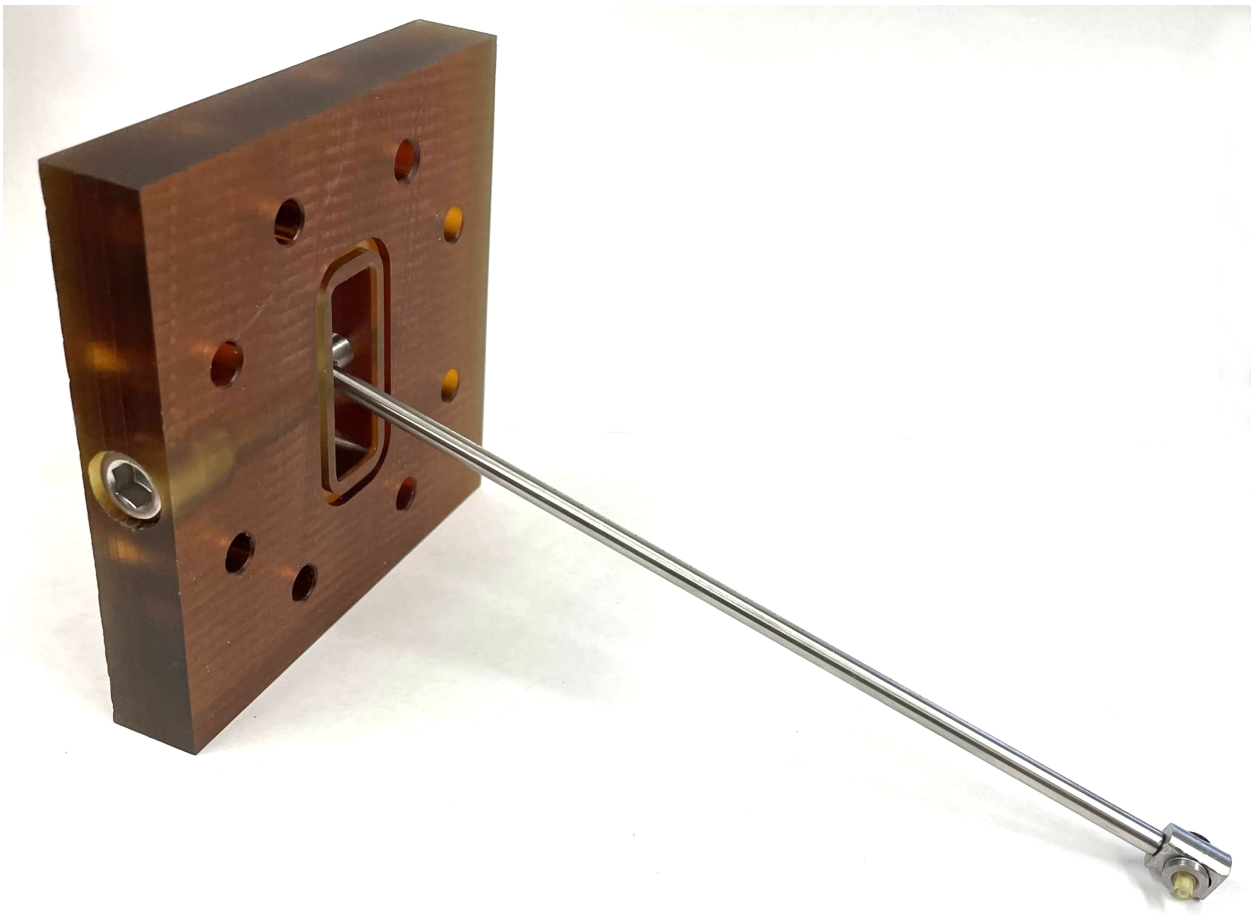

Figure 4.6: Fully assembled obstruction module.

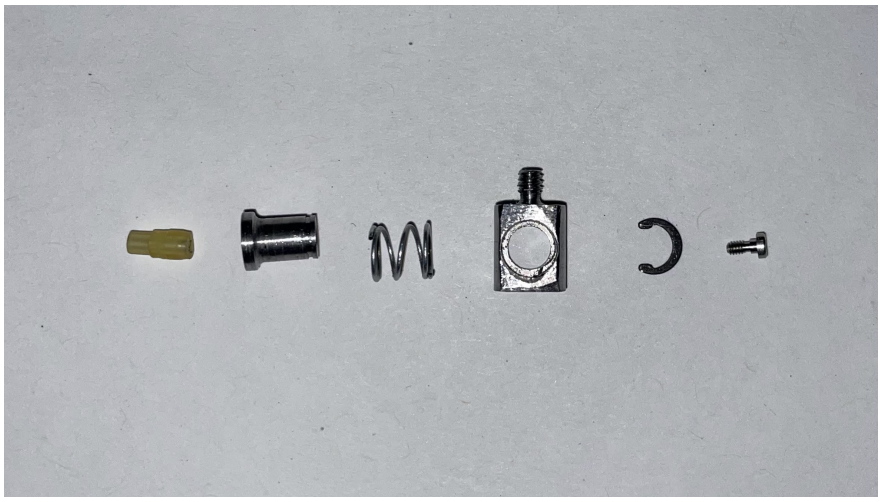

(a) Exploded view of the obstruction submodule. From left to right: PEI obstruction, obstruction chuck, spring, submodule body, C-clip, and #0-80 screw.

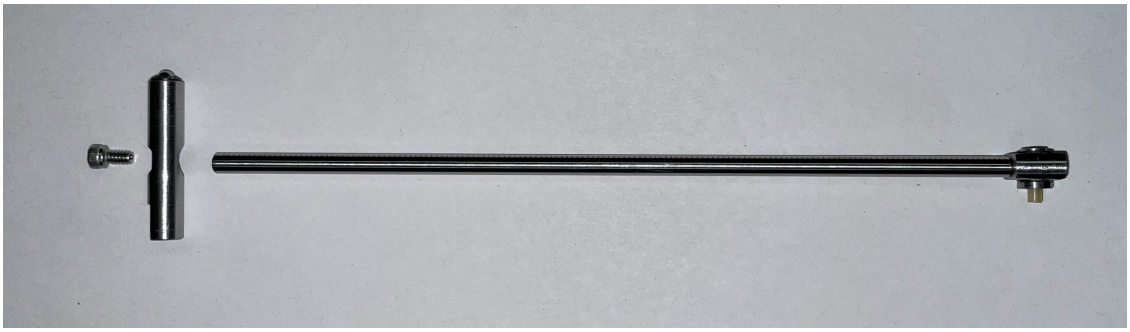

(b) Exploded view of the obstruction support submodule. From left to right: #4-40 vented screw, top-support bar (with spring-pin attached), extension rod, obstruction submodule (attached).

Figure 4.7: Exploded views of parts of the obstruction module.

Module assembly Assembly of the obstruction module is straightforward. The process starts with the assembly of the obstruction submodule. The spring is first fitted around the obstruction chuck, which is then inserted into the submodule body, and retained with the C-clip. The C-clip is installed in the groove on the chuck body. Finally, the PEI obstruction is inserted into the chuck from the left and screwed in place with the #0-80 screw on the right. The full module is assembled by first installing the top-support bar (shown in Figure 4.7b) into the module plate (square PEI plate in Figure 4.6). The end with the pressed-in spring pin is inserted first. Next, the #4-40 vented screw is loosely fastened to the extension rod

through the top-support bar. Then, the wall-contact surface of the obstruction is aligned with the appropriate face of the module plate, so that the obstruction will fully contact the inner test section wall upon installation. This is achieved by supporting the contact surface with a machinist screw jack (not shown), such that the appropriate module plate face is parallel to the obstruction wall-contact surface. Then, the #4-40 screw is tightened. Finally, the orientation of the top-support bar is fixed by tightening a 1/8"-long #6-32 brass set screw (anti-rotation set screw) into the upstream surface of the module plate. A 1/4"-20 positioning set screw is installed in the top-support bar insertion hole. The hole is then sealed by a 5/16"-18 sealing screw.

Module installation Installation of the obstruction module requires disconnecting the test section from the downstream refrigerant line at the flow adapter. Residual fluid in the test section is first rarefied by evaporation and condensation using the upstream heaters and the down stream condenser unit. Any liquid pooled upstream of the test section is vaporized and drawn into the condenser. Next, the downstream isolation valve is closed (upstream valves maintain close throughout the process) and the downstream flow adapter is separated from the test section top-plate. Then, the obstruction module is inserted into the test section from the top. The obstruction is first offset from the from window of the test section to avoid dragging the obstruction during insertion. The module plate is then placed on the test section top-plate. The flow adapter is then reinstalled on top of the module plate, bolting into the top-plate. The positioning set screw is turned counterclockwise to ease the obstruction to the front window. By design, the obstruction contacts the front window when the set screw is disengages from the top-bar. The set screw is left in the module plate. Finally, the sealing screw is installed.

Future improvements Two issues were identified when installing the obstruction module:

- **Bending of the extension rod** Due to the large amount of force applied to the extension rod when the module was first assembled, the extension rod was bent slightly.

In doing so, the mating hole for the rod in the top-bar was also slightly deformed, such that perfect alignment was not automatically achieved during assembly. While the bend was minor (estimated less than 1°C), it was sufficient to prevent the obstruction from fully contacting the test section window. This was realized when liquid droplets were observed flowing between the obstruction and the glass wall. A replacement extension rod remedied the issue. Moving forward, a precision hardened steel rod should be used in lieu of the stainless steel optical cage rod. Further, the top-rod should be hardened as well to prevent fine features from deforming. Lastly, an assembly jig should be devised to prevent excessive manual turning and bending torque to the extension rod during the assembly process when screws are tightened while maintaining alignment.

- **Marring in the top-rod** Due to supply shortages of the brass anti-rotation set screw, steel replacements were used. In doing so, the mating surface on the top-rod was marred and prevented the top-bar from sliding when the set screw was loosely tightened. Filing the marred surface and using a brass set screw resolved the issue. However, in the future, a more robust method should be used. First, the top-rod should be hardened as mentioned previously. Second, instead of a pointed set screw, a ball-tipped set screw should be used. Alternatively, a square key and keyway can be used to prevent the top-rod from rotating while allowing sliding.

The issues are resolved and the obstruction module works as intended for the current study.

Electrical insulation

Due to the electrically conductive fluorine-doped tin oxide heater coating on the inner glass walls of the annular flow test section, any obstacle in contact with the wall surface needs to be electrically insulating to avoid damaging the heater and Ohmic heating of the obstruction. PEI has been previously used to construct the test section partly due to its chemical and electrical resistivity. According to a material supplier, the volumetric electrical

resistivity of PEI is on the order of 10^{15} [Ω-cm], which was considered sufficiently high in this application. It was selected as the material for the obstruction. During operation, no abnormalities were observed at and near the contact area between the obstruction and the electrically conductive wall surface. The heater resistance reading saw no measurable difference with the addition of the obstacle. This shows the obstruction does not contribute to the electrical characteristics of the wall heater.

Thermal constraints - temperature

The poor thermal conductivity of PEI is both desirable and of concern. Its low thermal conductivity (approximately 0.3 [W/m-K]) ensures little possibility of a local cool spot when the window heater is operating. On the flip side, a local hot spot, due to poor conductivity and little convective heat transfer in the contact area, can cause a concentrated thermal stress in the glass wall that can break the glass wall.

Figure 4.8a shows the obstruction module installed in the operating test section with a upwards flowing annular flow. A dry patch was observed downstream of the obstruction. Figure 4.8b shows the external wall temperature measured with a FLIR infrared camera. The infrared image shows a maximum temperature of 52°C occurring near the outlet, while the region close near the obstruction is approximately 20°C —the saturation temperature of the fluid. These images verify the wall temperature at the contact area between the obstruction and the heated wall is not noticeably higher than its surroundings.

(a) Image of the obstruction module in vertical two-phase annular flow.

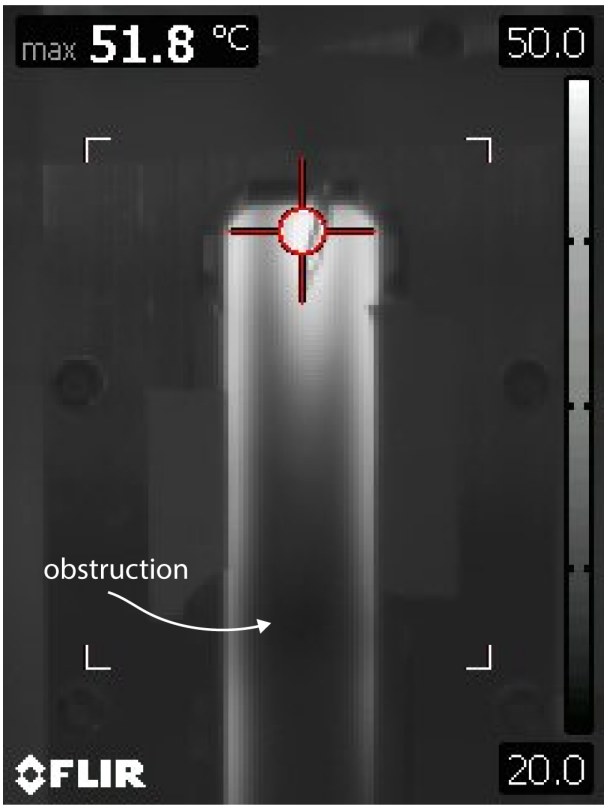

(b) Infrared image of the external test section wall.

Figure 4.8: Images of obstruction module in use

4.3 Experimental setup of initial study

Experiments were conducted using R-245fa as the working fluid. A flow obstruction (as described in Section 4.2) with a 2-mm diameter is positioned approximately 420 mm downstream from the start of the 525 mm long heated section.

4.3.1 Liquid-film thickness and direct observation

Optical film thickness measurements were taken 4 obstruction diameters (or 8 mm) upstream of the obstruction using a Phantom V311 high-speed camera with a AF-S NIKKOR 300 mm f/4E PF ED VR (Nikon) lens. High speed videos of the downstream flow field were recorded using a Phantom VEO-E 340L high-speed camera with a Nikon 60 mm AF-D lens. All images were recorded at 2000 frames per second (fps).

4.3.2 Experimental procedure

The process of measuring flow characteristics starts by allowing the test section to reach steady-state without wall heating. The first set of high-speed video and optical film thickness measurements are taken during this stage. Next, wall heating is applied using two 6 kW Xantrex XDC power supplies. Heating power is applied incrementally and increased only when the highest exterior wall temperature stabilizes. The highest exterior wall temperature is measured at the center most downstream position of the glass window. This is the only exterior wall temperature measurement in this experiment. Two additional sets of videos and film thickness measurements are recorded at moderate and high power conditions. The second set (moderate power) is taken when a visually apparent change occurs in the downstream flow field. The third set (high power) is taken when the highest exterior temperature reaches 40°C or the dry wake region expands rapidly in size. Data collection is stopped and the heating power is ramped down after the last set of images are taken. Key steps of this procedure are illustrated in Fig. 4.9. The range of flow conditions investigated during this

work are listed in Table 4.1.

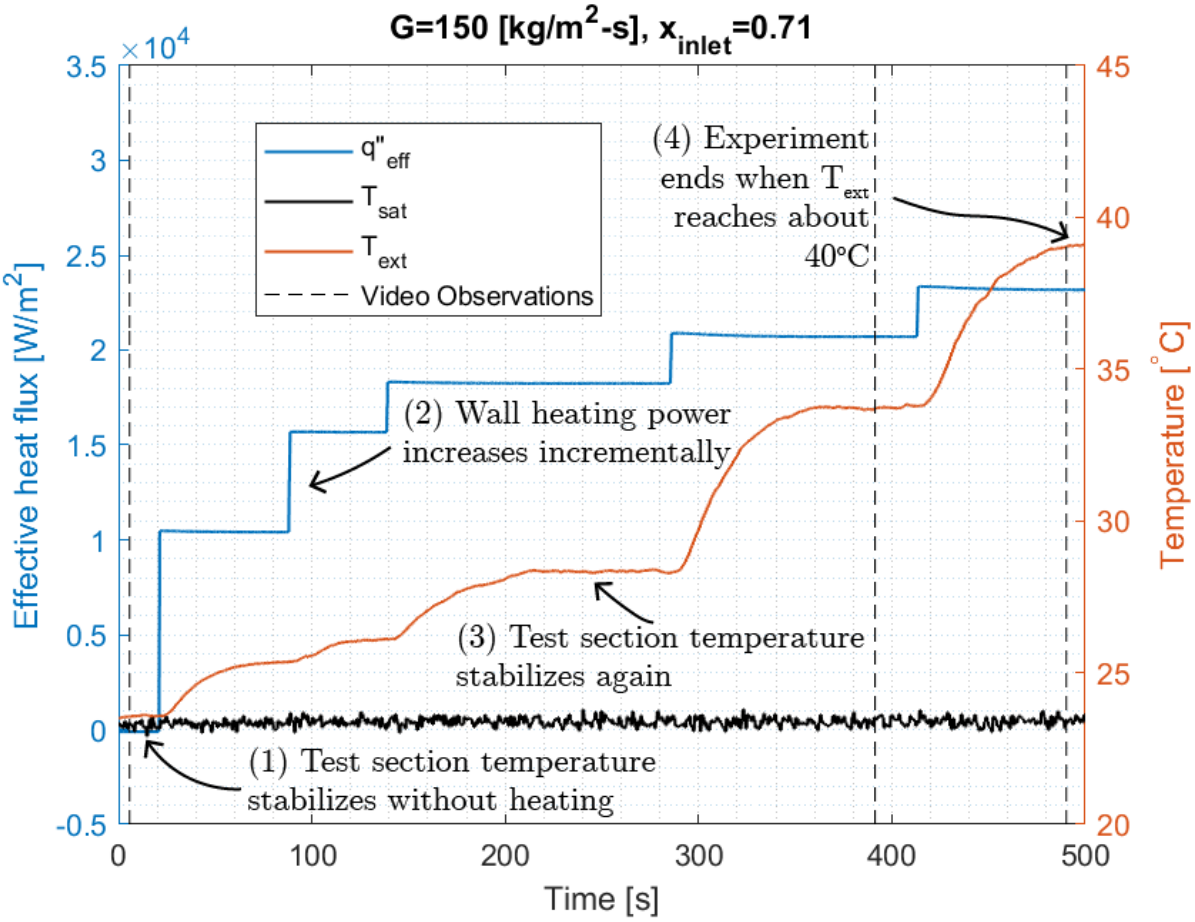

Figure 4.9: The four key steps of the experimental procedure are (1) wait for test section temperature to stabilize, (2) increase wall heating power incrementally, (3) wait for test section temperature to stabilize, and (4) stop test when the external temperature reaches 40°C or the dry wake region expands rapidly in size.

Table 4.1: Experimental flow parameters used for initial study.

x_{inlet} [-]	G [kg/m^2-s]	T_{sat} [°C]	$\dot{m}_l$ [g/s]	$\dot{m}_v$ [g/s]
0.62	150	25	23.98	40.82
0.71	150	25	19.60	45.20
0.79	150	25	15.23	49.57
0.87	150	25	10.85	53.95
0.94	150	25	6.48	58.32

4.4 Results from initial study

Results of this experiment are presented in three sections. First, corresponding time traces for varying flow conditions are presented; degradation of the local HTC associated with boiling crisis is observed. Second, images taken from high-speed video allow for direct observation of the dryout phenomenon in a region downstream from the obstruction. Finally, time-resolved measurements of liquid-film thickness upstream from the obstruction are presented.

4.4.1 Onset of heat transfer degradation

The onset and severity of local heat transfer degradation at the heater wall can be quantified by the ratio of effective heat flux, q''_{eff}, to the difference in wall temperature and the saturation temperature, ΔT. This relationship is defined by the heat transfer coefficient, HTC:

$$HTC = \frac{q''_{eff}}{\Delta T} \tag{4.1}$$

When the exterior wall temperature, T_{ext}, reaches steady-state, it can be used in place of the inner wall temperature, T_w, because of the low amount of conductive heat loss through the wall. Figures 4.10 to 4.10b are unfiltered time series data of the following: effective heat flux in blue, highest exterior wall temperature (T_{ext}) in orange, and local saturation temperature (T_{sat}) in black. The effective heat flux shown in the figures in this section are calculated by accounting heat losses in the same manner described in Morse et al. (2021).

As shown in Figure 4.10, the increase in ΔT is not always proportional to the increase in q''_{eff}. From 200 sec to 550 sec, ΔT remains roughly constant at 4°C . After 550 sec, ΔT increases with q''_{eff} while T_{sat} remains roughly constant. According to Equation 4.1, the only way to account for this change is the decrease of the local HTC. For $x_{inlet} = 0.62$, the effective wall heat flux and temperature difference associated with the onset of heat transfer degradation are approximately 29 kW/m^2 and 4°C , respectively. Conversely, for

$x_{inlet} = 0.94$, as shown in Figure 4.10b, the onset of heat transfer degradation occurs as soon as heating is applied. The associated effective wall heat flux and temperature difference in this case is 10 kW/m^2 and 10°C , respectively.

Figures 4.11 to 4.13 show q''_{eff} and T_{ext} at intermediate x_{inlet}. These results illustrate that for the same mass flux, as vapor quality increases, the lower the heat flux threshold for heat transfer degradation, and the reduction of the maximum attainable heat flux that keeps T_{ext} below the cutoff temperature of 40°C .

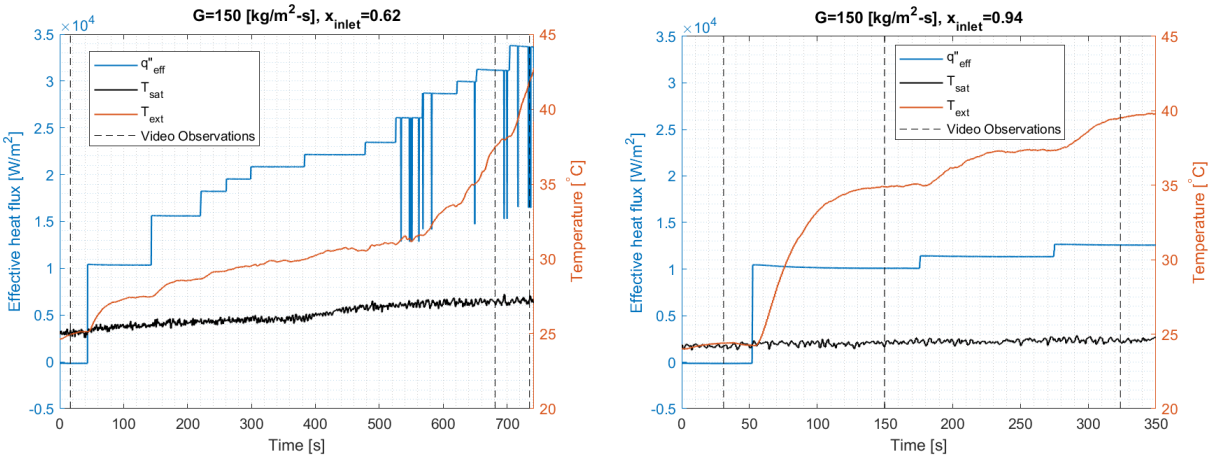

(a) $x_{inlet} = 0.62$ (b) $x_{inlet} = 0.94$

Figure 4.10: Time trace of effective heat flux and external wall temperature for $x_{inlet} = 0.62$ and 0.94

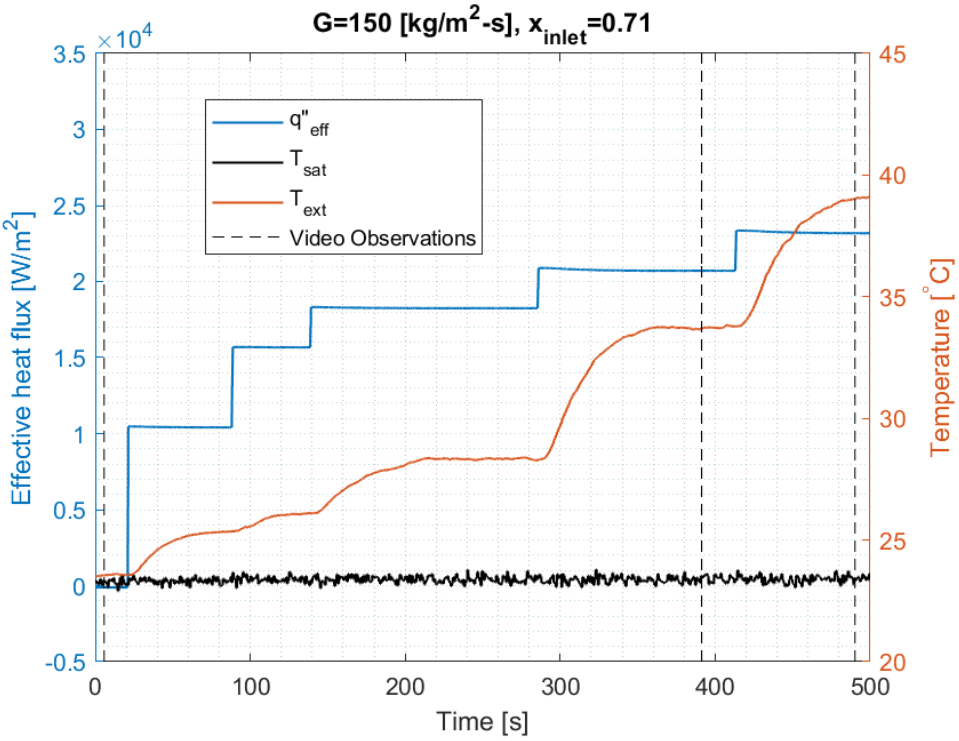

Figure 4.11: Time trace of effective heat flux and external wall temperature for $x_{inlet} = 0.71$

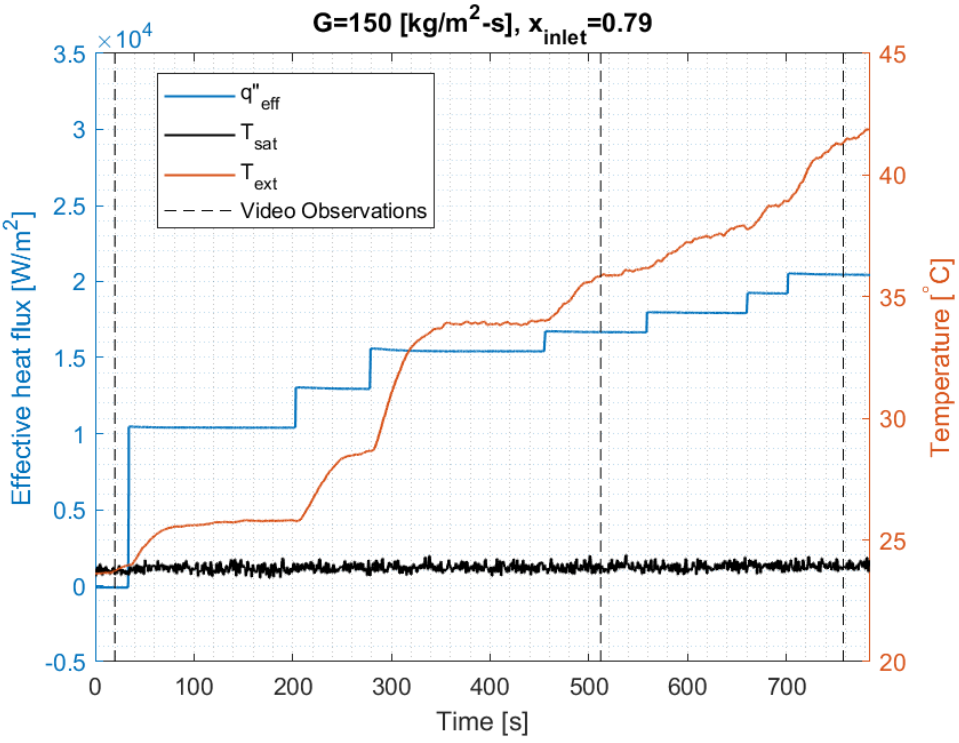

Figure 4.12: Time trace of effective heat flux and external wall temperature for $x_{inlet} = 0.79$

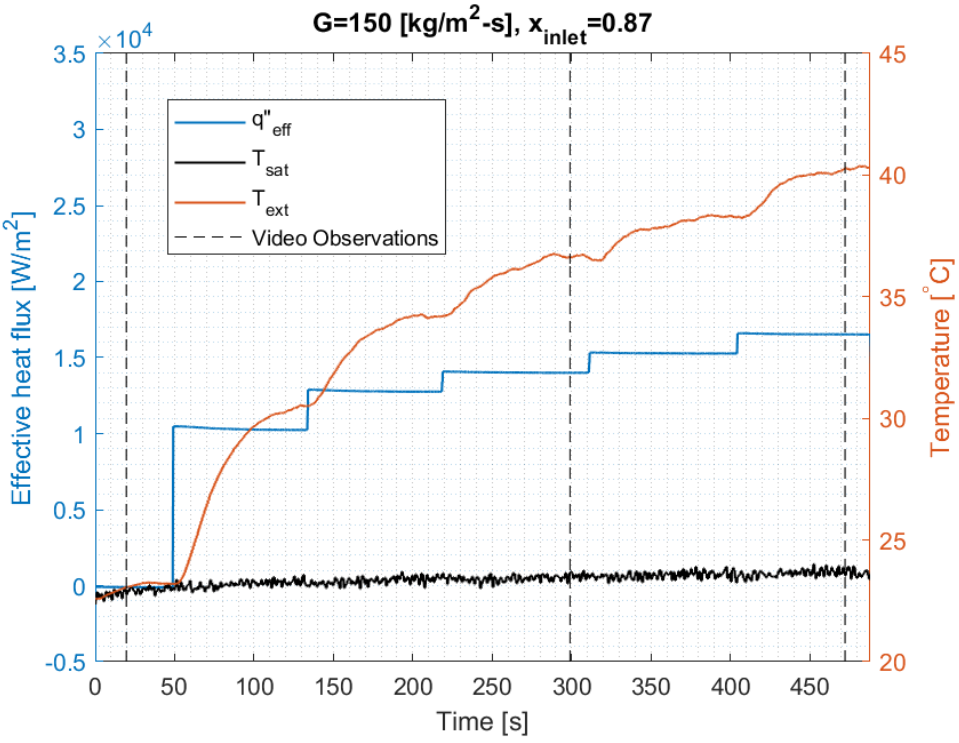

Figure 4.13: Time trace of effective heat flux and external wall temperature for $x_{inlet} = 0.87$

One explanation of the different trend of the local HTC with wall heat flux is lateral conductive heat transfer through the heated wall from the dry region to the wet region. Despite dryout in the heated wake region, the high HTC on the wetted side of the triple contact lines of the wake border effectively cools the wake region, keeping it at a steady temperature. As the heating is increased further, the wake region expands laterally and can no longer effectively conduct heat transversely from the center of the wake region.

The shape of the dry wake region resemble logarithmic curves; the steepest portion tends to occur upstream, at the base of the region, and the downstream border of the dry region is nearly parallel to the streamwise direction. The shape of the base (most upstream position) of the wake is not clearly defined as impinging droplets and rivulets regularly wet the region. The downstream wake border can be wavy as high momentum disturbance waves pass by either side of the dry region. The evolution of the border with the passing of a disturbance wave is shown in Fig. 4.14. This behavior can be most clearly seen under lower vapor quality

conditions, where disturbance waves exhibit highly turbulent flow patterns. Between waves, the border advances as the wake region liquid film evaporates. As a wave approaches, its momentum forces the contact line to recede. Effectively, the surface tension of the liquid film at the contact line cannot support the excess mass carried by the waves, causing the mass to spill over into and cool the dry wake region. Under high vapor quality conditions, as shown in Figure 4.19, the lower liquid mass flux reduces disturbance wave momentum and turbulence. These waves provide less effective cooling at the dry region border. Unlike the base shape of the dry region, a clear shape of the downstream wake border can be obtained by averaging high-speed images.

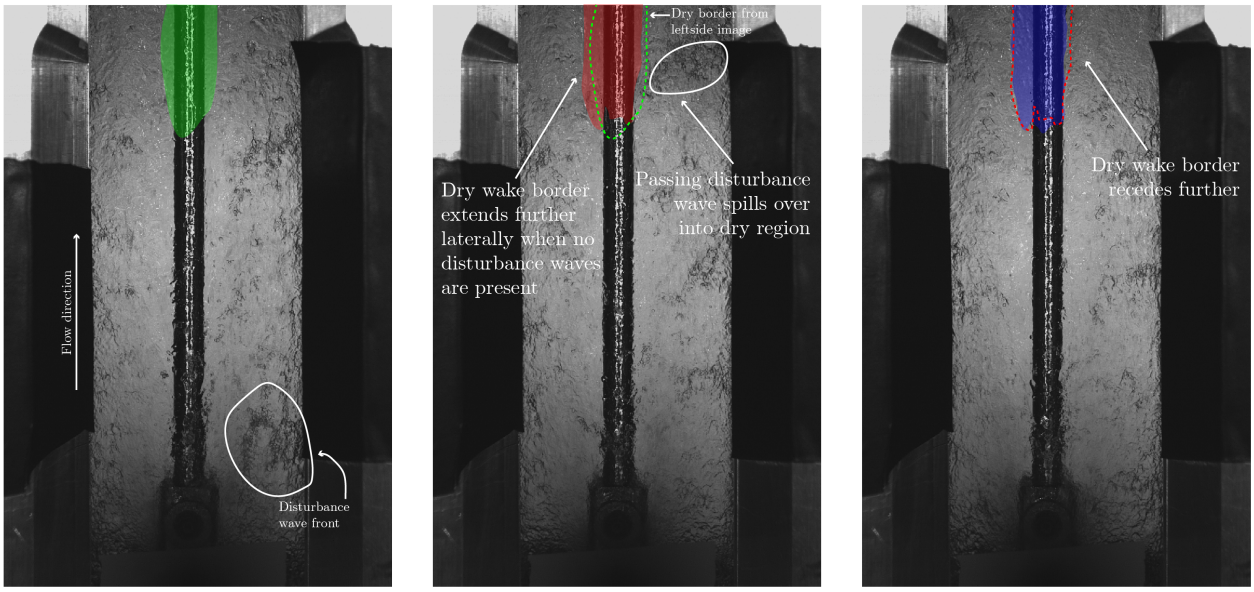

Figure 4.14: Evolution of dry wake region border during passing of a disturbance wave. Color-shaded regions represent the dry area in each image. Dashed lines represent the dry area from the previous image.

4.4.2 Behavior of the downstream flow field

Time-averaged behavior of the flow field is investigated by direct observation. The time-averaged images are made using 100 high-speed images taken at 2000 fps. In Figures 4.15 to 4.19, time-averaged images are shown corresponding to the same mass flux and saturation

temperature, but differing inlet quality and heat flux. Observation 1 refers to the unheated condition. These images suggest a thin layer of liquid film in the wake region when the wall is unheated. Observations 2 and 3 refer to flow conditions with increasing heat flux. The dry regions are shaded red in Figures 4.15 to 4.19.

For each flow condition, a low heat flux results in sustained dryout of the region downstream of the obstruction. Increasing the heat flux causes dry regions to increase in width and length. The base of dry regions extend upstream, closer to the trailing edge of the obstruction. This can be especially seen in Figure 4.18. In Figure 4.19, since the onset of heat transfer degradation occurred immediately upon applying wall heating, and a high heat flux (compared to those applied to the $x_{inlet} = 0.62$ test case) was not applied, expansion of the dry region was not observed. Instead, a dry region larger than those of all other test cases was observed.

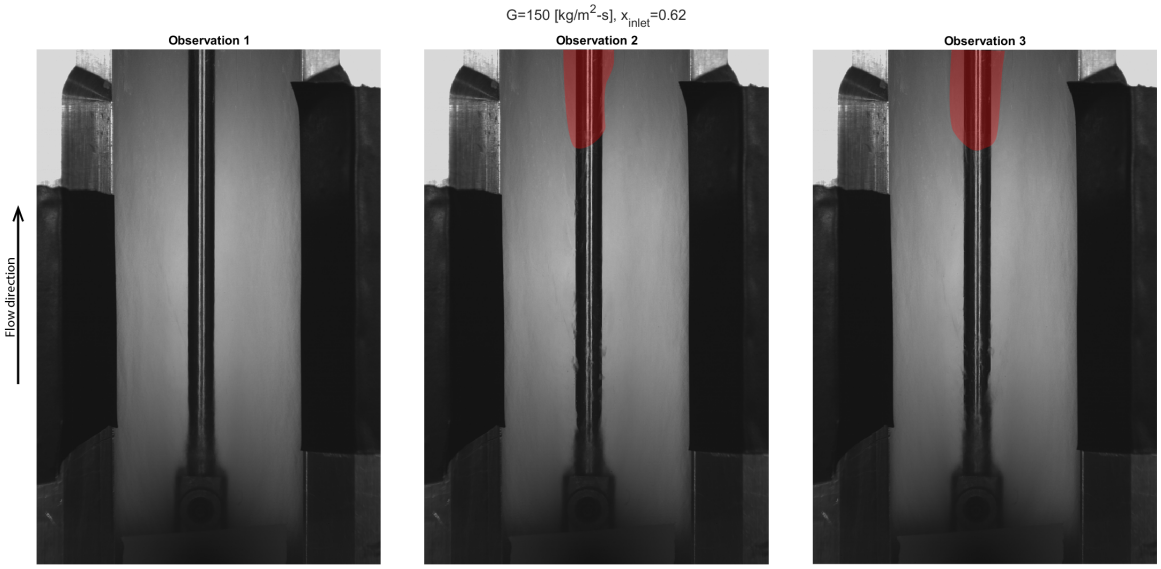

Figure 4.15: Average stacked-image of downstream flow field for $x_{inlet} = 0.62$

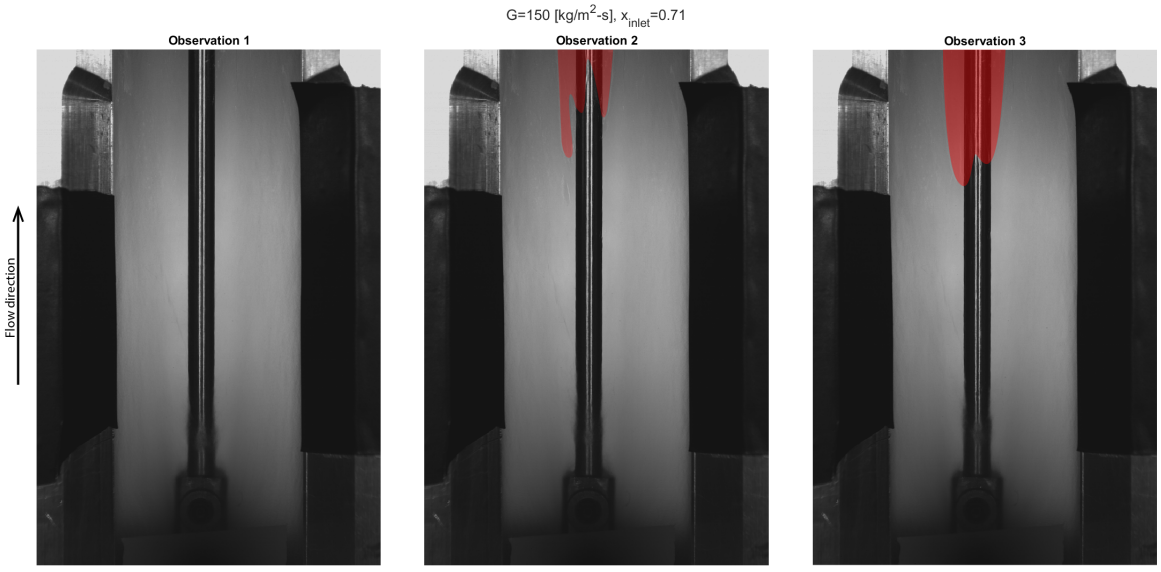

Figure 4.16: Average stacked-image of downstream flow field for $x_{inlet} = 0.71$

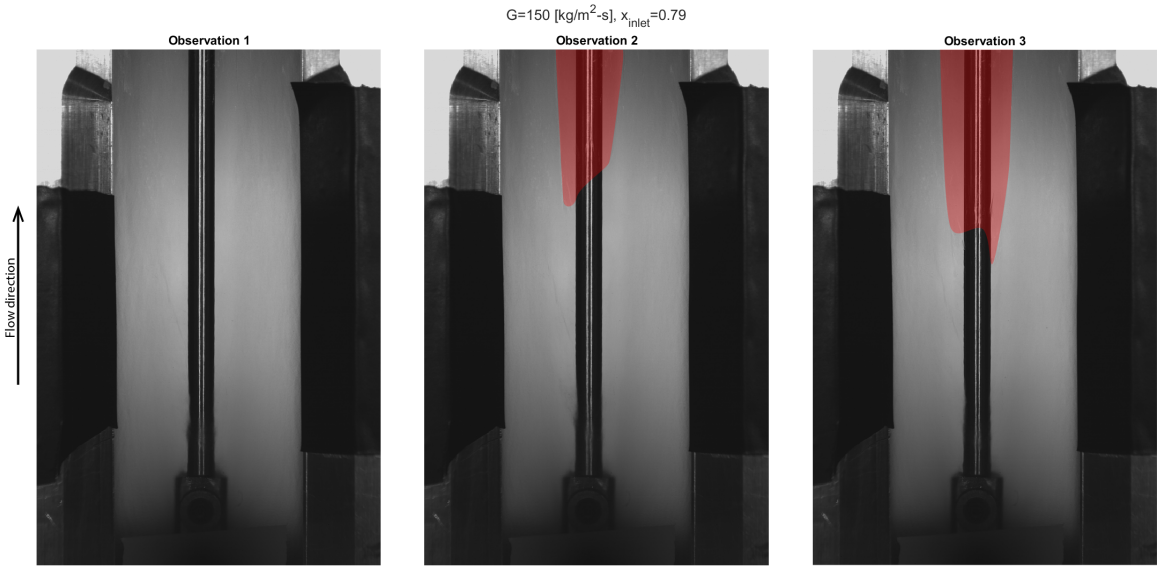

Figure 4.17: Average stacked-image of downstream flow field for $x_{inlet} = 0.79$

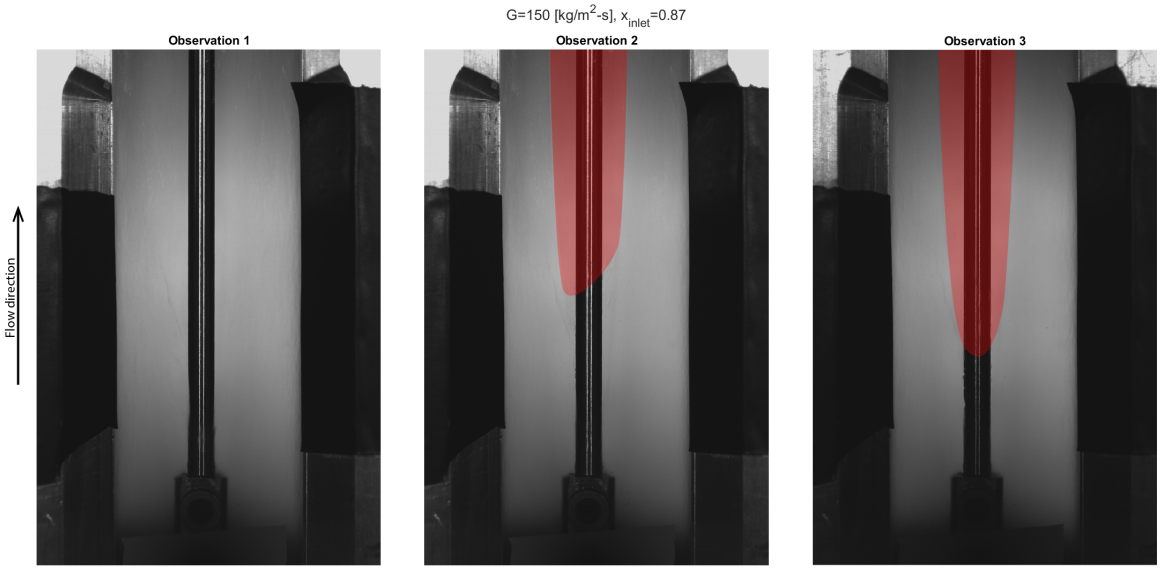

Figure 4.18: Average stacked-image of downstream flow field for $x_{inlet} = 0.87$

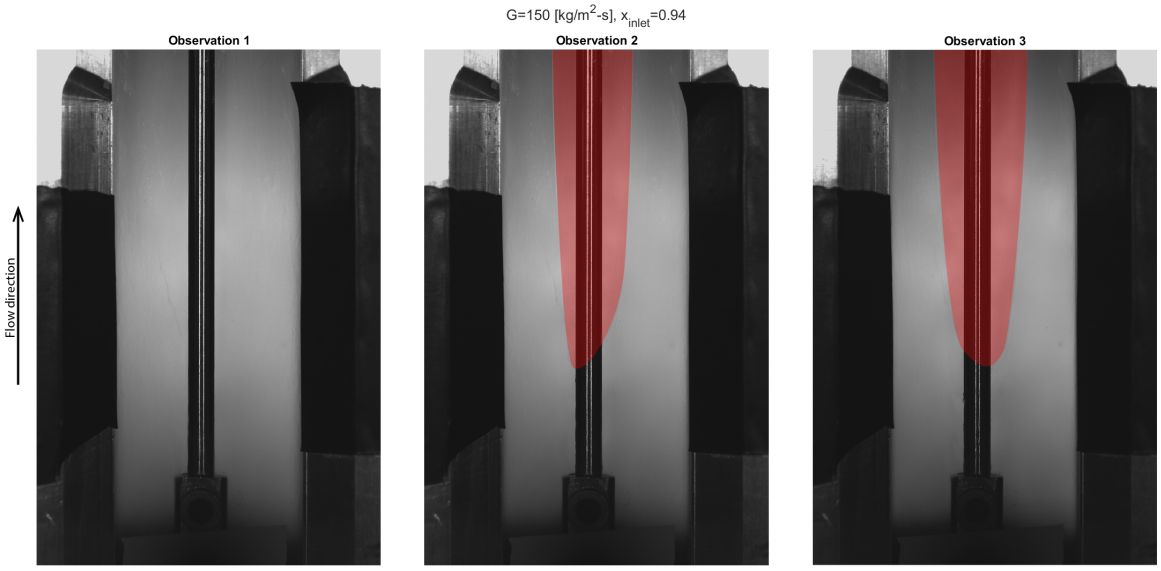

Figure 4.19: Average stacked-image of downstream flow field for $x_{inlet} = 0.94$

4.4.3 Film thickness measurements

Film thickness measurements show that the film upstream of the flow obstruction behaves similarly as the film in unobstructed annular flow under similar flow conditions. The mean and the standard deviation of film thickness decreases with increasing test section inlet vapor quality as shown in Fig. 4.20. Probability distributions, as shown in Fig 4.21, show normal distributions of film thickness regardless of inlet quality. No dryout occurred in this region for all flow conditions. The film thickness signal is filtered using a moving average (mean) filter with a window size of 5 samples. This is equivalent to a 0.0025 sec window.

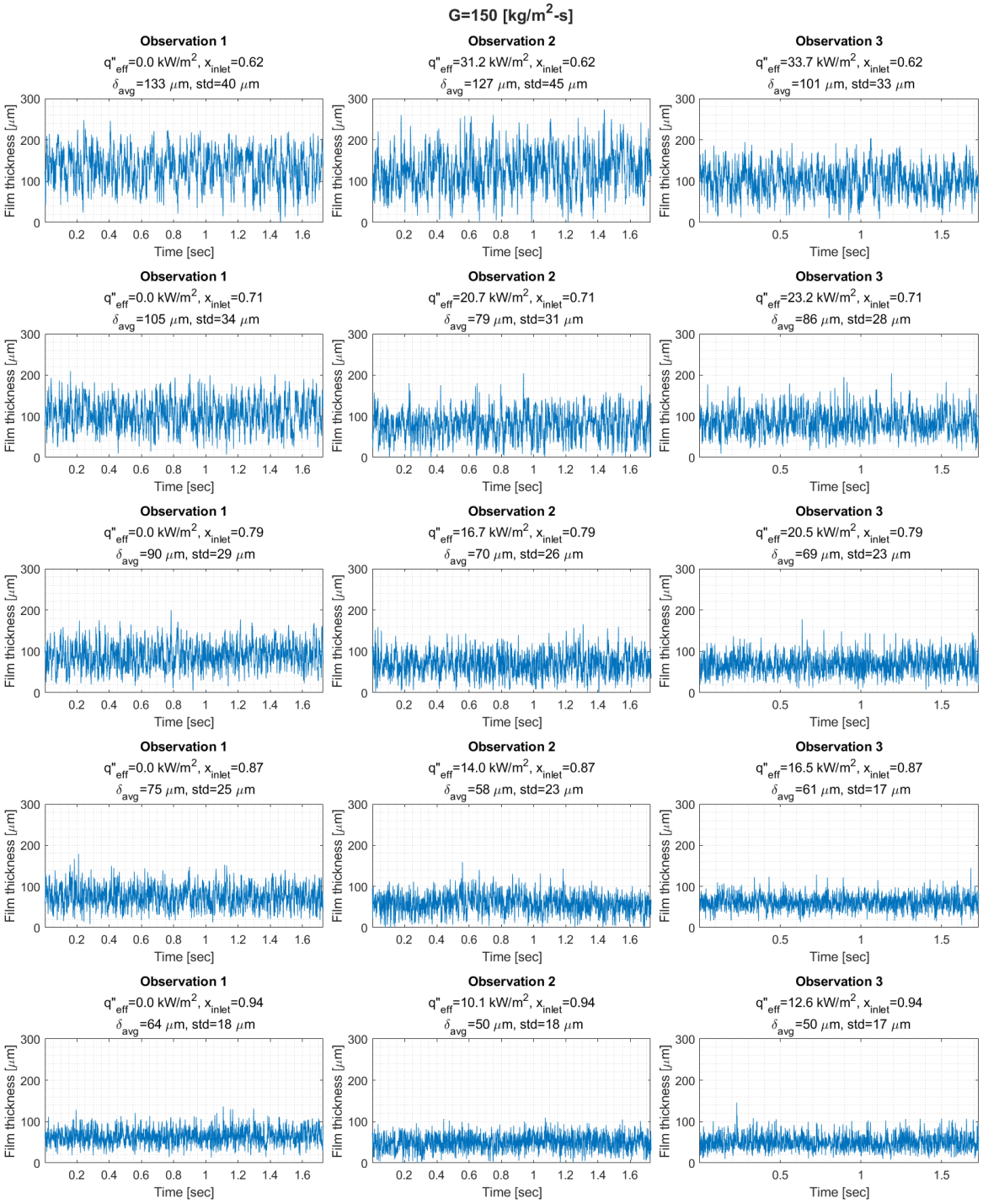

Figure 4.20: Film thickness upstream of flow obstruction versus time for all flow parameters

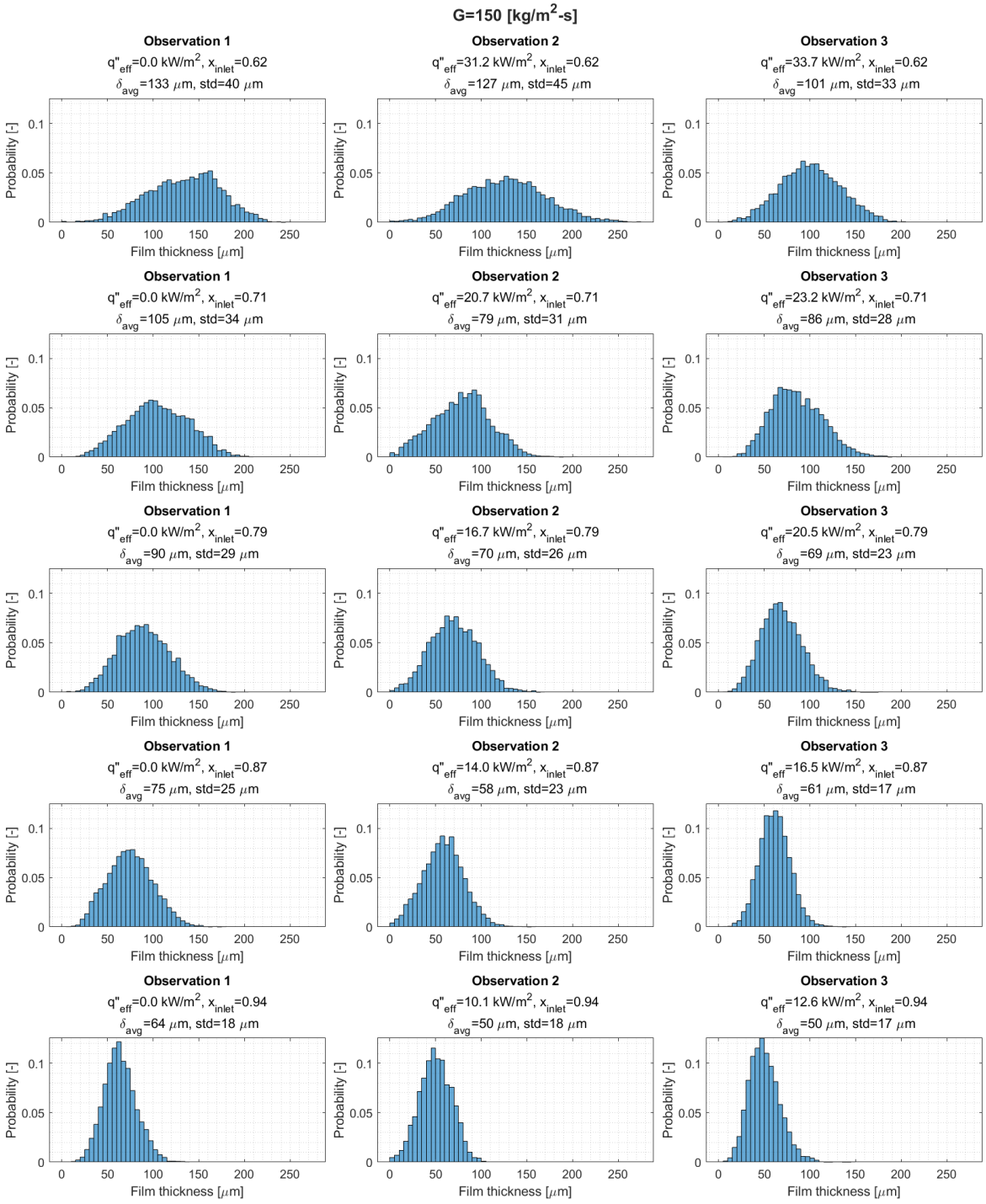

Figure 4.21: Probability distribution of film thickness upstream of flow obstruction for all flow parameters

4.5 Experimental setup of parametric study

Results from Section 4.4 indicate a general trend of the dry wake geometry as a function of inlet vapor quality at a constant total mass flux. The start of the dry wake region moves upstream with increasing wall heat flux, and its width increases with inlet quality. No dry out was observed upstream of the flow obstruction. In this section, the experimental setup for a similar parametric study under three different mass fluxes are presented and shown in Figure 4.22. In addition to the film thickness measurements upstream of the flow obstruction, downstream film thickness and wake region external wall temperatures are measured. The range of flow conditions investigated in this study are listed in Table 4.2. High speed video of the dry wake regions are recorded. Due to limitations in available physical space around the test section, film thickness measurements were taken during a separate run of the experiment as the high speed video and wall temperature measurements.

Table 4.2: Experimental flow parameters used for parametric study.

x_{inlet} [-]	G [kg/m^2-s]	T_{sat} [°C]	$\dot{m}_l$ [g/s]	$\dot{m}_v$ [g/s]
0.63	130	25	20.78	35.38
0.70	130	25	16.99	39.17
0.77	130	25	13.20	42.96
0.83	130	25	9.41	46.75
0.90	130	25	5.62	50.54
0.63	150	25	23.98	40.82
0.70	150	25	19.60	45.20
0.77	150	25	15.23	49.57
0.83	150	25	10.85	53.95
0.90	150	25	6.48	58.32
0.63	170	25	27.17	46.27
0.70	170	25	22.22	51.22
0.77	170	25	17.26	56.18
0.83	170	25	12.30	61.14
0.90	170	25	7.34	66.10

4.5.1 Downstream film thickness measurement

An additional film thickness measurement setup is added to quantify the film thickness down stream of the flow obstruction. The measurement location is approximately 5 times the obstruction diameter downstream of the obstruction. The measurement technique is described in Section 2.2.1 and 3.3. The light rings for both film thickness measurements were taken simultaneously using a Phantom VEO-E 340L high-speed camera with a AF-S NIKKOR 300 mm f/4E PF ED VR (Nikon) lens. Figure 4.23 is a sample image of the two light rings captured by the high-speed camera. A red light band-pass filter was placed immediately before the lens to increase contrast of the light ring illuminated by a HeNe laser at 632.8 nm. The band-pass filter is necessary to attenuate the white LED light used to illuminate the downstream wake region for the high-speed video. The white light was overexposing and effectively washing out the red light rings.

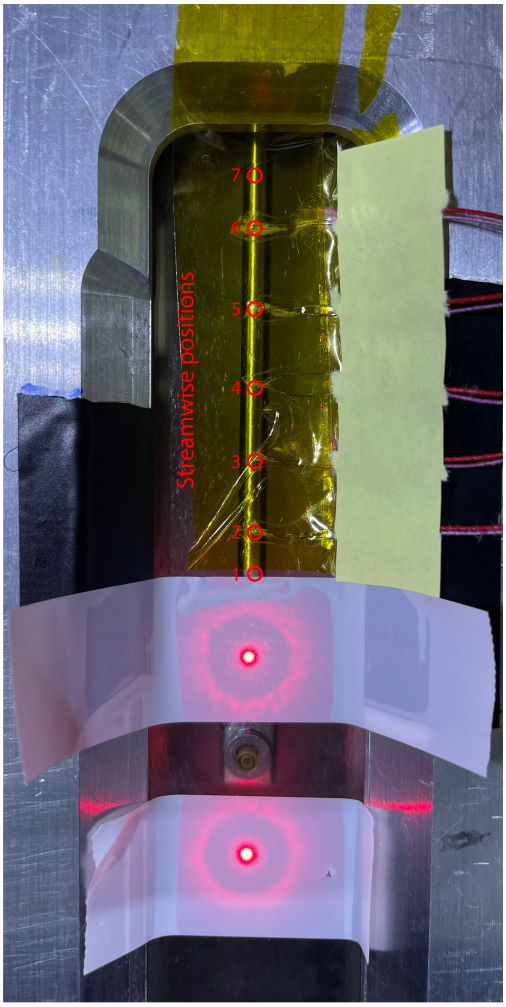

Figure 4.22: Implementation of downstream film thickness and wake region external wall temperature measurements.

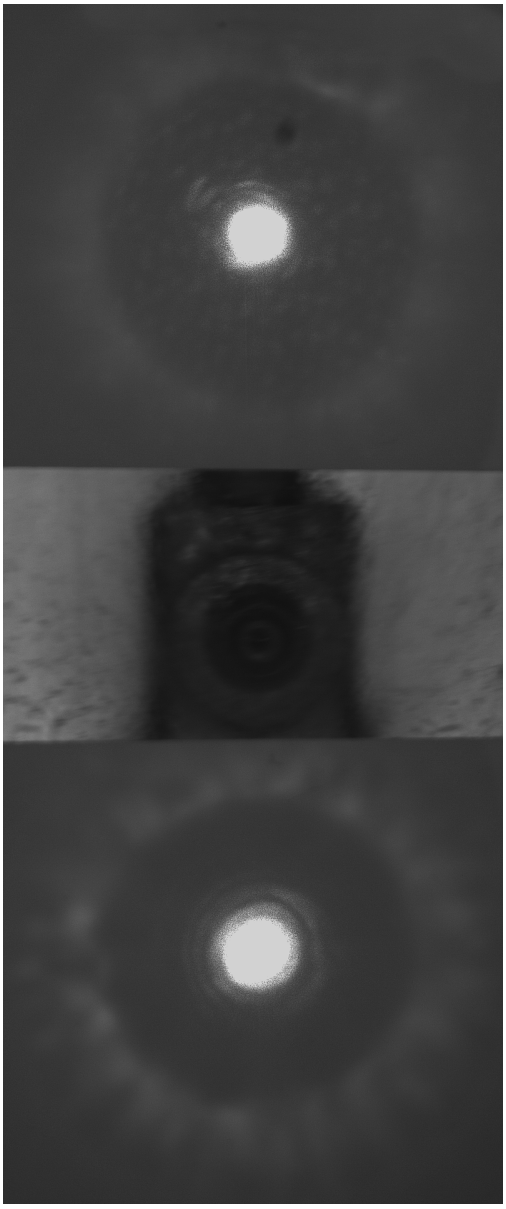

Figure 4.23: Sample image of both upstream and downstream film thickness light rings captured simultaneously.

4.5.2 External wall temperature measurement

Five type-E 30-gauge thermocouple sensors (TCs) are surface mounted to the exterior wall of the test section. The TCs are horizontally centered on the wall, and evenly spaced vertically, as shown in Figure 4.22. The vertical spacing of the TCs is 1 cm. The TCs are affixed to the external wall using Kapton (polyimide) tape that is approximately 0.010”

thick.

The TCs were calibrated using a circulating water bath with a Pt100 resistance temperature detector and temperature stability of 0.01°C . The calibrated temperature range is 15°C to 70°C . A linearity coefficient and a DC-offset was determined for each TC. The linearity of each TC was greater than 99% compared to the known calibration target temperature.

4.6 Results from parametric study

Results of the parametric study are presented in three sections. First, the time-average film thickness upstream and downstream of the obstruction are presented. Second, high-speed images of the dry wake regions are presented. Here, the widths of the dry wake regions are compared with respect to total mass flow rate and inlet vapor quality at various wall heat fluxes. Third, the external wall temperature measurements along the dry wake region are presented as a function of time.

4.6.1 Film thickness around obstacle

Time average film thickness (FT) measurements upstream and downstream of the flow obstruction are presented in Figure 4.24. The uncertainty in the measurements is approximately 20 μm, due to the light ring image resolution, as described in Section 3.3. The upstream FT varies with the inlet vapor quality, and does not vary greatly with mass flow rate. With increasing wall heat flux, the upstream FT tends to decrease due to evaporation of the liquid film. These values largely agree with those reported by Morse under similar conditions, but without a flow obstruction. The downstream FT is generally thinner than the upstream FT. This is expected as the obstruction diverts the liquid film as it passes. The axial momentum of the film causes a low-flow region immediately downstream of the obstruction. This low-flow region does not, however, dry-out under the heating conditions applied in this study. By observation, the liquid in this region is replenished by imping-

ing droplets and rivulets that form in the area. Time-traces of the FT measurements are presented in Appendix B.1.

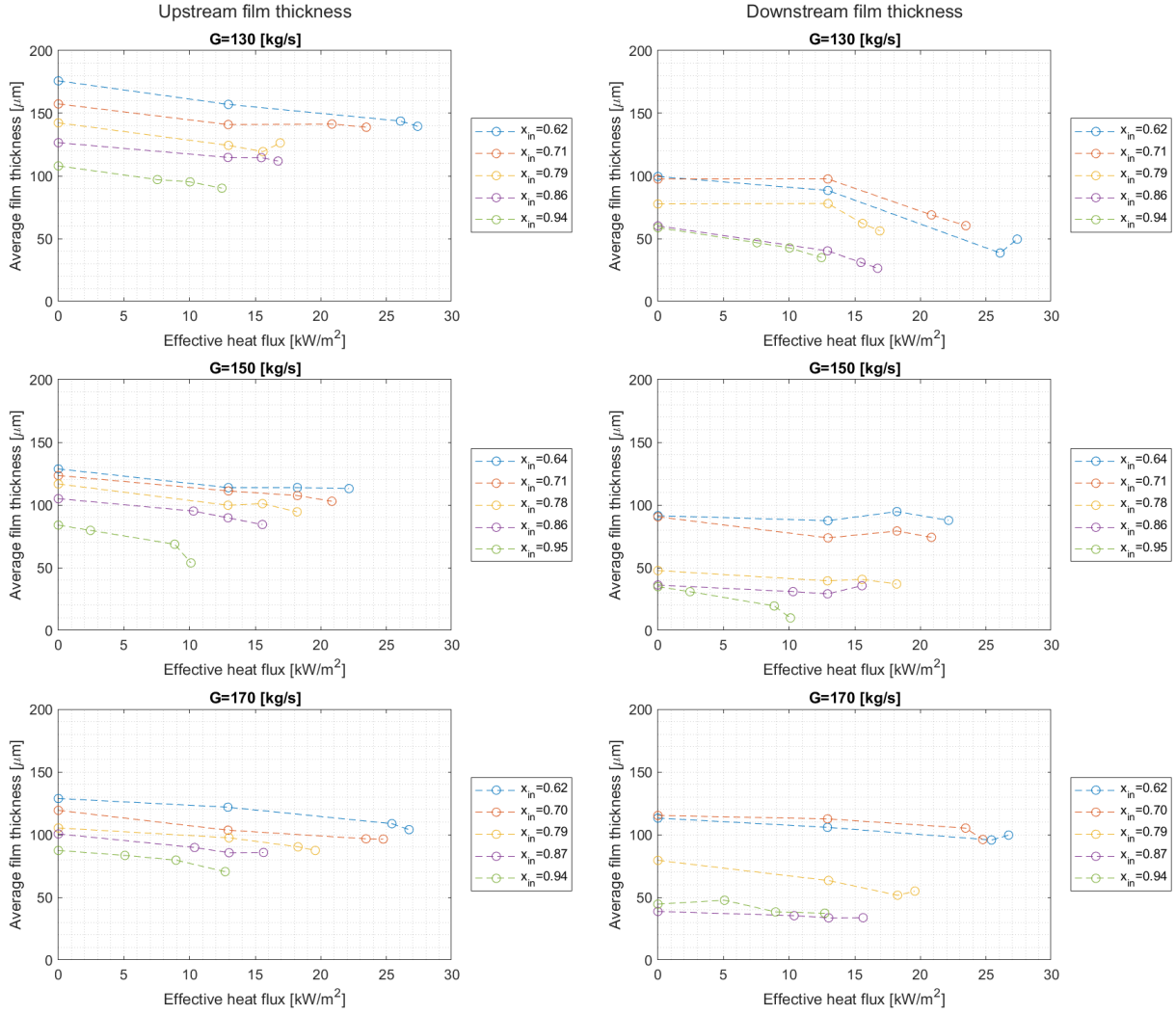

(a) (b)

Figure 4.24: Time-average film thickness (a) upstream and (b) downstream of the flow obstruction.

4.6.2 Dry wake region geometry

The wake region starts to dry out some distance downstream of the obstruction. Figure 4.25 shows the width of the wake regions under the different flow conditions described in Section 4.2 and effective wall heat fluxes. The streamwise positions in Figure 4.25 are defined

in Figure 4.22. The dry wake widths presented were manually measured from time-averaged images shown in Appendix B.3. Eight consecutive high-speed images from each image set were used to obtain the time-averaged images. Including more images to the average blurs the dry-wet interface of the wake region. This is mainly due to the oscillatory movement of the dry region border. As disturbance waves pass by, the dry border recedes, decreasing the dry region area, and vise versa.

At streamwise position 1, the wake region dries out only under the lowest mass flow rate condition and high inlet vapor qualities. The threshold inlet vapor quality in which the wake dries out decreases the further downstream from the obstruction. At streamwise position 7, the wake dries out above a lower heat flux threshold regardless of inlet vapor quality.

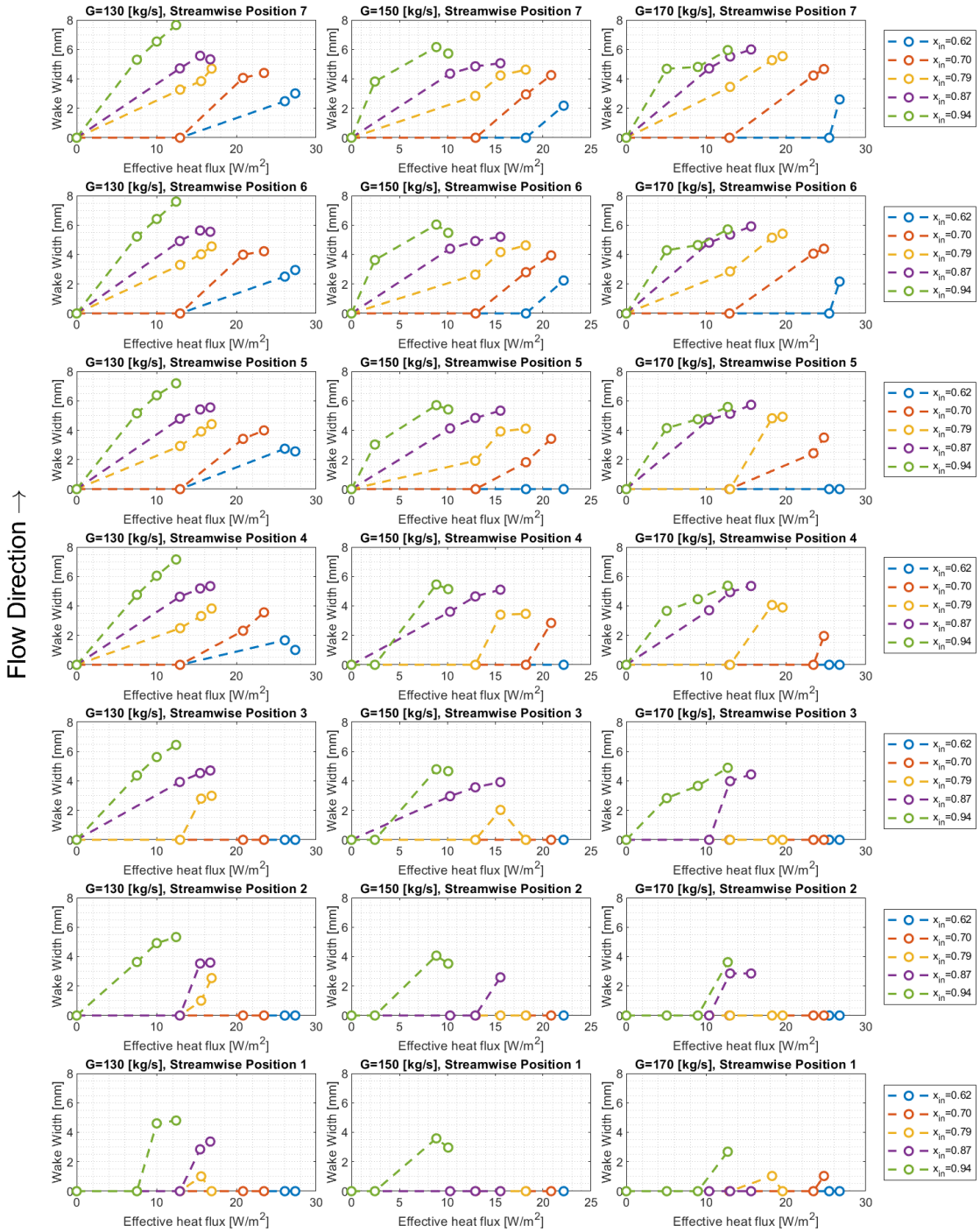

Figure 4.25: Comparison of width of dry wake regions at different streamwise positions, inlet qualities, mass flow rate, and effective wall heat flux.

4.6.3 External wall temperature

The external wall temperature measurements in this parametric study show that the wall temperature does not reach runaway conditions under the applied flow and heating conditions. Instead, the wall temperature reaches a steady state after each step increase in wall heat flux. Two time traces of the wall temperature evolution with increasing heat flux at G=148 [kg/m^2-s] are shown in Figure 4.26. The inlet vapor qualities of Figure 4.26a and Figure 4.26b are 0.71 and 0.86, respectively. In Figure 4.26a, the 5 wall temperature measurements increase synchronously with increasing heat flux until t=280 [s], when the most downstream temperature, $T_{ext,05}$), starts to increase more rapidly than the other temperature measurements. The onset of heat transfer degradation occurred during this time as the effective wall heat flux reaches 18 kW/m^2. When the wall heat flux is increased to 20 kW/m^2, $T_{ext,05}$ is approximately 10°C higher than the most upstream temperature measurement, $T_{ext,01}$. $T_{ext,04}$ also starts to increase more rapidly. Over a 20 kW/m^2 increase in effective wall heat flux, $T_{ext,01}$ increased a total of about 4°C , while $T_{ext,05}$ increased about 15°C , all while the liquid saturation temperature remained essentially constant at 24.5°C .

The onset of heat transfer degradation occurred at a lower wall heat flux of 7.7 kW/m^2 when the $x_{inlet} = 0.86$. As seen in Figure 4.26b, the temperature at the four most downstream positions deviated significantly from the most upstream position as the wall heat flux reached 13 kW/m^2. No deviations were observed at this wall heat flux when $x_{inlet} = 0.71$, as shown in Figure 4.26a.

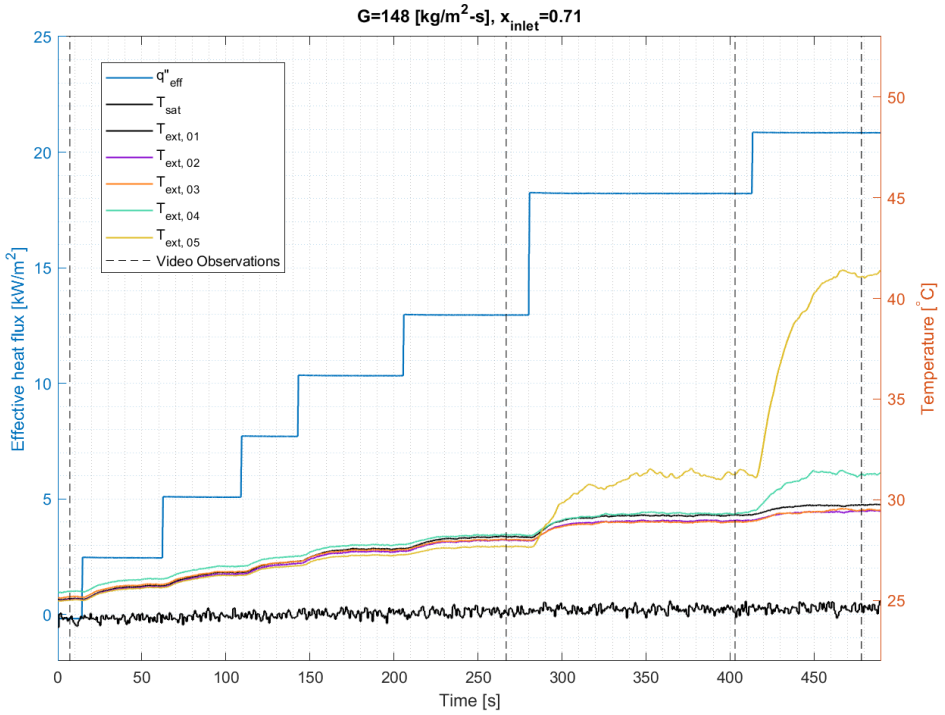

(a)

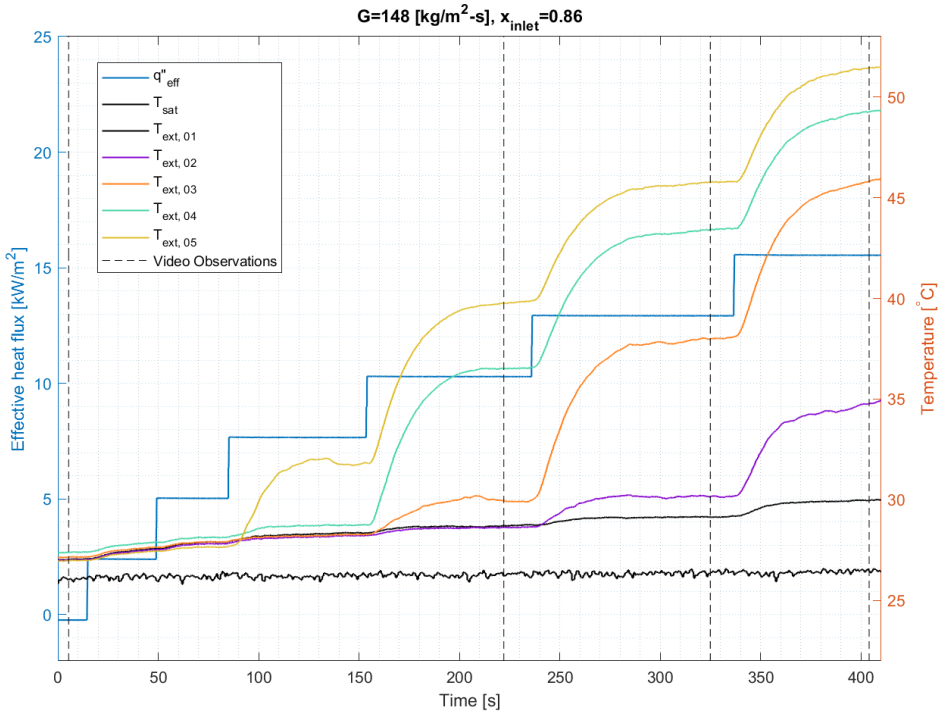

(b)

Figure 4.26: Time traces of effective heat flux and external wall temperature for (a) $x_{inlet} = 0.71$ and (b) $x_{inlet} = 0.86$ at G=148 [kg/m^2-s]

A key feature of the wall temperature downstream of the flow obstruction is that it increases and reaches a steady-state temperature for a given wall heat flux. Even as the wake region dries out, as the temperature increases more significantly, it still reaches a steady-state. This behavior contrasts greatly with results obtained under similar flow and heating conditions, but without the flow obstruction. Figure 4.27 shows that without a flow obstruction, the external wall temperature increases no more than 5°C from the saturation temperature for effective wall heat fluxes ranging from 0 to 22 kW/m^2. However, past the optimum heat flux, the wall temperature increases sharply and would reach a stead-state temperature far exceeding the observations in this study. This transition from a high HTC associated with the near-constant wall temperature to a lower HTC that leads to an increase in wall temperature is termed the critical boiling transition by Morse et al. (2024).

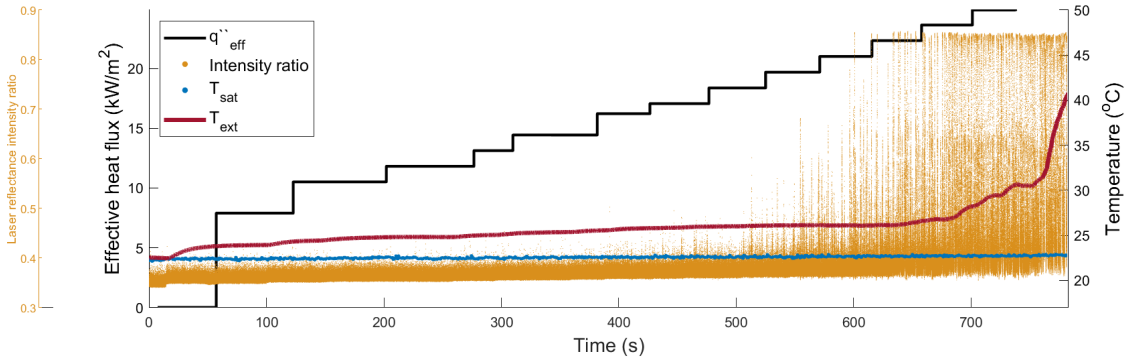

Figure 4.27: Wall temperature under similar conditions as Figure 4.26b, without flow obstruction. Excerpt from Morse (2020).

Comparison of wall temperature with and without a flow obstruction suggests a difference in heat transfer mechanisms in the wake region. Without a flow obstruction, convective heat transfer dominates. The local HTC is a function of the intermittency of dryout events. As the fraction of time in which dryout events increase past a critical point compared to the rewet duration, the local HTC decreases (Morse et al., 2024). In this study with a flow obstruction, parts of the wake region dries out without rewetting, while reaching a steady-state temperature. In this case, thermal conduction in the wall dominates the dry wake regions, transferring heat spanwise to the wetted areas surrounding the dry wake region.

Chapter 5

Conclusion

This chapter summarizes the main findings and future work that can be pursued.

5.1 Validation of film thickness measurement technique

The non-invasive and instantaneous optical liquid film thickness measurement technique was validated using the falling water film facility. The validation compared calculated values of wave velocities using the optical technique against independently recorded observations, and showed great agreement. Using the wave velocity, the wave shapes were able to be reconstructed. The two-layer characterization framework was then applied to the wave shapes to estimate the associated wave and base film mass flow rates. The validity of the framework was established by comparing some of its results with published correlations.

5.1.1 Future work

Characterization of the wave shapes can be done for comparison against existing correlations. One method of quantifying the wave shape is to define a shape factor that is the ratio between the wave amplitude and streamwise wave length (Le Corre, 2022). Modeling the correlation between wave shape factors and falling film flow conditions can be useful as a

way of estimating the wave mass flux in relevant flow conditions without having to measure the film thickness with high temporal and spatial resolution.

5.2 Wake region behavior downstream of annular flow obstruction

This work presents high-speed images and film thickness measurements of the wake region around an obstruction in annular flow. By observation, the obstruction diverts the liquid film to its sides, creating a low-flow wake region. Comparison of the film thickness measurements upstream and downstream the flow obstruction confirms this phenomenon; the downstream film thickness is generally thinner than the upstream film thickness. The wake region immediately downstream of the obstruction never dried out under the flow and wall heating conditions applied in this study. Effects of the disturbance waves were observed in the oscillatory motion of the dry wake region border. The advance and recession of the dry region border with the passing of disturbance waves can be of importance in the thermal behavior of the dry region. Compared to similar flows without a flow obstruction, external wall temperature measurements recorded in this work shows that the wall temperature does not reach runaway conditions. Instead, for all tested wall heat fluxes, the wall temperature reaches a steady-state. This is true even in the case at regions where the wake is dry. When parts of the wake is dry, local degradation of heat transfer was observed through the array of external wall temperature measurements.

The geometry of the dry wake region is quantitatively presented. The spanwise width of the dry wake region at different streamwise positions were reported. Under all flow conditions, the width increases with streamwise position. Under the tested conditions, the width does not span the entire heated area. The width generally increases with increasing vapor quality and decreasing total mass flux.

5.2.1 Future work

More work is needed to connect a) flow conditions, b) wake region geometry, and c) wake region HTC. Flow conditions include fluid properties and obstruction geometries. By relating these three aspects of the flow, a phenomenological model can be constructed to predict the heat transfer behavior of the wake region under different conditions. Using the work done in this study as the basis, a model can be applied in annular flow heat transfer applications.

For calculating the wake region HTC, a half-symmetric inverse heat transfer approach can be used. The wet or dry area HTC at a particular streamwise position can be iteratively solved using reasonable estimates of boundary conditions, wall conductivity, fluid properties, and the experimentally measured external wall temperature.

The effects of obstruction geometry on the wake region heat transfer can be investigated. For different obstruction shapes, threshold dimensions may exist that transition the wake region behavior between different regimes. When the obstruction blocks the liquid film nearly entirely, there is likely insufficient liquid in the wake region to maintain sufficient heat transfer form the heated wall. Conversely, when the obstruction size is on the order of the film thickness, little to no effect on heat transfer may be observed. Furthermore, arranging multiple obstructions in an array may cause an entirely different flow and heat transfer behavior. Effects of all of these conditions are not available in literature, and requires further investigation.

Bibliography

H. Ahn, C. Lee, H. Kim, H. Jo, S. Kang, J. Kim, J. Shin, and M. H. Kim. Pool boiling CHF enhancement by micro/nanoscale modifications of zircaloy-4 surface. *Nuclear Engineering and Design*, 240(10):3350–3360, 2010.

N. Borhani, B. Agostini, and J. R. Thome. A novel time strip flow visualisation technique for investigation of intermittent dewetting and dryout in elongated bubble flow in a microchannel evaporator. *International Journal of Heat and Mass Transfer*, 53:4809–4818, 2010.

V.P. Carey. *Liquid-vapor Phase-change Phenomena: An Introduction to the Thermophysics of Vaporization and Condensation Processes in Heat Transfer Equipment*. Series in chemical and mechanical engineering. Hemisphere Publishing Corporation, 1992. ISBN 9780891168362.

Jason Chan, Brian E. Fehring, Roman W. Morse, Kristofer M. Dressler, Gregory F. Nellis, Evan T. Hurlburt, and Arganthaël Berson. Thermoreflectance Wall Temperature Measurement in Annular Two-Phase Flow. volume ASME 2019 17th International Conference on Nanochannels, Microchannels, and Minichannels of *International Conference on Nanochannels, Microchannels, and Minichannels*, 06 2019. doi: 10.1115/ICNMM2019-4249. URL `https://doi.org/10.1115/ICNMM2019-4249`. V001T02A007.

J. C. Chen. Correlation for boiling heat transfer to saturated fluids in convective flow.

Industrial & Engineering Chemistry Process Design and Development, 5(3):322–329, 1966. doi: 10.1021/i260019a023. URL https://doi.org/10.1021/i260019a023.

W W Clark. Liquid film thickness measurement. *Multiphase science and technology*, 14, 2002.

J.G. Collier and G.F. Hewitt. Film thickness measurement. *ASME paper 64–WA/HT–41*, 1964. first conductance probe.

Dassault Systemes. Technical reference: Solidworks flow simulation 2021. Technical report, Dassault Systemes, July 2020.

F.W Dittus and L.M.K Boelter. Heat transfer in automobile radiators of the tubular type. *Publications in Engineering*, 2:443–461, 1930.

B. E. Fehring. Transient wall temperature and film thickness of vertical annular two-phase pulsatile flow. Master's thesis, University of Wisconsin - Madison, 2018.

H. Fujita, K. Katoh, and H. Takahama. Falling water films on a vertical cylinder with a downward step. *International Journal of Engineering Science*, 24(8):1405–1418, 1986. ISSN 0020-7225. doi: https://doi.org/10.1016/0020-7225(86)90069-8. URL https://www.sciencedirect.com/science/article/pii/0020722586900698.

J.E. Galloway and I. Mudawar. Chf mechanism in flow boiling from a short heated wall - I: Examination of near-wall conditions with the aid of photomicrography and high-speed video imaging. *International Journal of Heat and Mass Transfer*, 36(10):2511–2526, 1993.

William H. Henstock and Thomas J. Hanratty. The interfacial drag and the height of the wall layer in annular flows. *AIChE Journal*, 22(6):990–1000, 1976. doi: https://doi.org/10.1002/aic.690220607. URL https://aiche.onlinelibrary.wiley.com/doi/abs/10.1002/aic.690220607.

G. F. Hewitt. Disturbance waves in annular two-phase flow. *Proceedings of the Institution of Mechanical Engineers, Conference Proceedings*, 184(3):142–150, 1969.

G F Hewitt, R D King, and P C Lovegrove. Techniques for liquid film and pressure drop studies in annular two-phase flow. 3 1962. URL https://www.osti.gov/biblio/4804286.

E. Hurlburt and T. Newell. Optical measurement of liquid film thickness and wave velocity in liquid film flows. *Experiments in Fluids*, 21:357–362, 1996.

Ulf Jonsson and Erik Höglund. Determination of viscosities of oil-refrigerant mixtures at equilibrium by means of film thickness measurements. *ASHRAE Transactions*, 99(2): 1129–1136, 1993. Godkänd; 1993; Bibliografisk uppgift: Proceedings of the 1993 Annual Meeting of the American Society of Heating, Refrigerating and Air-Conditioning Engineers; 20070205 (cira).

Jean-Marie Le Corre. Phenomenological model of disturbance waves in annular two-phase flow. *International Journal of Multiphase Flow*, 151:104057, 2022. ISSN 0301-9322. doi: https://doi.org/10.1016/j.ijmultiphaseflow.2022.104057. URL https://www.sciencedirect.com/science/article/pii/S0301932222000696.

Guillermo E Morales-Espejel, Ralph Meeuwenoord, Armando Félix Quiñonez, and Rudolf Hauleitner. Film thickness and traction measurements of refrigerant r1233zd used as lubricant in elastohydrodynamic conditions. *Proceedings of the Institution of Mechanical Engineers, Part C: Journal of Mechanical Engineering Science*, 229(2):244–253, 2015. doi: 10.1177/0954406214533530. URL https://doi.org/10.1177/0954406214533530.

T. A. Moreira, R. W. Morse, K. M. Dressler, G. Ribatski, and A. Berson. Liquid-film thickness and disturbance-wave characterization in a vertical, upward, two-phase annular flow of saturated R245fa inside a rectangular channel. *International Journal of Multiphase Flow*, 132(103412), 2020.

R. W. Morse. Critical Heat Flux and the Dryout of Liquid Film in Two-phase Annular Flow. Master's thesis, University of Wisconsin - Madison, 2020.

Roman W. Morse, Jason Chan, Evan T. Hurlburt, Jean-Marie Le Corre, Arganthaël Berson, Gregory F. Nellis, and Kristofer M. Dressler. A new paradigm for the role of disturbance waves on film dryout and wall heat transfer in annular two-phase flow. *International Journal of Heat and Mass Transfer*, 219:124812, 2024. ISSN 0017-9310. doi: https://doi.org/10.1016/j.ijheatmasstransfer.2023.124812. URL https://www.sciencedirect.com/science/article/pii/S0017931023009572.

R.W. Morse, T.A. Moreira, J. Chan, K.M. Dressler, G. Ribatski, E.T. Hurlburt, L.L. McCarroll, G.F. Nellis, and A. Berson. Critical heat flux and the dryout of liquid film in vertical two-phase annular flow. *International Journal of Heat and Mass Transfer*, 177:121487, 2021. ISSN 0017-9310. doi: https://doi.org/10.1016/j.ijheatmasstransfer.2021.121487. URL https://www.sciencedirect.com/science/article/pii/S0017931021005901.

L. G. Neal and S. G. Bankoff. A high resolution resistivity probe for determination of local void properties in gas-liquid flow. *AIChE Journal*, 9:490–494, 1963. ISSN 15475905. doi: 10.1002/AIC.690090415.

T. Nosoko, P.N. Yoshimura, T. Nagata, and K. Oyakawa. Characteristics of two-dimensional waves on a falling liquid film. *Chemical Engineering Science*, 51(5):725–732, 1996. ISSN 0009-2509. doi: https://doi.org/10.1016/0009-2509(95)00292-8. URL https://www.sciencedirect.com/science/article/pii/0009250995002928.

Michael D Pearlman. Dynamic calibration of wave probes. *Massachusetts Institute of Technology, MIT, Department of Naval Architecture and Marine Engineering, Cambridge, USA, Contract No. DSR 6913*, 1963.

D. Schubring, T.A. Shedd, and E.T. Hurlburt. Studying disturbance waves in vertical annular flow with high-speed video. *International Journal of Multiphase Flow*, 36:385–396, 2010a.

D. Schubring, T.A. Shedd, and E.T. Hurlburt. Planar laser-induced fluorescence (PLIF) measurements of liquid film thickness in annular flow. part ii: Analysis and comparison to models. *International Journal of Multiphase Flow*, 36:825–835, 2010b.

T.A. Shedd and T.A. Newell. Automated optical liquid film thickness measurement method. *The American Institute of Physics - Review of Scientific Instruments*, 69, 1998.

Guanyu Su. *Thermohydraulics and suppression of nucleate boiling in upward two-phase annular flow : probing multiscale physics by innovative diagnostics*. PhD thesis, Massachusetts Institute of Technology, 2018.

Cristiano Bigonha Tibiriçá, Francisco Júlio do Nascimento, and Gherhardt Ribatski. Film thickness measurement techniques applied to micro-scale two-phase flow systems. *Experimental Thermal and Fluid Science*, 34(4):463–473, 2010. ISSN 0894-1777. doi: https://doi.org/10.1016/j.expthermflusci.2009.03.009. URL `https://www.sciencedirect.com/science/article/pii/S0894177709000557`. ECI International Conference on Heat Transfer and Fluid Flow in Microscale.

Tsutomu Ubara, Katsumi Sugimoto, and Hitoshi Asano. Film thickness and heat transfer characteristics of r1233zd(e) falling film with nucleate boiling on an inclined plate. *International Journal of Heat and Mass Transfer*, 198:123423, 2022. ISSN 0017-9310. doi: https://doi.org/10.1016/j.ijheatmasstransfer.2022.123423. URL `https://www.sciencedirect.com/science/article/pii/S0017931022008924`.

Jie Zeng, Yifei Wang, Zongyao Wei, Liang Wang, Tingting Li, and Guangsuo Yu. Thickness distribution and fluctuation characteristics of liquid falling film under turbulent conditions. *Chemical Engineering Science*, 248:117172, 2022. ISSN 0009-2509. doi: https://doi.org/10.1016/j.ces.2021.117172. URL `https://www.sciencedirect.com/science/article/pii/S0009250921007375`.

B.J Zhang, K.J. Kim, and H. Yoon. Enhanced heat transfer performance of alumina sponge-

like nano-porous structures through surface wettability control in nucleate pool boiling. *International Journal of Heat and Mass Transfer*, 55(25-26):7487–7498, 2012.

T. Zhao, C. N. Markides, O. K. Matar, and G.F. Hewitt. Disturbance wave development in two-phase gas-liquid upwards vertical annular flow. *International Journal of Multiphase Flow*, 55:111–129, 2013.

Appendix A

Appendix: Falling Film

A.1 Wave recognition in film thickness time trace

Figures in this section show film thickness versus time on the left axis and wave velocity on the right axis. Start and end points of waves are found using the peaks and troughs of the upstream film thickness signal and are illustrated by the vertical green lines.

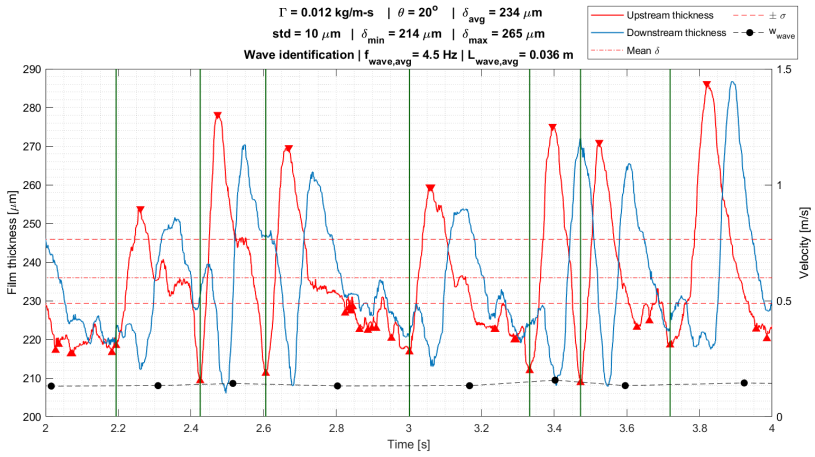

Wave recognition for test condition No. 1.1

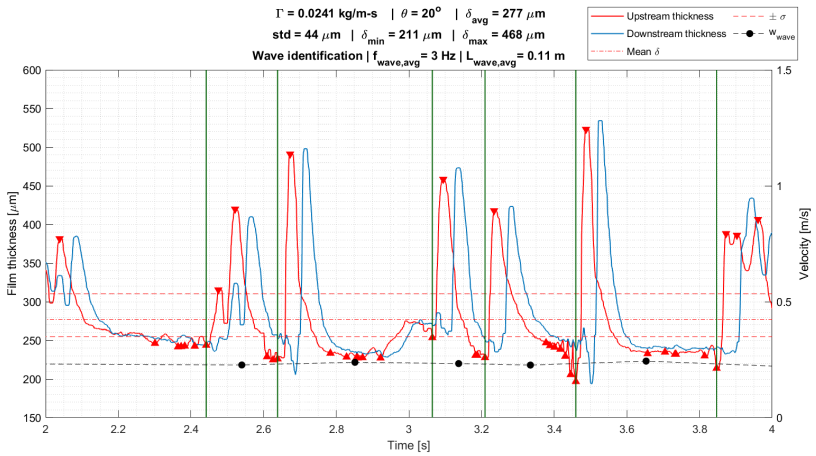

Wave recognition for test condition No. 1.2

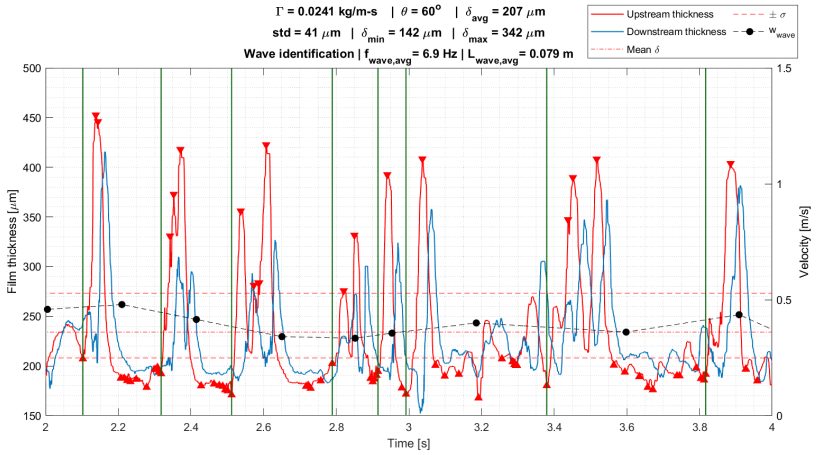

Wave recognition for test condition No. 1.3

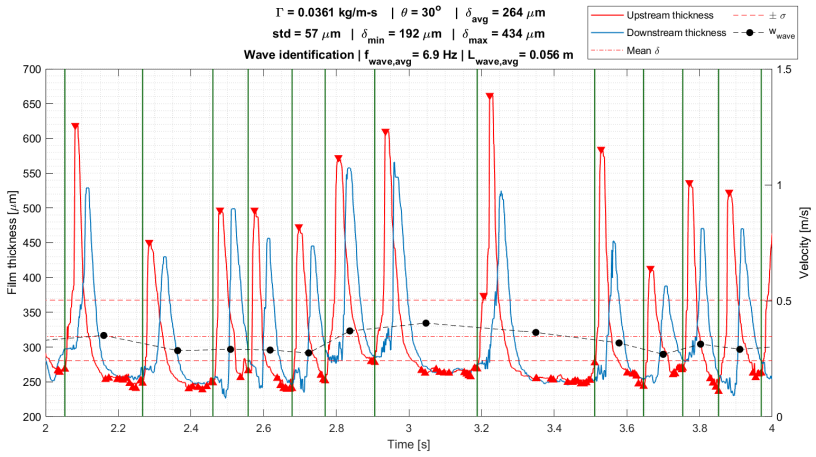

Wave recognition for test condition No. 1.4

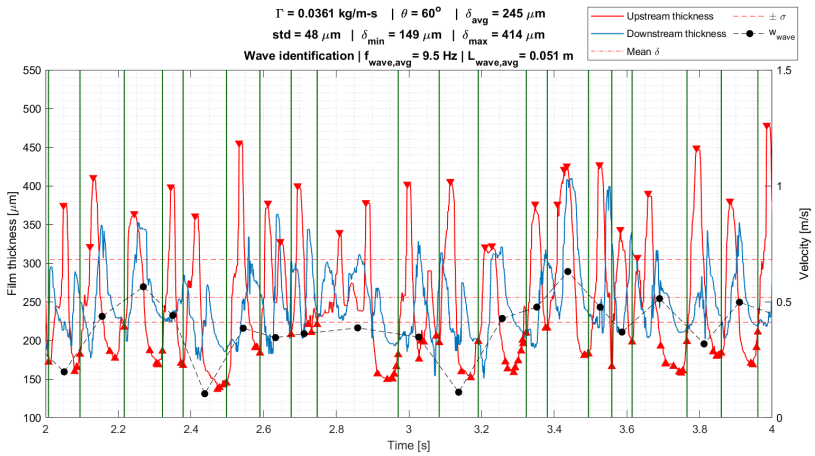

Wave recognition for test condition No. 1.5

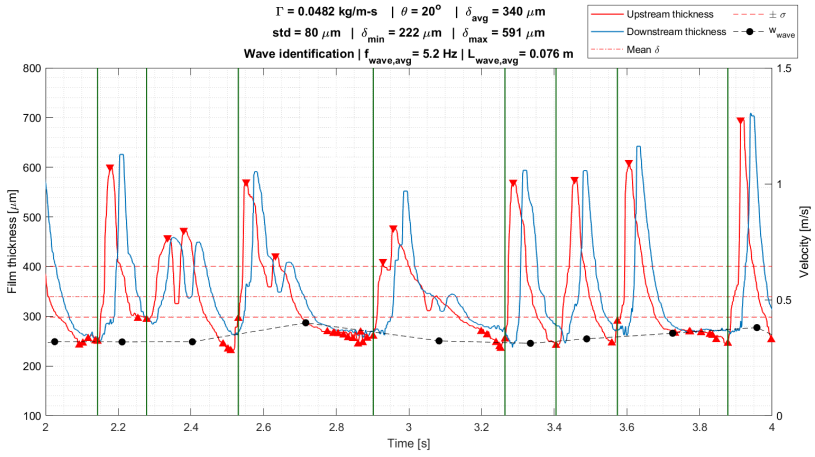

Wave recognition for test condition No. 1.6

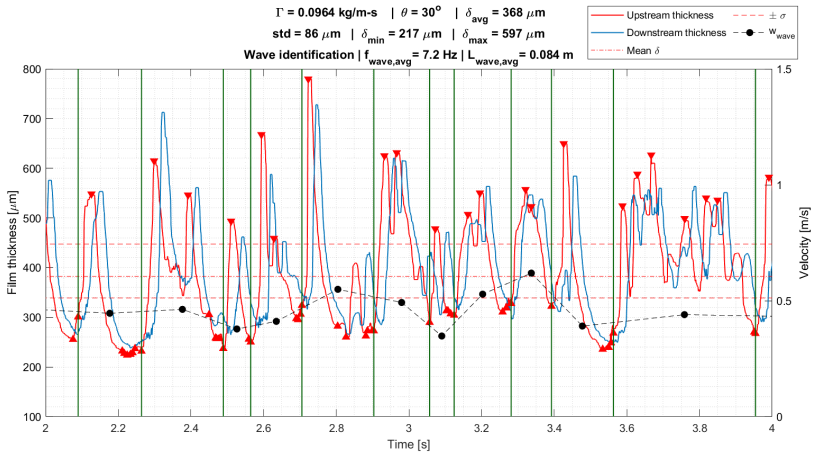

Wave recognition for test condition No. 1.7

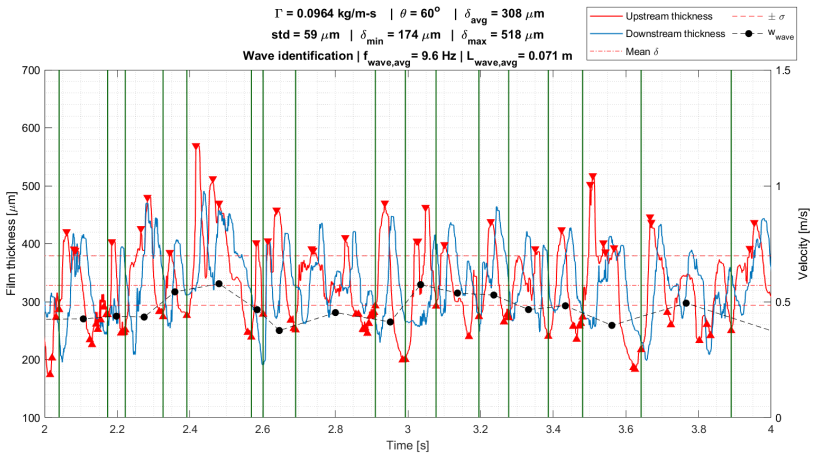

Wave recognition for test condition No. 1.8

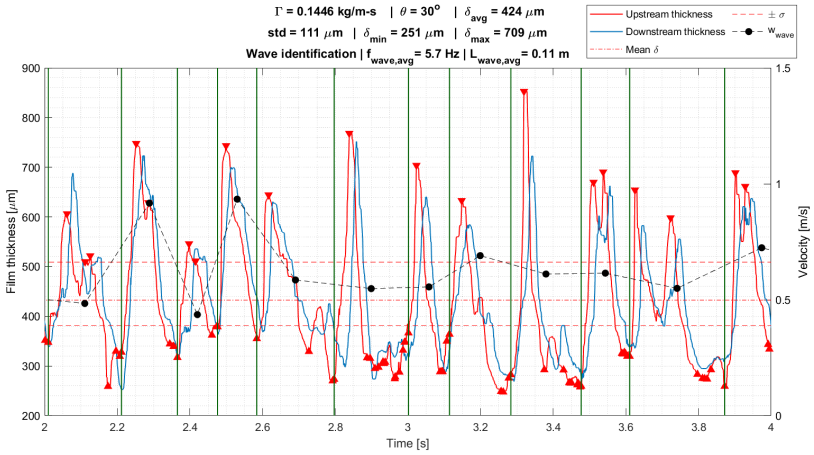

Wave recognition for test condition No. 1.9

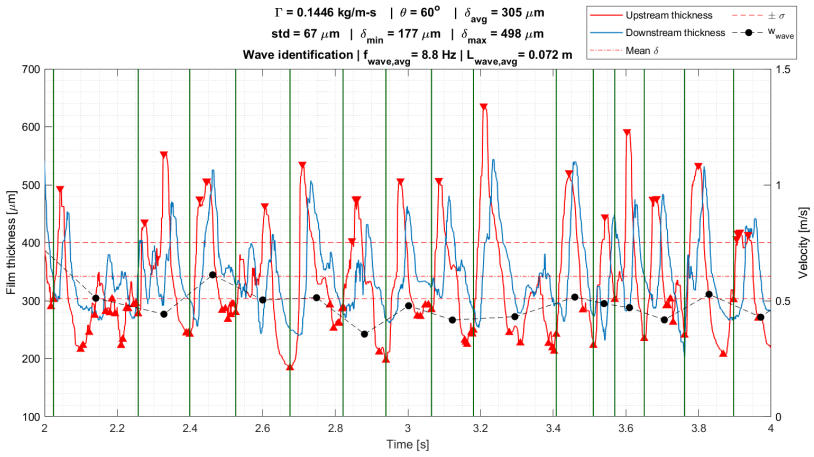

Wave recognition for test condition No. 1.10

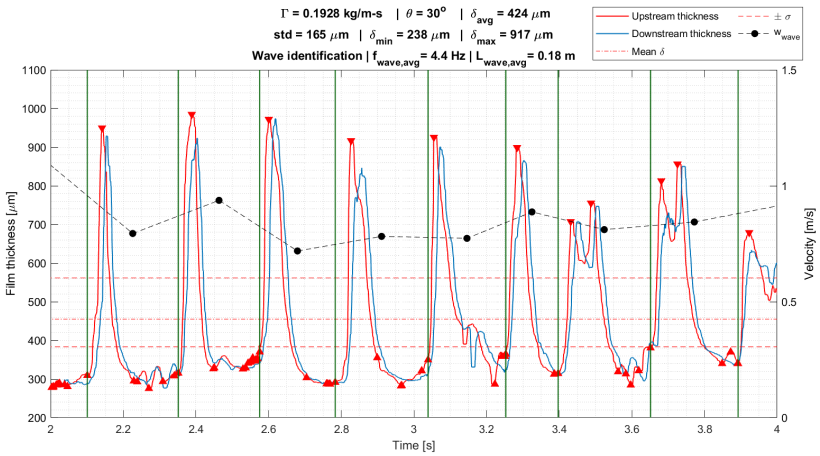

Wave recognition for test condition No. 1.11

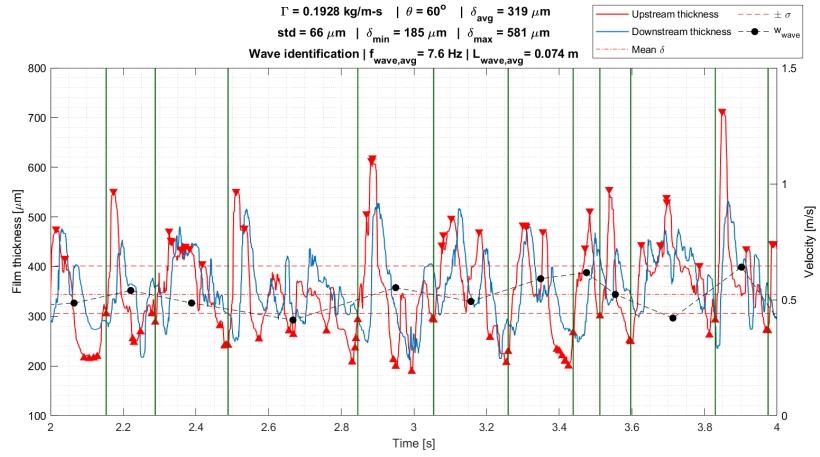

Wave recognition for test condition No. 1.12

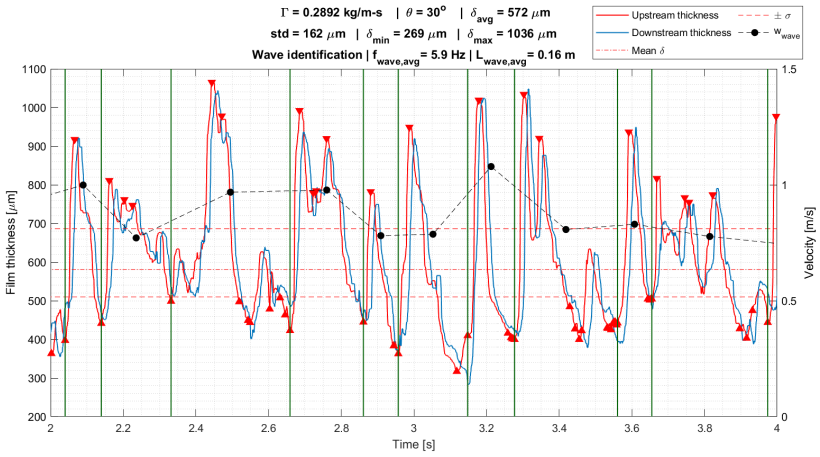

Wave recognition for test condition No. 1.13

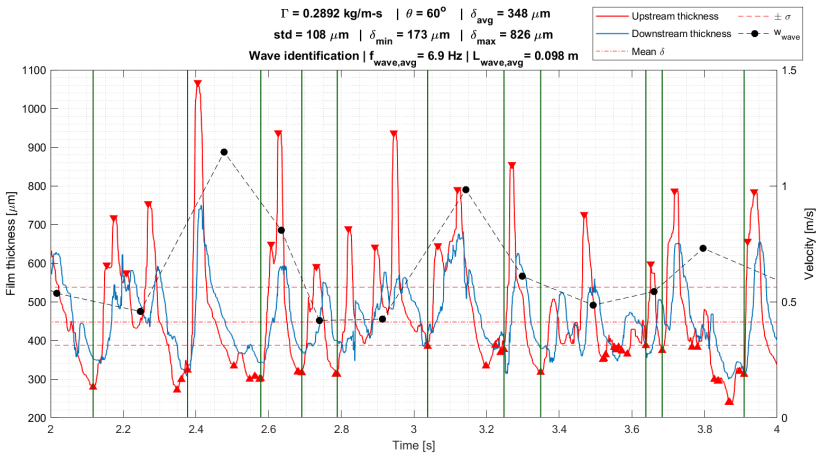

Wave recognition for test condition No. 1.14

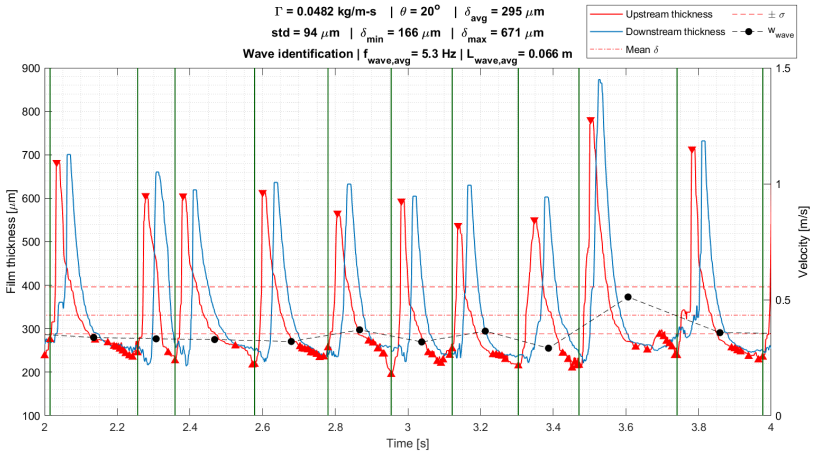

Wave recognition for test condition No. 2.1

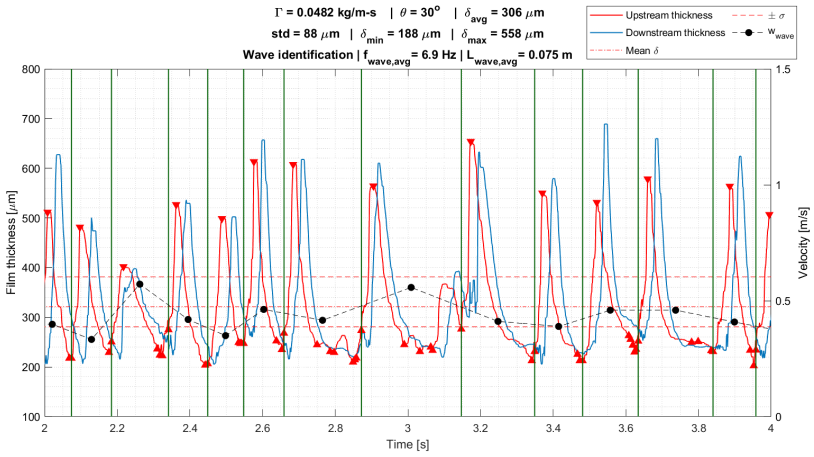

Wave recognition for test condition No. 2.2

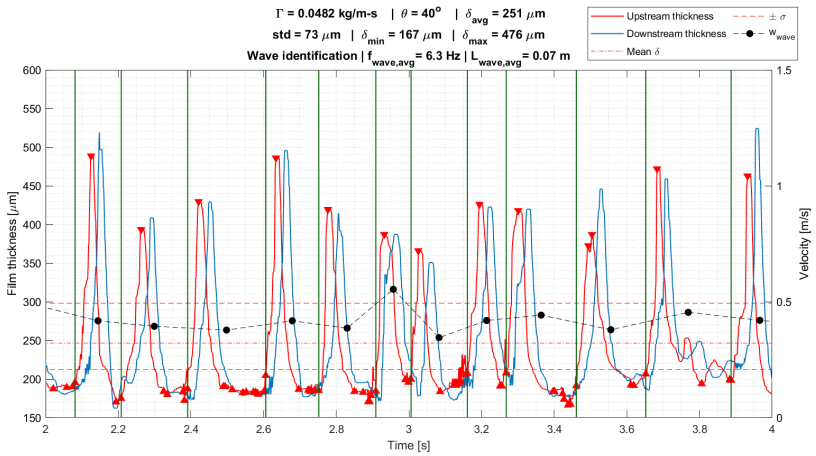

Wave recognition for test condition No. 2.3

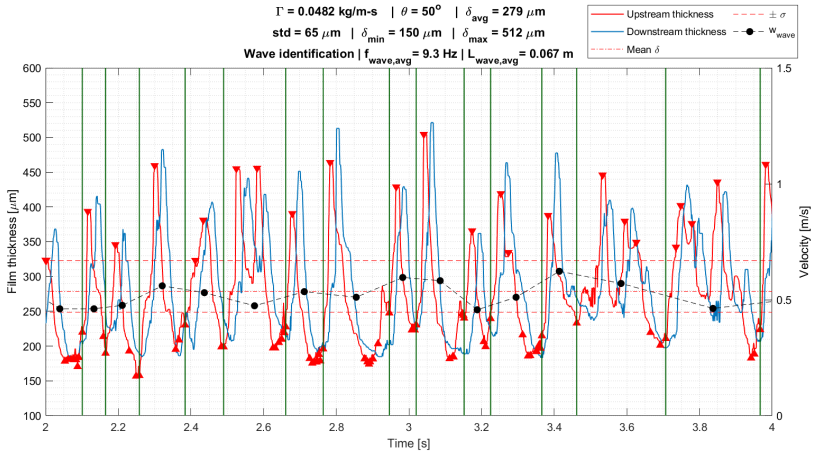

Wave recognition for test condition No. 2.4

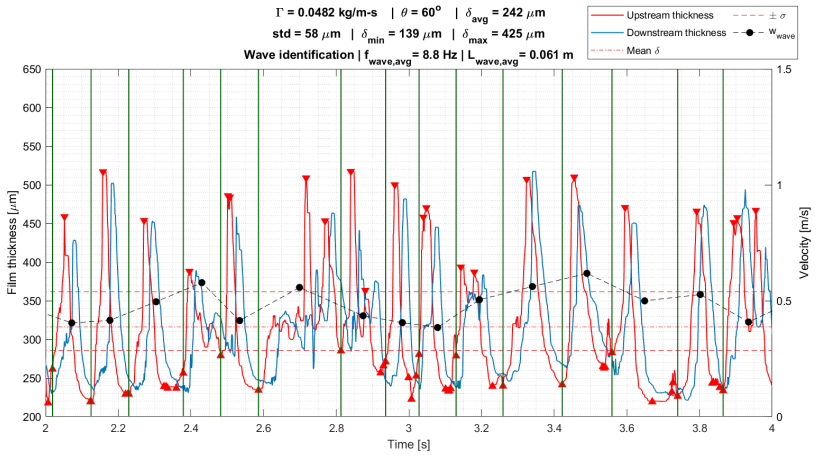

Wave recognition for test condition No. 2.5

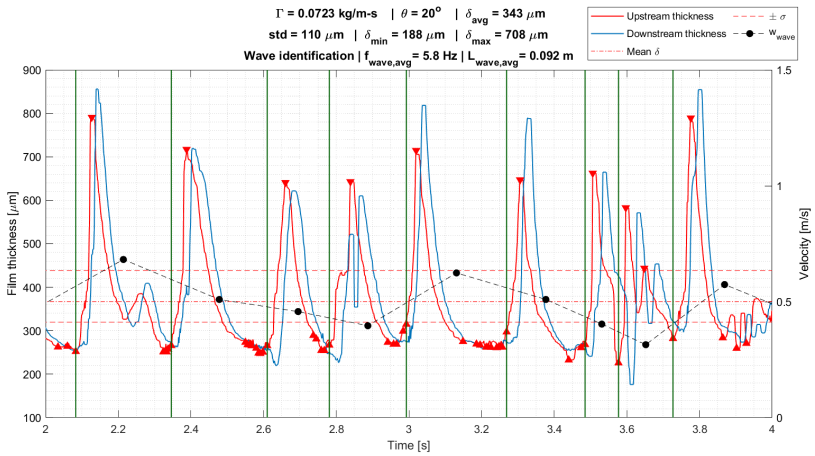

Wave recognition for test condition No. 2.6

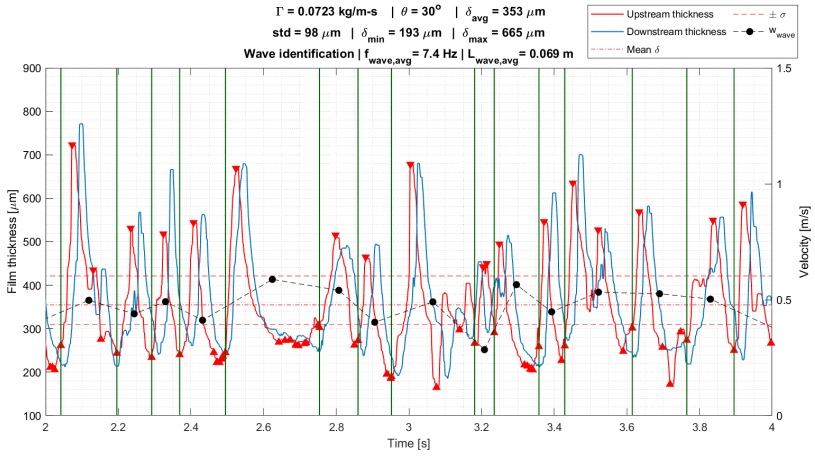

Wave recognition for test condition No. 2.7

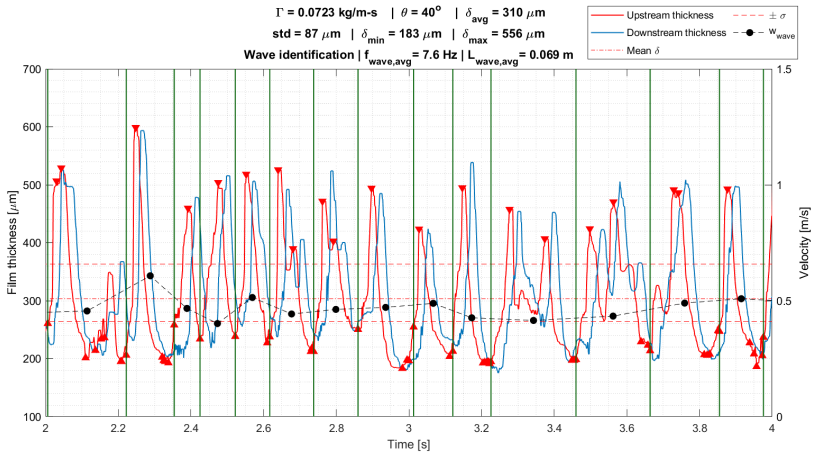

Wave recognition for test condition No. 2.8

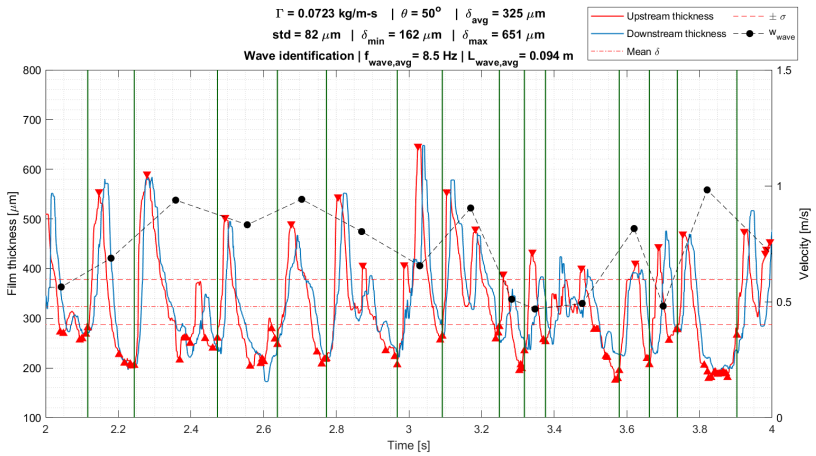

Wave recognition for test condition No. 2.9

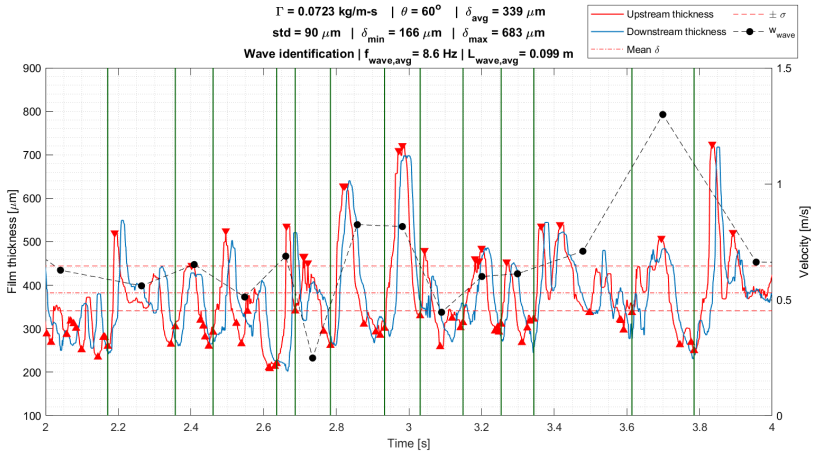

Wave recognition for test condition No. 2.10

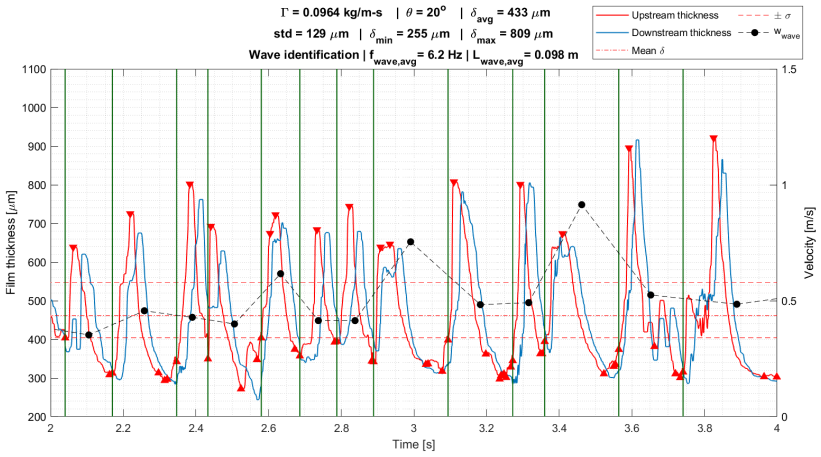

Wave recognition for test condition No. 2.11

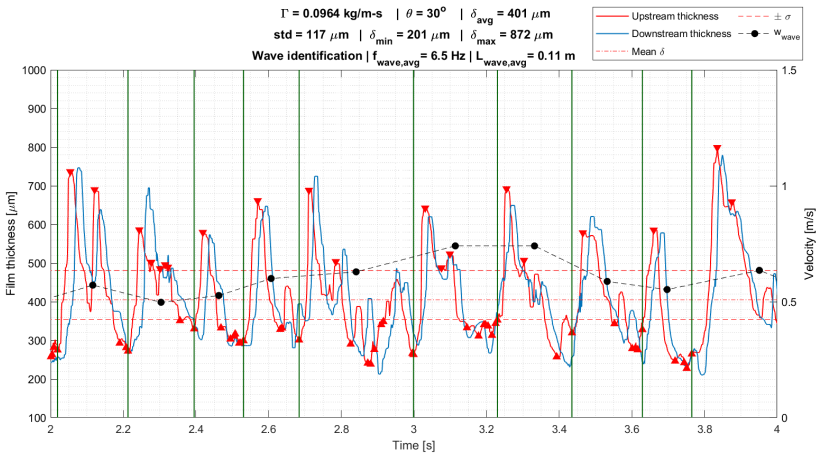

Wave recognition for test condition No. 2.12

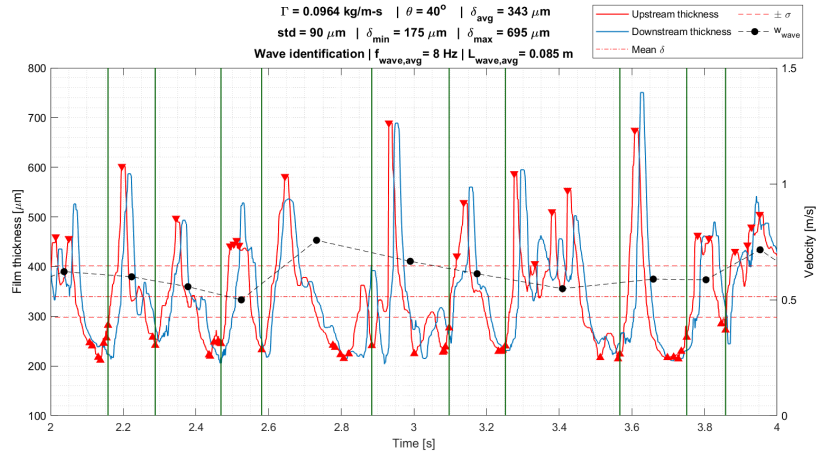

Wave recognition for test condition No. 2.13

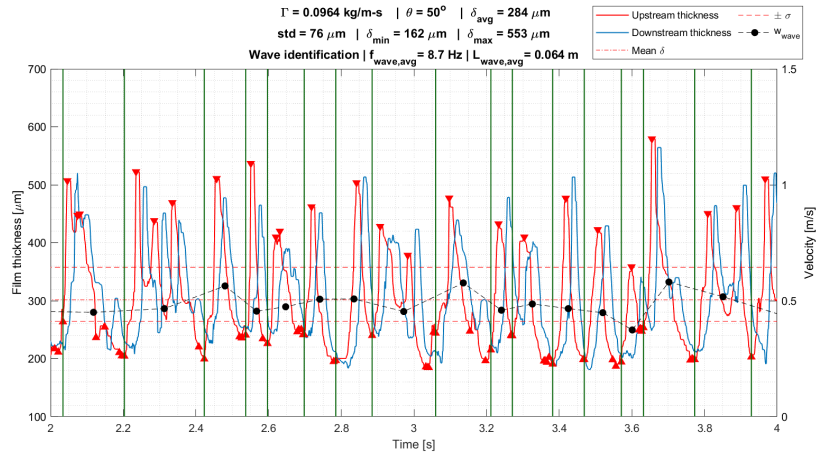

Wave recognition for test condition No. 2.14

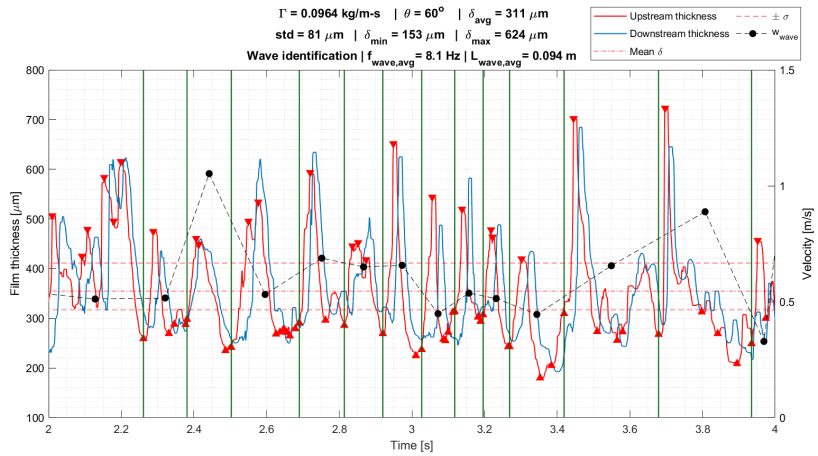

Wave recognition for test condition No. 2.15

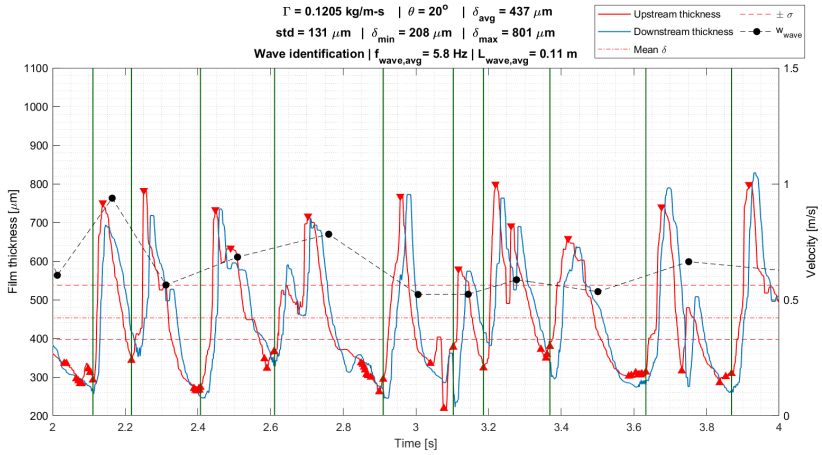

Wave recognition for test condition No. 2.16

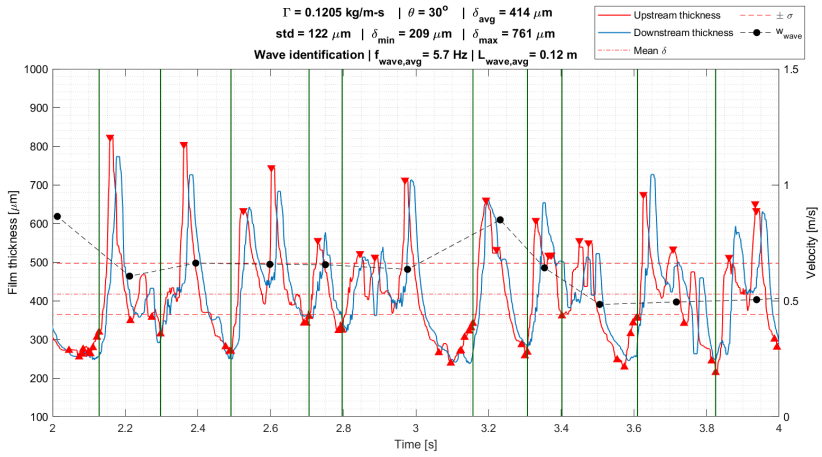

Wave recognition for test condition No. 2.17

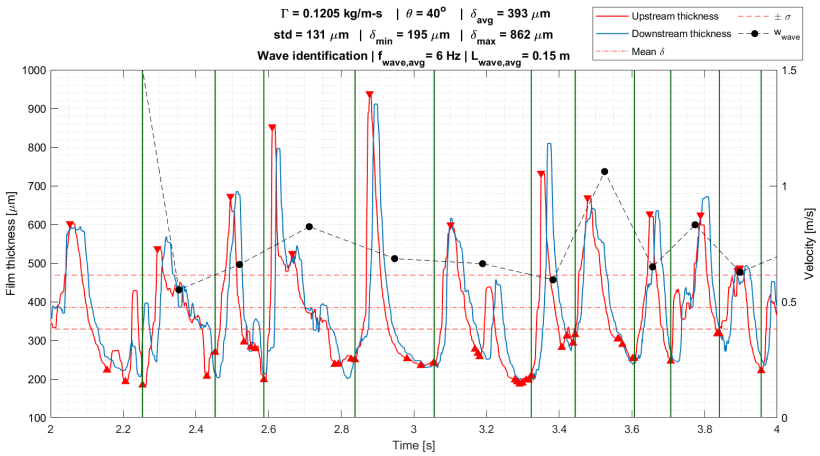

Wave recognition for test condition No. 2.18

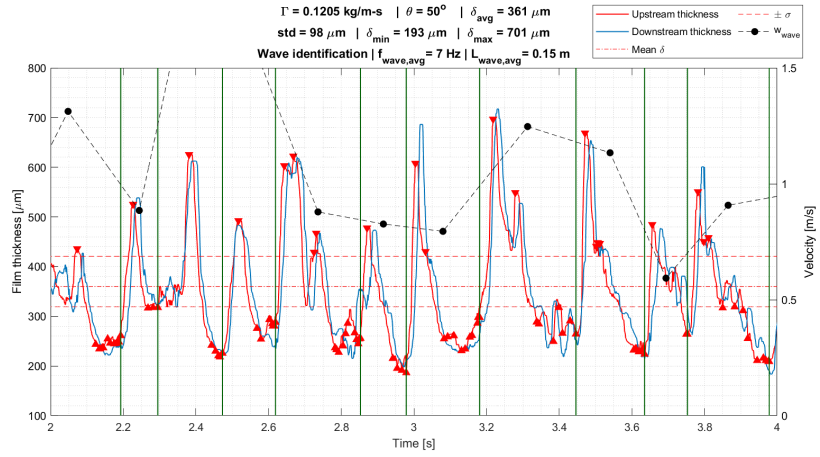

Wave recognition for test condition No. 2.19

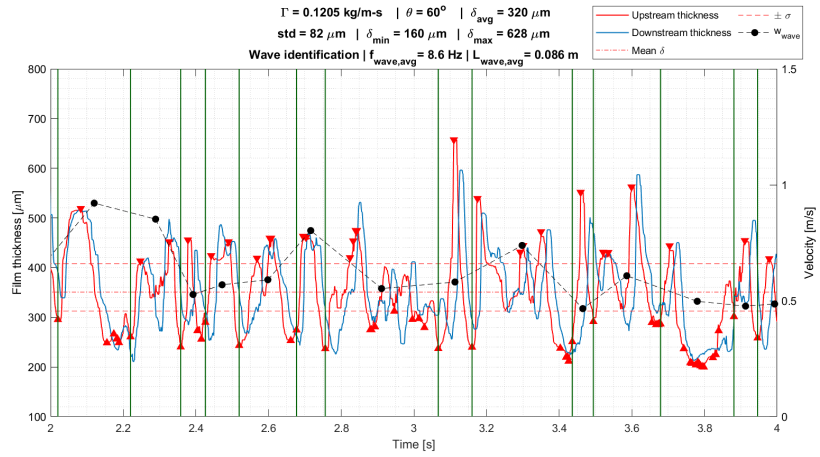

Wave recognition for test condition No. 2.20

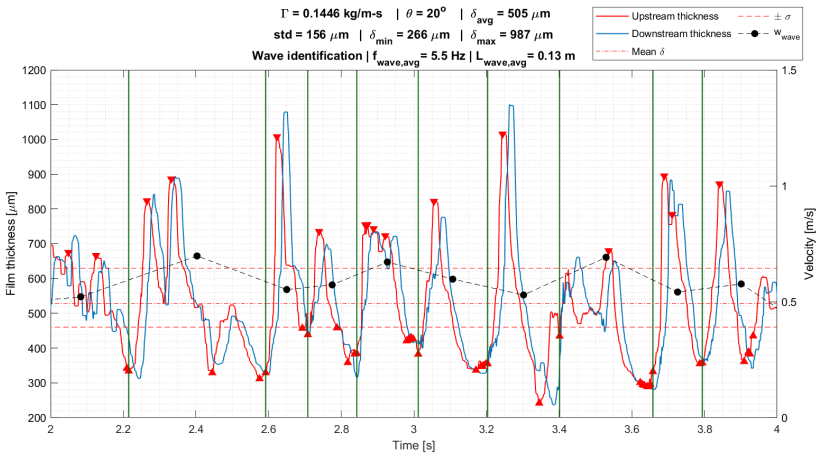

Wave recognition for test condition No. 2.21

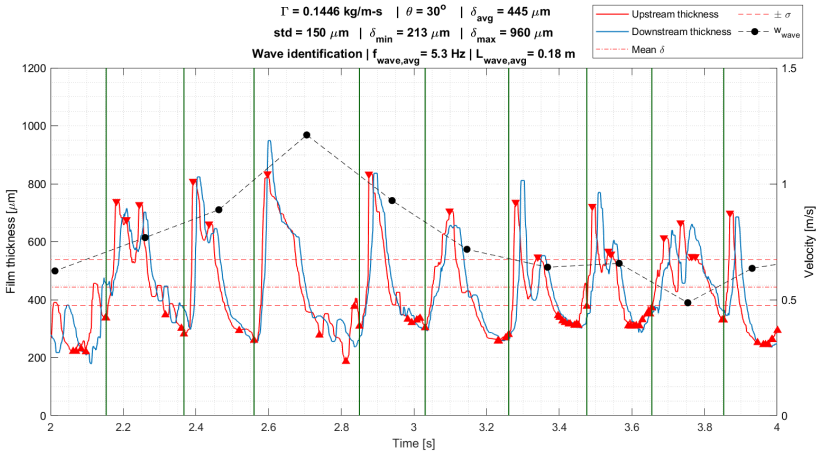

Wave recognition for test condition No. 2.22

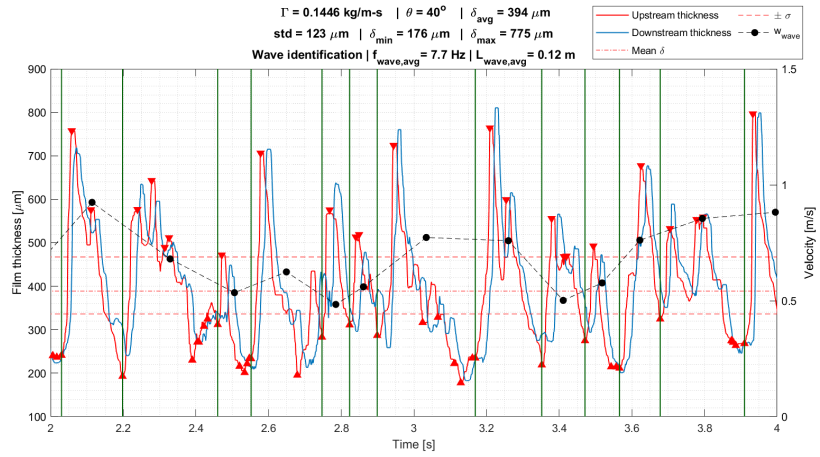

Wave recognition for test condition No. 2.23

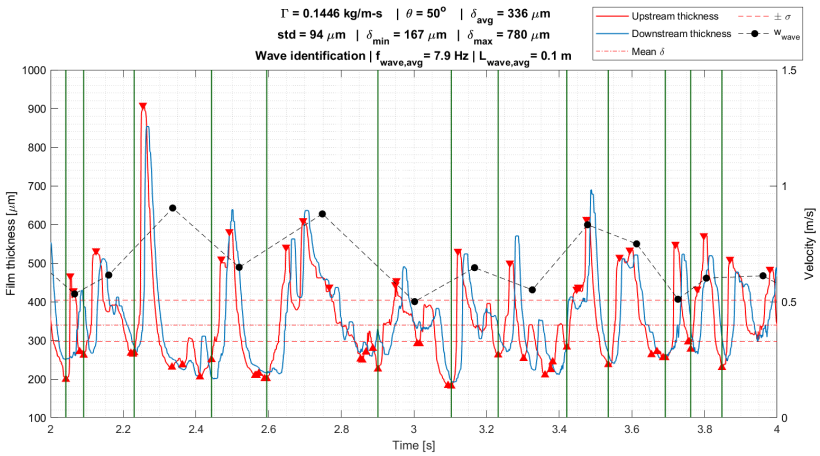

Wave recognition for test condition No. 2.24

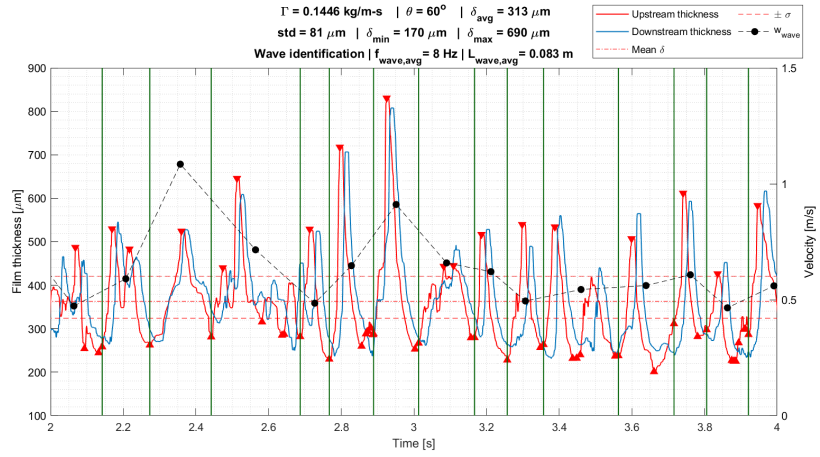

Wave recognition for test condition No. 2.25

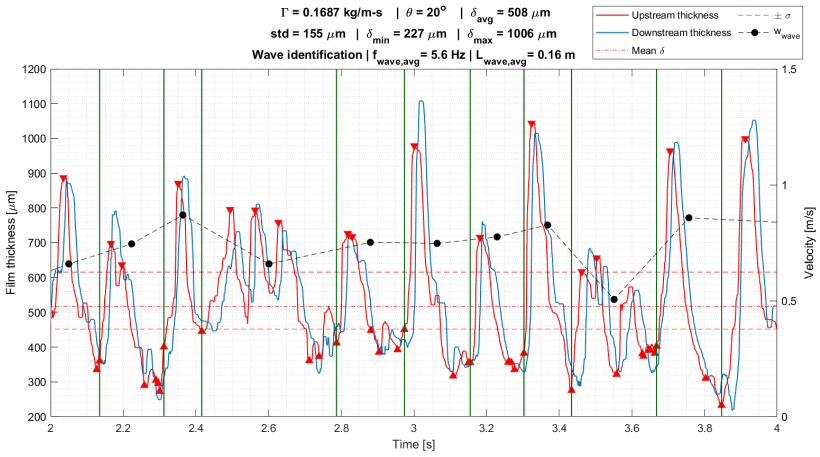

Wave recognition for test condition No. 2.26

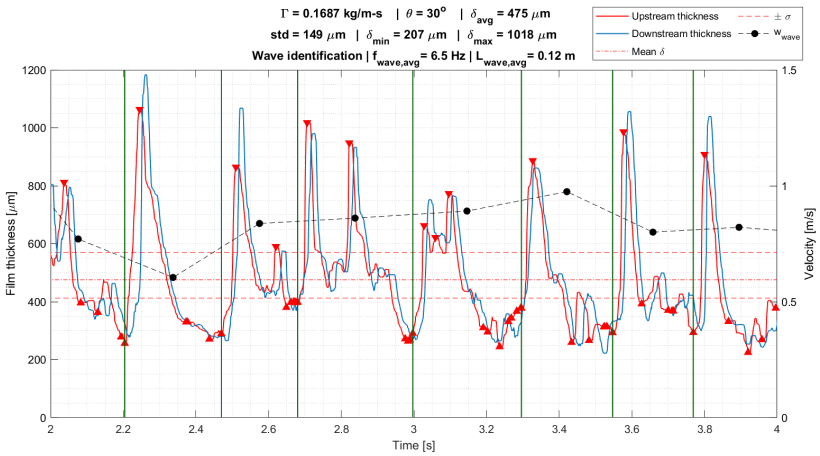

Wave recognition for test condition No. 2.27

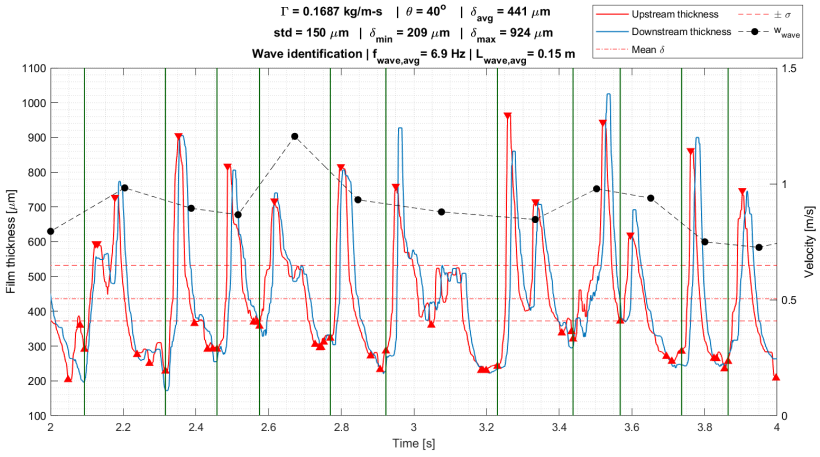

Wave recognition for test condition No. 2.28

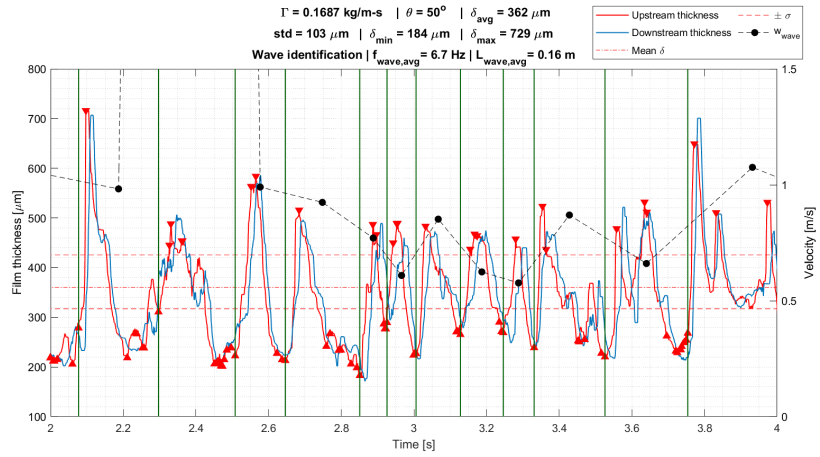

Wave recognition for test condition No. 2.29

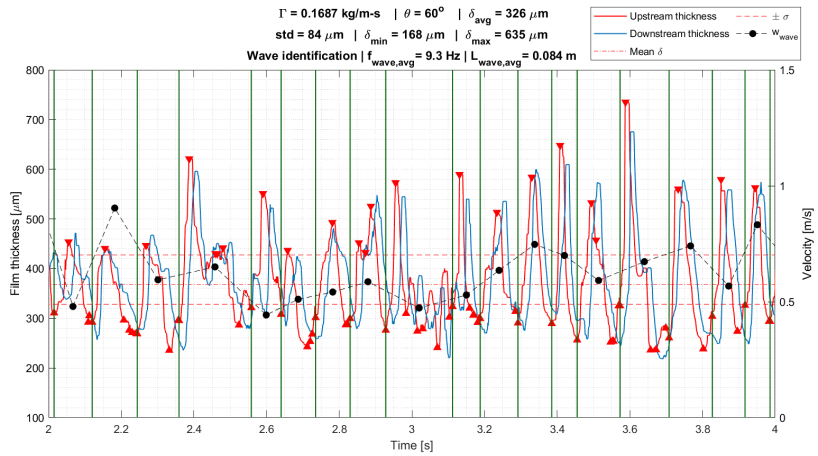

Wave recognition for test condition No. 2.30

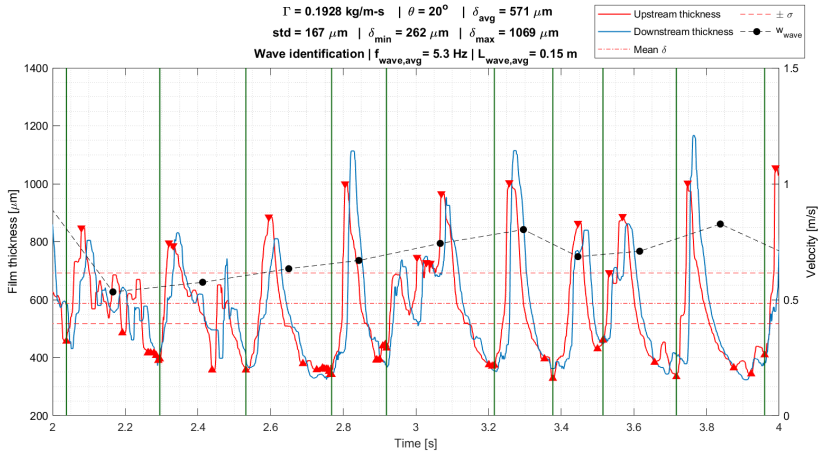

Wave recognition for test condition No. 2.31

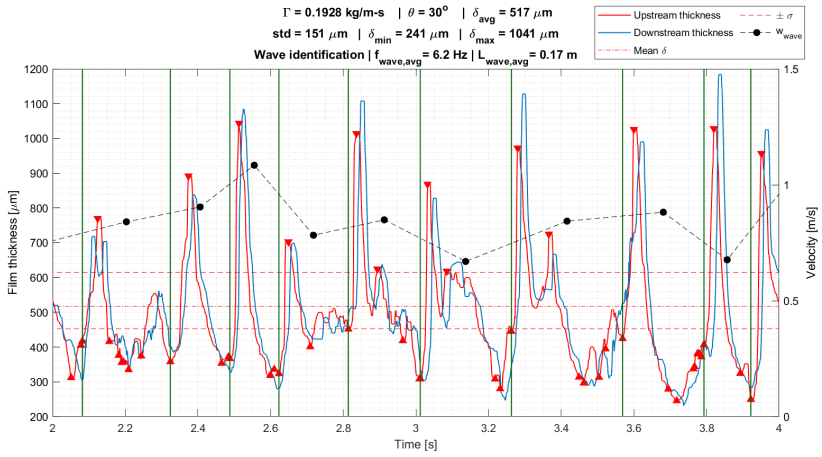

Wave recognition for test condition No. 2.32

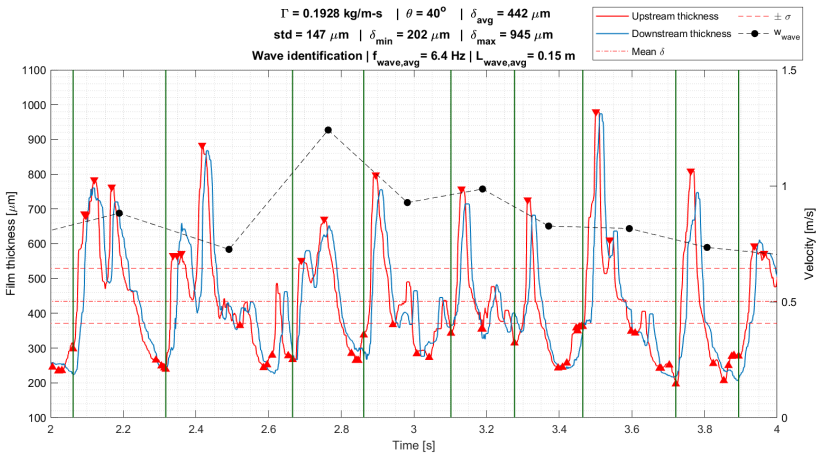

Wave recognition for test condition No. 2.33

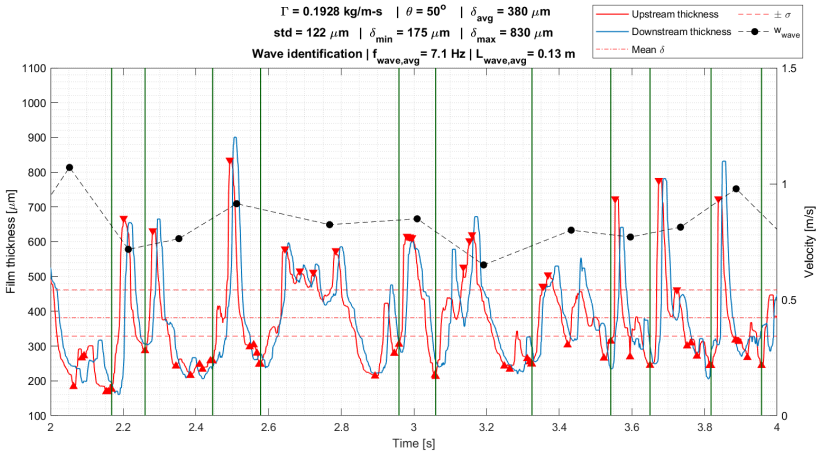

Wave recognition for test condition No. 2.34

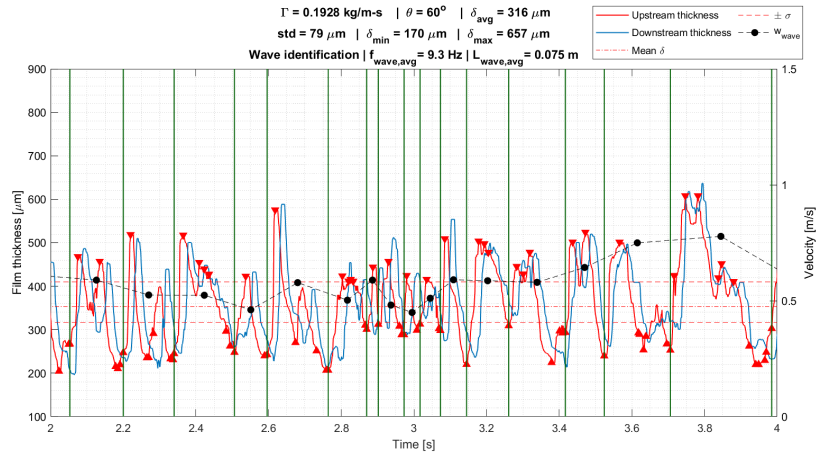

Wave recognition for test condition No. 2.35

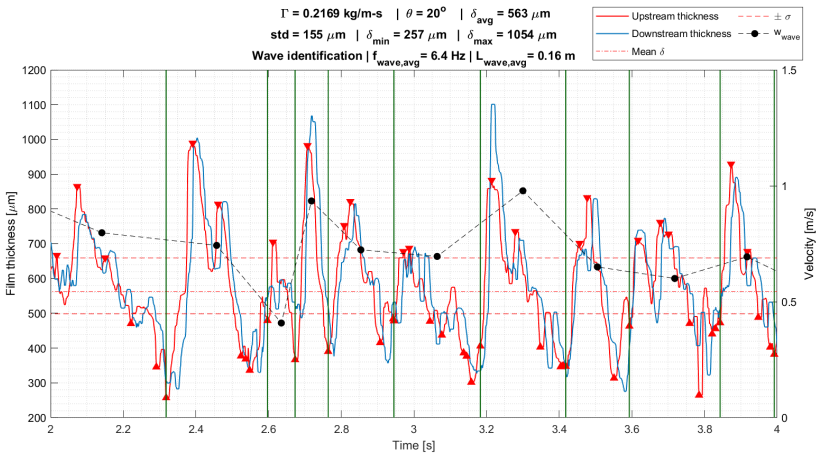

Wave recognition for test condition No. 2.36

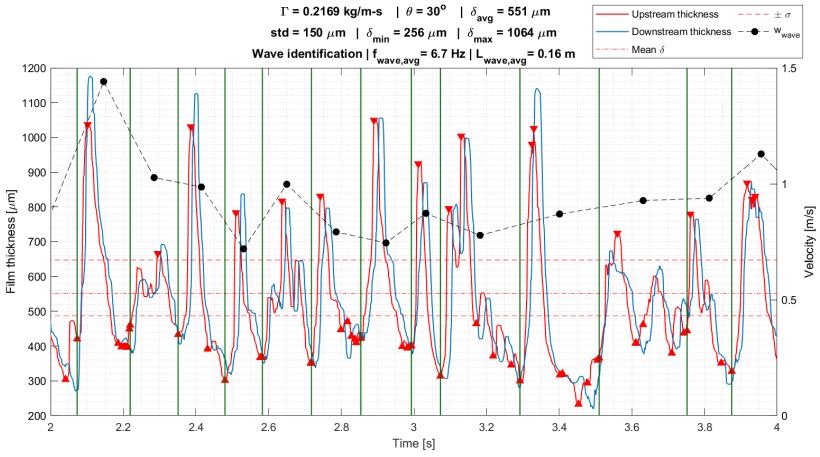

Wave recognition for test condition No. 2.37

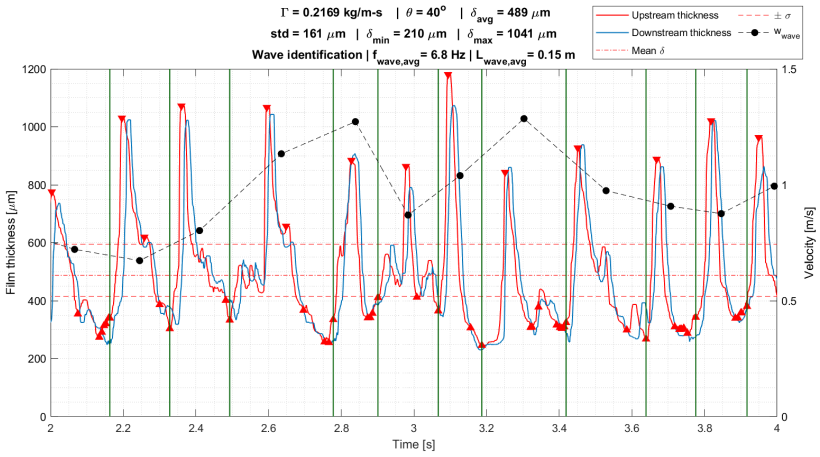

Wave recognition for test condition No. 2.38

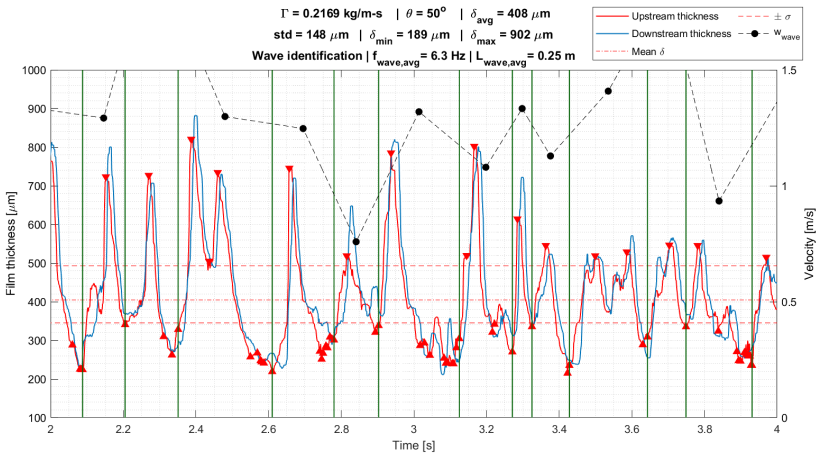

Wave recognition for test condition No. 2.39

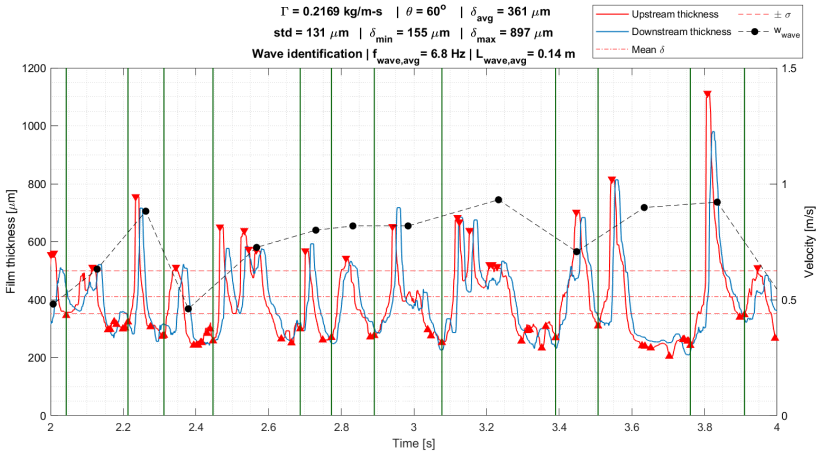

Wave recognition for test condition No. 2.40

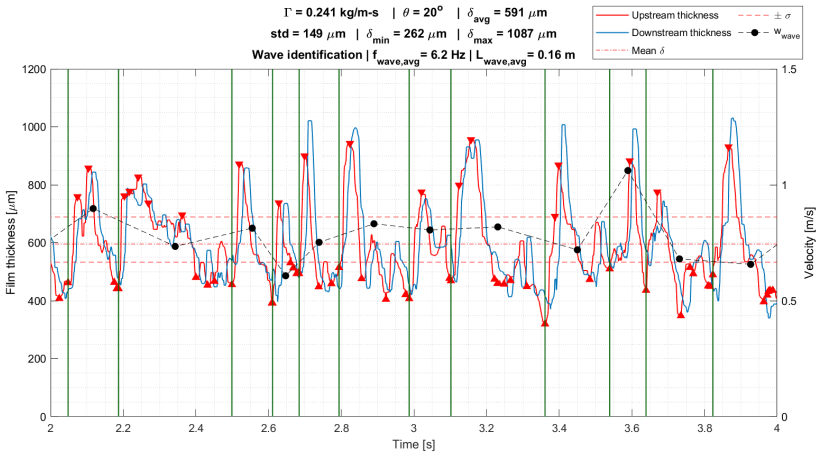

Wave recognition for test condition No. 2.41

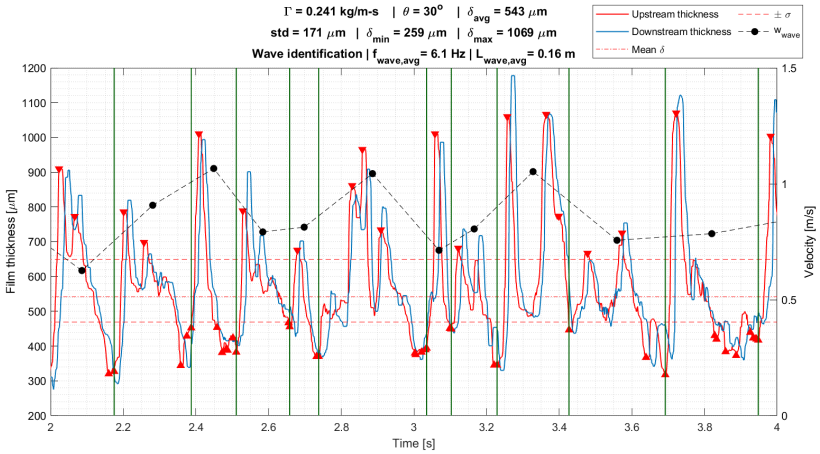

Wave recognition for test condition No. 2.42

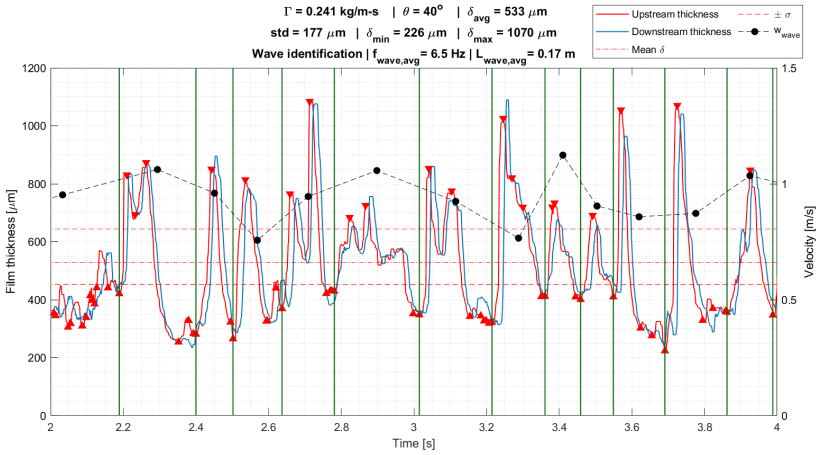

Wave recognition for test condition No. 2.43

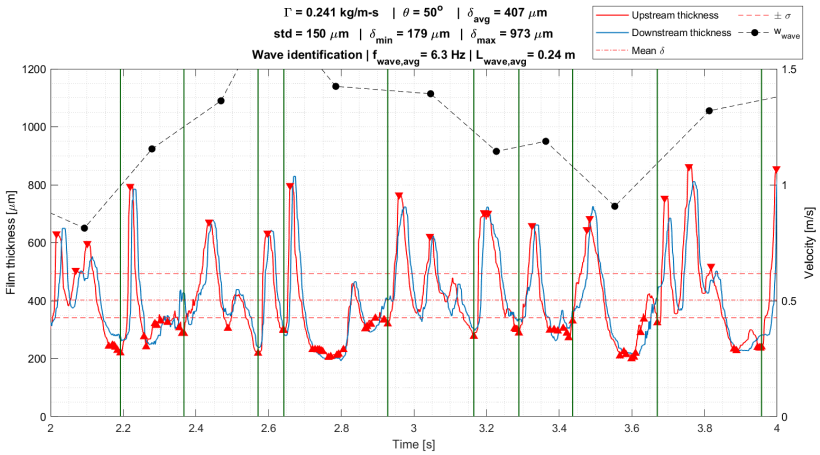

Wave recognition for test condition No. 2.44

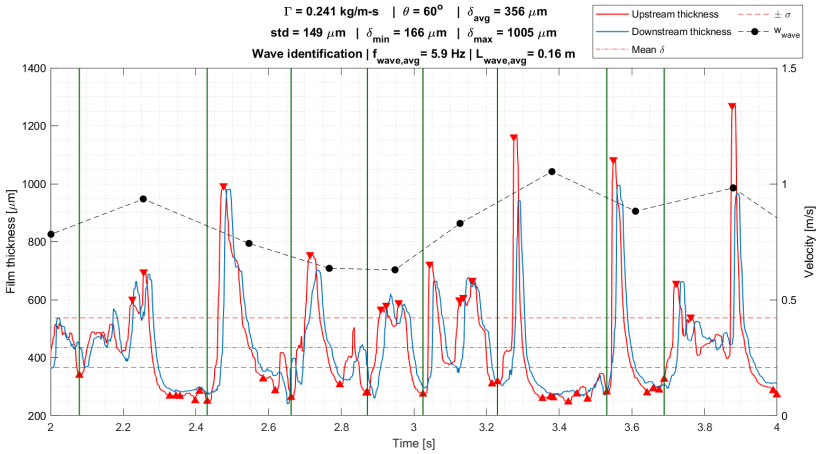

Wave recognition for test condition No. 2.45

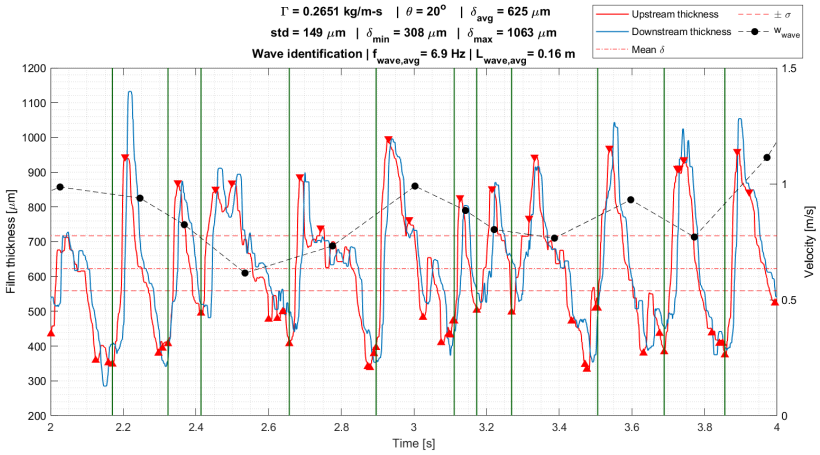

Wave recognition for test condition No. 2.46

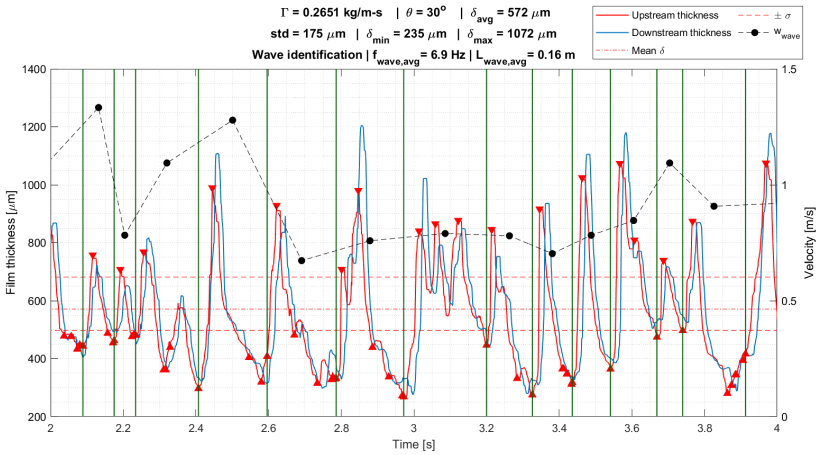

Wave recognition for test condition No. 2.47

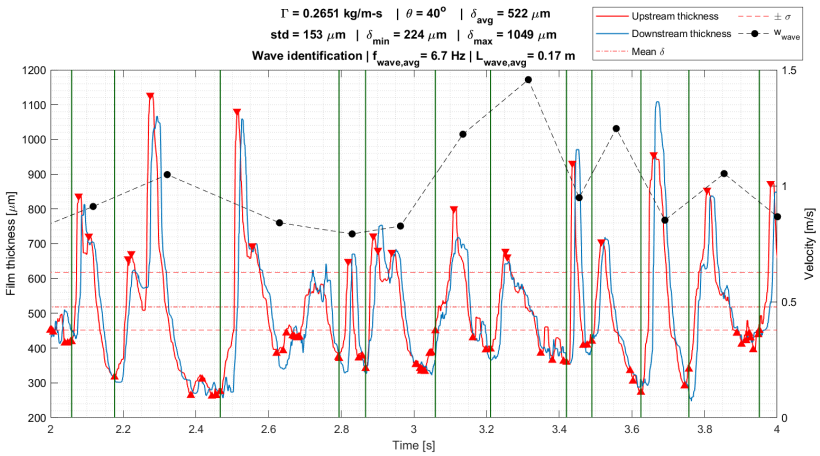

Wave recognition for test condition No. 2.48

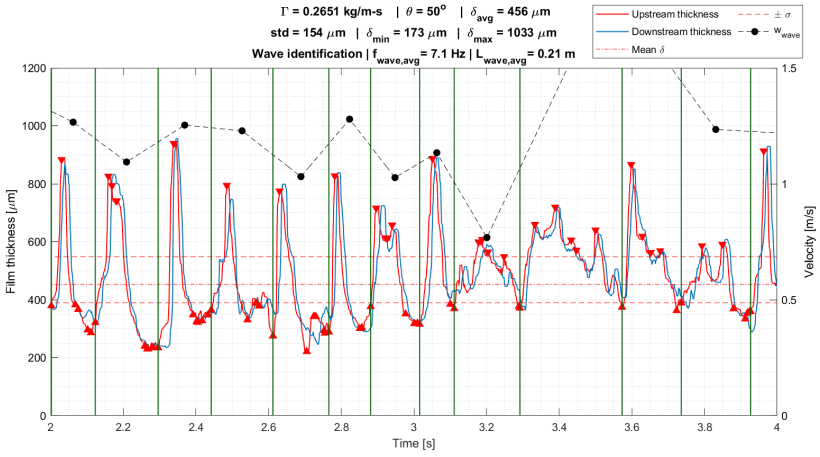

Wave recognition for test condition No. 2.49

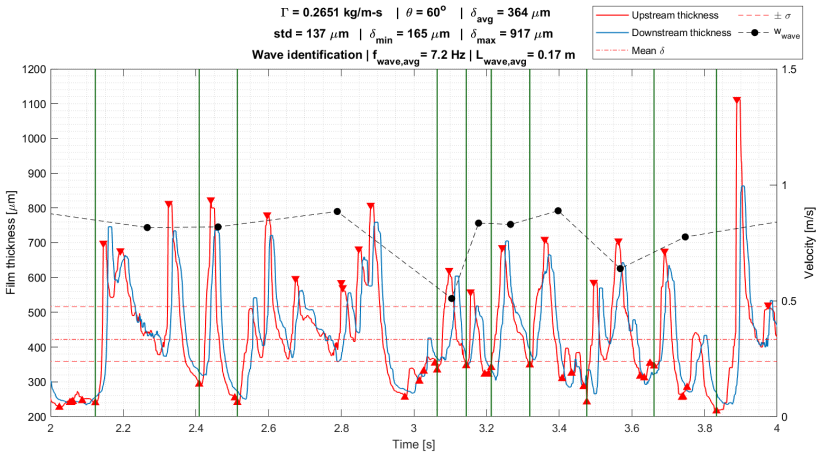

Wave recognition for test condition No. 2.50

A.2 Wave shapes, overlaid

Wave shapes overlaid on each other for each test condition are presented in this section. Waves with outlying streamwise length are removed in these figures.

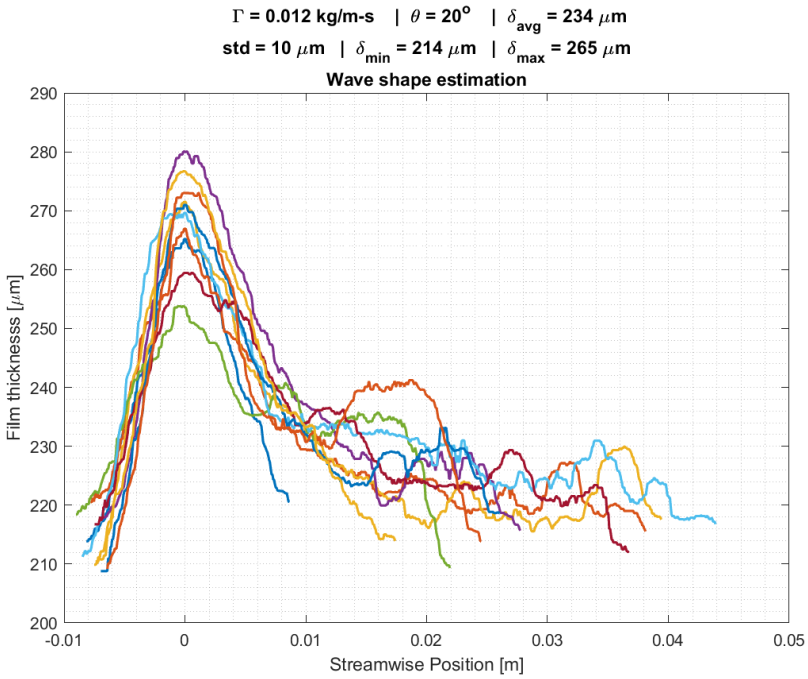

Wave shapes for test condition No. 1.2

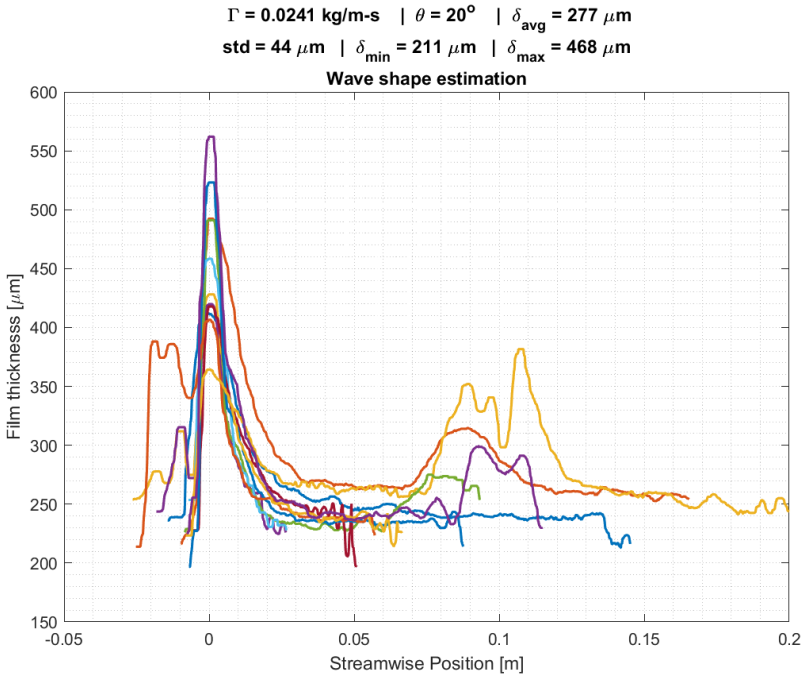

Wave shapes for test condition No. 1.2

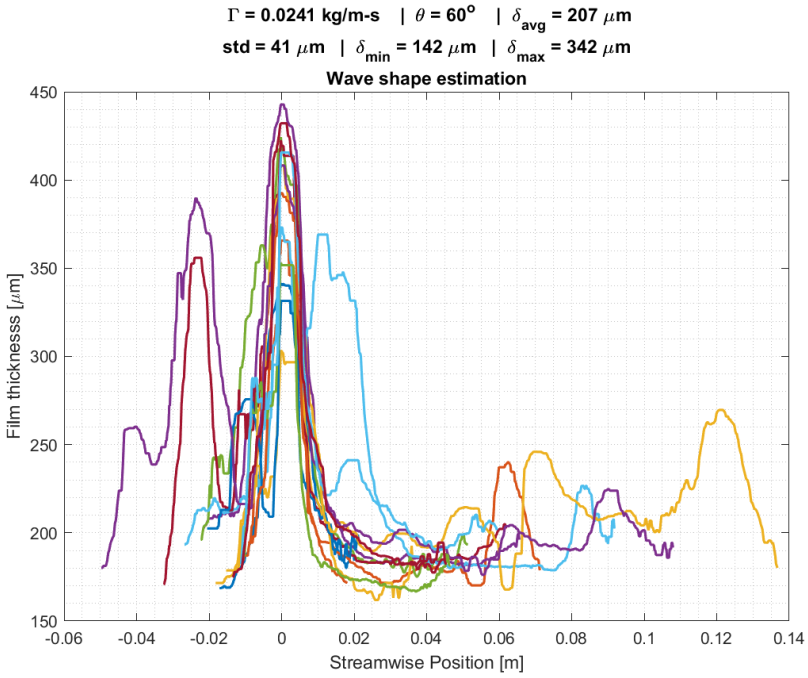

Wave shapes for test condition No. 1.3

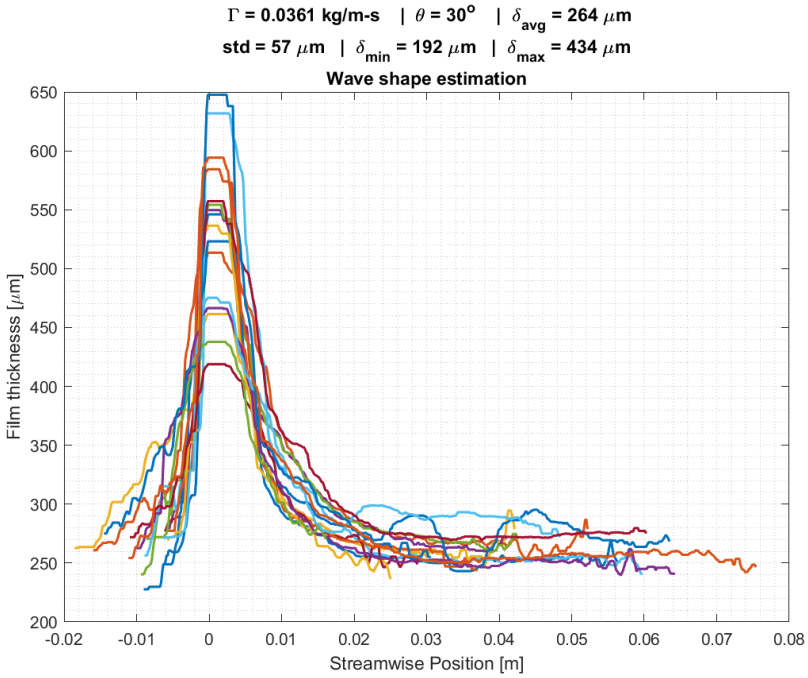

Wave shapes for test condition No. 1.4

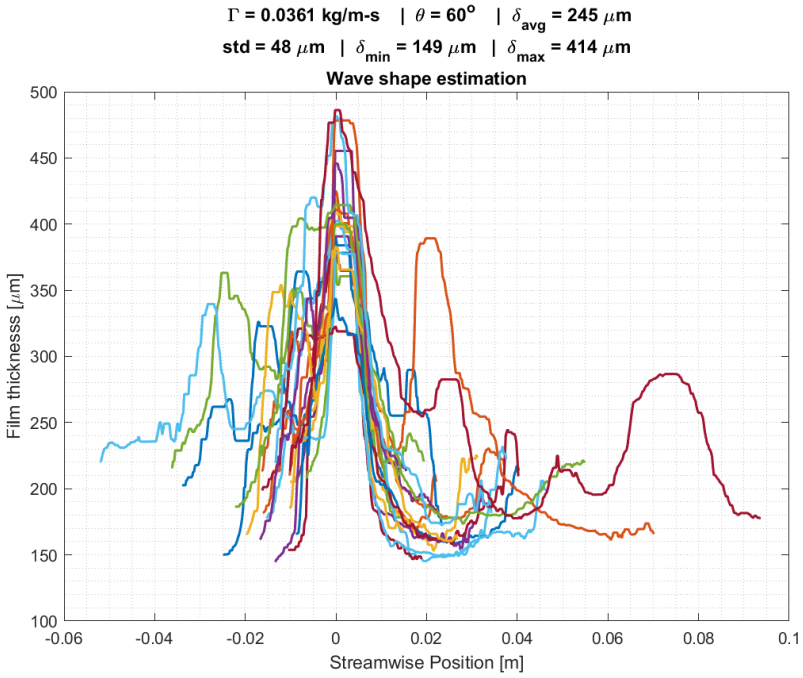

Wave shapes for test condition No. 1.5

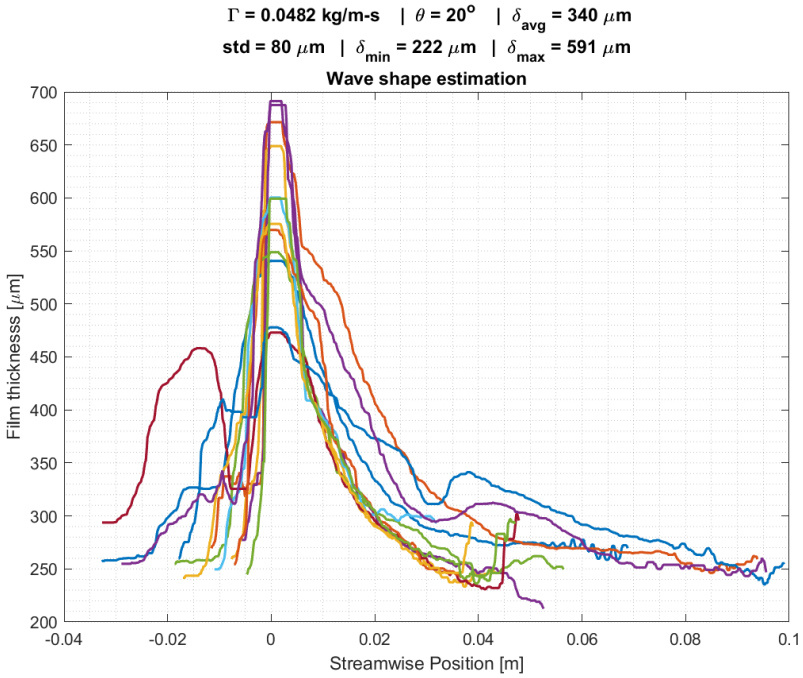

Wave shapes for test condition No. 1.6

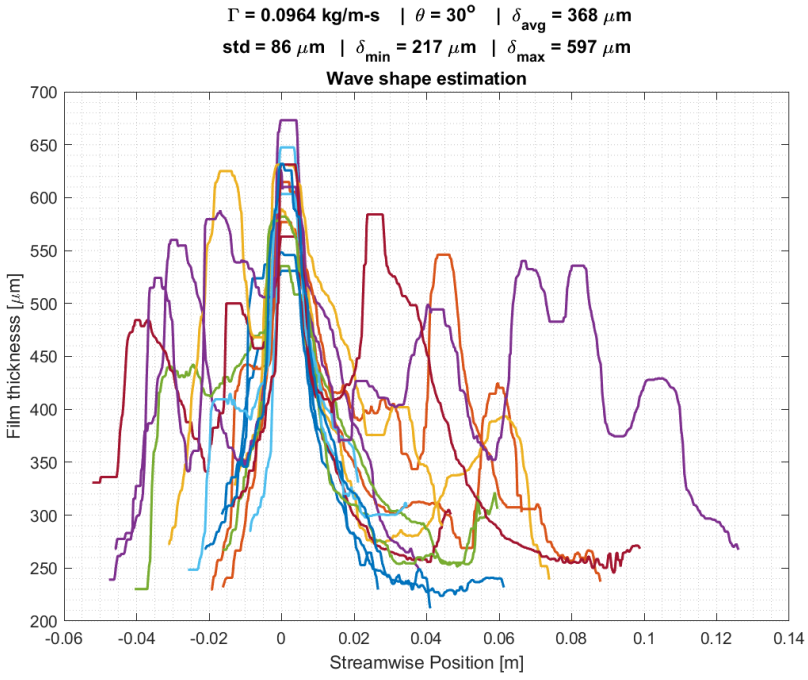

Wave shapes for test condition No. 1.7

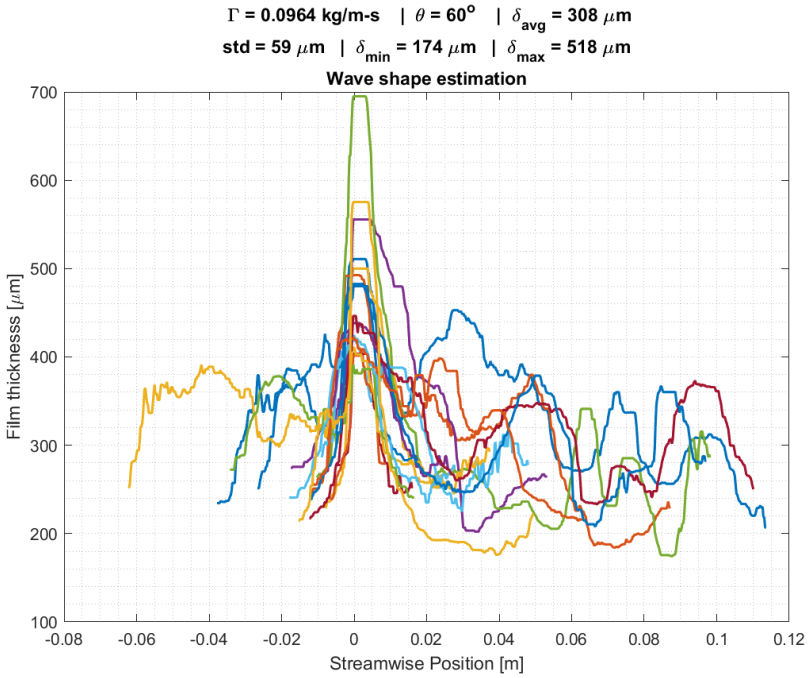

Wave shapes for test condition No. 1.8

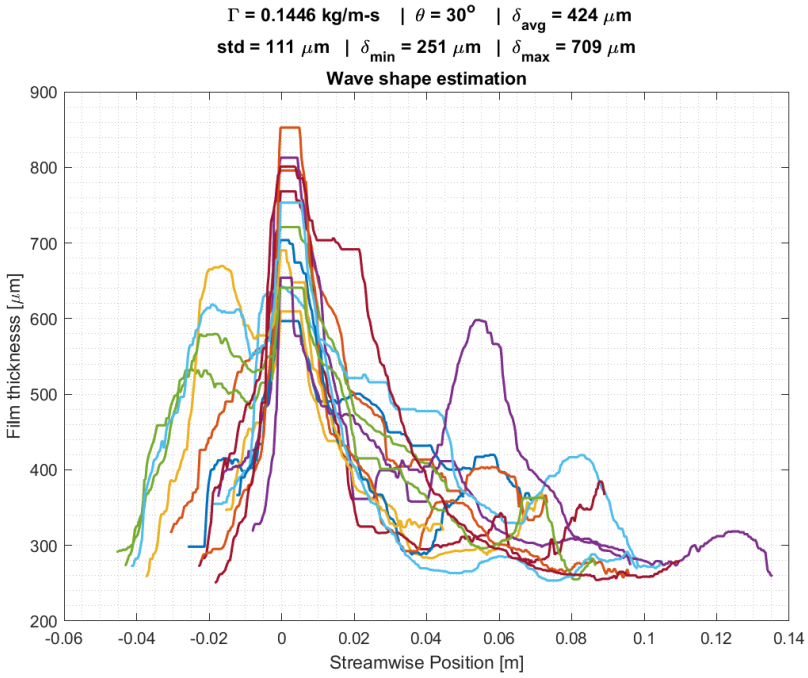

Wave shapes for test condition No. 1.9

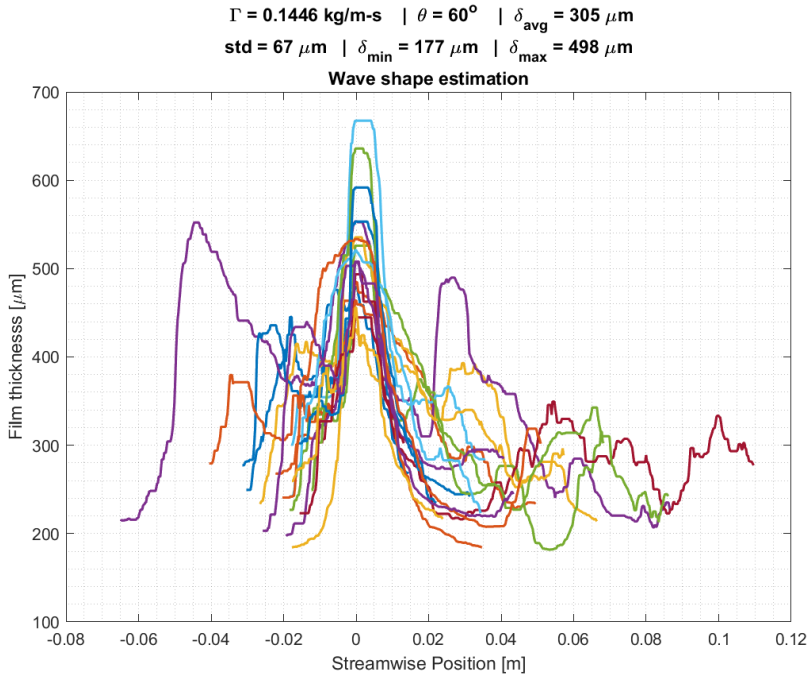

Wave shapes for test condition No. 1.10

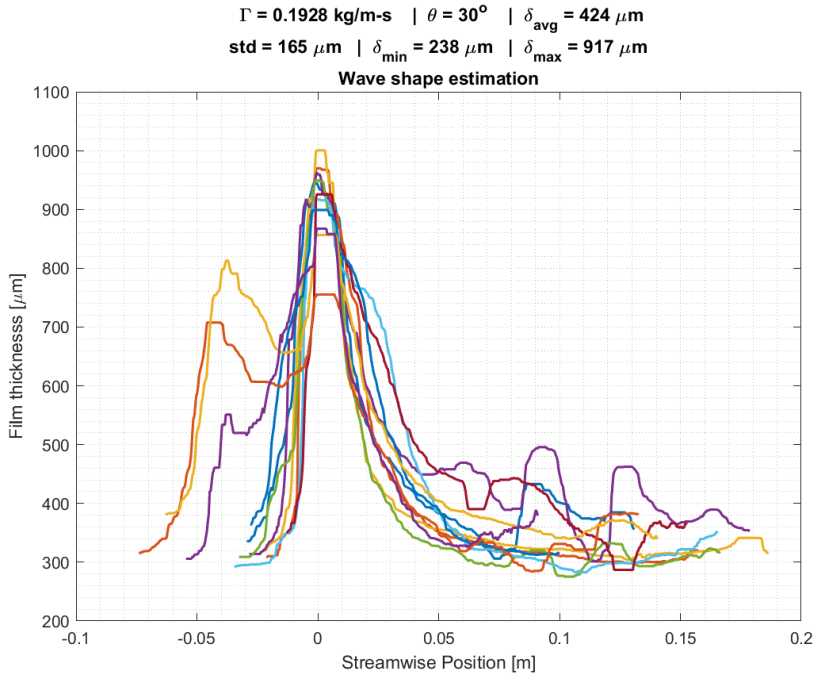

Wave shapes for test condition No. 1.11

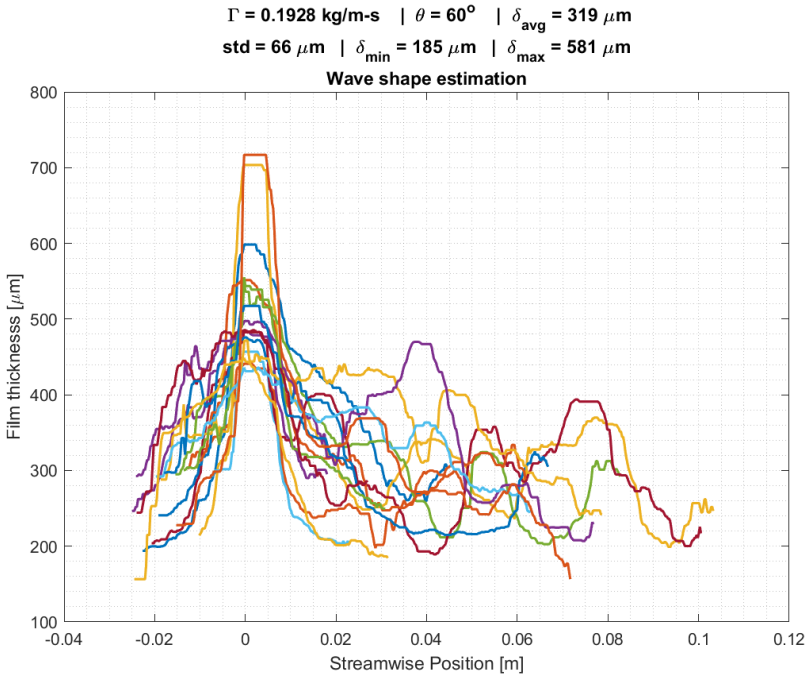

Wave shapes for test condition No. 1.12

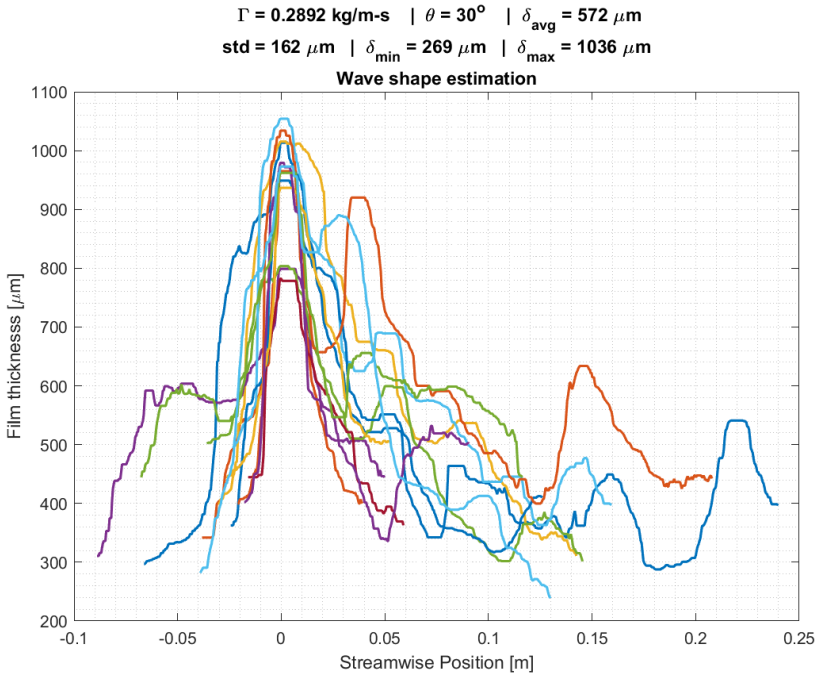

Wave shapes for test condition No. 1.13

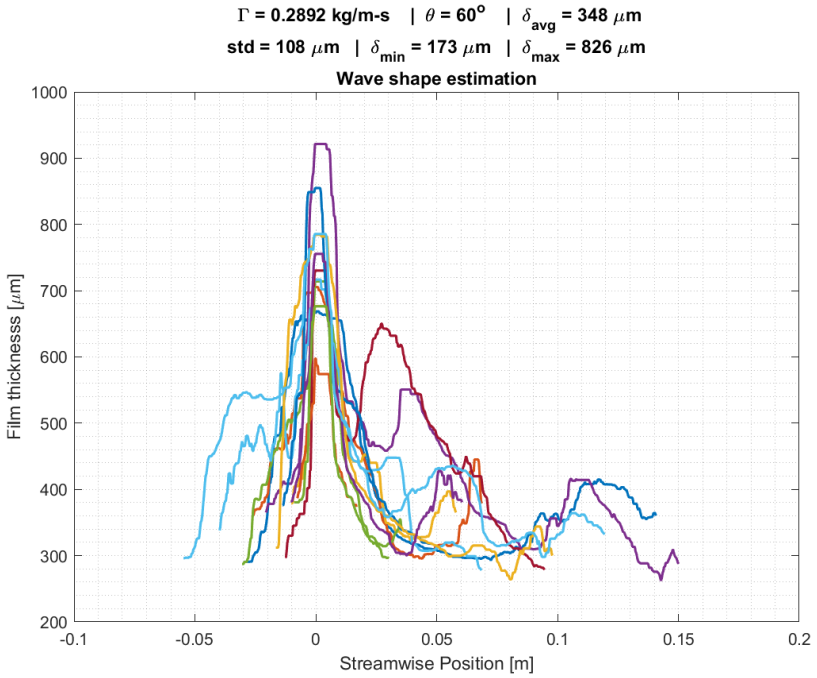

Wave shapes for test condition No. 1.14

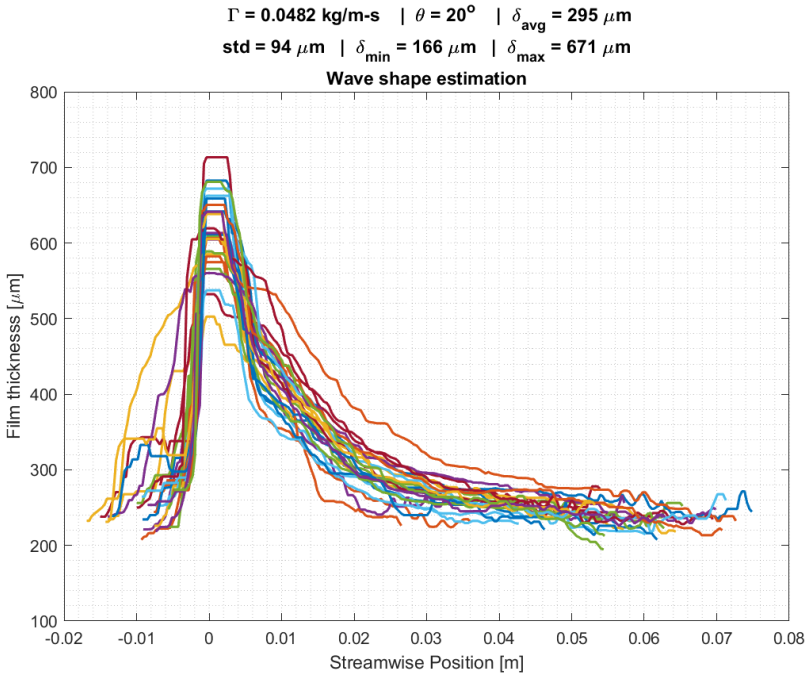

Wave shapes for test condition No. 2.1

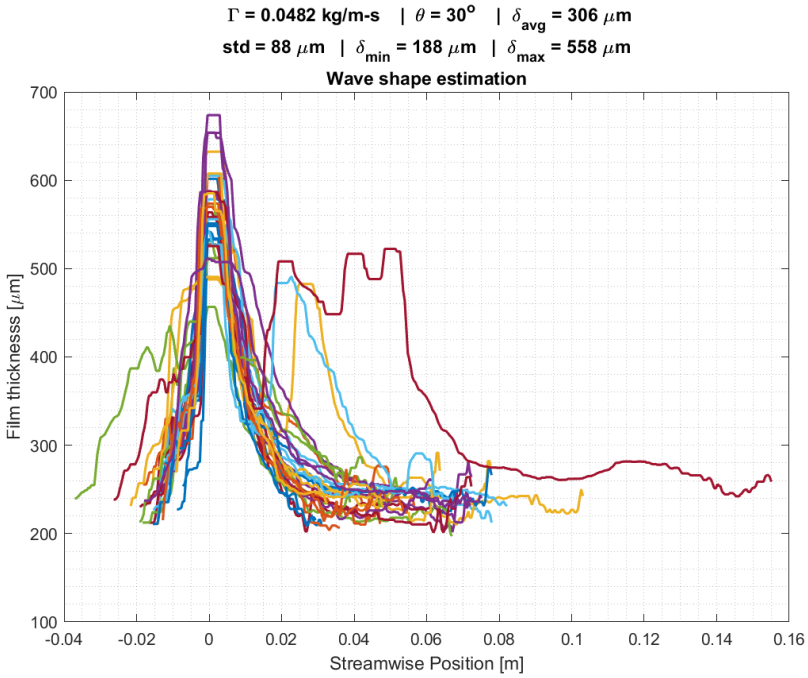

Wave shapes for test condition No. 2.2

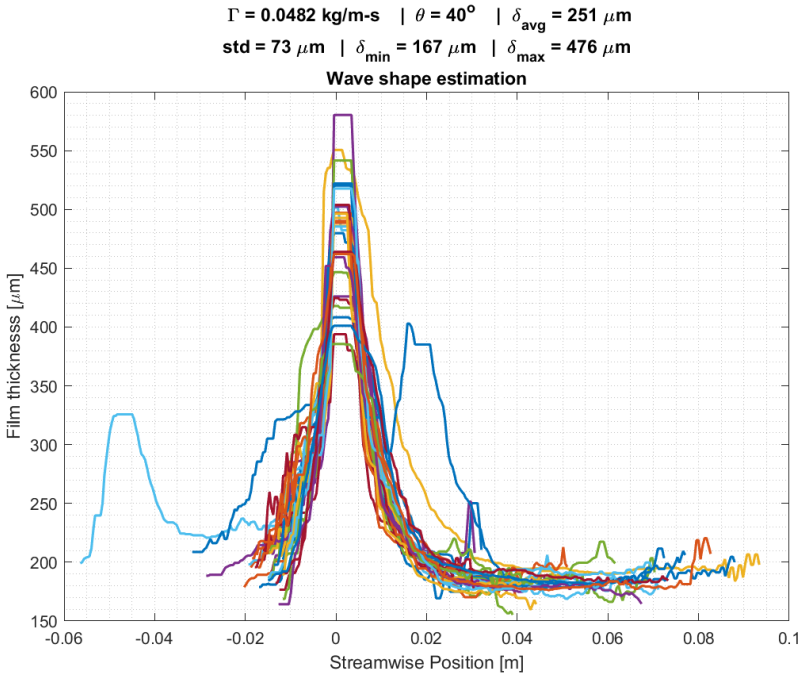

Wave shapes for test condition No. 2.3

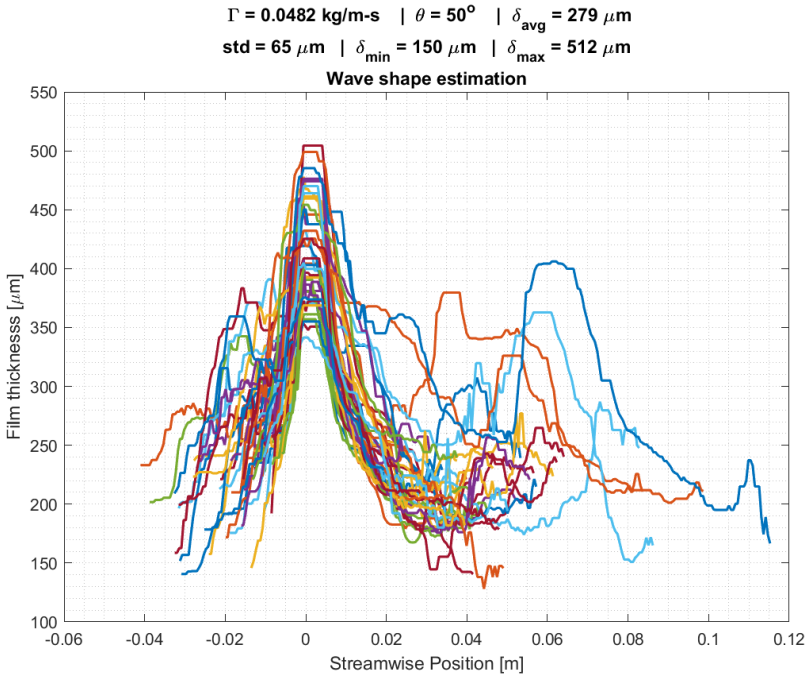

Wave shapes for test condition No. 2.4

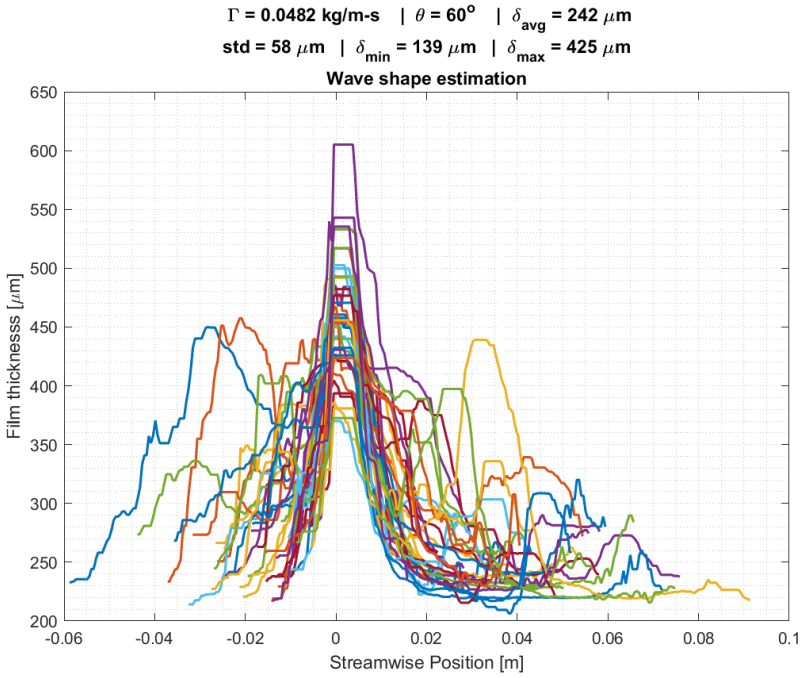

Wave shapes for test condition No. 2.5

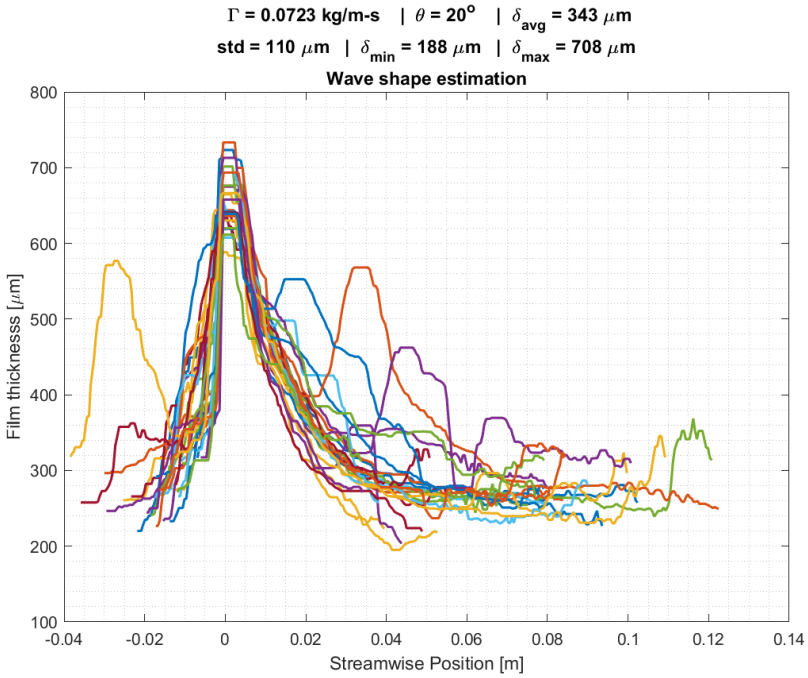

Wave shapes for test condition No. 2.6

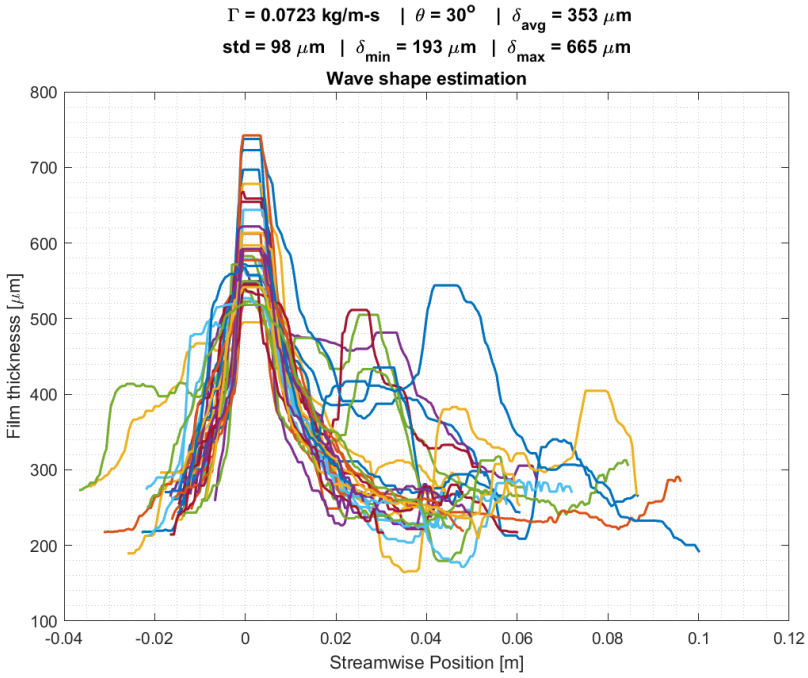

Wave shapes for test condition No. 2.7

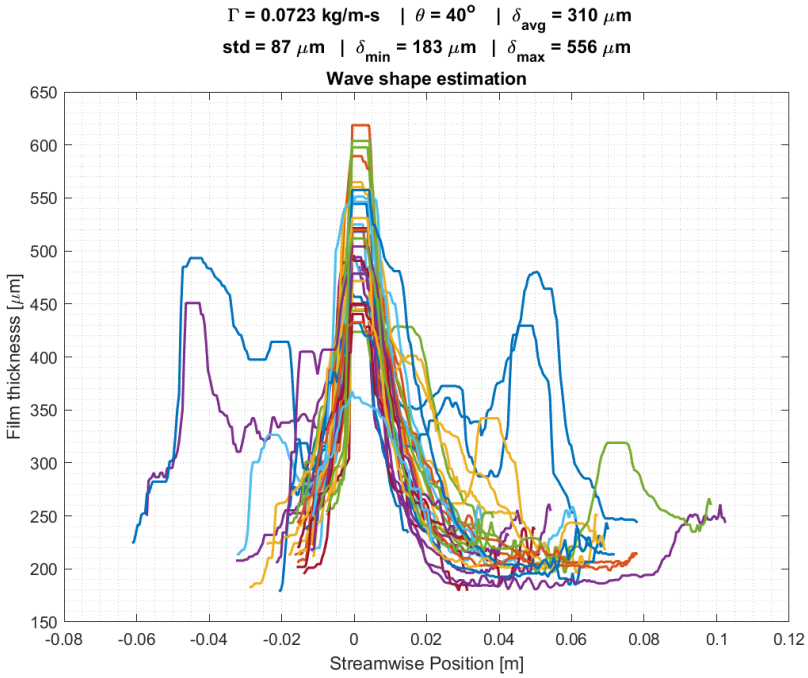

Wave shapes for test condition No. 2.8

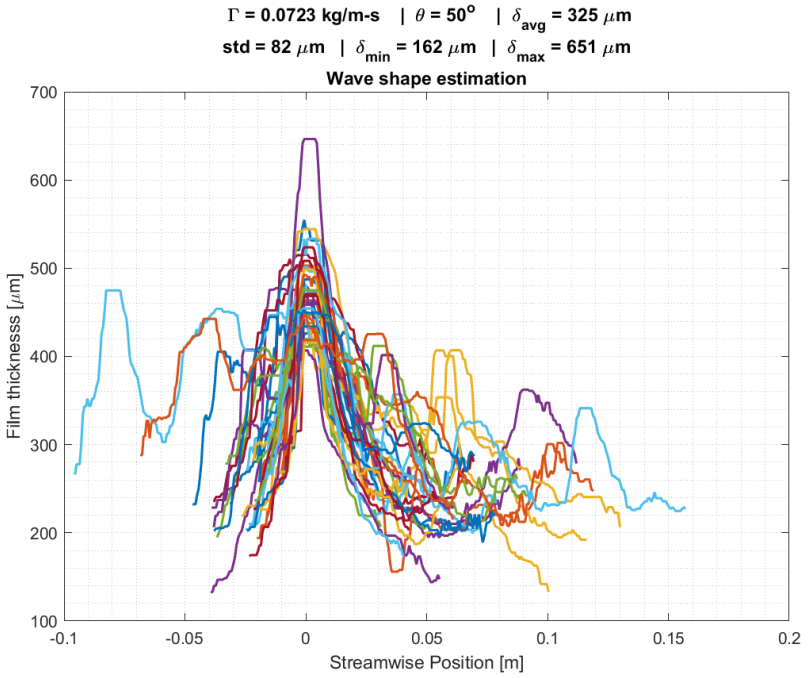

Wave shapes for test condition No. 2.9

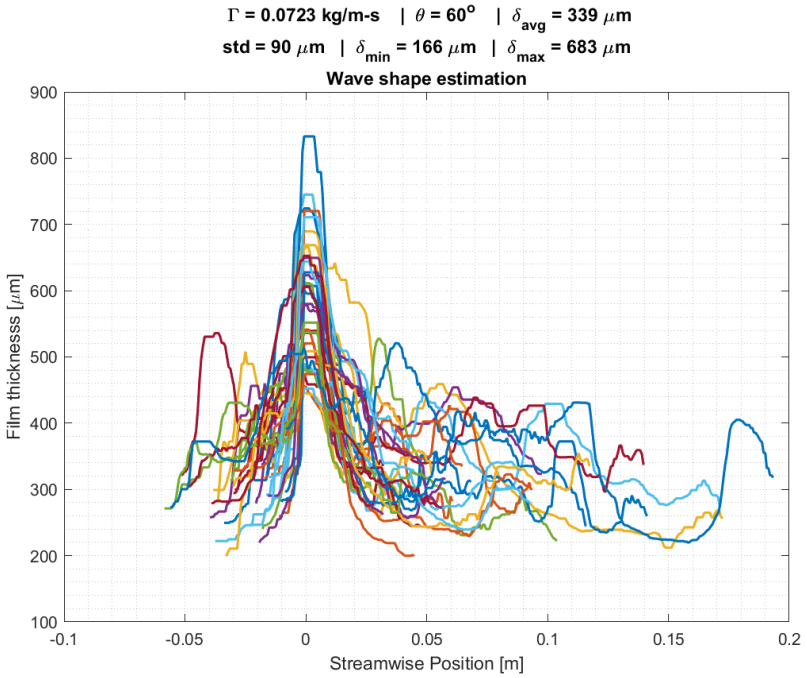

Wave shapes for test condition No. 2.10

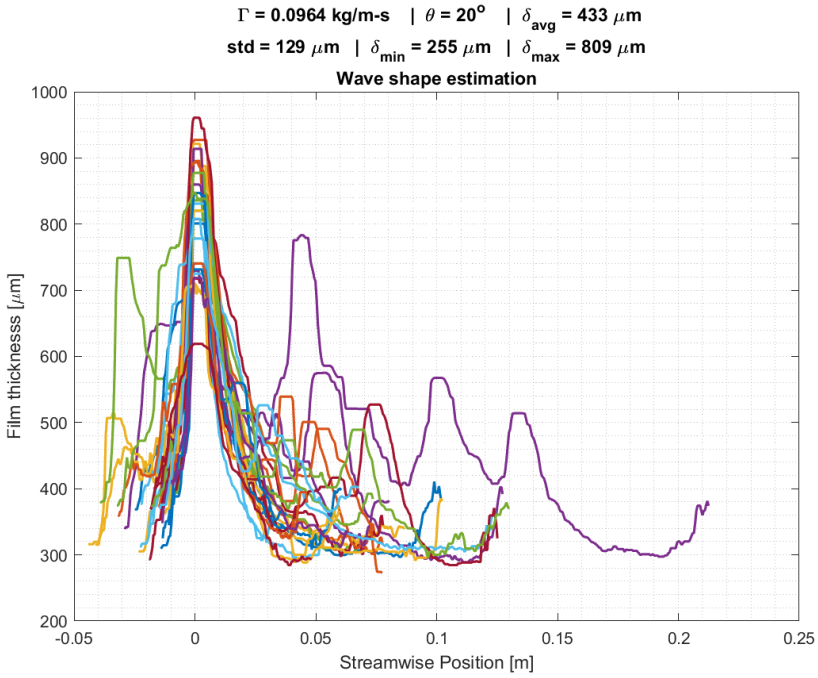

Wave shapes for test condition No. 2.11

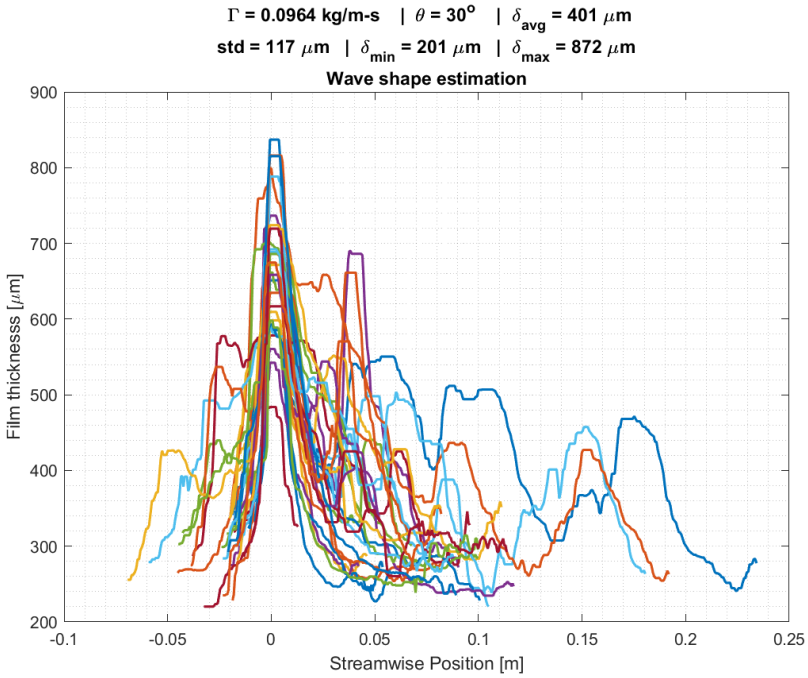

Wave shapes for test condition No. 2.12

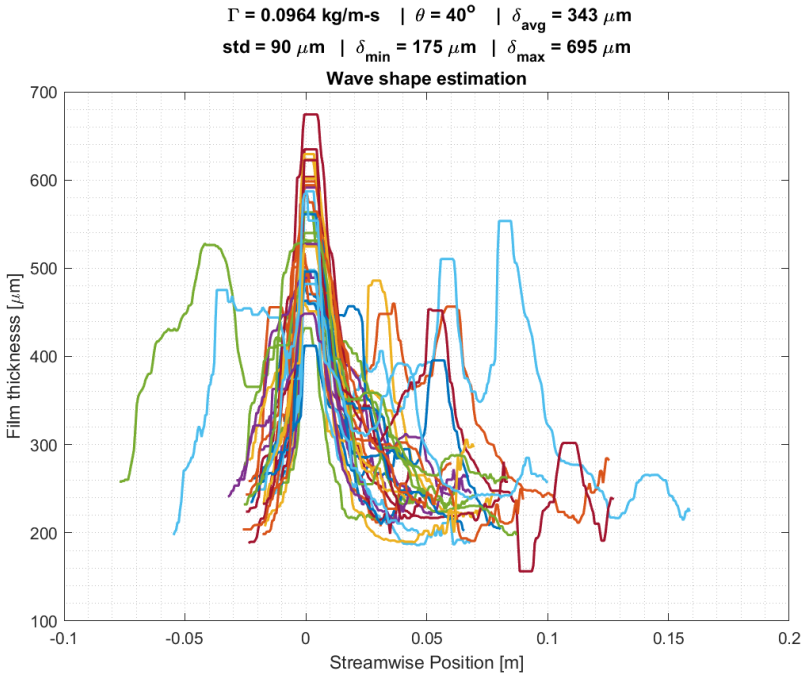

Wave shapes for test condition No. 2.13

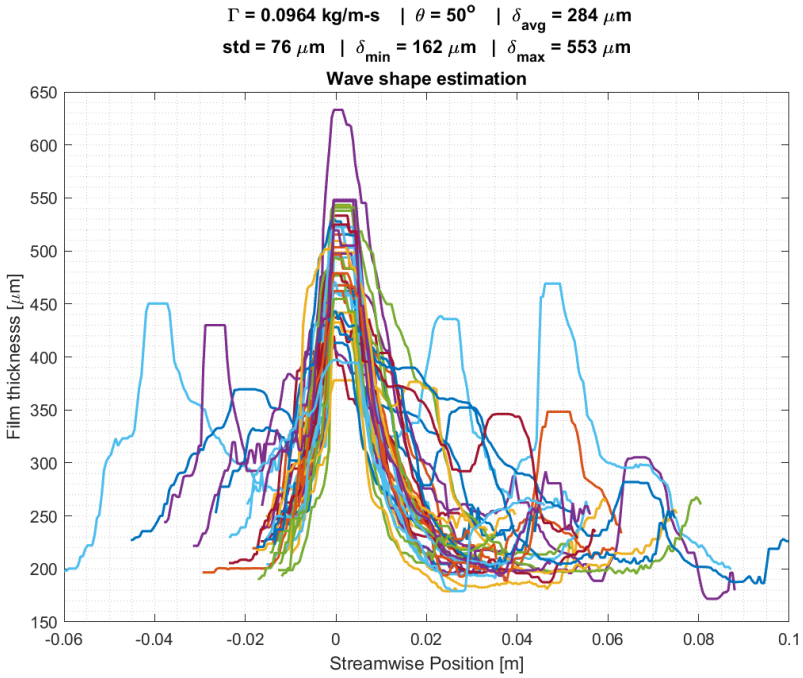

Wave shapes for test condition No. 2.14

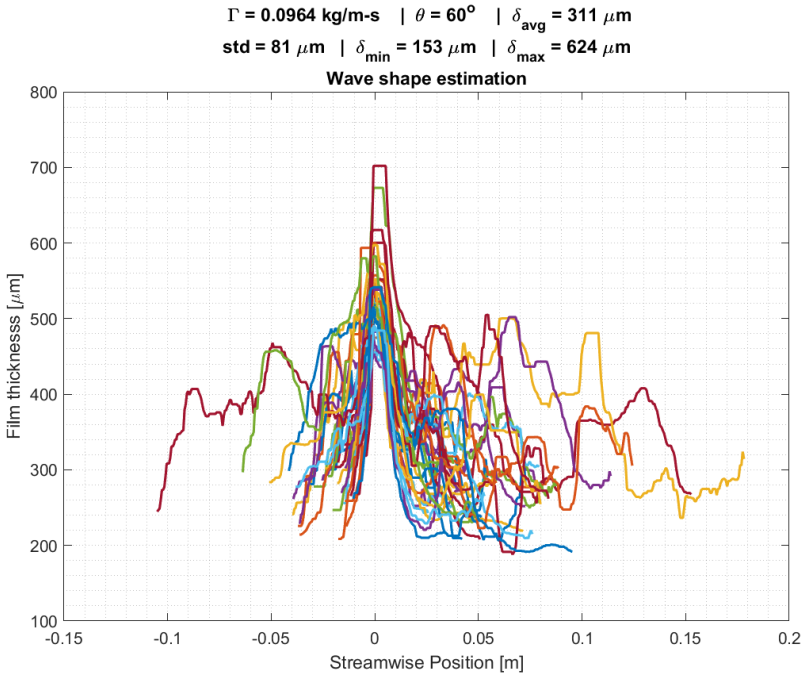

Wave shapes for test condition No. 2.15

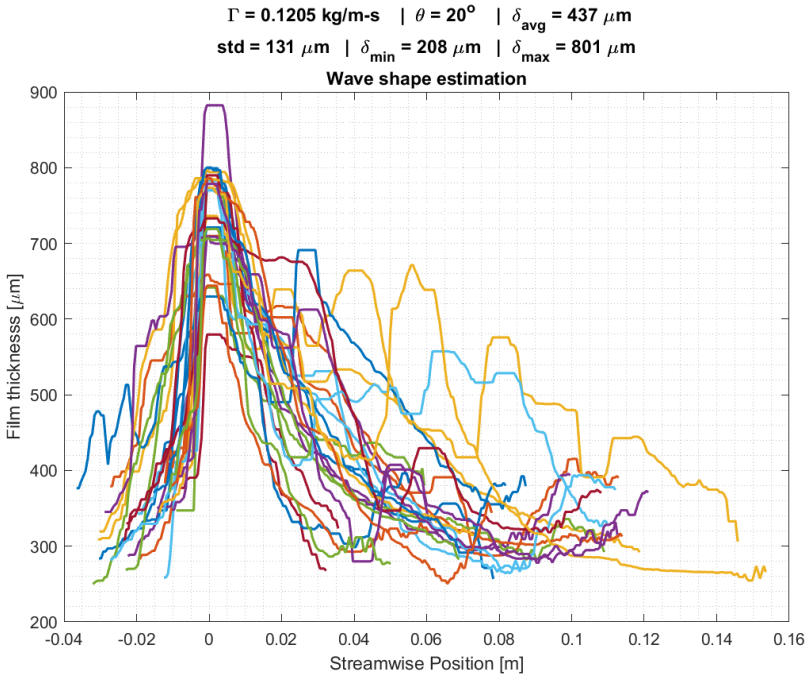

Wave shapes for test condition No. 2.16

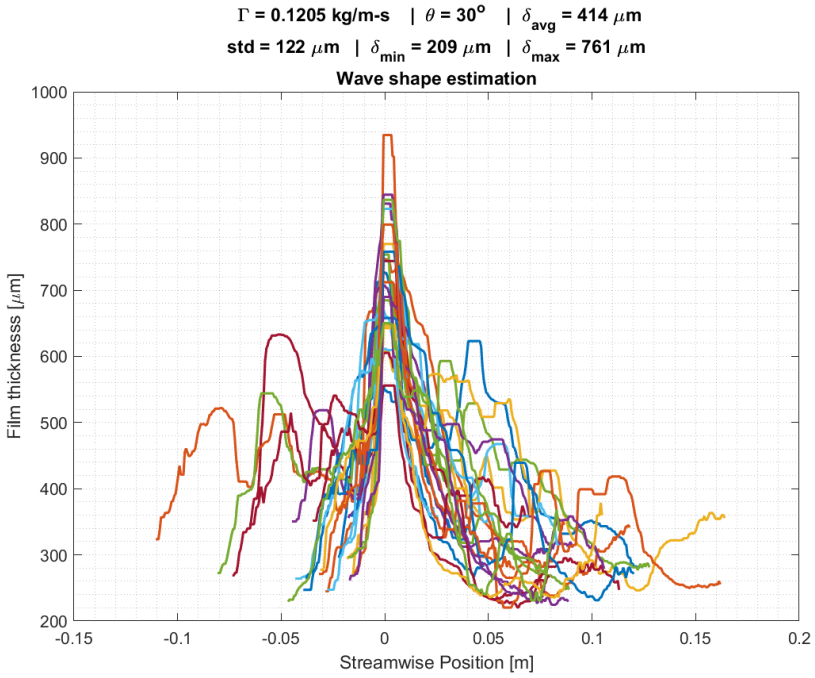

Wave shapes for test condition No. 2.17

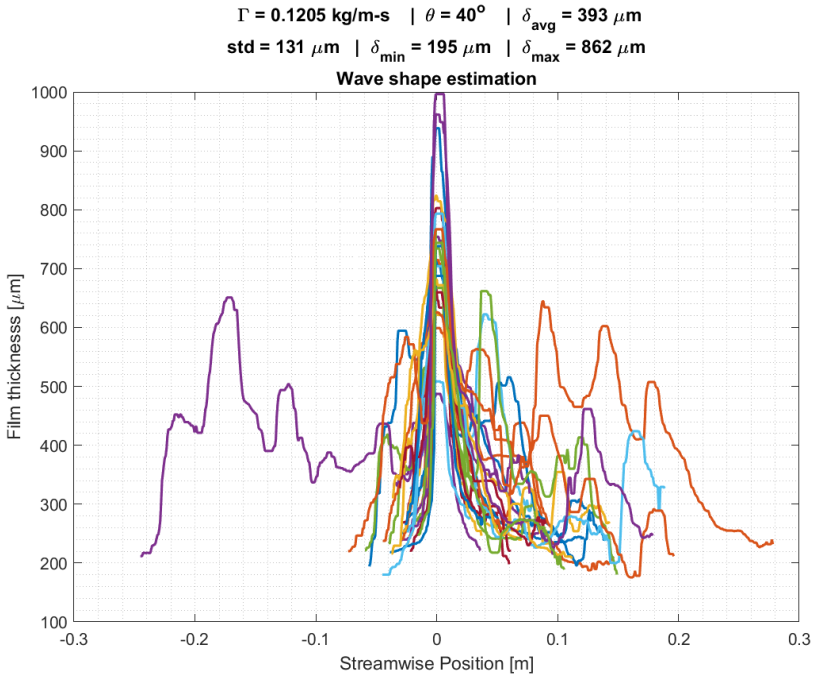

Wave shapes for test condition No. 2.18

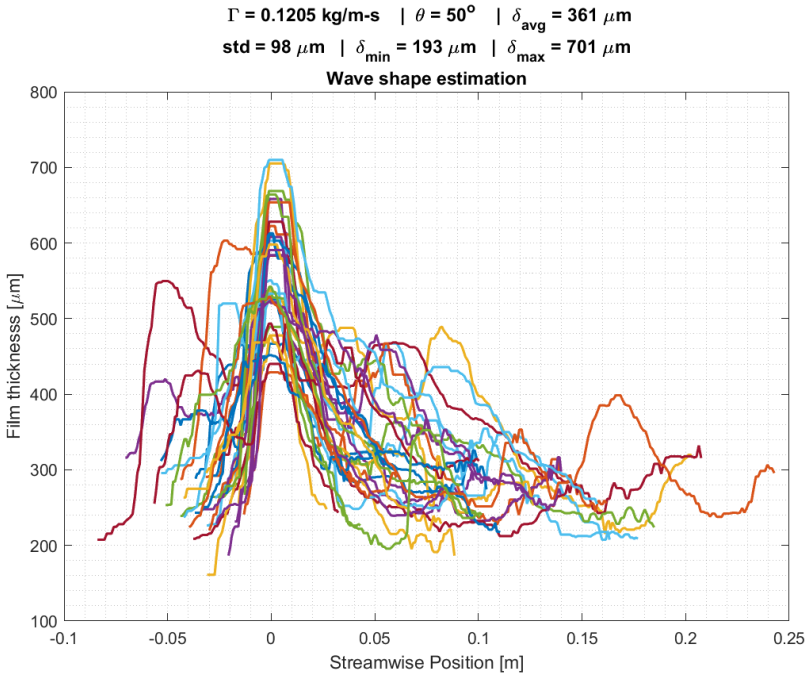

Wave shapes for test condition No. 2.19

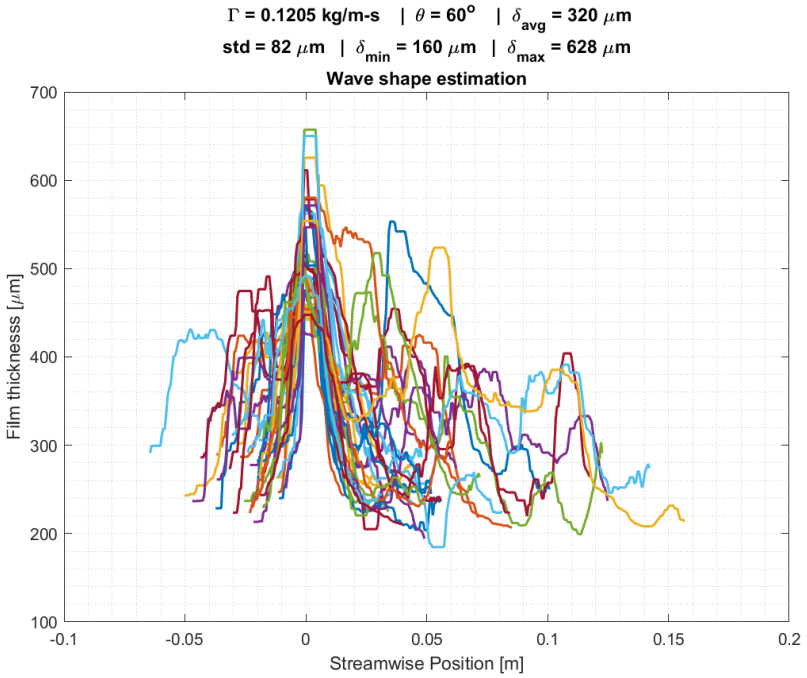

Wave shapes for test condition No. 2.20

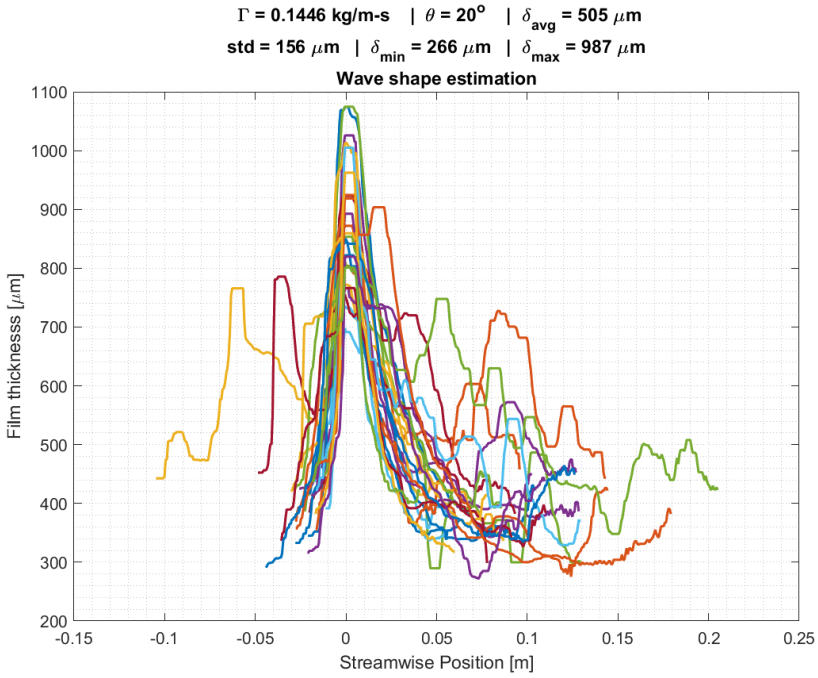

Wave shapes for test condition No. 2.21

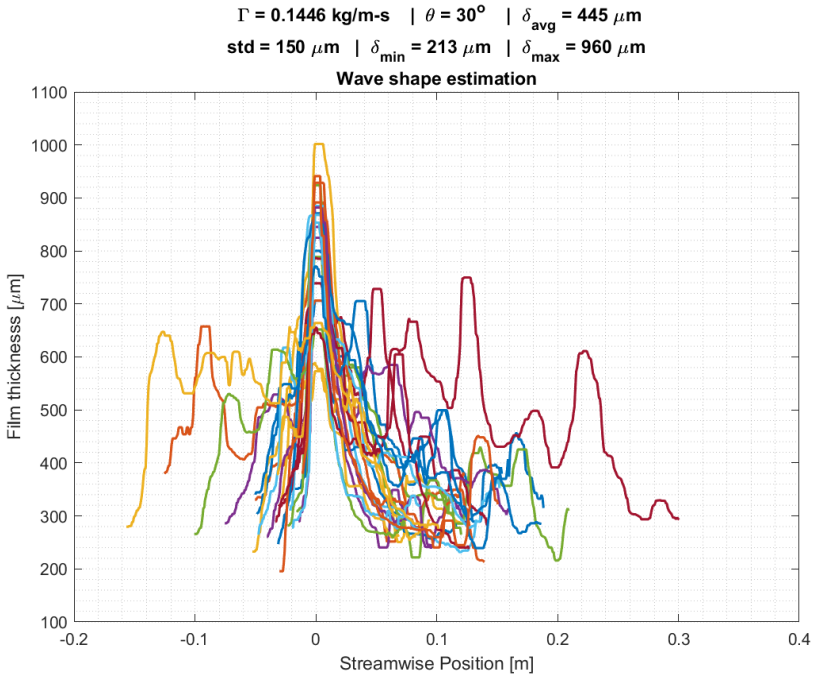

Wave shapes for test condition No. 2.22

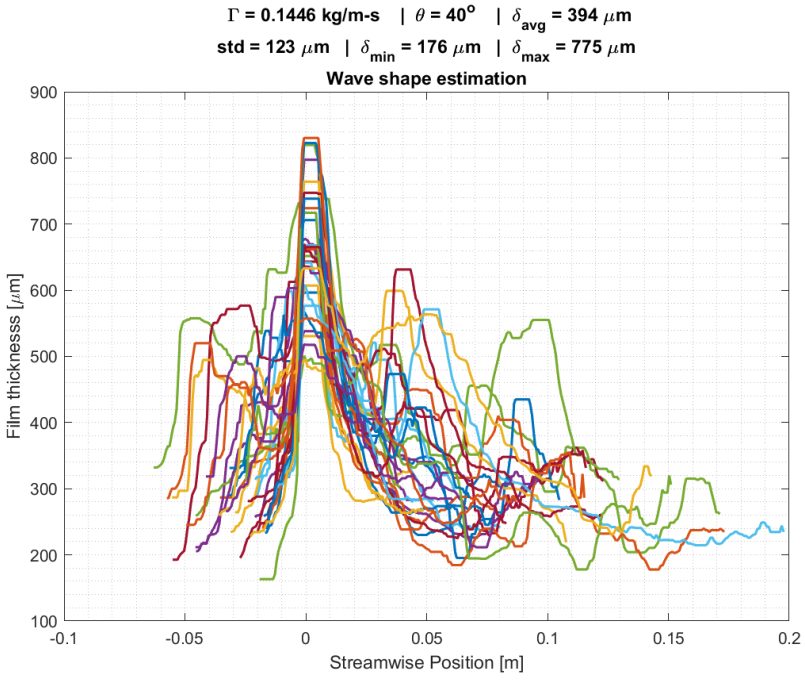

Wave shapes for test condition No. 2.23

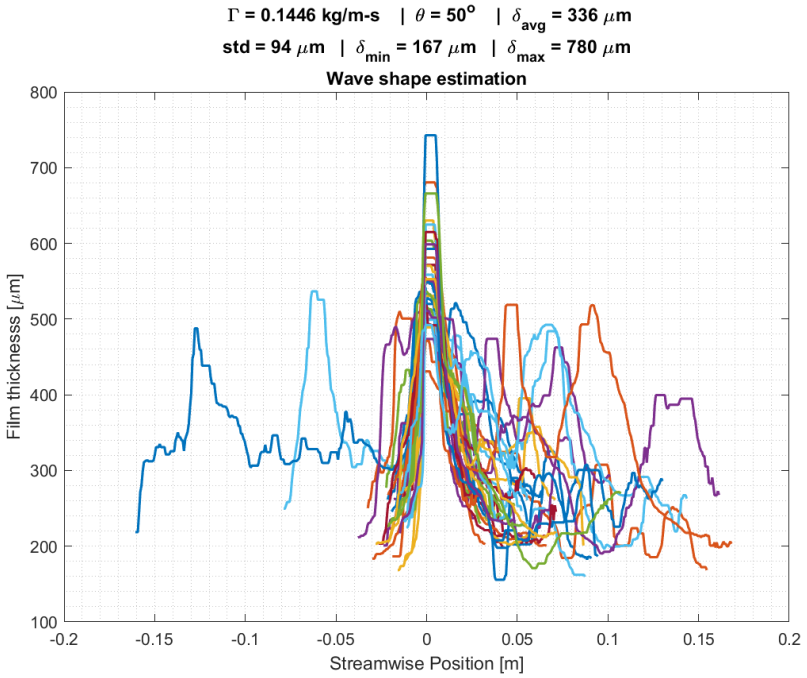

Wave shapes for test condition No. 2.24

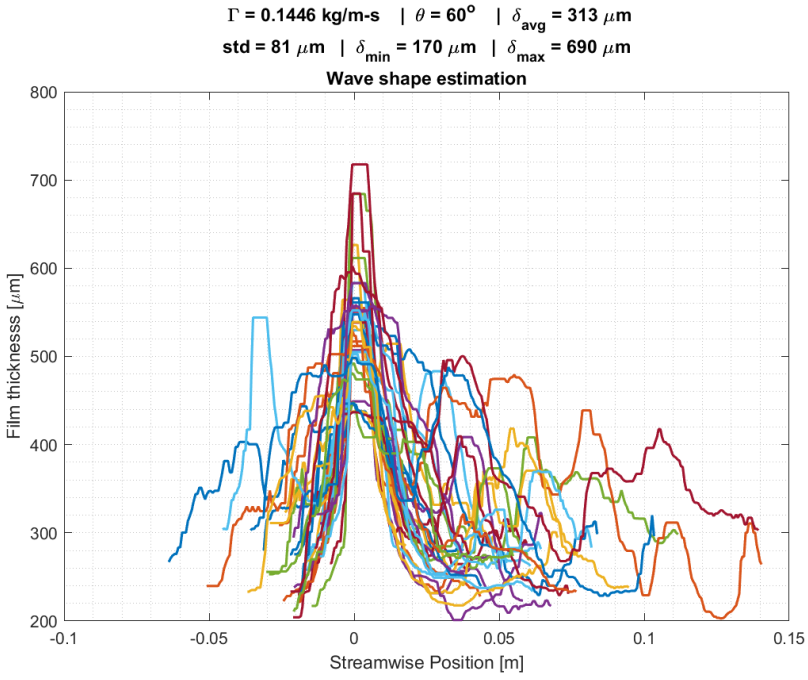

Wave shapes for test condition No. 2.25

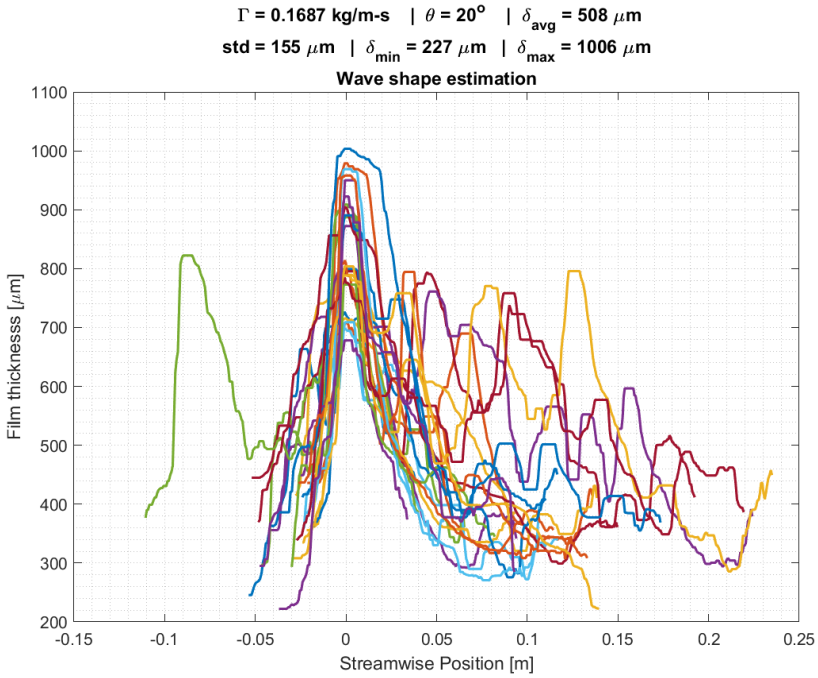

Wave shapes for test condition No. 2.26

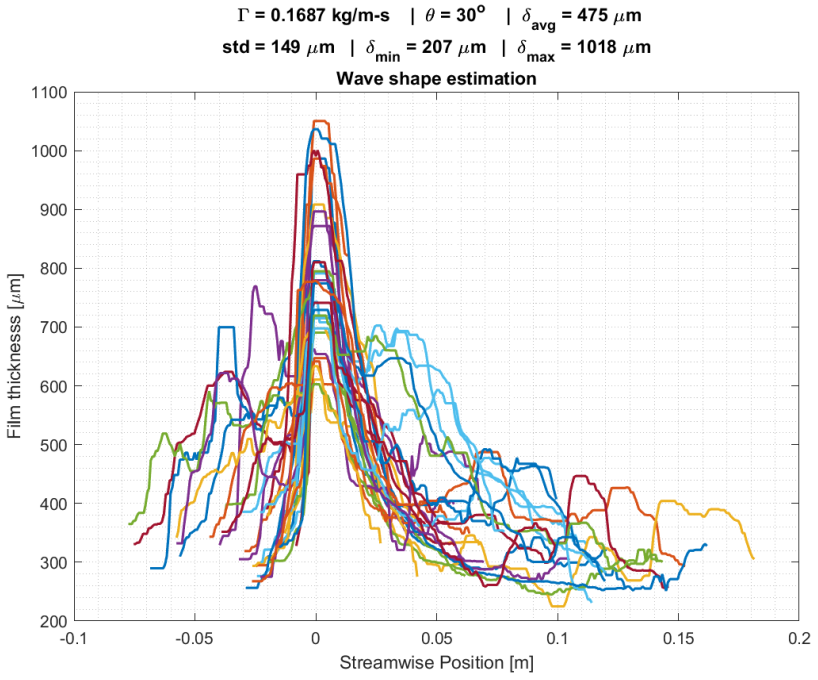

Wave shapes for test condition No. 2.27

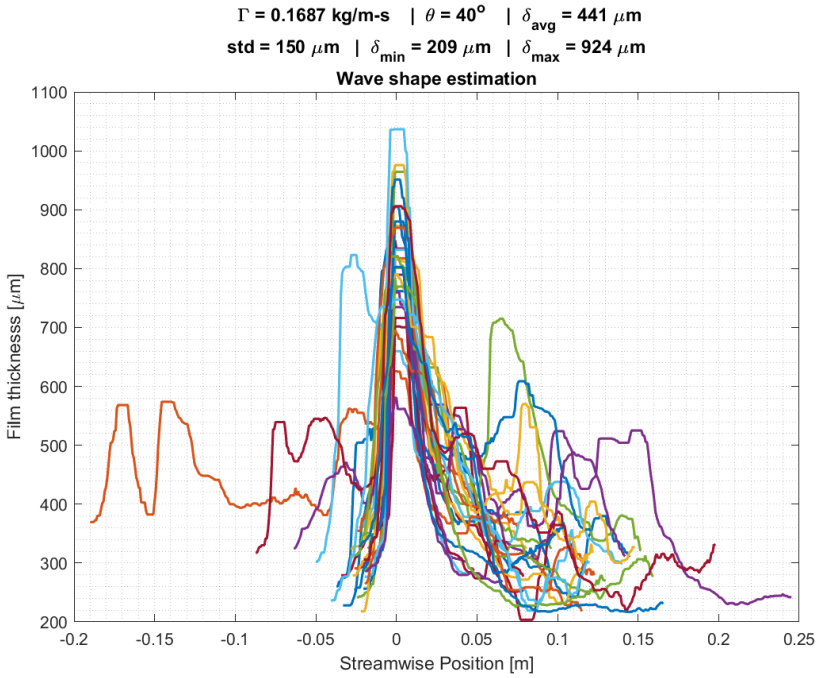

Wave shapes for test condition No. 2.28

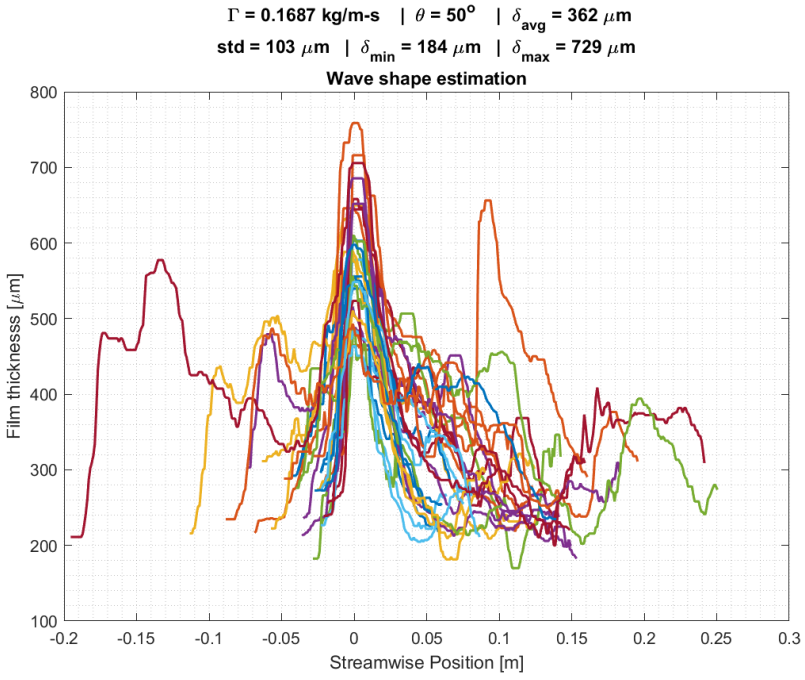

Wave shapes for test condition No. 2.29

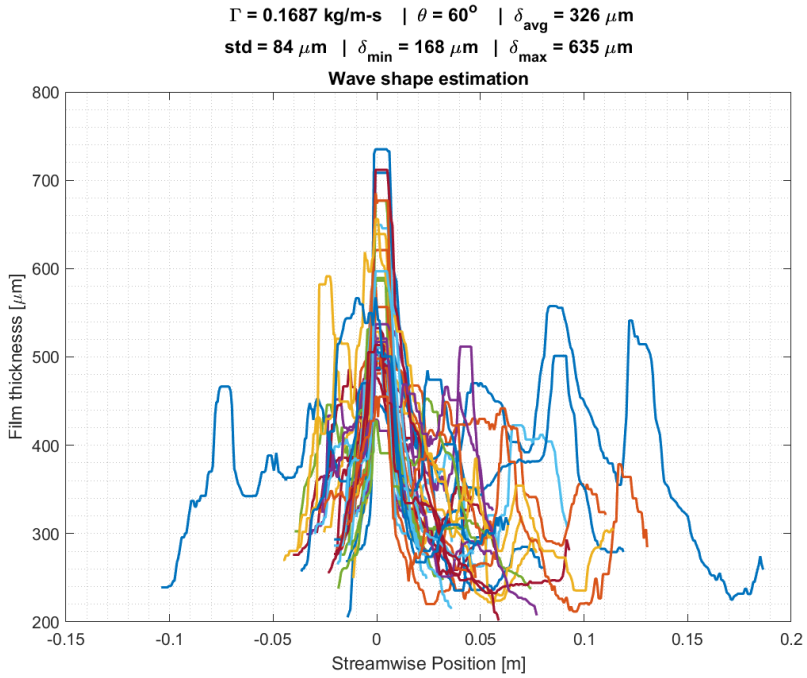

Wave shapes for test condition No. 2.30

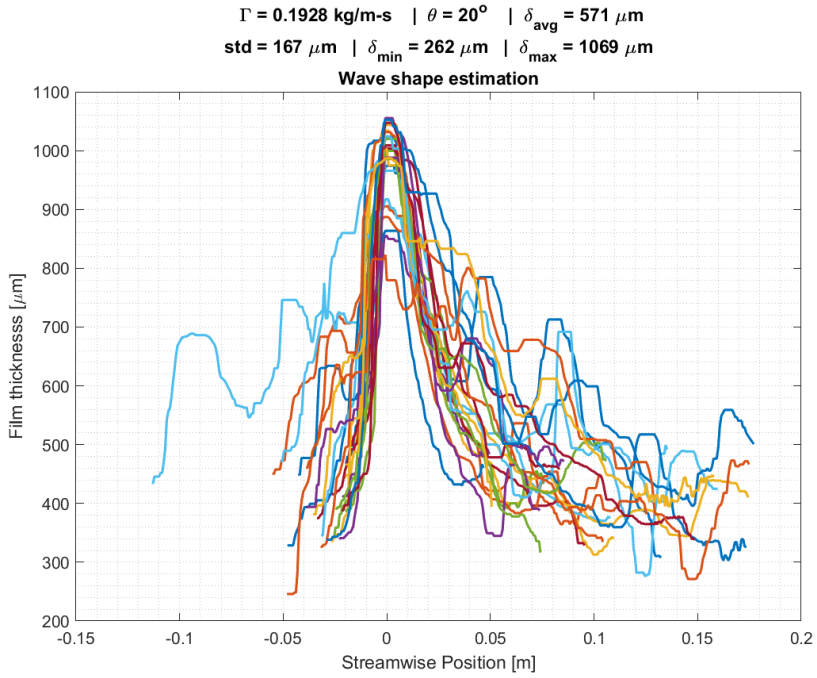

Wave shapes for test condition No. 2.31

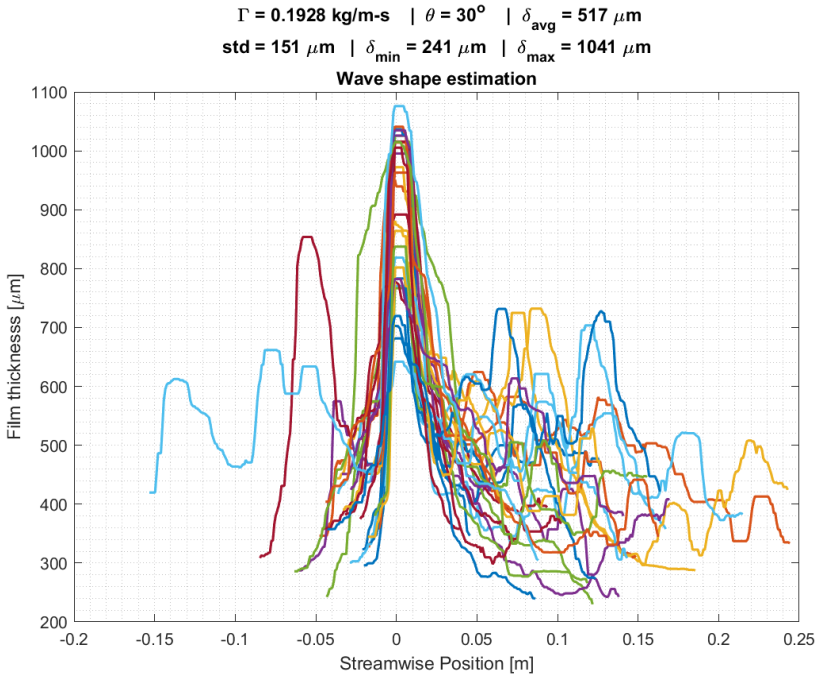

Wave shapes for test condition No. 2.32

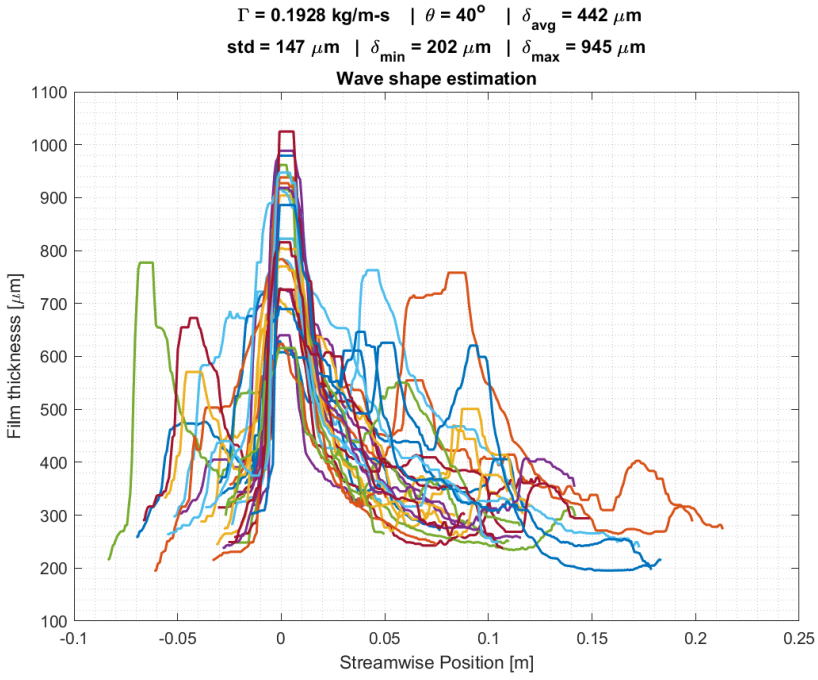

Wave shapes for test condition No. 2.33

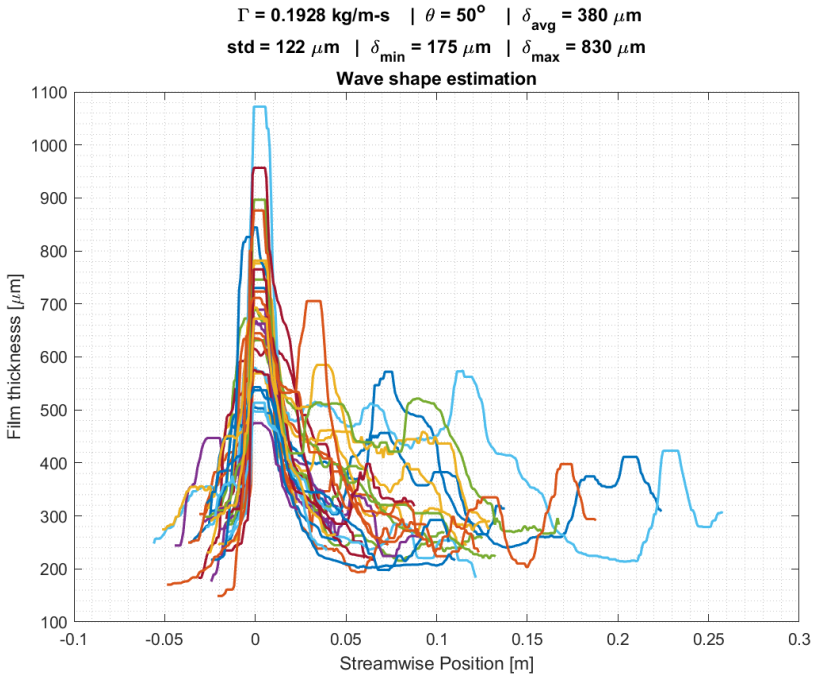

Wave shapes for test condition No. 2.34

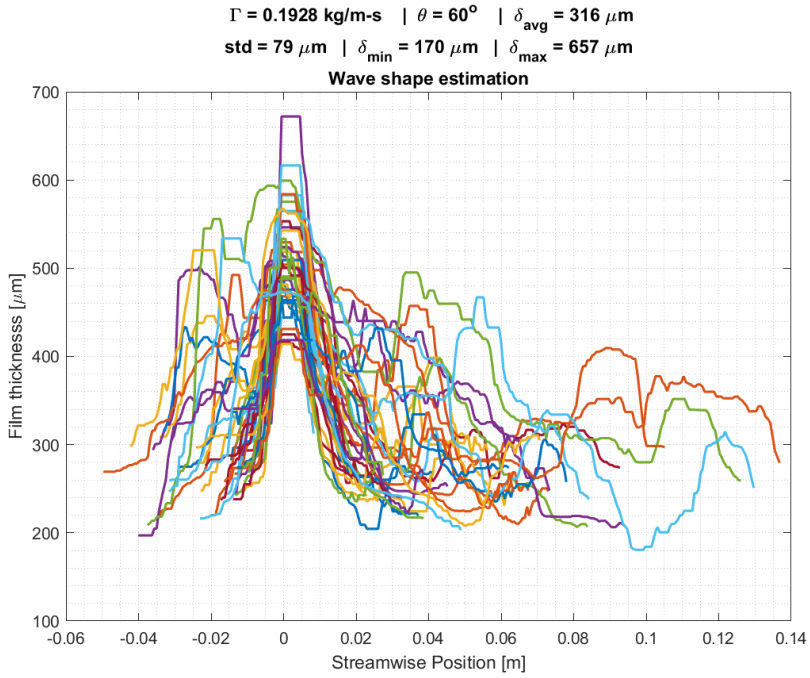

Wave shapes for test condition No. 2.35

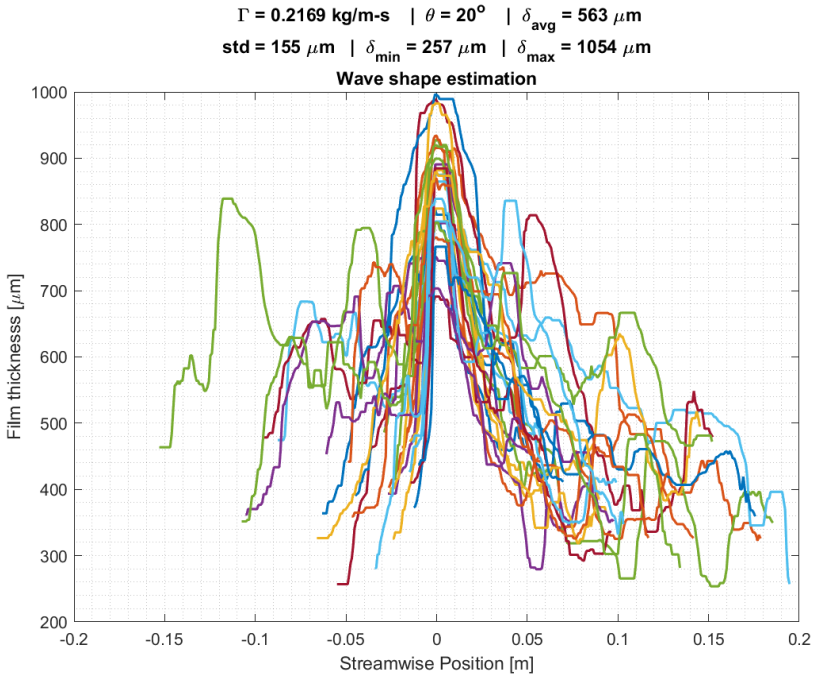

Wave shapes for test condition No. 2.36

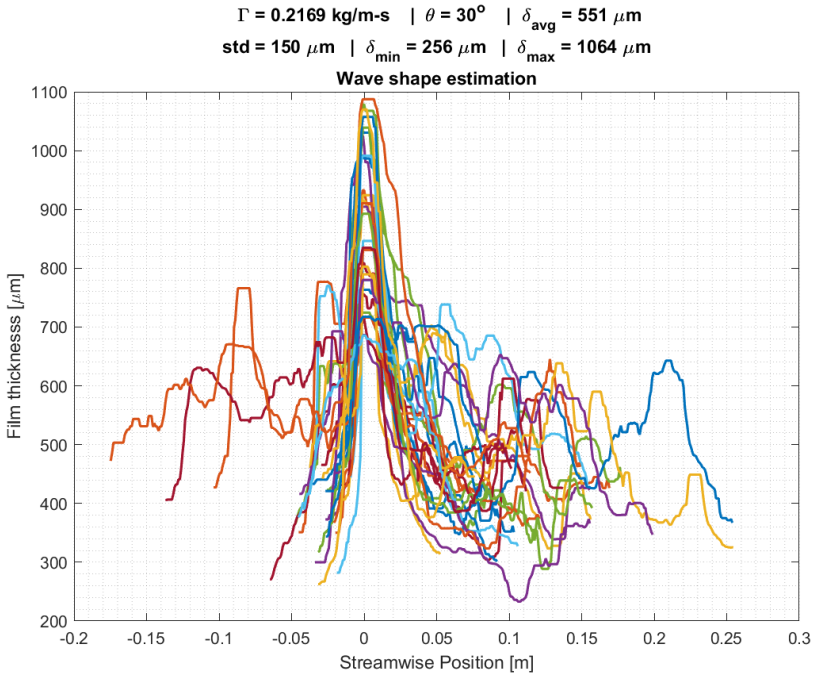

Wave shapes for test condition No. 2.37

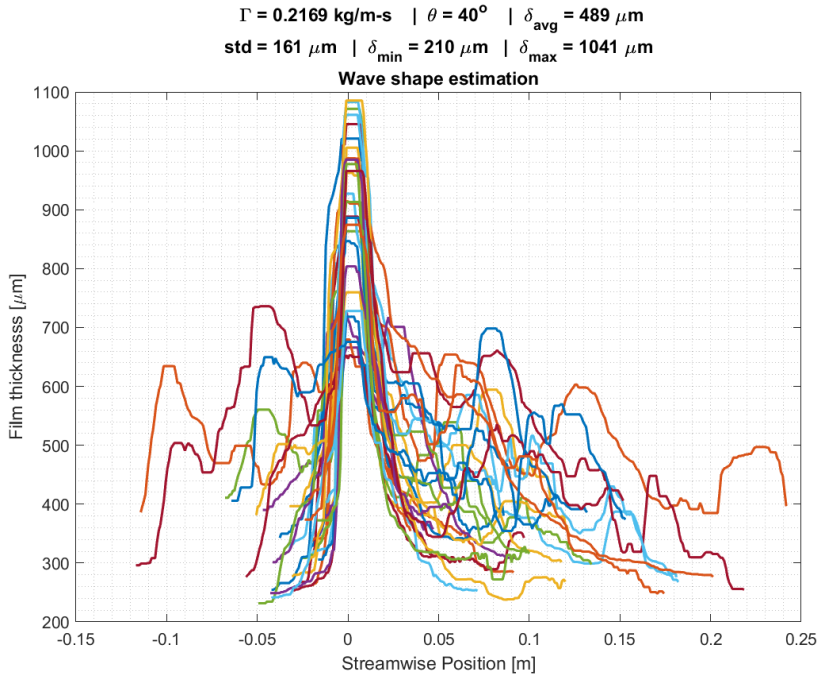

Wave shapes for test condition No. 2.38

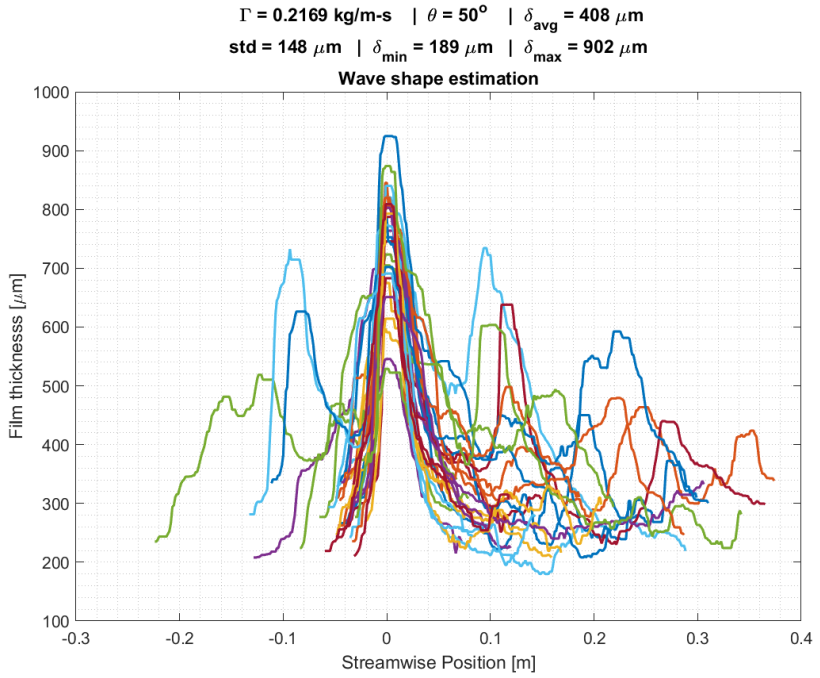

Wave shapes for test condition No. 2.39

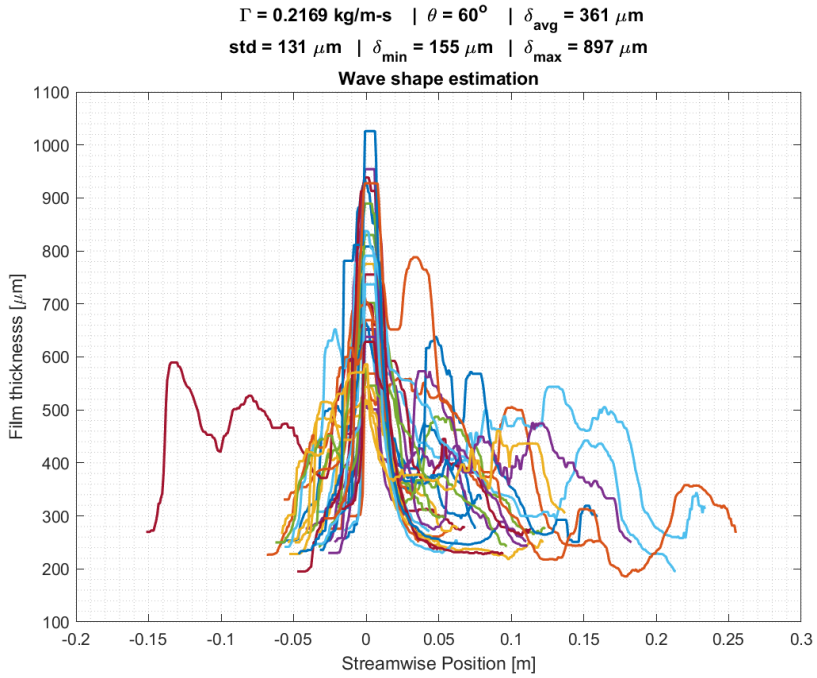

Wave shapes for test condition No. 2.40

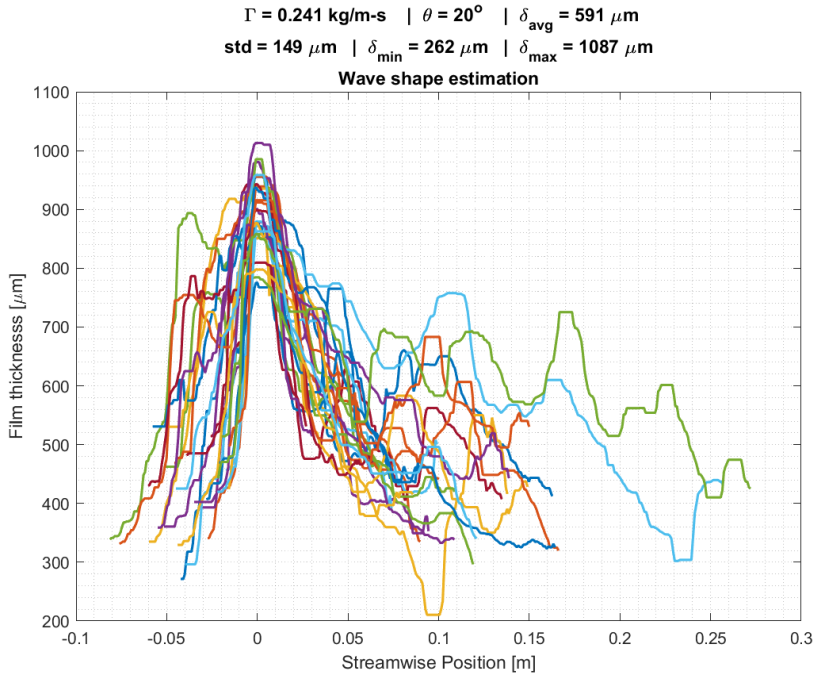

Wave shapes for test condition No. 2.41

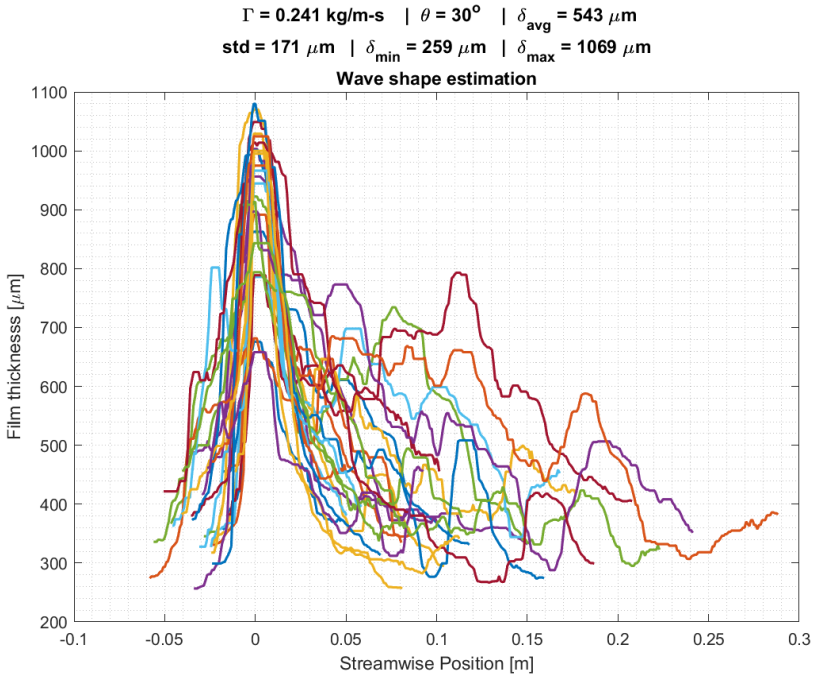

Wave shapes for test condition No. 2.42

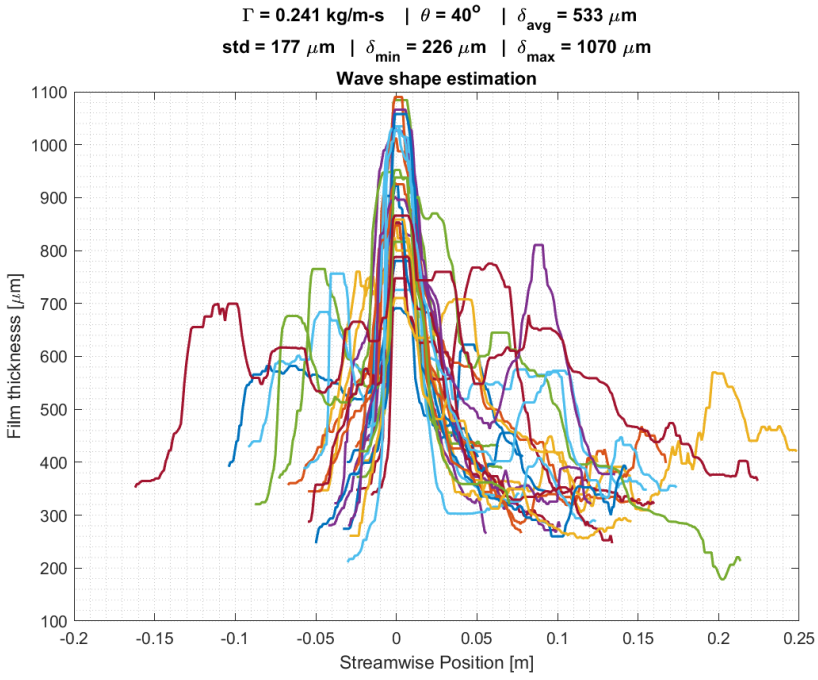

Wave shapes for test condition No. 2.43

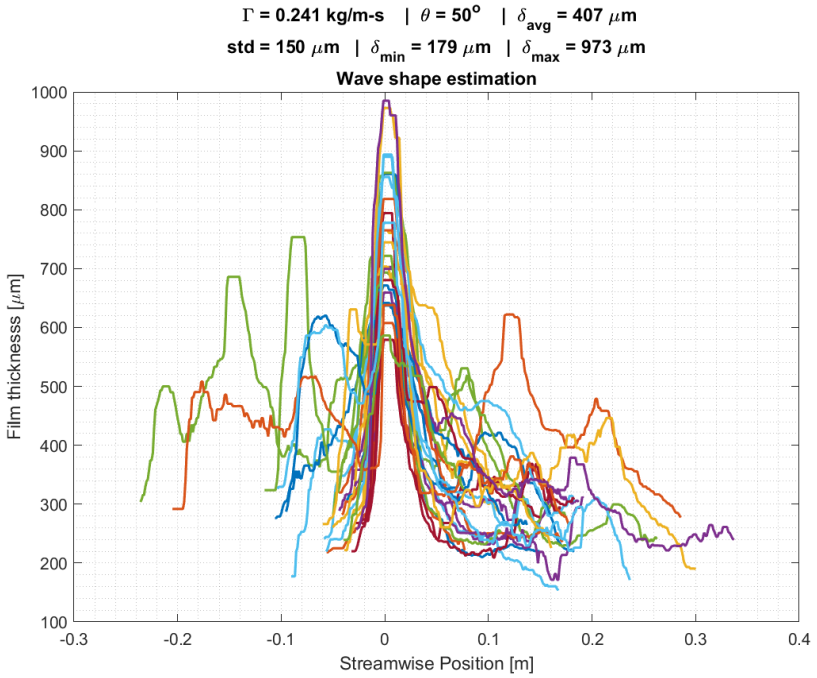

Wave shapes for test condition No. 2.44

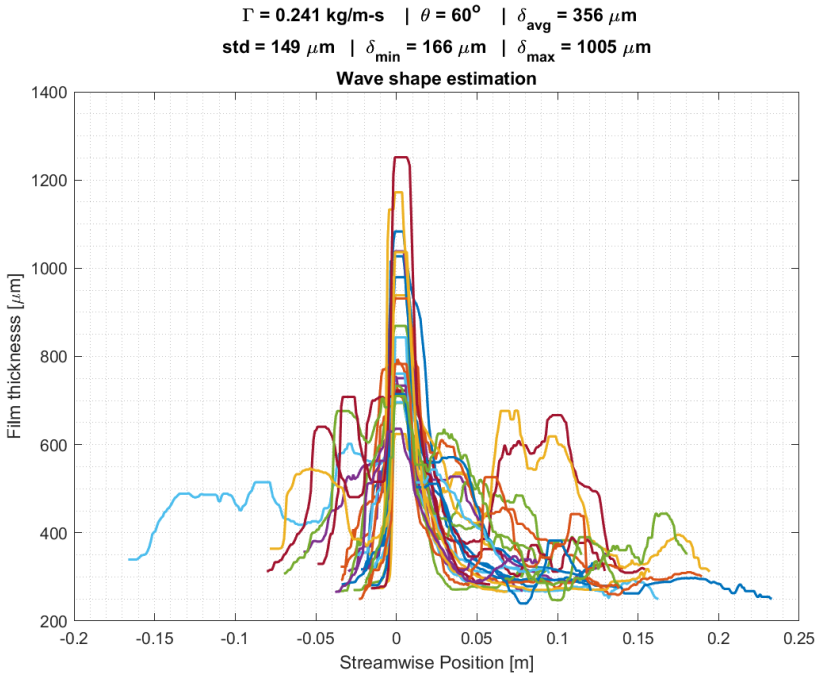

Wave shapes for test condition No. 2.45

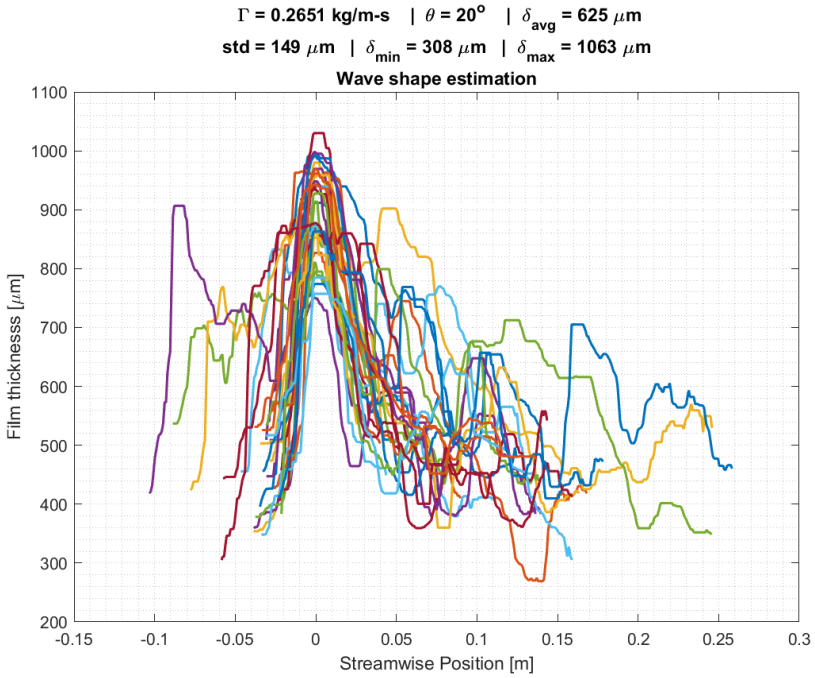

Wave shapes for test condition No. 2.46

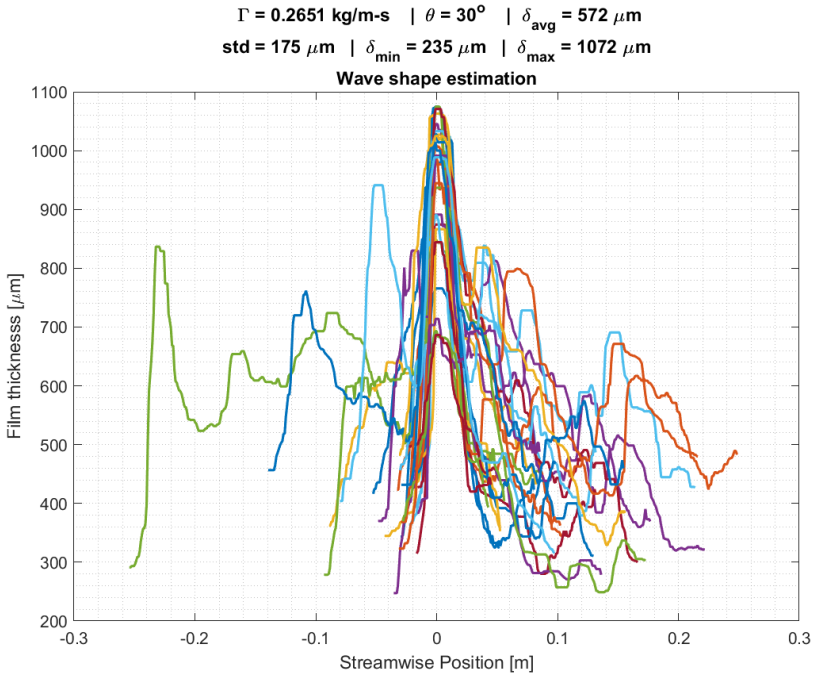

Wave shapes for test condition No. 2.47

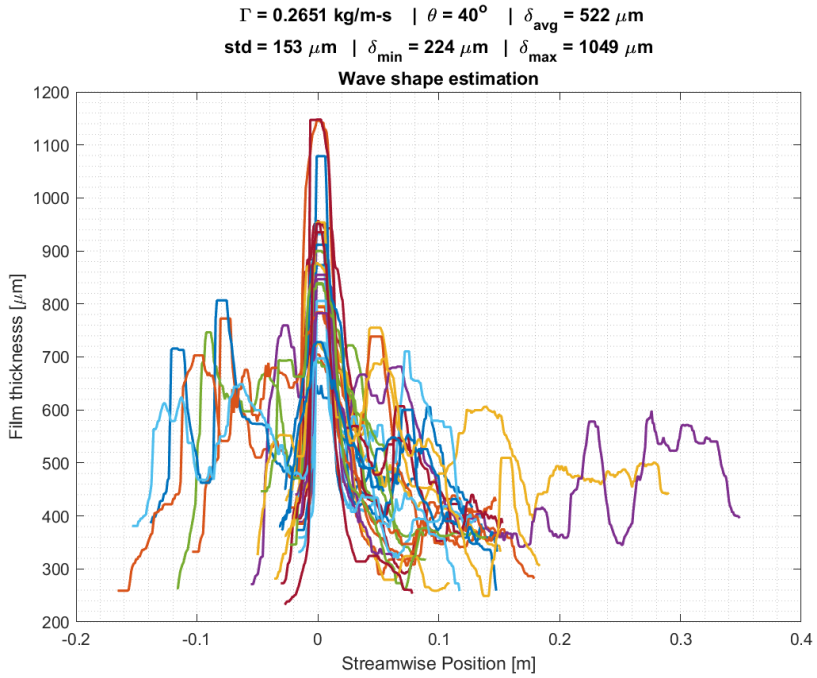

Wave shapes for test condition No. 2.48

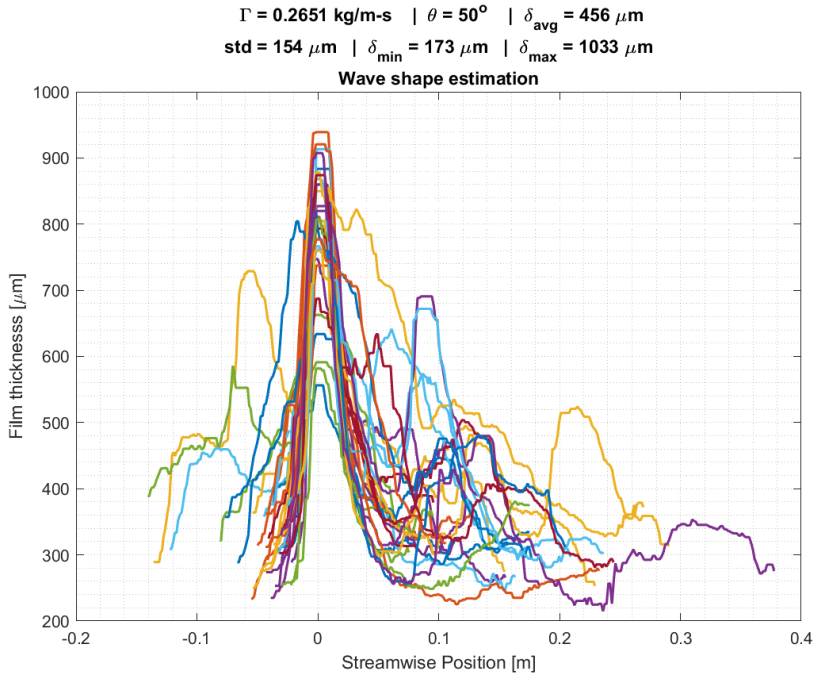

Wave shapes for test condition No. 2.49

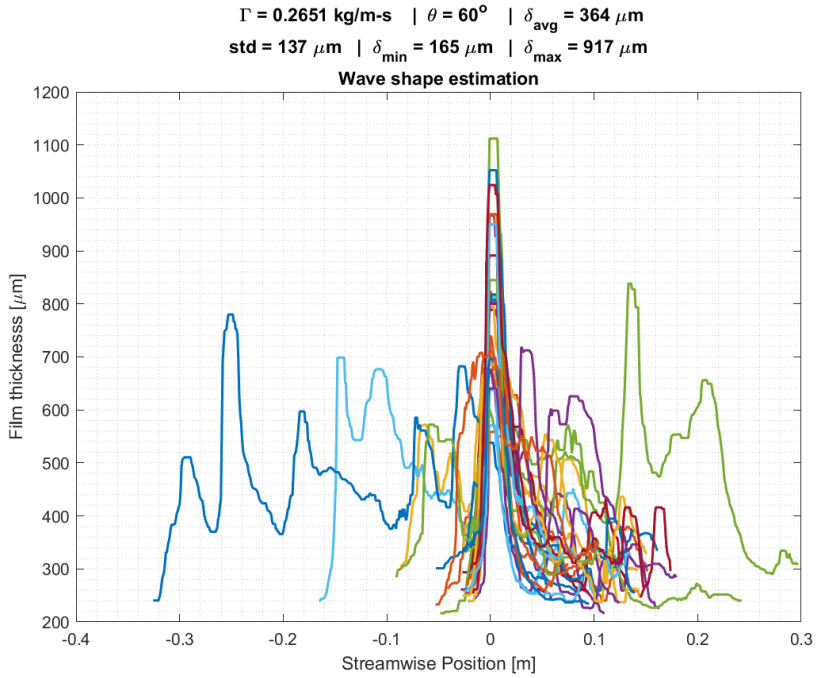

Wave shapes for test condition No. 2.50

A.3 Wave shape comparison array

The first 12 wave shapes identified are compiled in a 2-by-6 grid for each test condition. The raw signal associated with each wave shape is also shown in the background (shaded) to illustrate the slight difference between the filtered and unfiltered data.

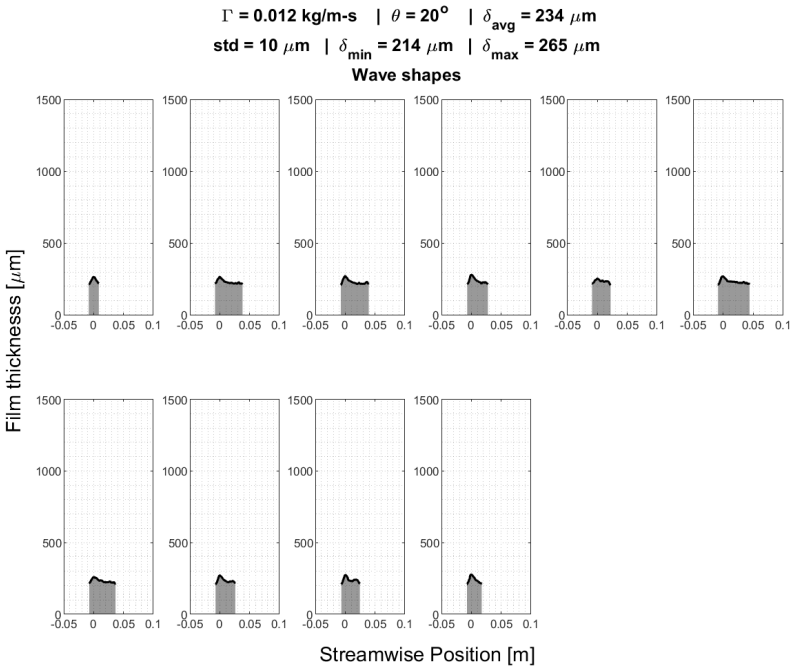

Wave shape comparison array for test condition No. 1.2

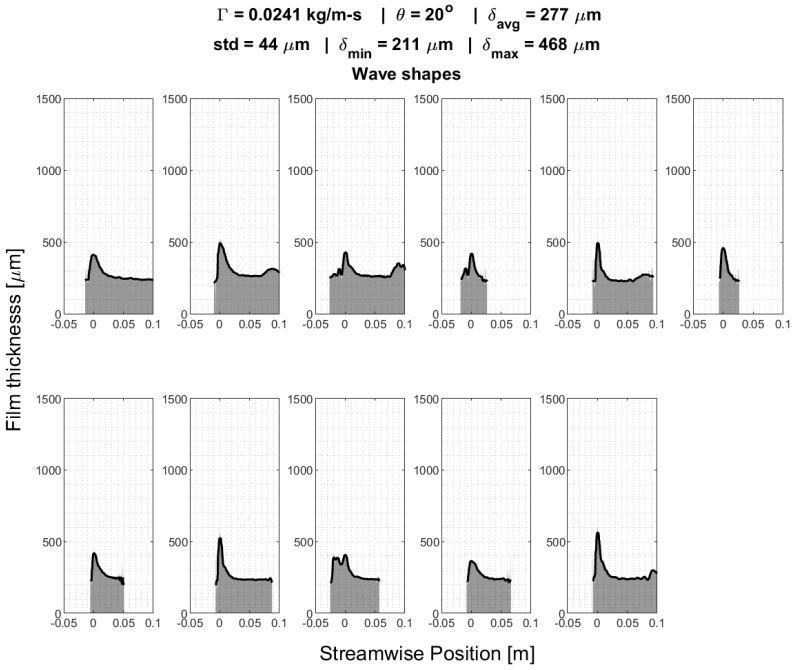

Wave shape comparison array for test condition No. 1.2

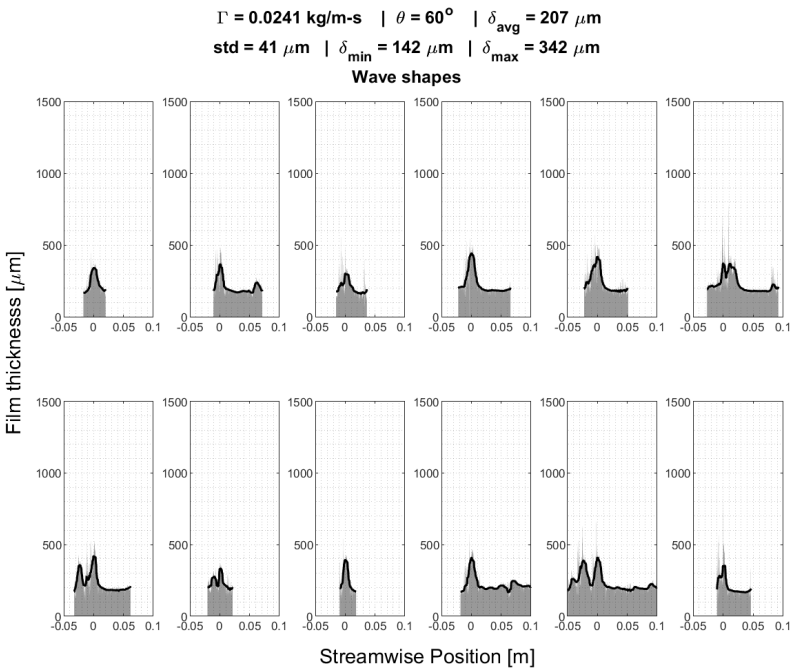

Wave shape comparison array for test condition No. 1.3

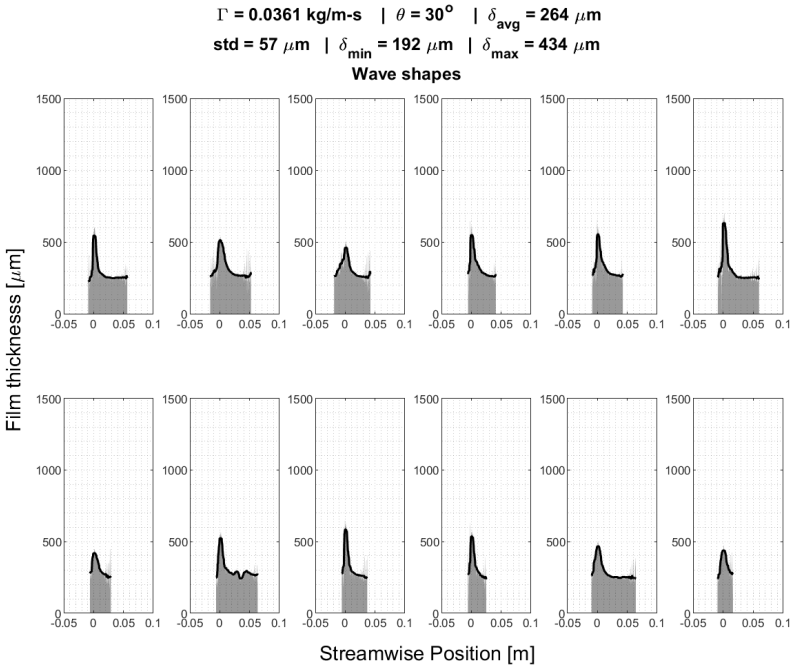

Wave shape comparison array for test condition No. 1.4

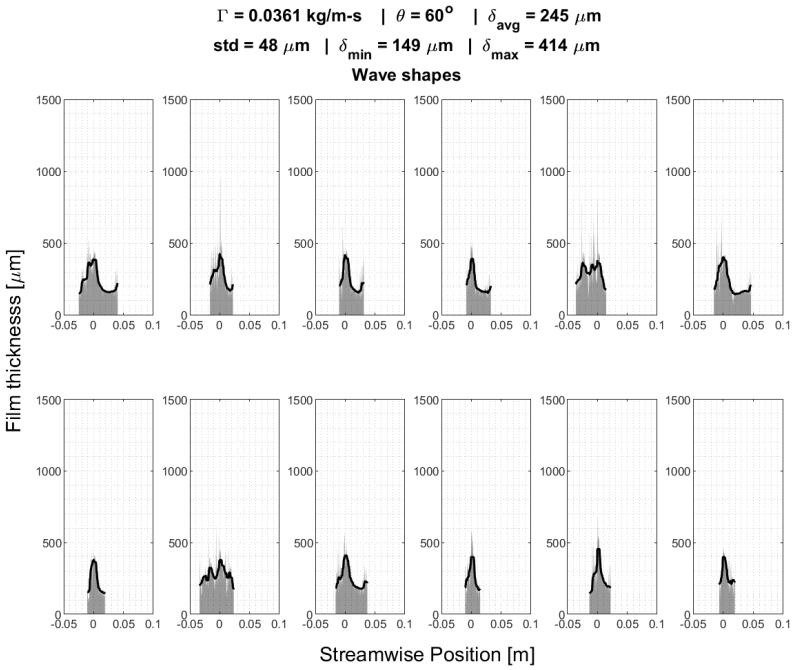

Wave shape comparison array for test condition No. 1.5

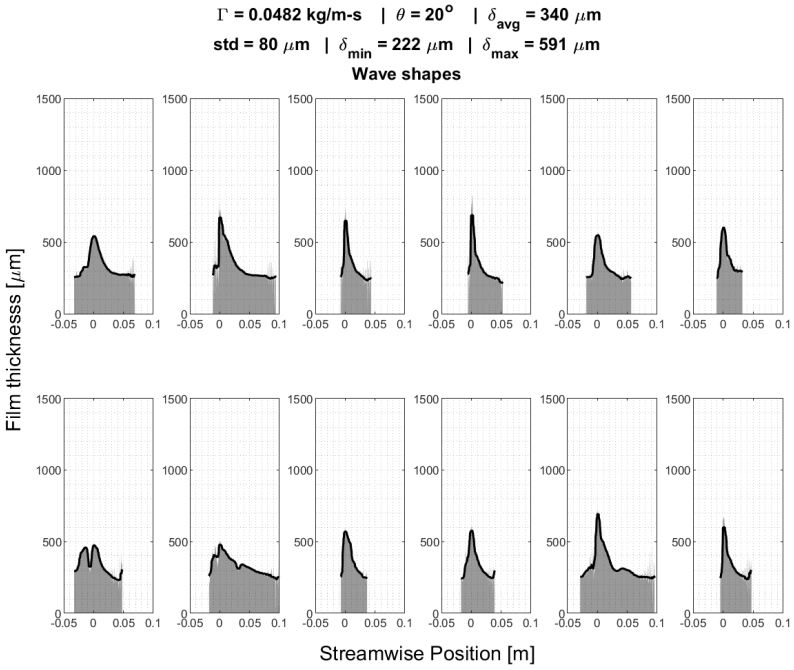

Wave shape comparison array for test condition No. 1.6

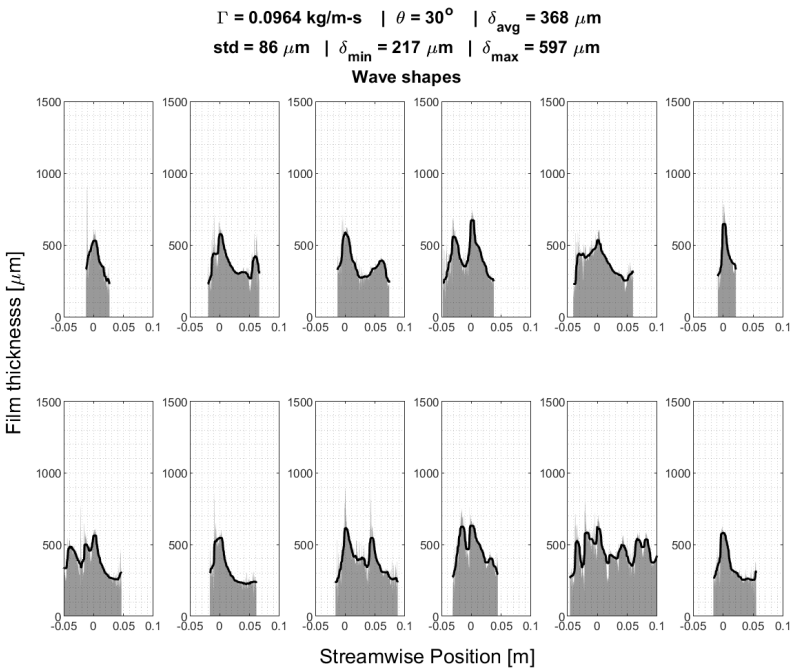

Wave shape comparison array for test condition No. 1.7

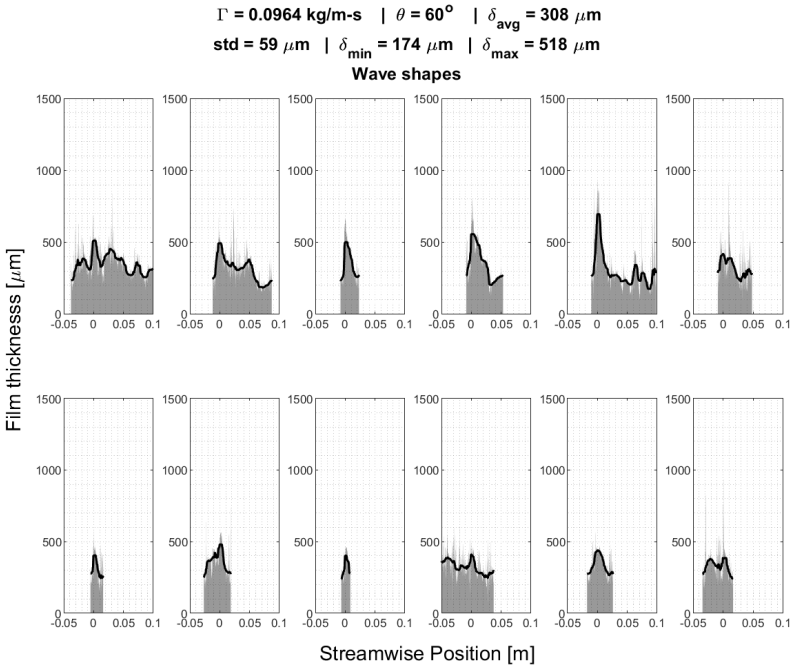

Wave shape comparison array for test condition No. 1.8

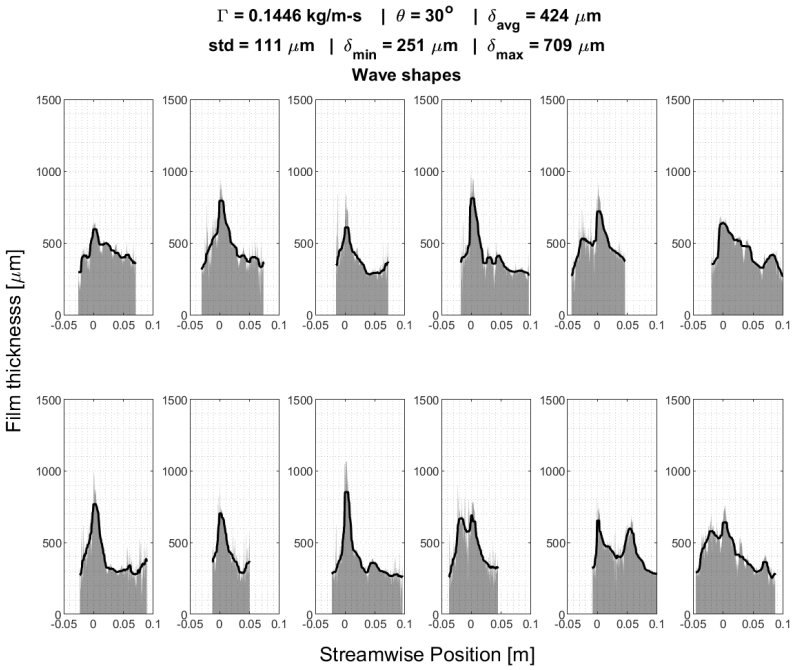

Wave shape comparison array for test condition No. 1.9

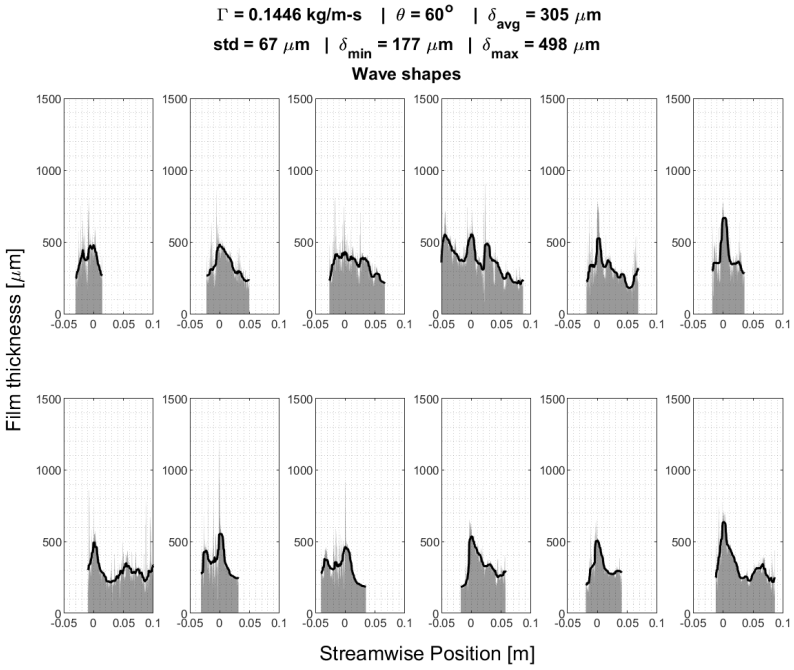

Wave shape comparison array for test condition No. 1.10

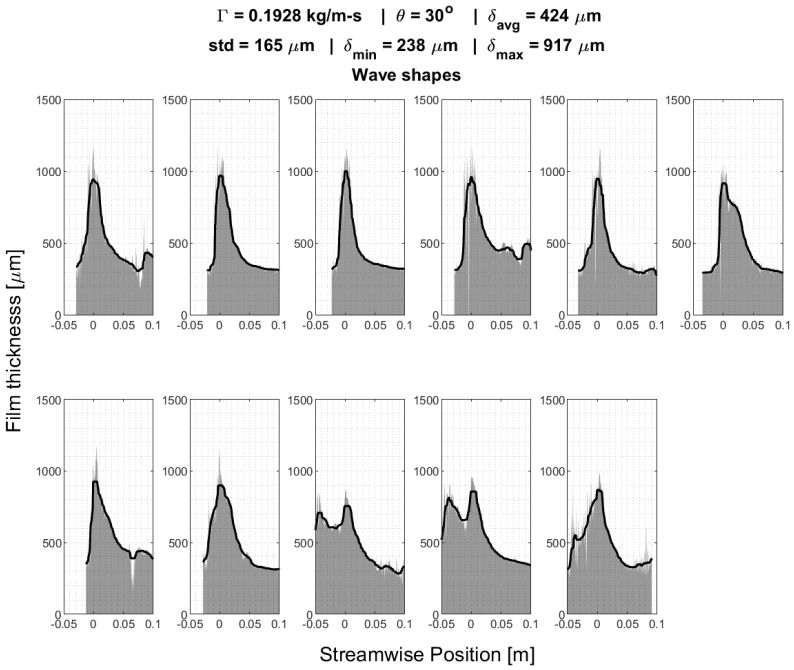

Wave shape comparison array for test condition No. 1.11

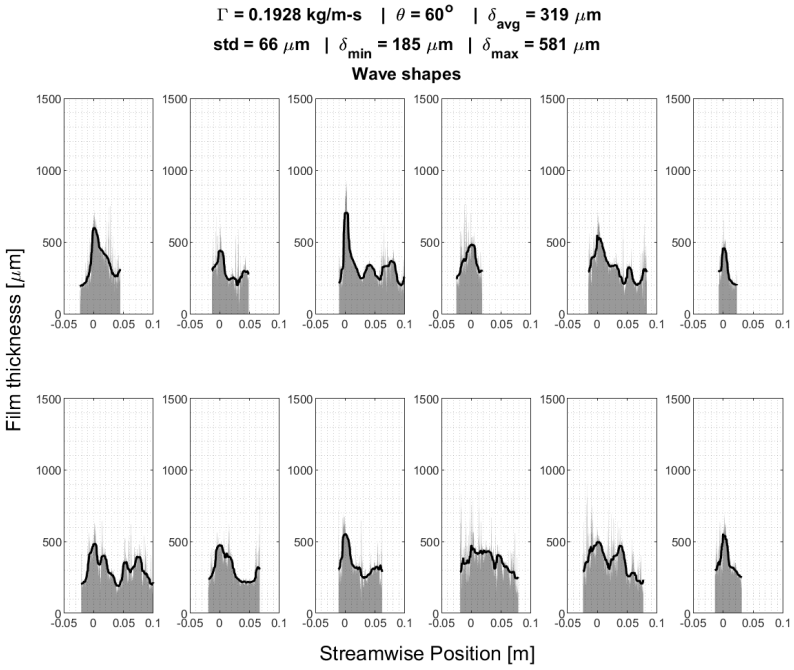

Wave shape comparison array for test condition No. 1.12

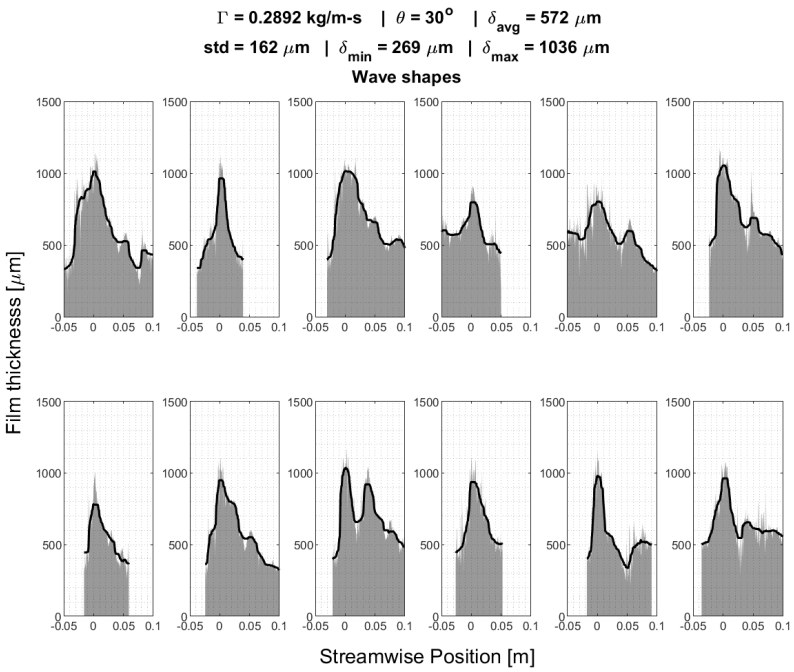

Wave shape comparison array for test condition No. 1.13

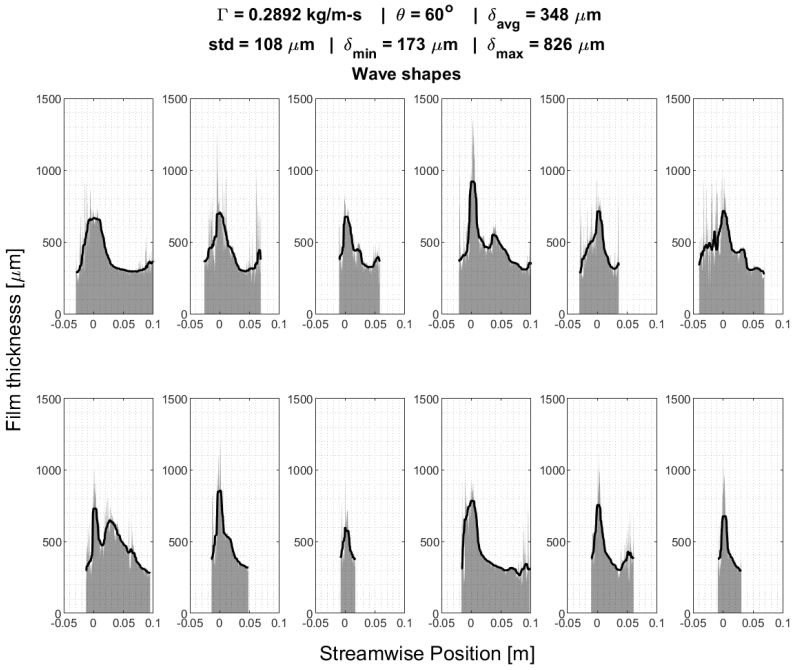

Wave shape comparison array for test condition No. 1.14

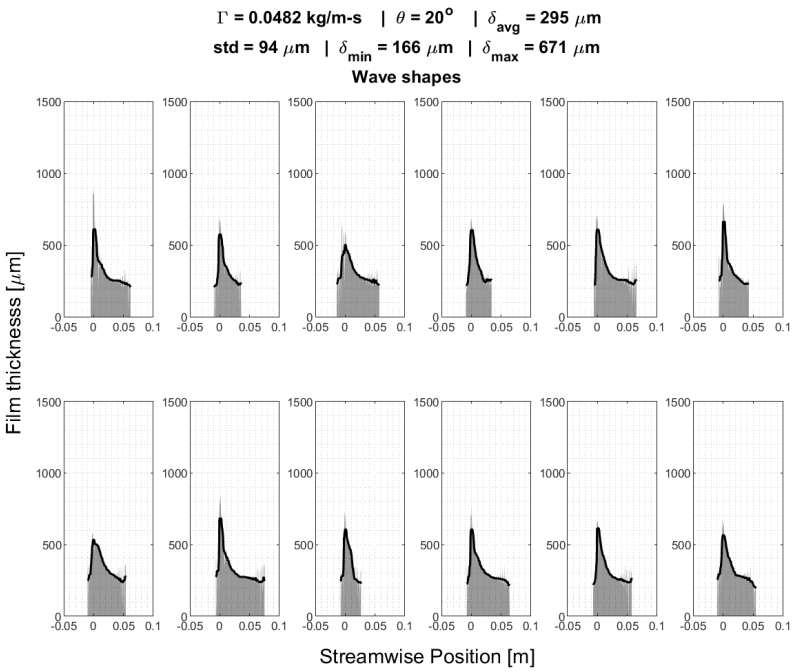

Wave shape comparison array for test condition No. 2.1

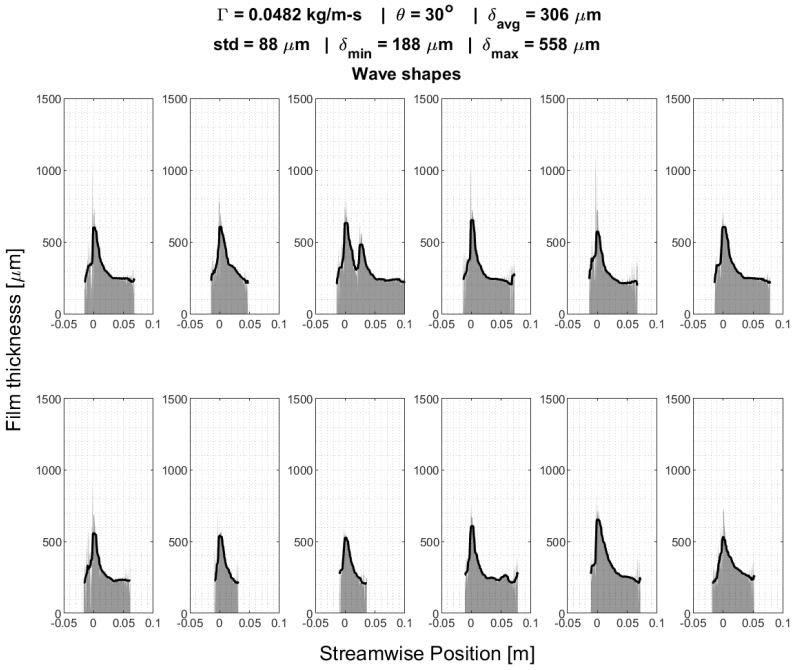

Wave shape comparison array for test condition No. 2.2

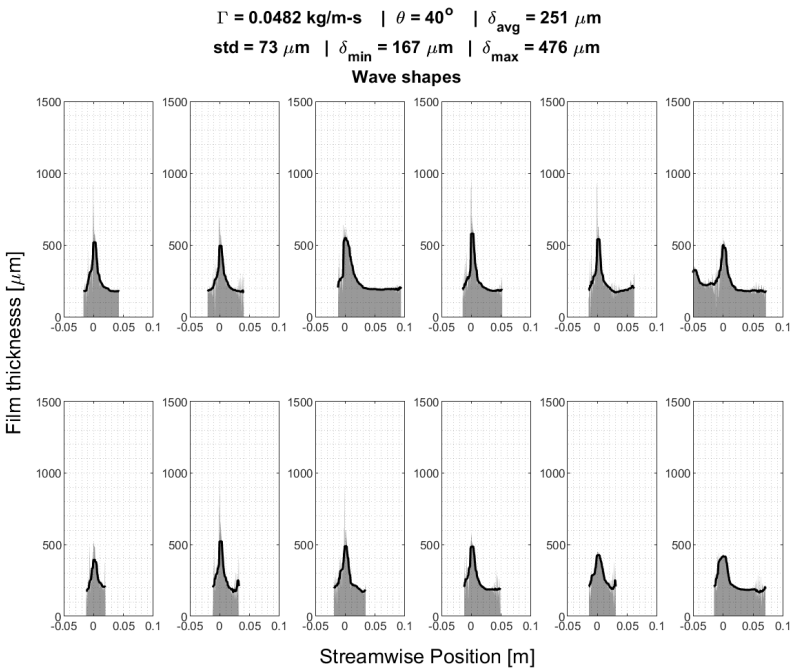

Wave shape comparison array for test condition No. 2.3

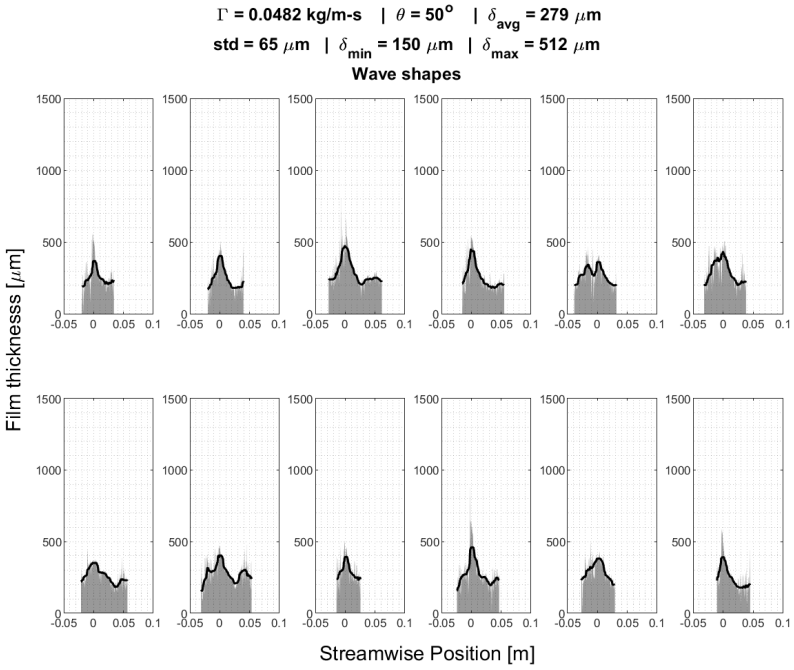

Wave shape comparison array for test condition No. 2.4

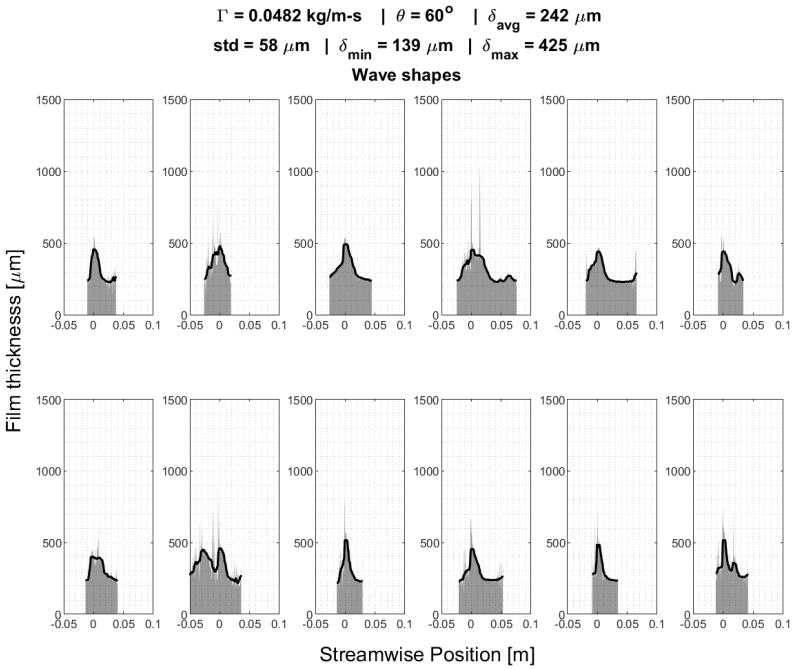

Wave shape comparison array for test condition No. 2.5

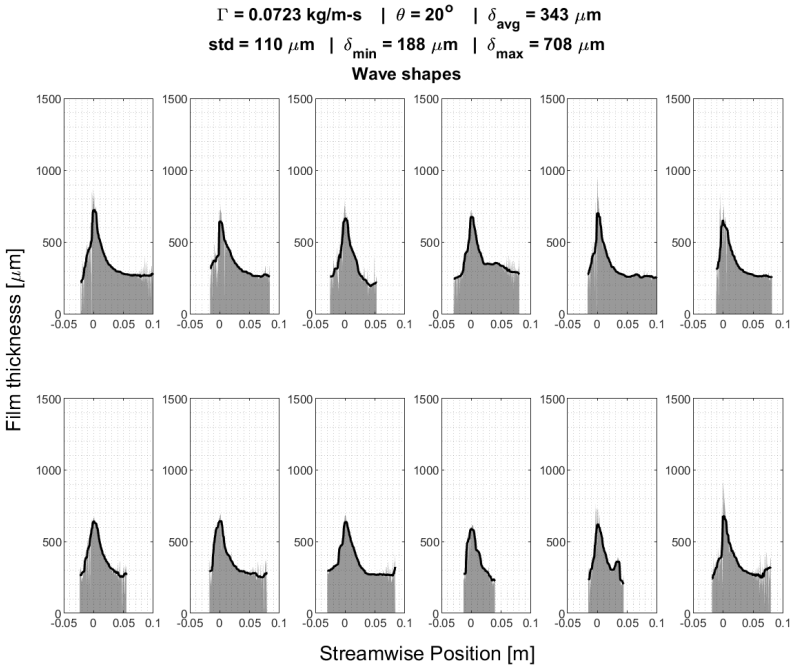

Wave shape comparison array for test condition No. 2.6

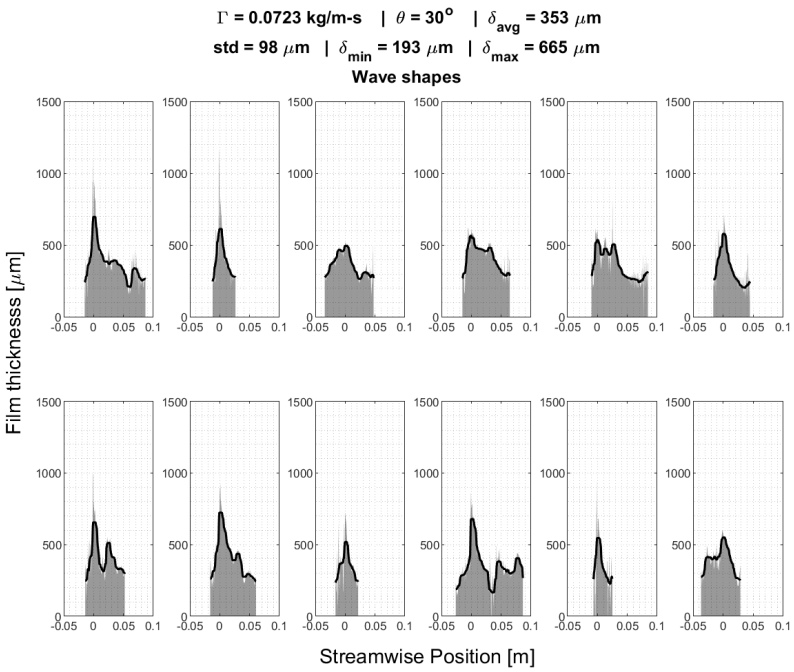

Wave shape comparison array for test condition No. 2.7

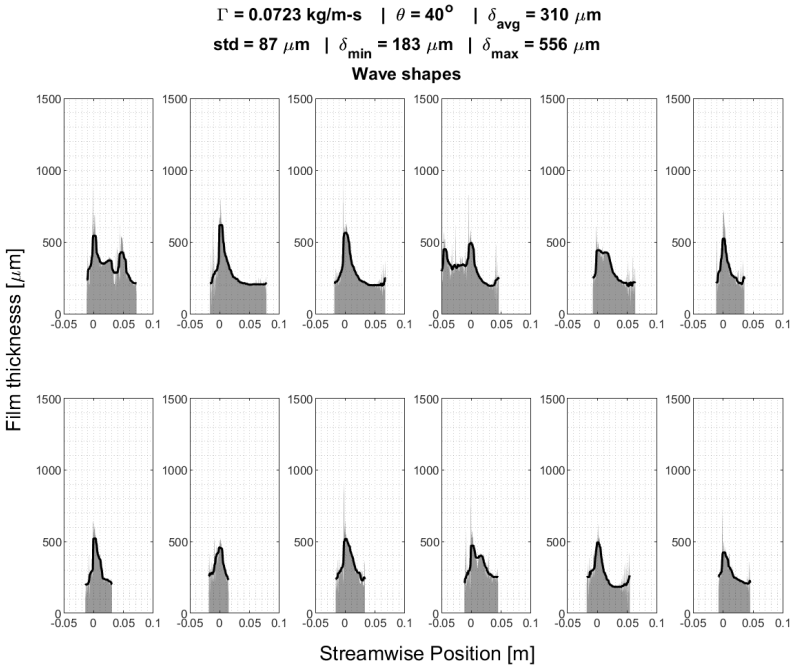

Wave shape comparison array for test condition No. 2.8

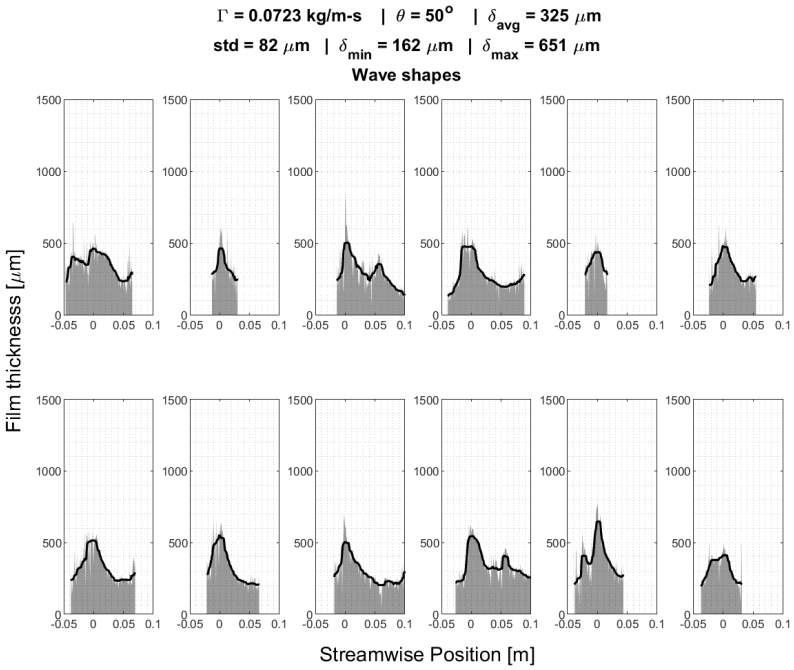

Wave shape comparison array for test condition No. 2.9

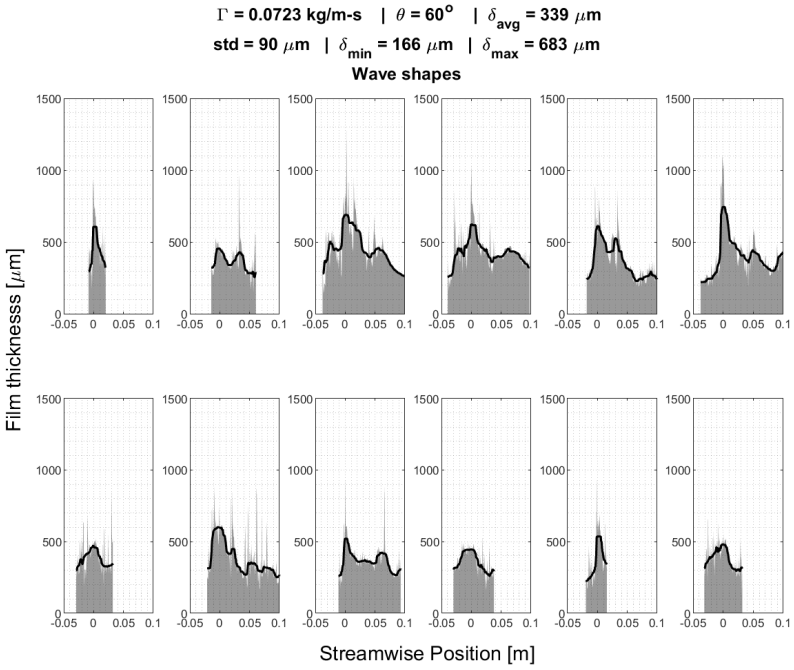

Wave shape comparison array for test condition No. 2.10

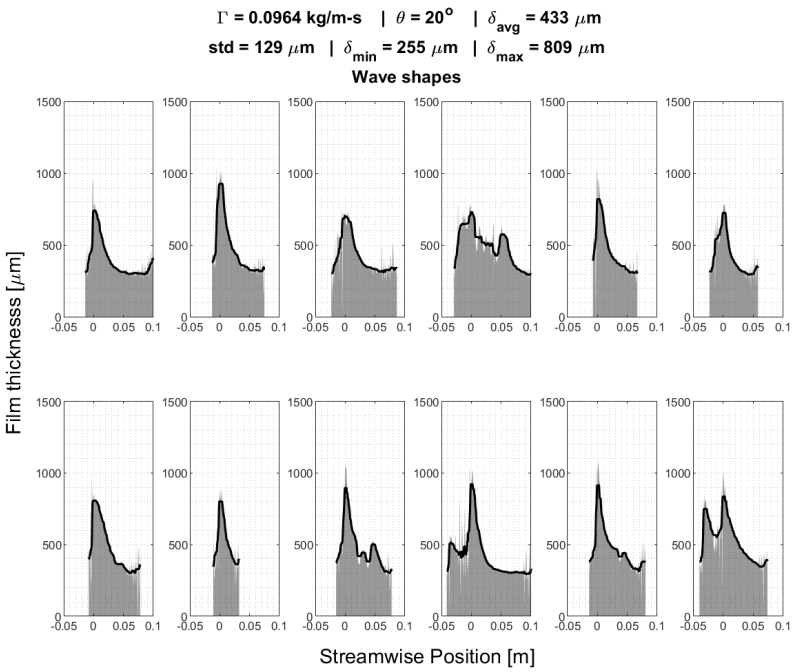

Wave shape comparison array for test condition No. 2.11

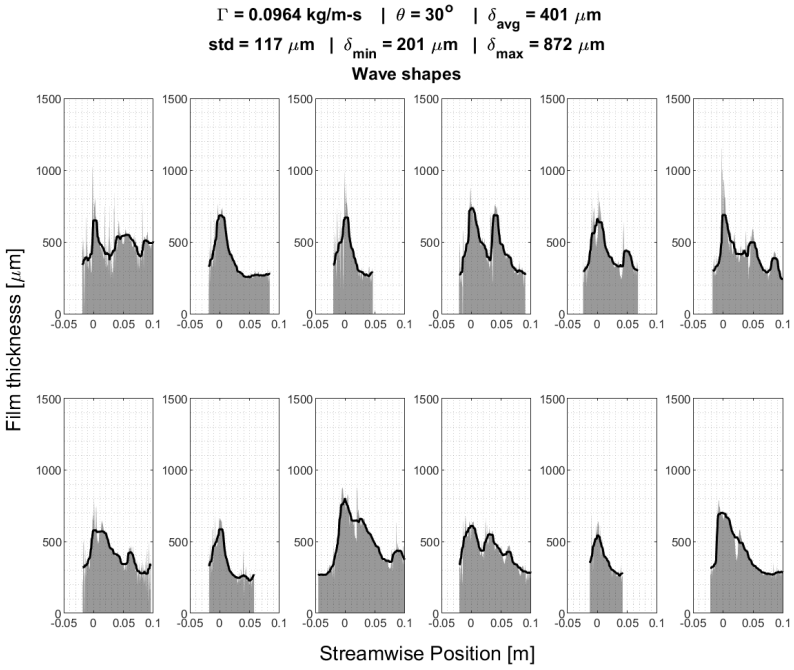

Wave shape comparison array for test condition No. 2.12

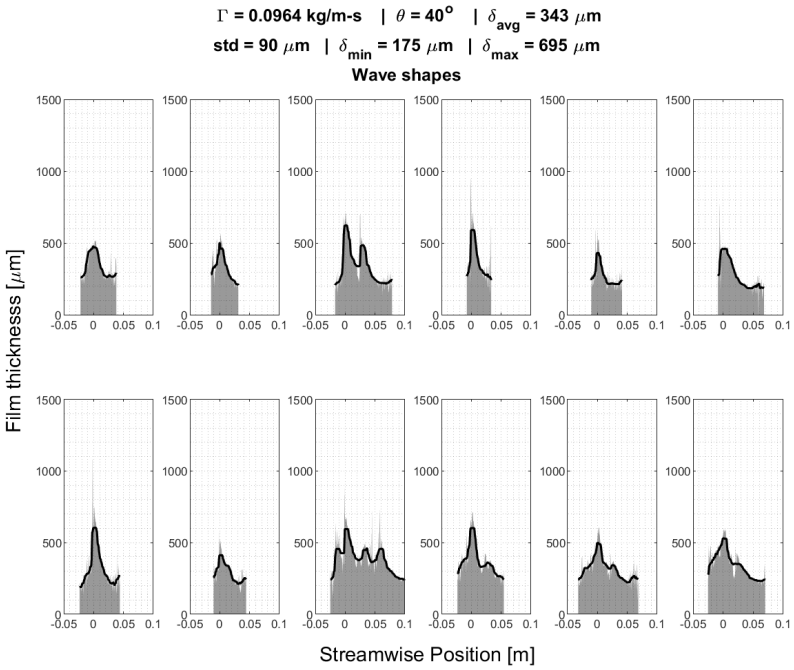

Wave shape comparison array for test condition No. 2.13

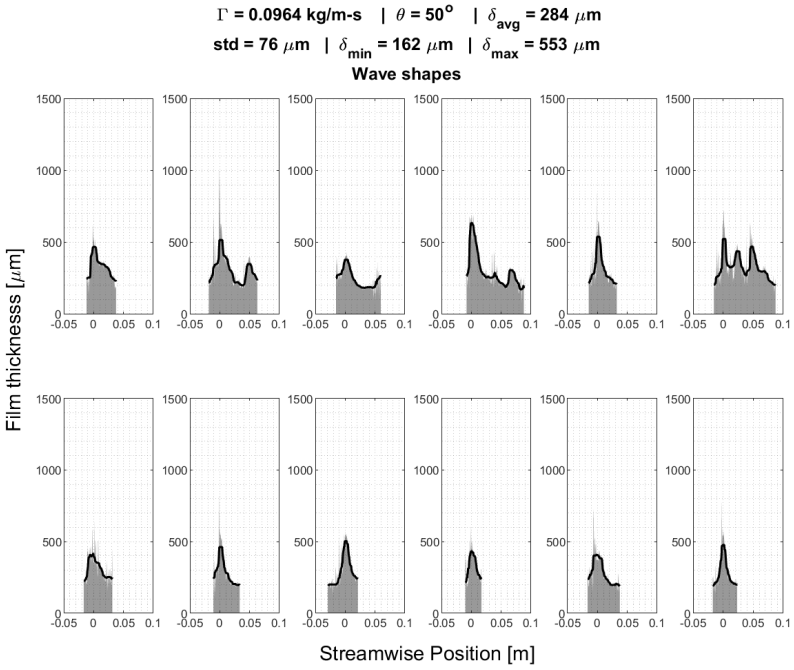

Wave shape comparison array for test condition No. 2.14

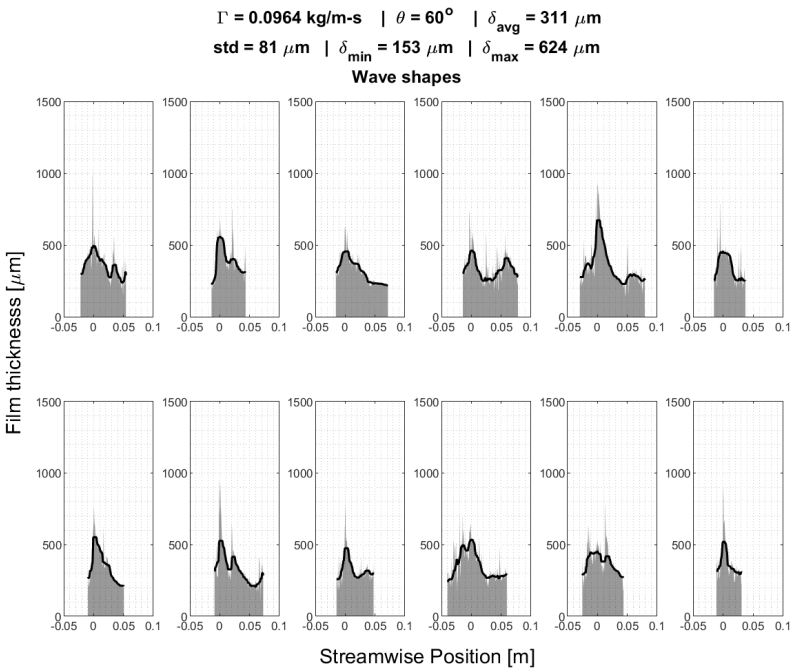

Wave shape comparison array for test condition No. 2.15

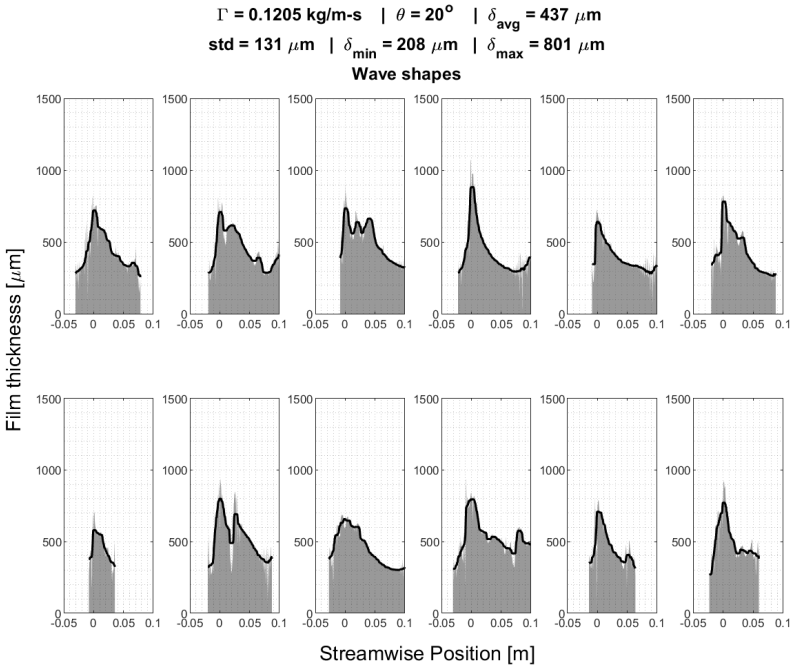

Wave shape comparison array for test condition No. 2.16

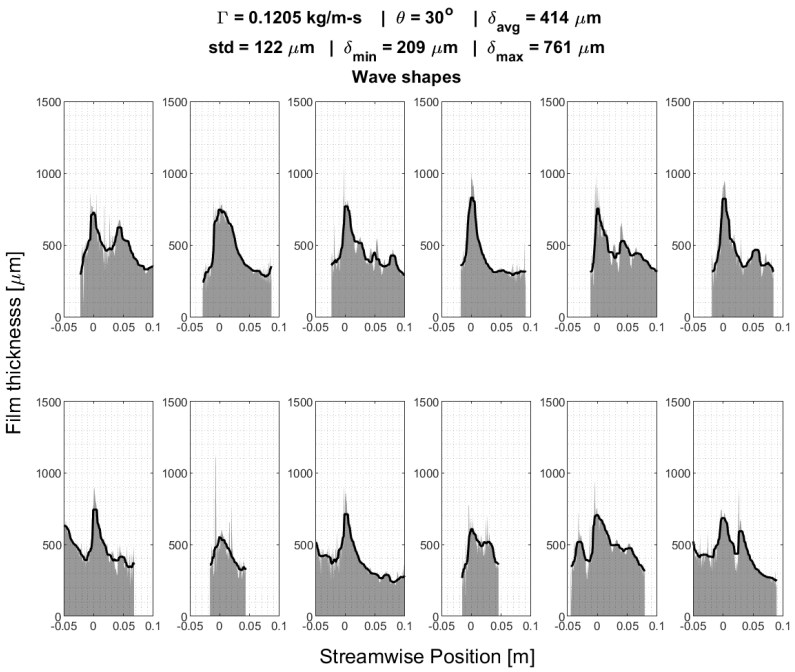

Wave shape comparison array for test condition No. 2.17

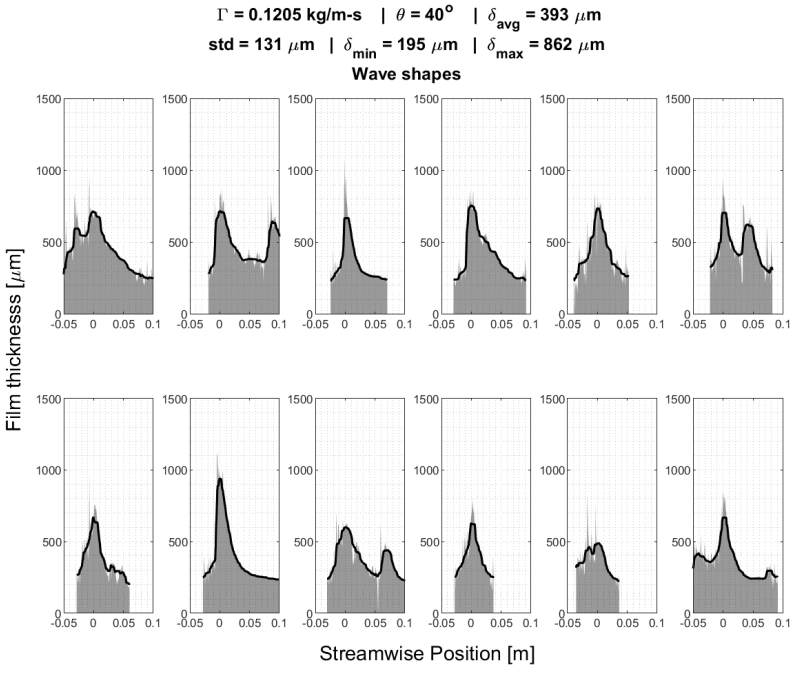

Wave shape comparison array for test condition No. 2.18

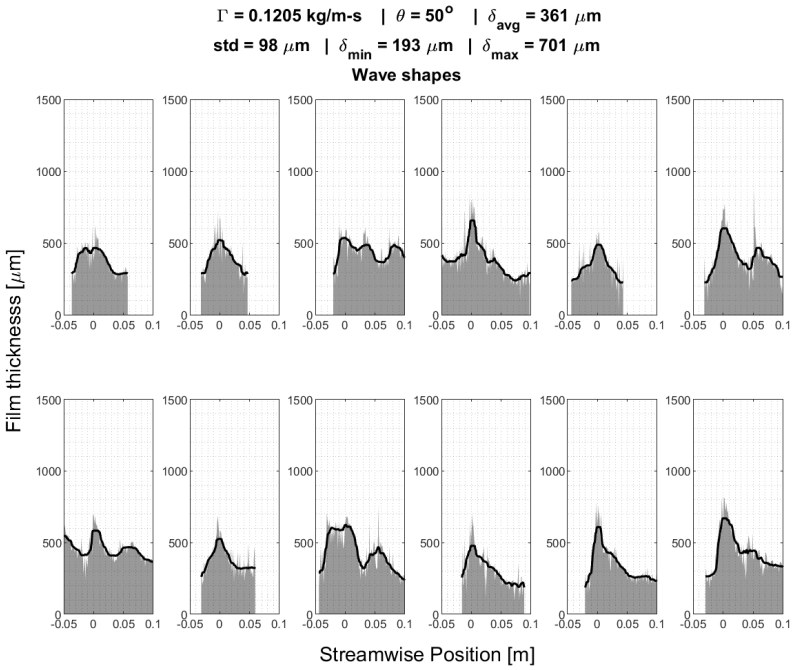

Wave shape comparison array for test condition No. 2.19

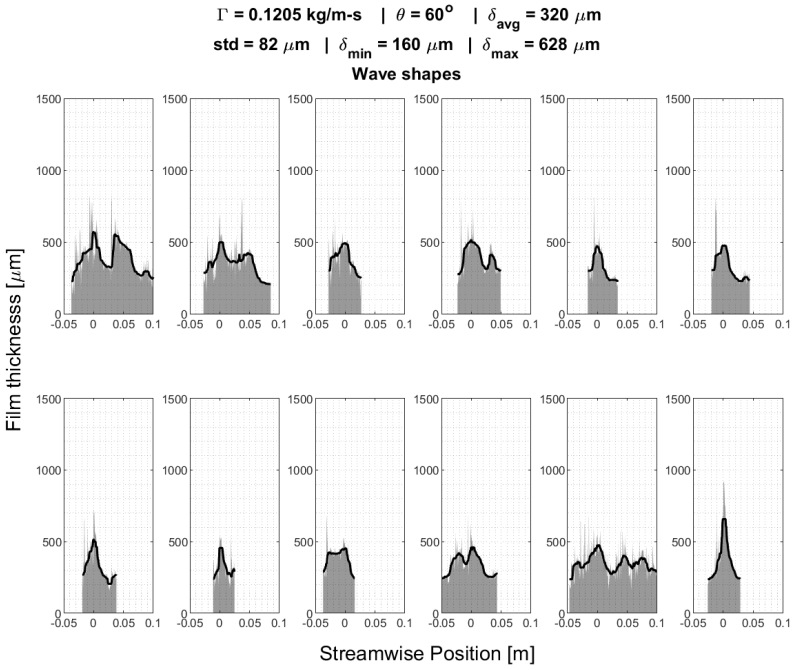

Wave shape comparison array for test condition No. 2.20

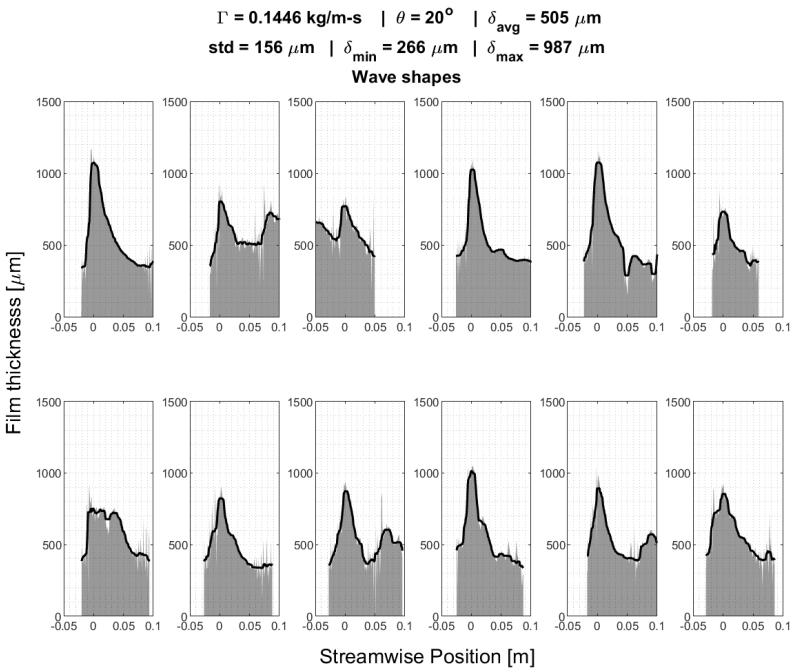

Wave shape comparison array for test condition No. 2.21

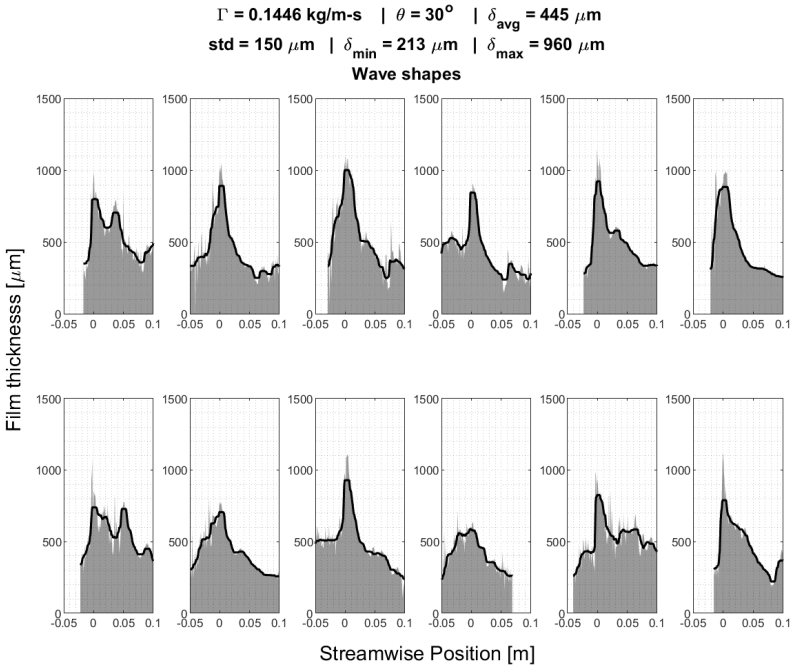

Wave shape comparison array for test condition No. 2.22

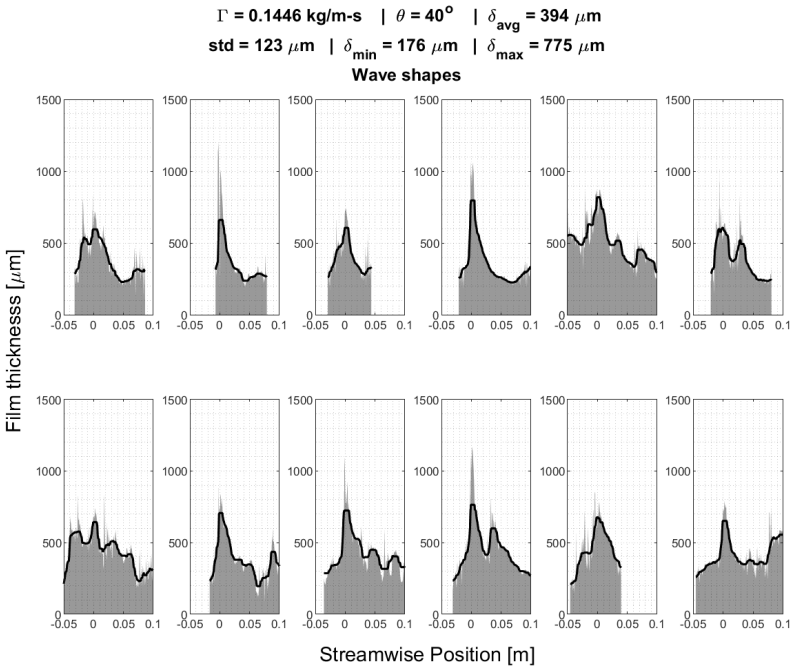

Wave shape comparison array for test condition No. 2.23

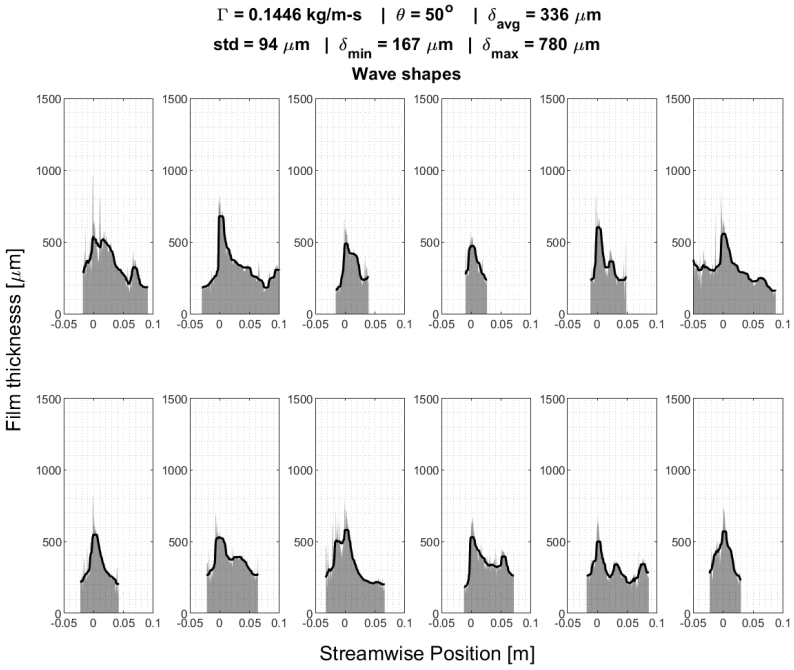

Wave shape comparison array for test condition No. 2.24

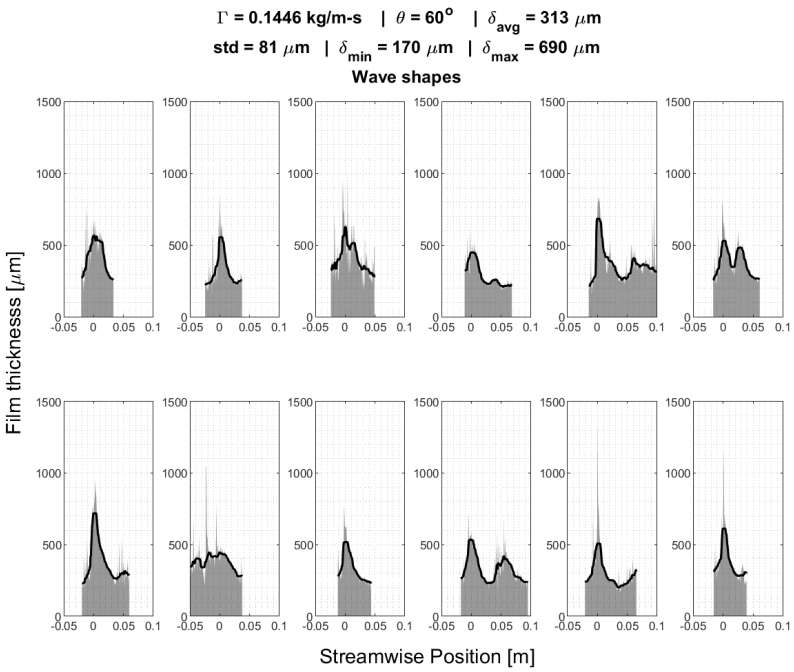

Wave shape comparison array for test condition No. 2.25

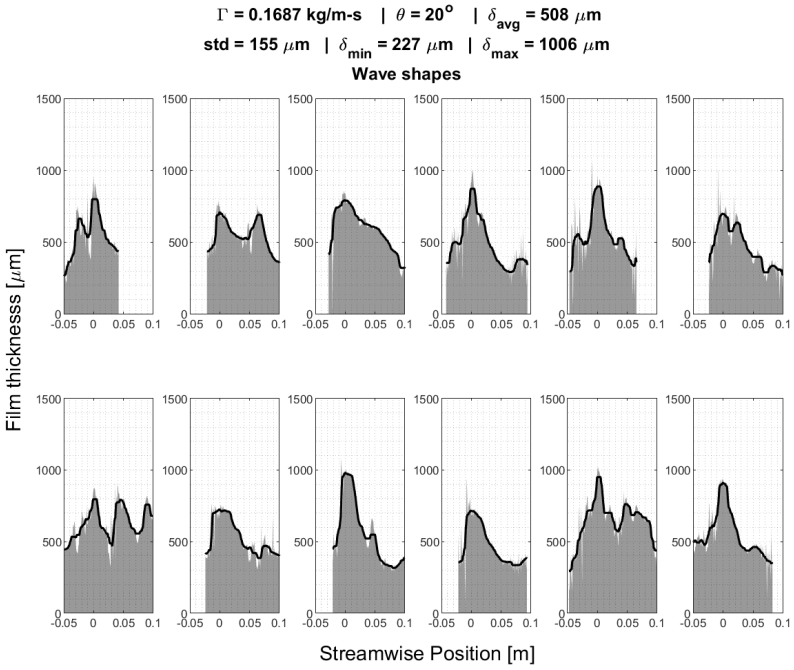

Wave shape comparison array for test condition No. 2.26

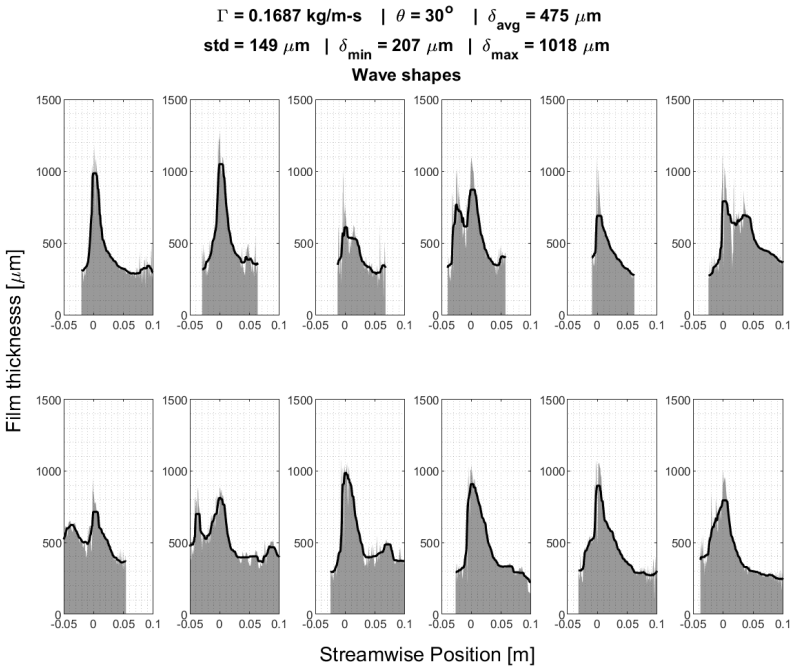

Wave shape comparison array for test condition No. 2.27

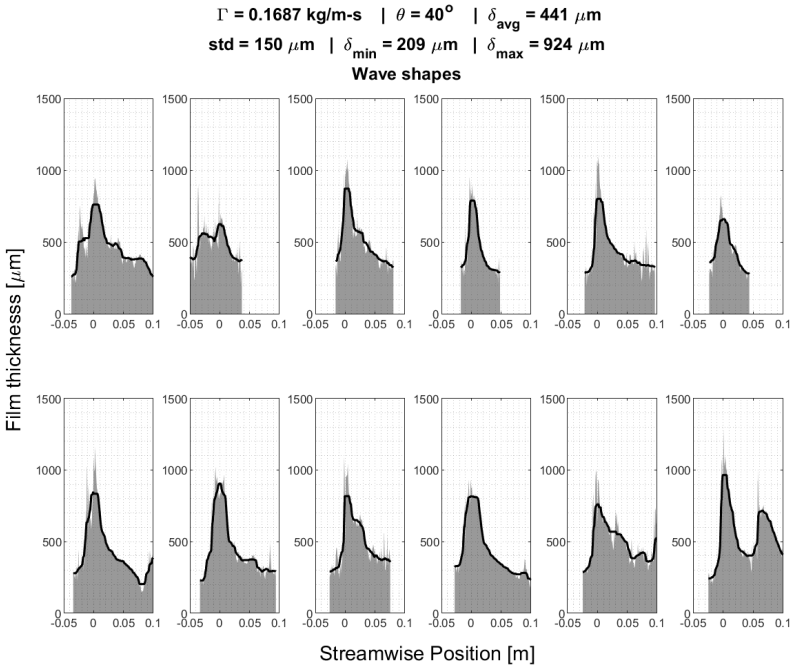

Wave shape comparison array for test condition No. 2.28

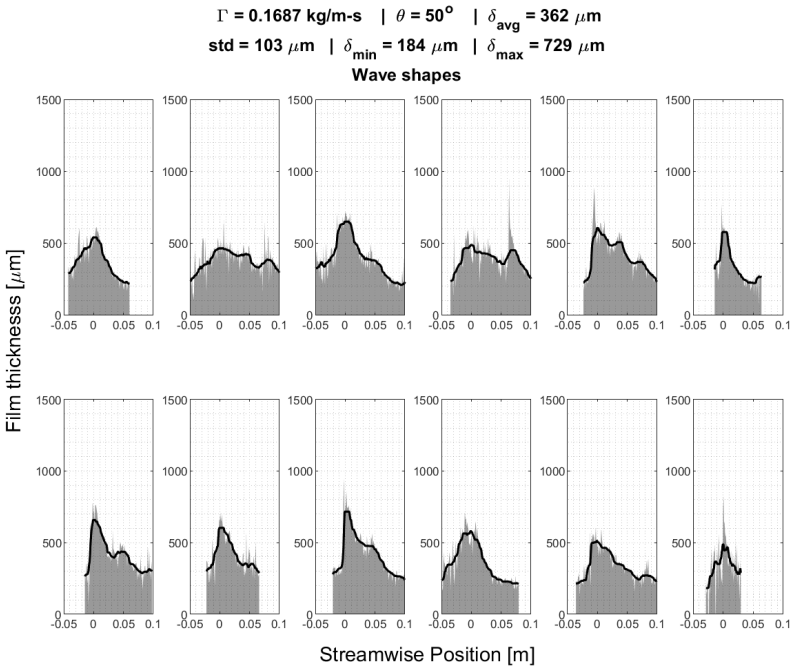

Wave shape comparison array for test condition No. 2.29

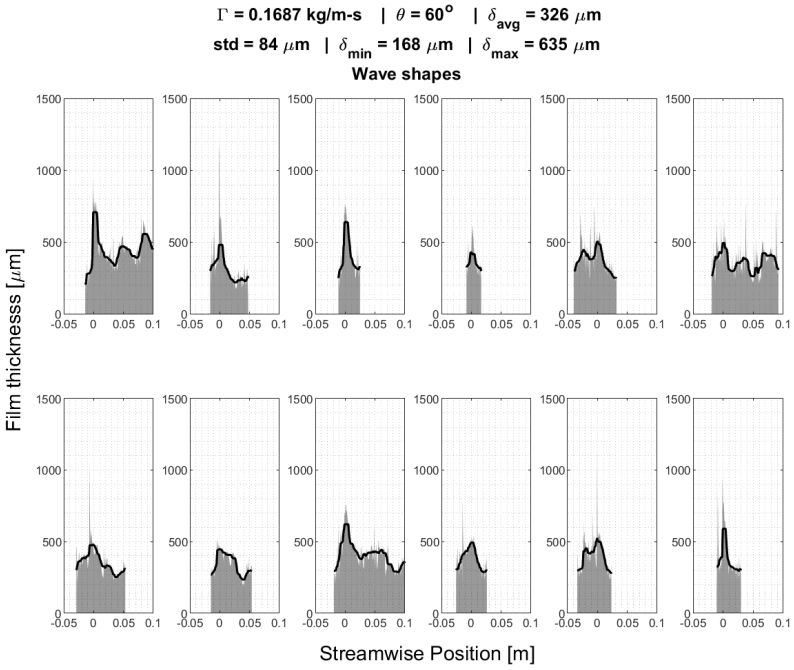

Wave shape comparison array for test condition No. 2.30

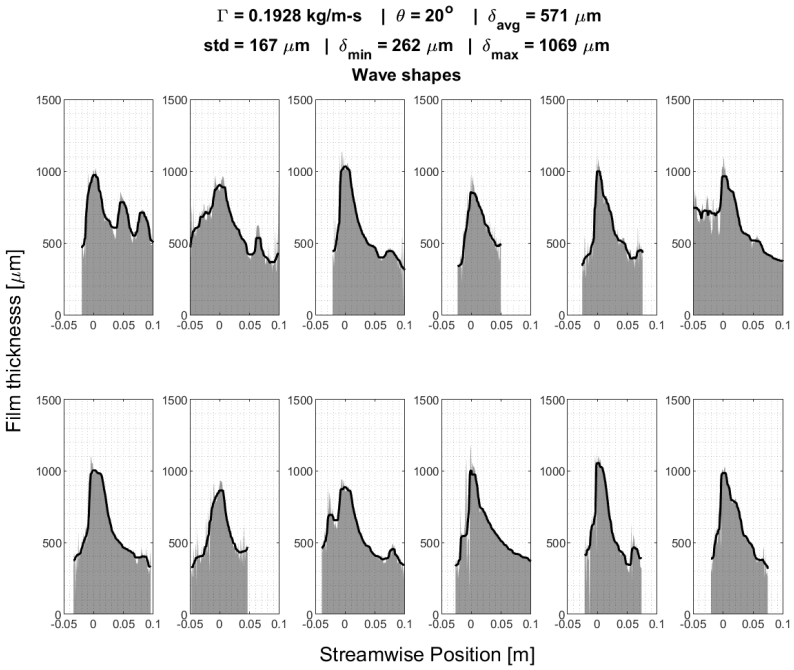

Wave shape comparison array for test condition No. 2.31

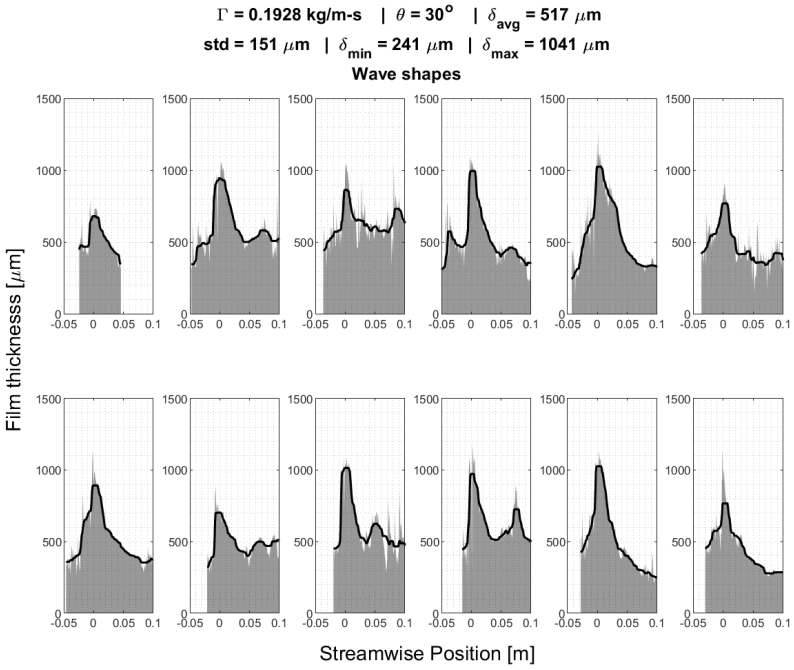

Wave shape comparison array for test condition No. 2.32

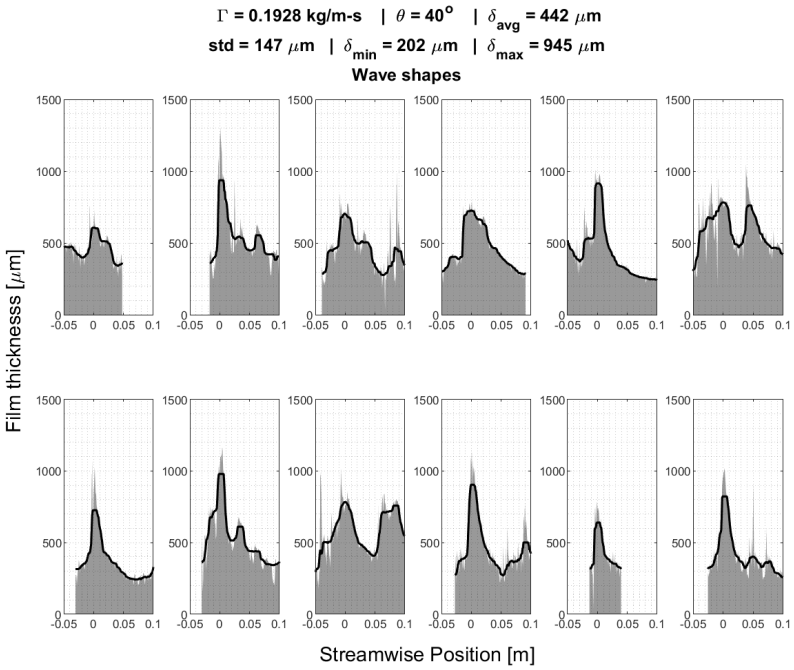

Wave shape comparison array for test condition No. 2.33

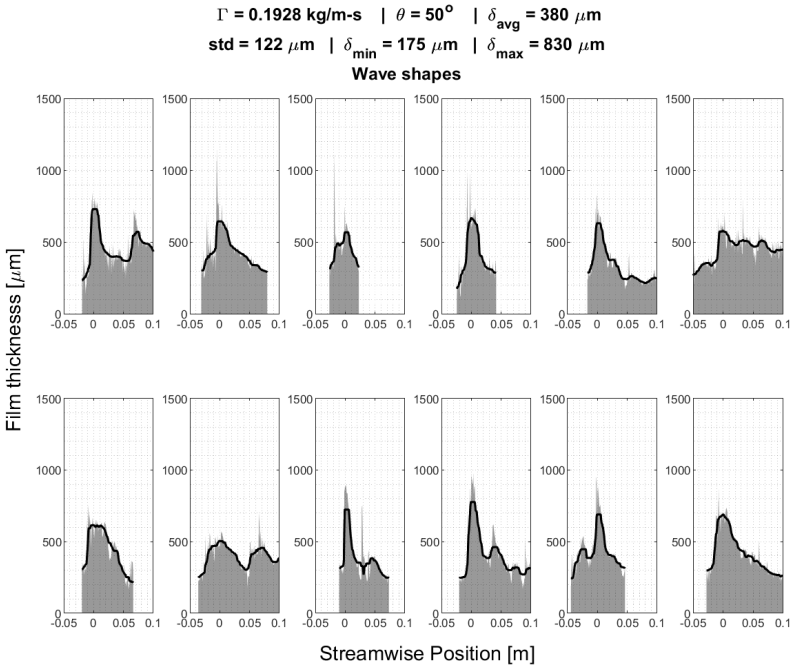

Wave shape comparison array for test condition No. 2.34

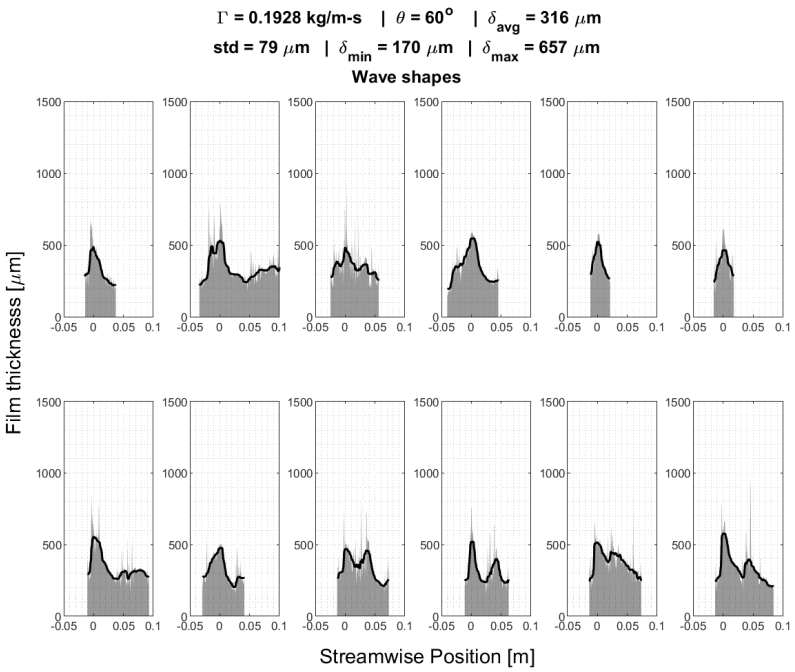

Wave shape comparison array for test condition No. 2.35

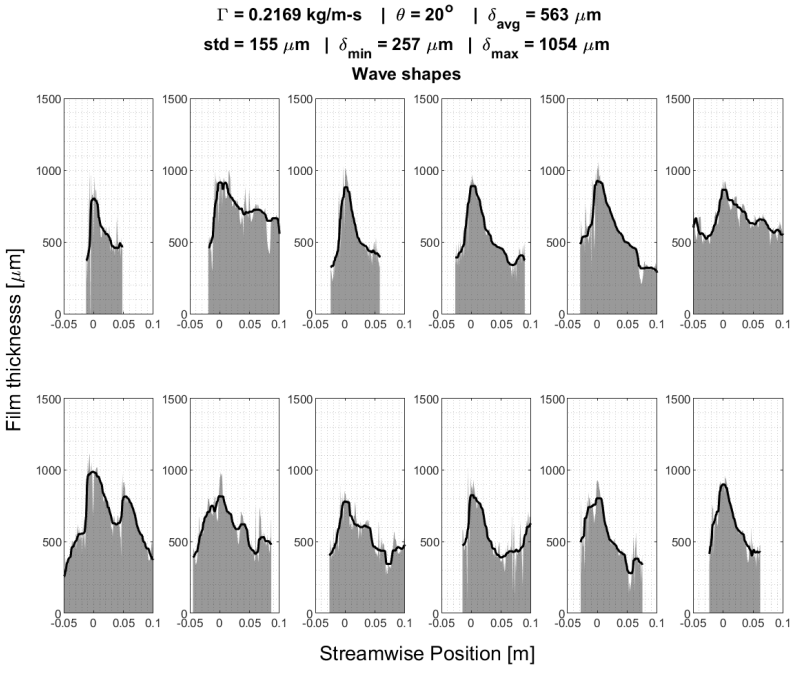

Wave shape comparison array for test condition No. 2.36

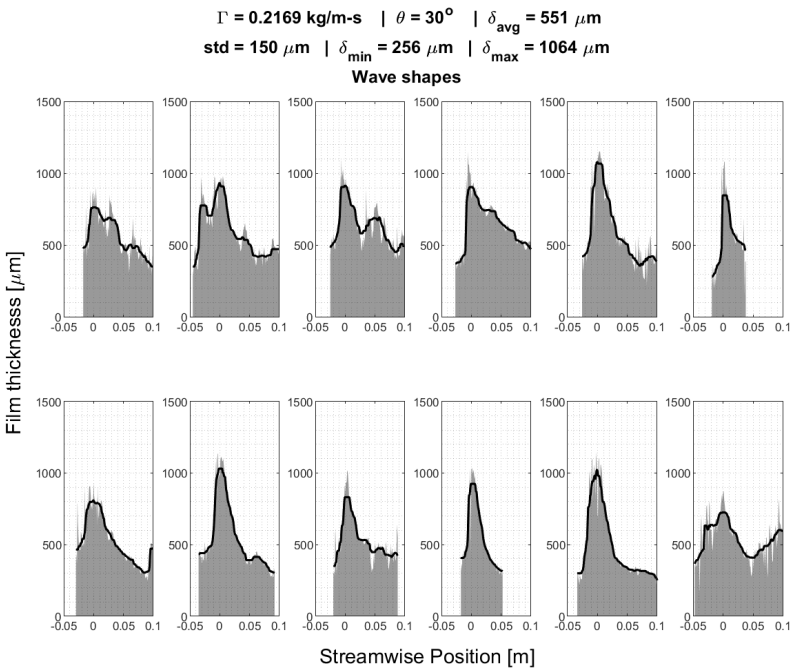

Wave shape comparison array for test condition No. 2.37

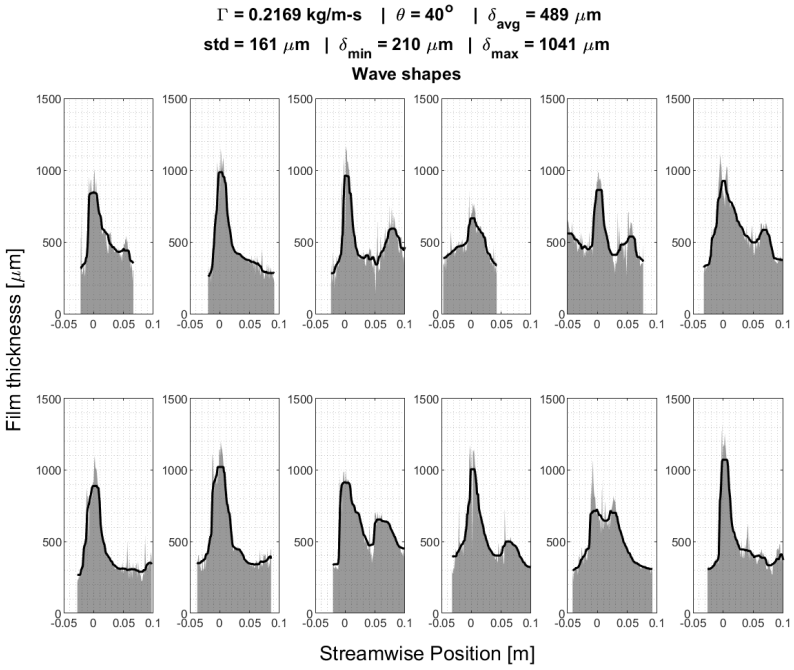

Wave shape comparison array for test condition No. 2.38

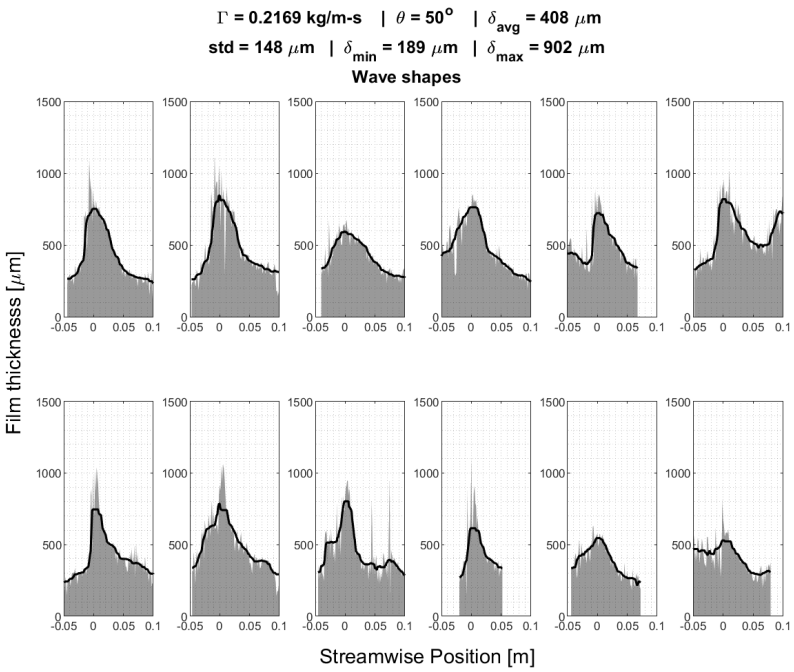

Wave shape comparison array for test condition No. 2.39

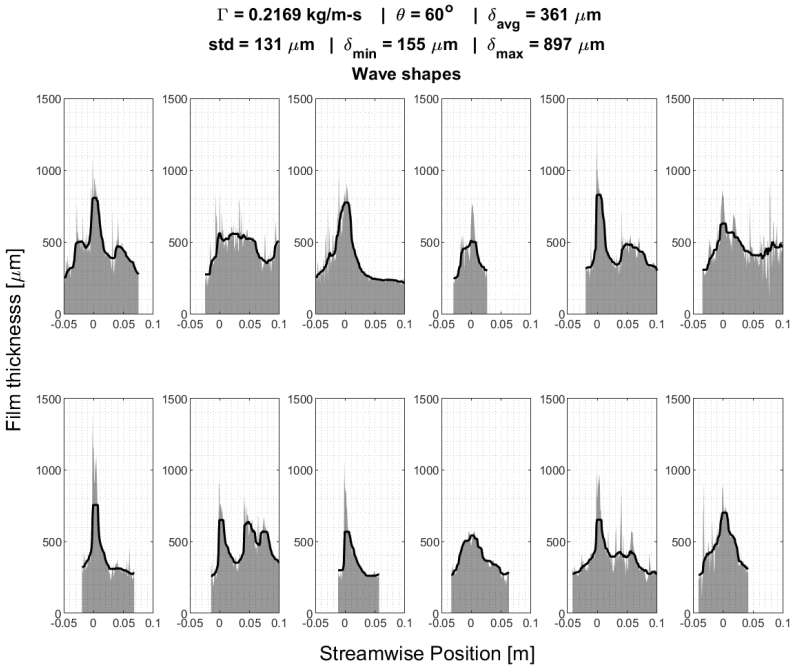

Wave shape comparison array for test condition No. 2.40

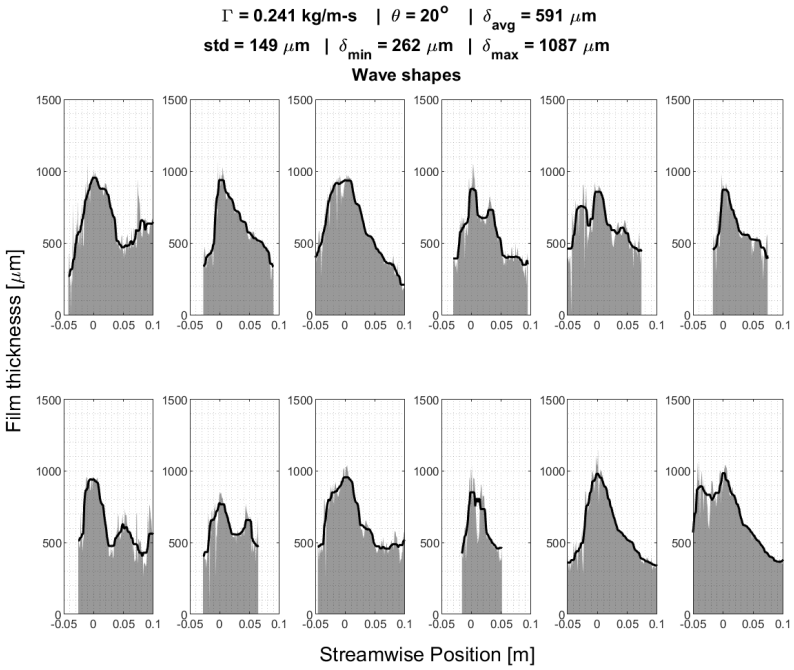

Wave shape comparison array for test condition No. 2.41

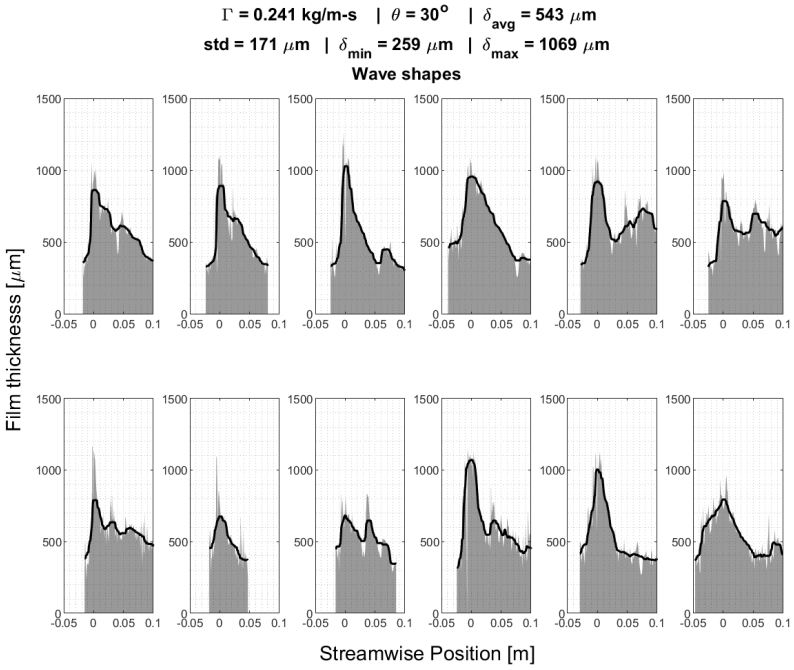

Wave shape comparison array for test condition No. 2.42

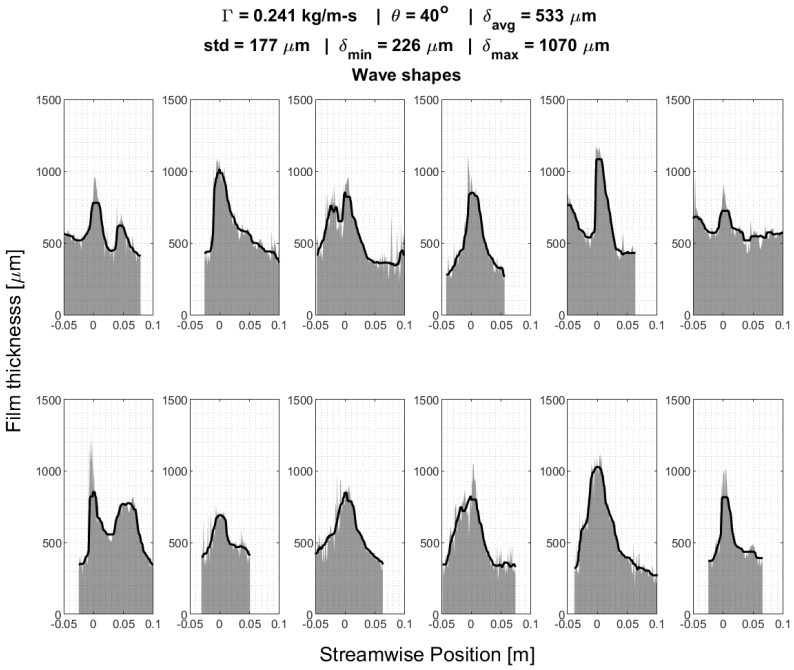

Wave shape comparison array for test condition No. 2.43

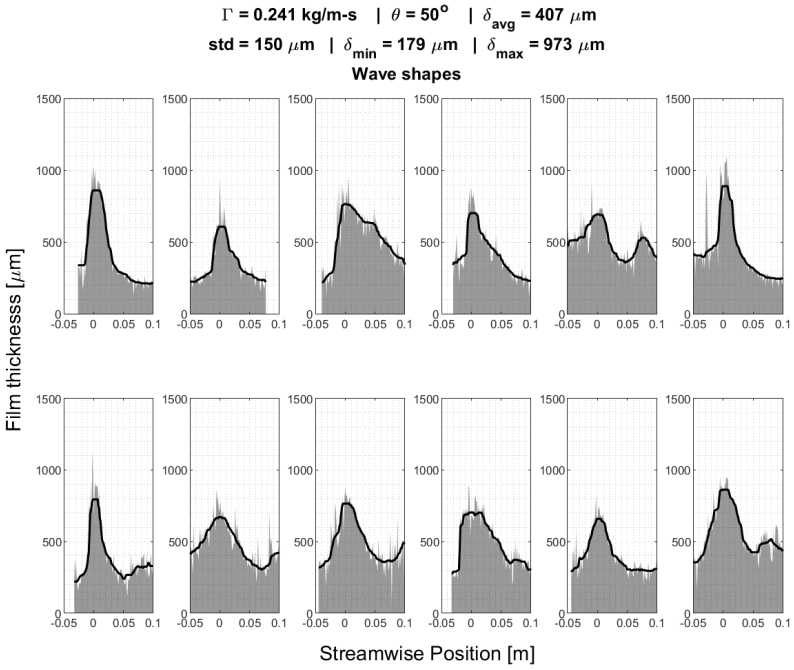

Wave shape comparison array for test condition No. 2.44

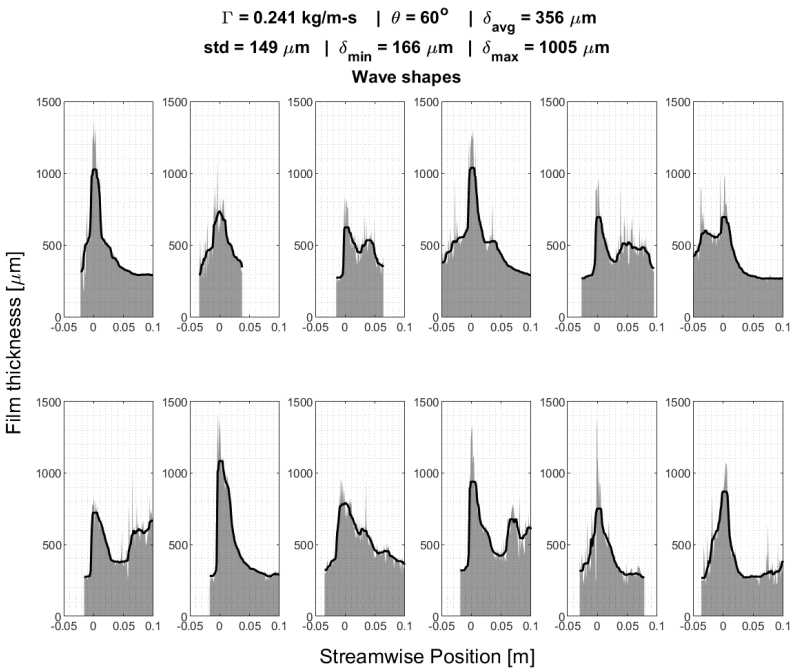

Wave shape comparison array for test condition No. 2.45

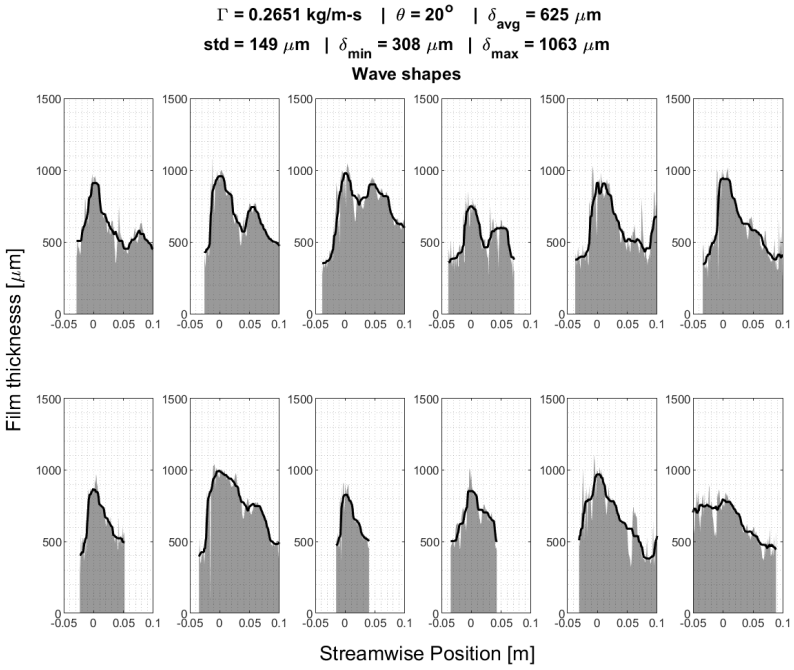

Wave shape comparison array for test condition No. 2.46

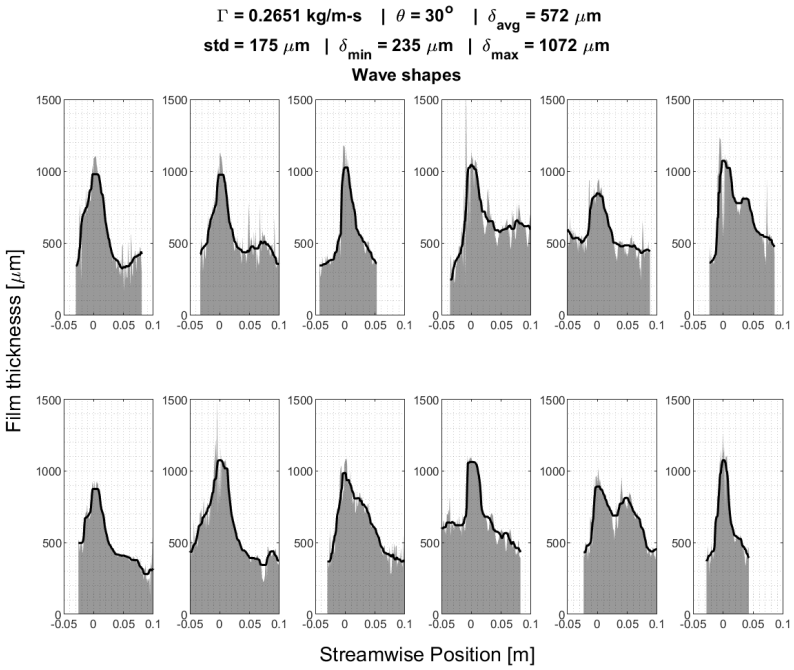

Wave shape comparison array for test condition No. 2.47

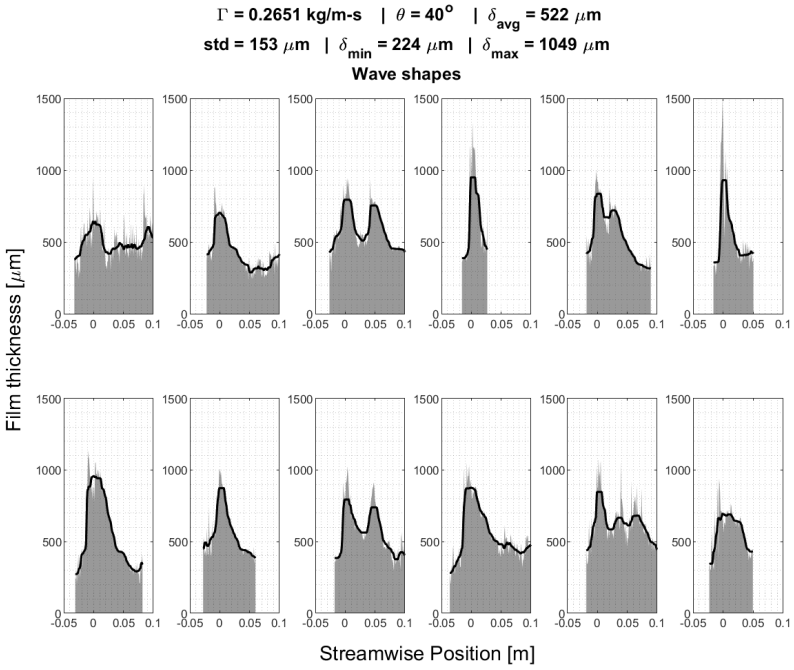

Wave shape comparison array for test condition No. 2.48

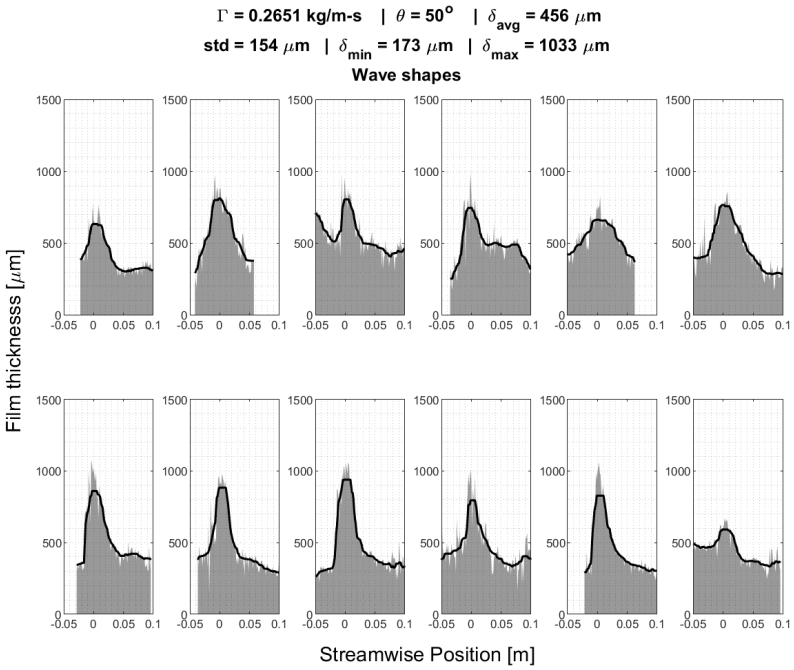

Wave shape comparison array for test condition No. 2.49

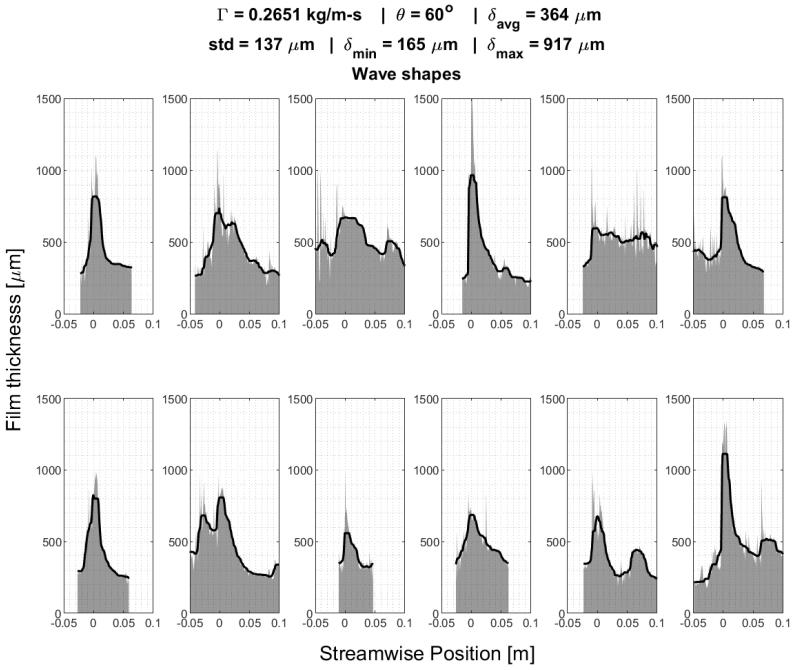

Wave shape comparison array for test condition No. 2.50

A.4 Wave velocity PDFs

The velocity distribution of waves for each flow condition is shown in figures in this section. The velocities are calculated using the automated algorithm, with outliers removed.

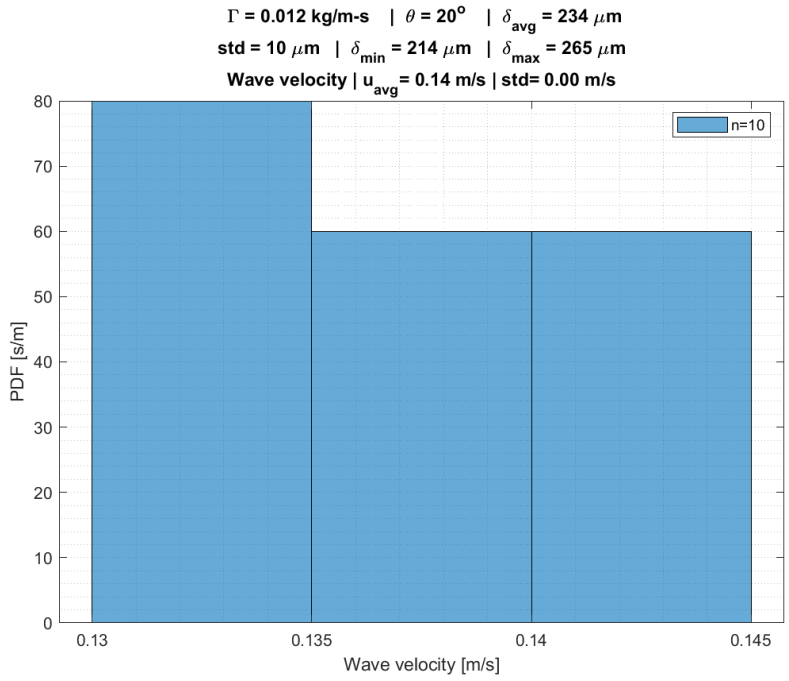

Wave velocity PDF for test condition No. 1.2

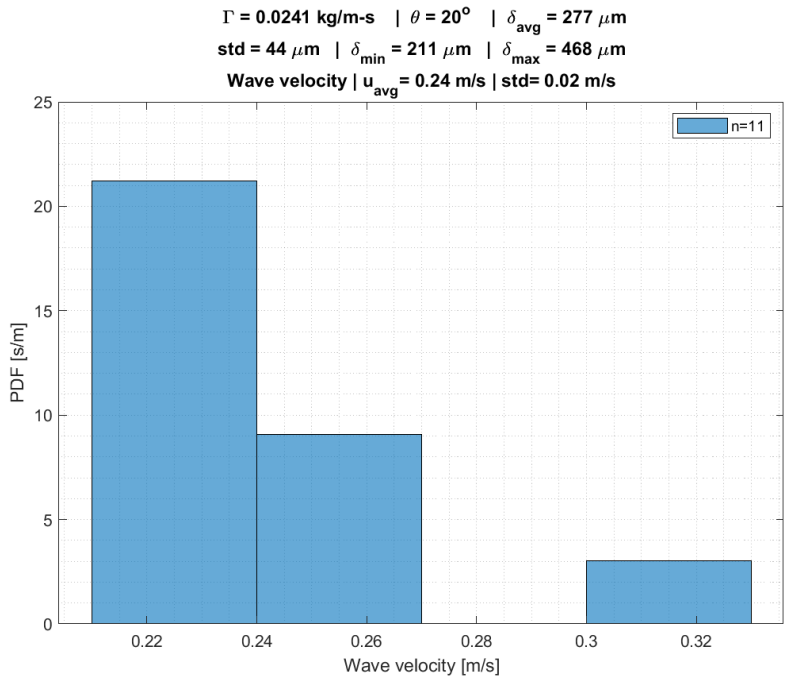

Wave velocity PDF for test condition No. 1.2

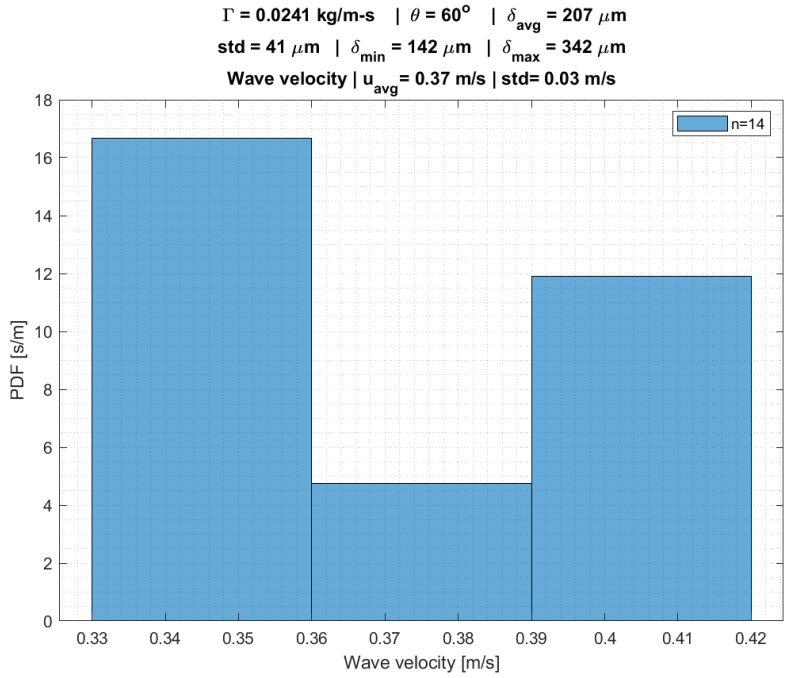

Wave velocity PDF for test condition No. 1.3

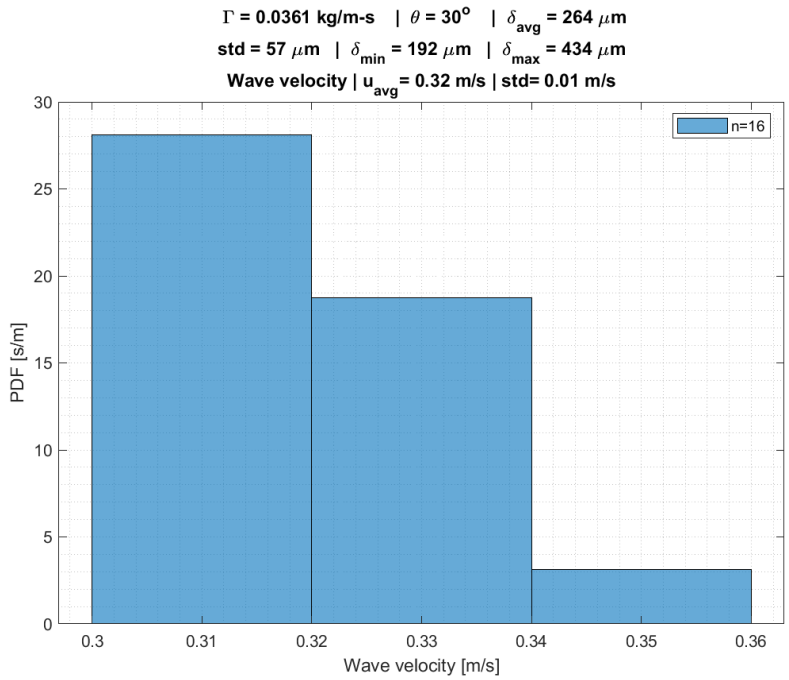

Wave velocity PDF for test condition No. 1.4

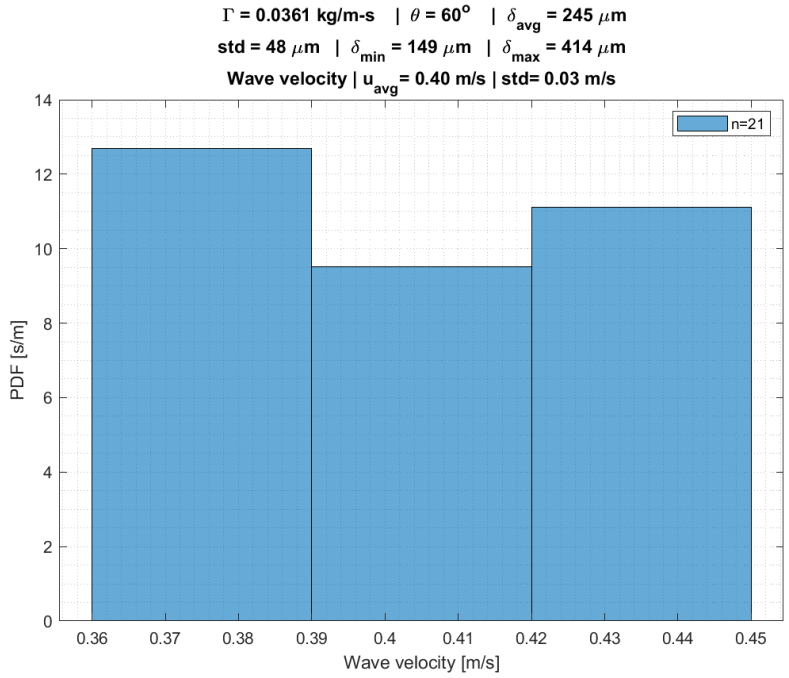

Wave velocity PDF for test condition No. 1.5

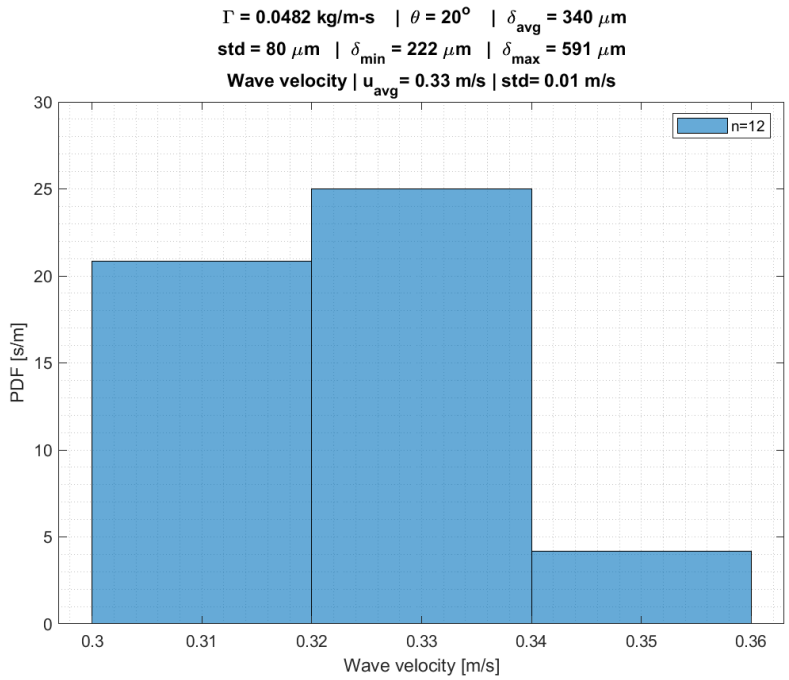

Wave velocity PDF for test condition No. 1.6

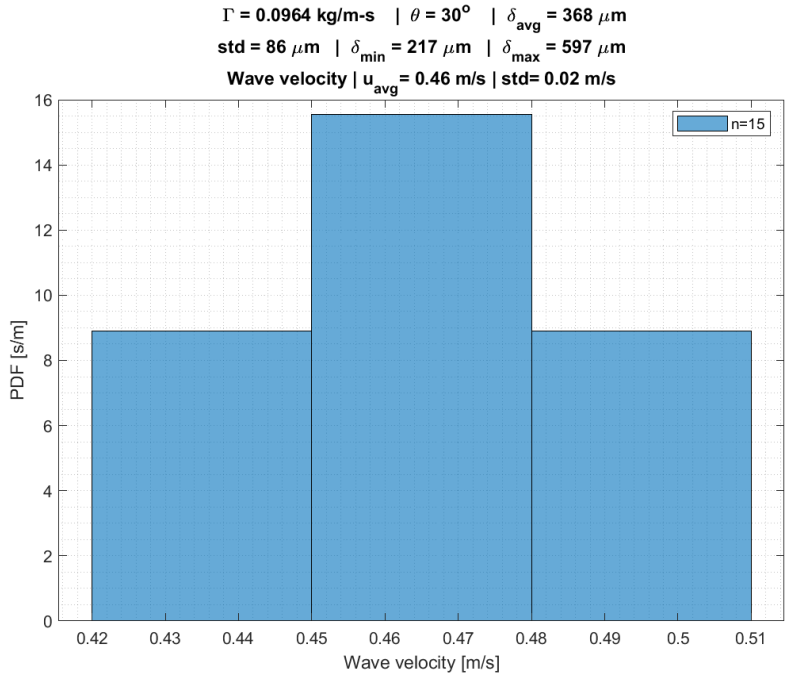

Wave velocity PDF for test condition No. 1.7

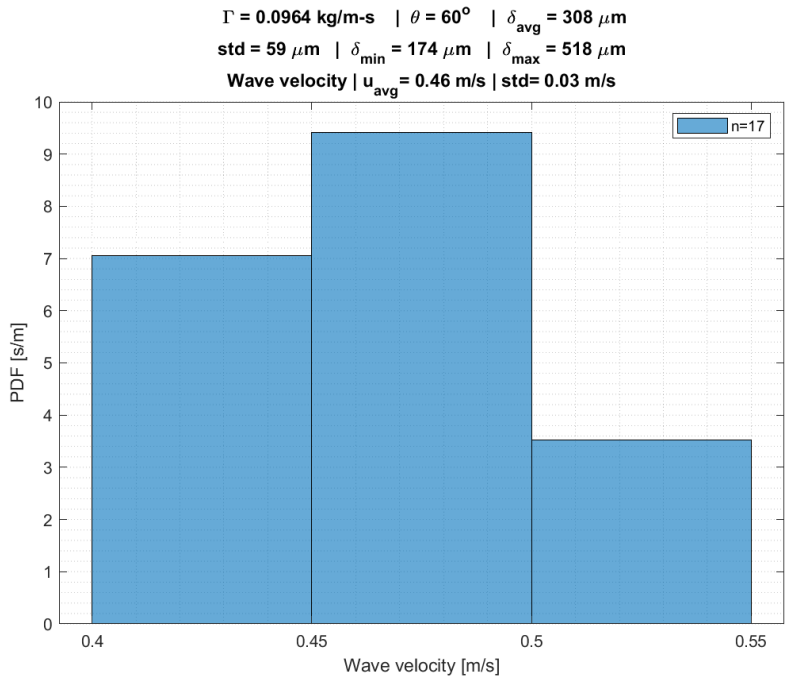

Wave velocity PDF for test condition No. 1.8

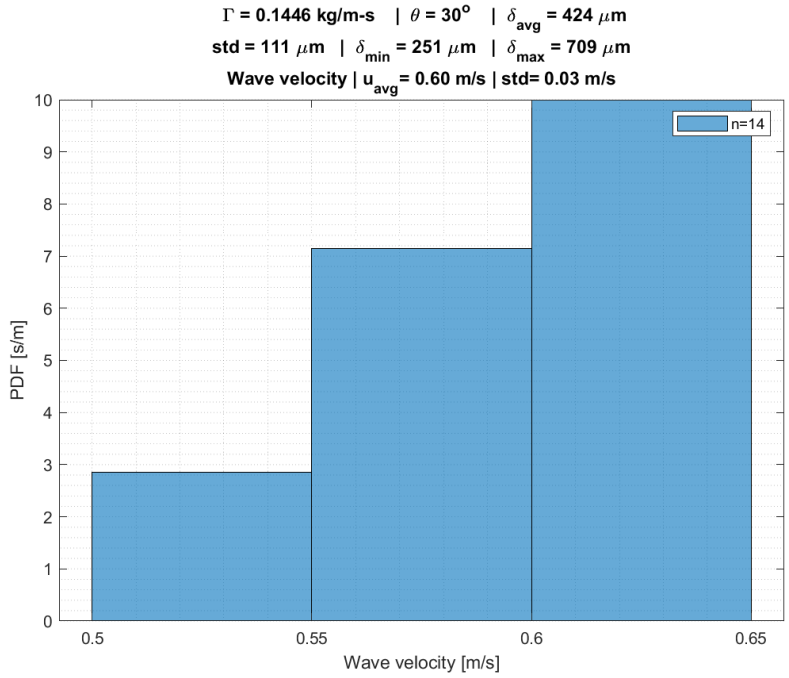

Wave velocity PDF for test condition No. 1.9

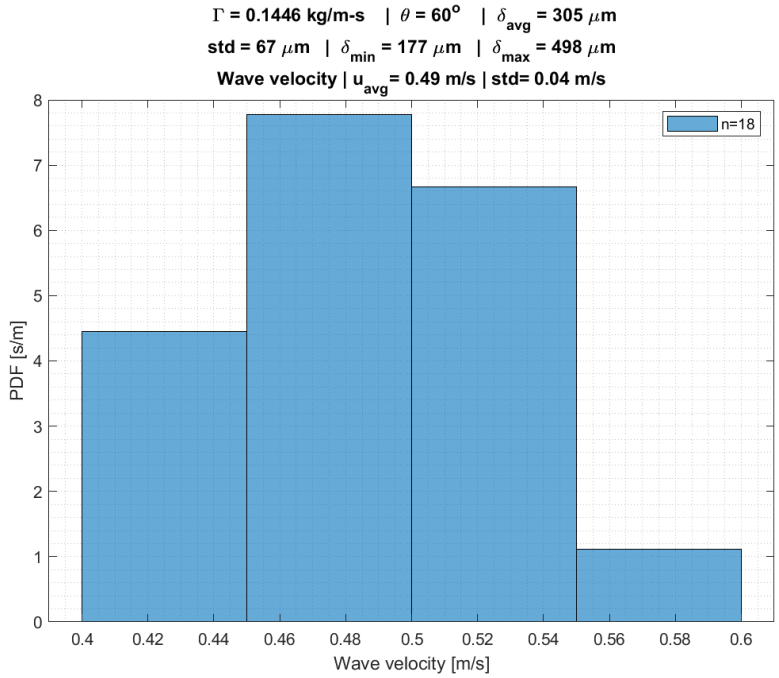

Wave velocity PDF for test condition No. 1.10

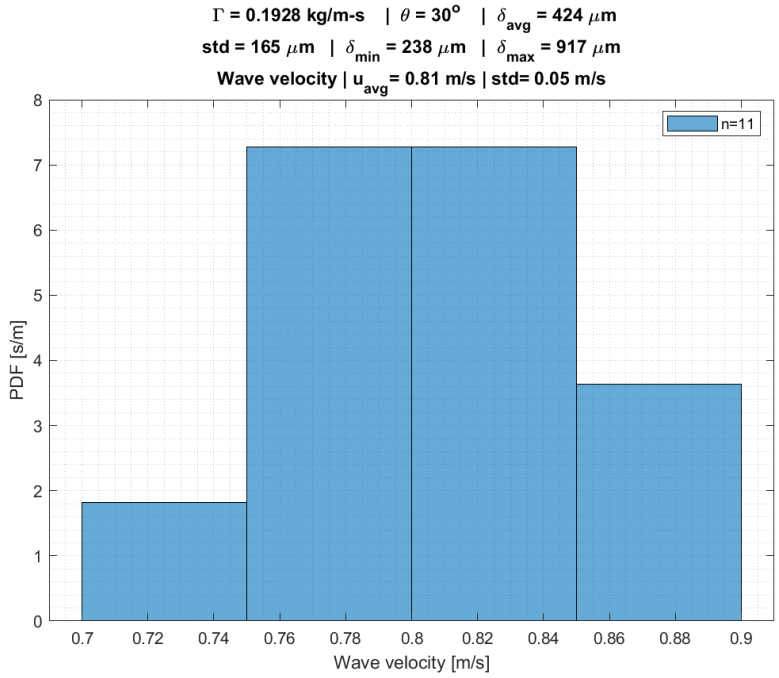

Wave velocity PDF for test condition No. 1.11

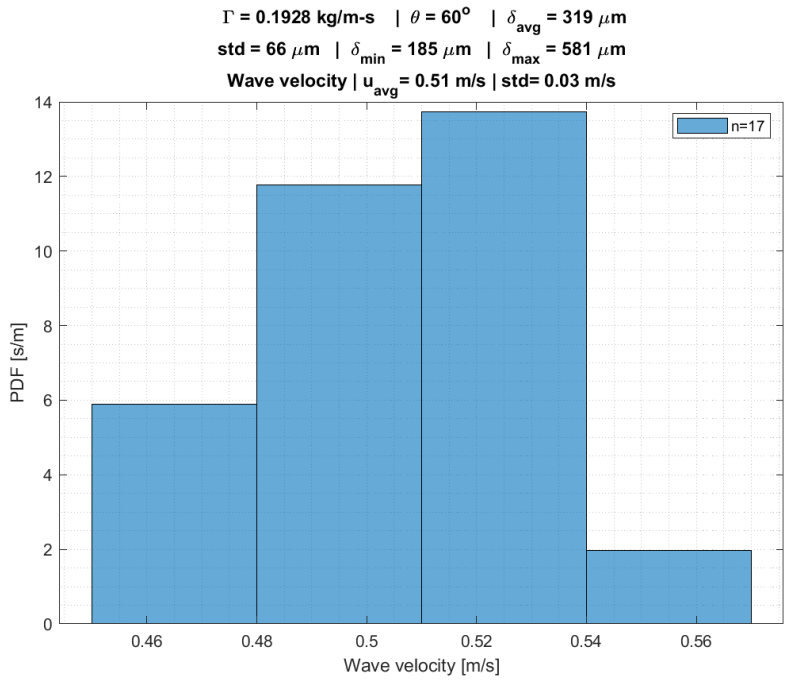

Wave velocity PDF for test condition No. 1.12

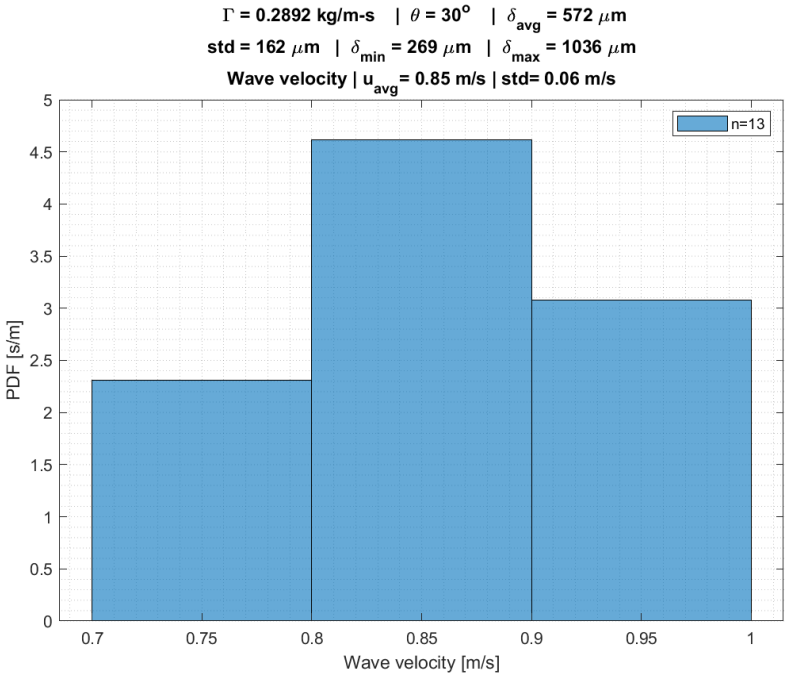

Wave velocity PDF for test condition No. 1.13

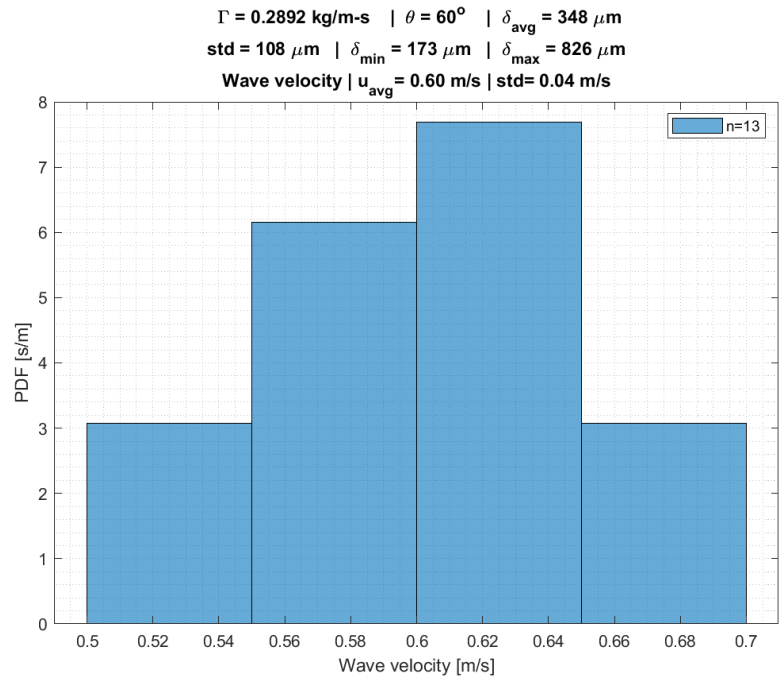

Wave velocity PDF for test condition No. 1.14

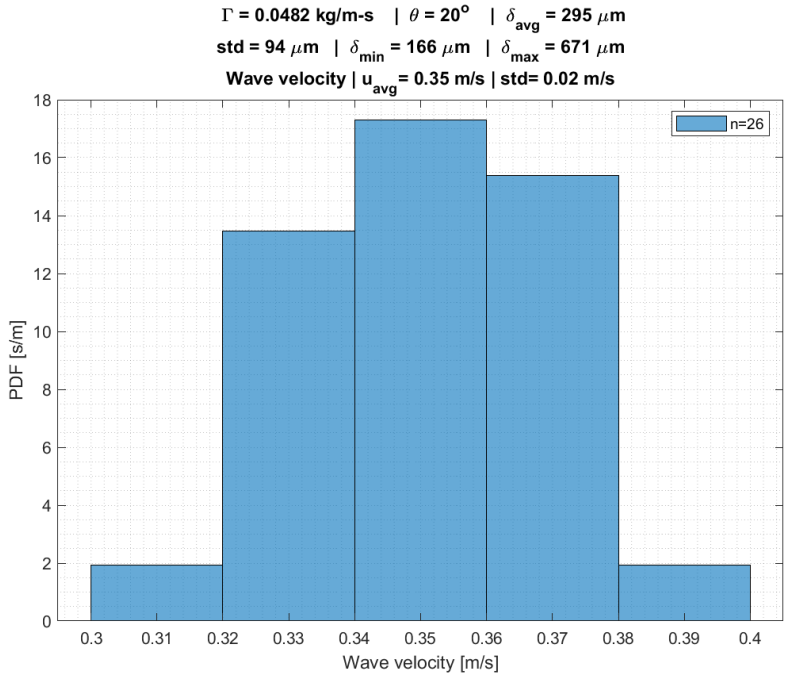

Wave velocity PDF for test condition No. 2.1

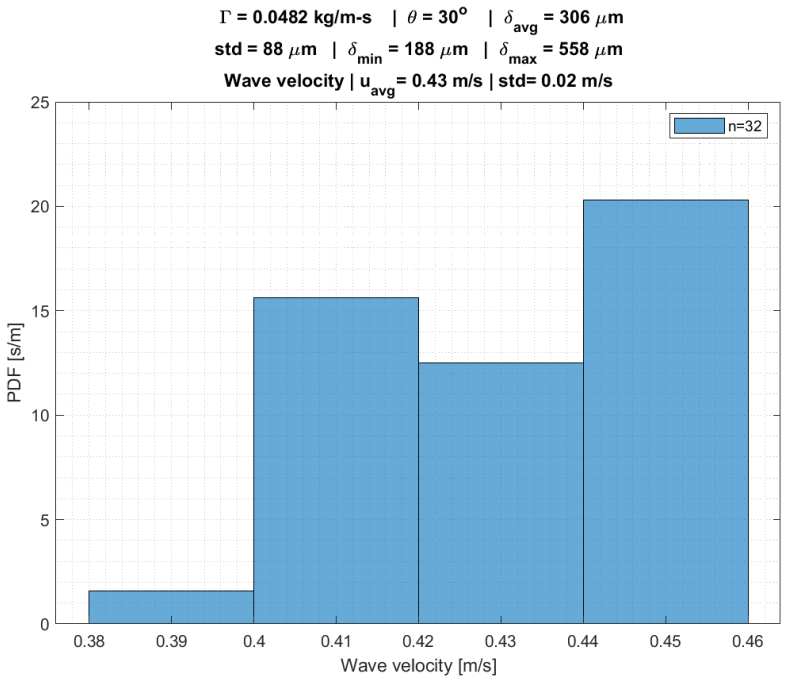

Wave velocity PDF for test condition No. 2.2

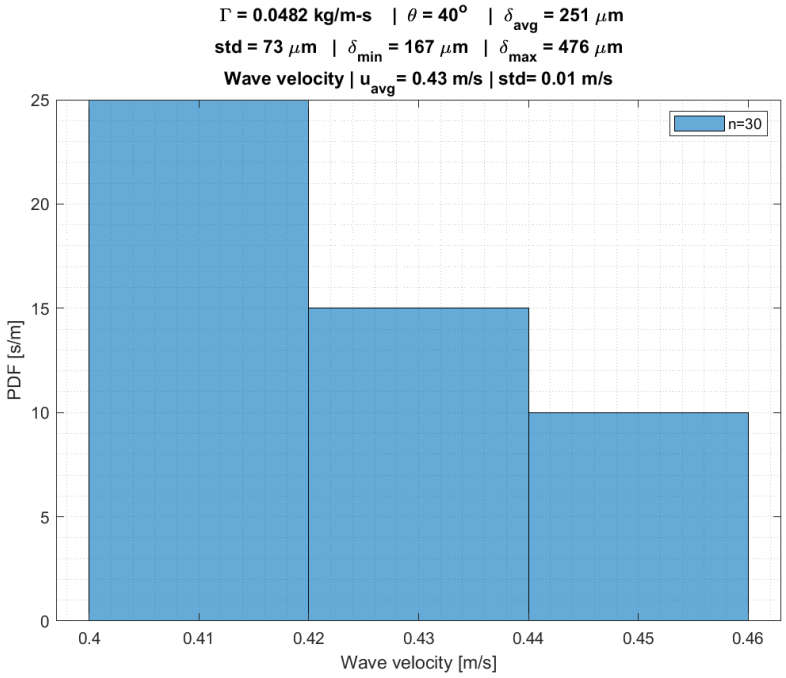

Wave velocity PDF for test condition No. 2.3

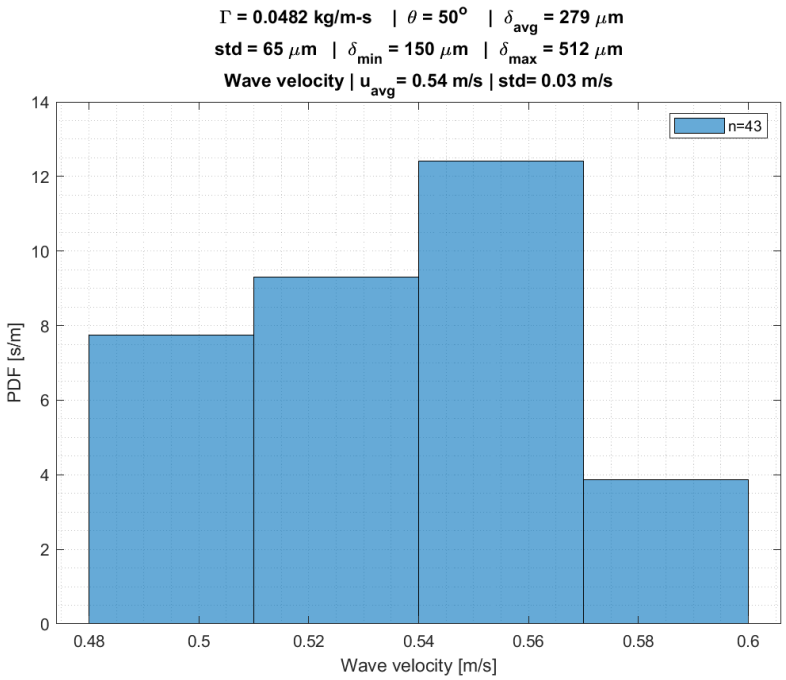

Wave velocity PDF for test condition No. 2.4

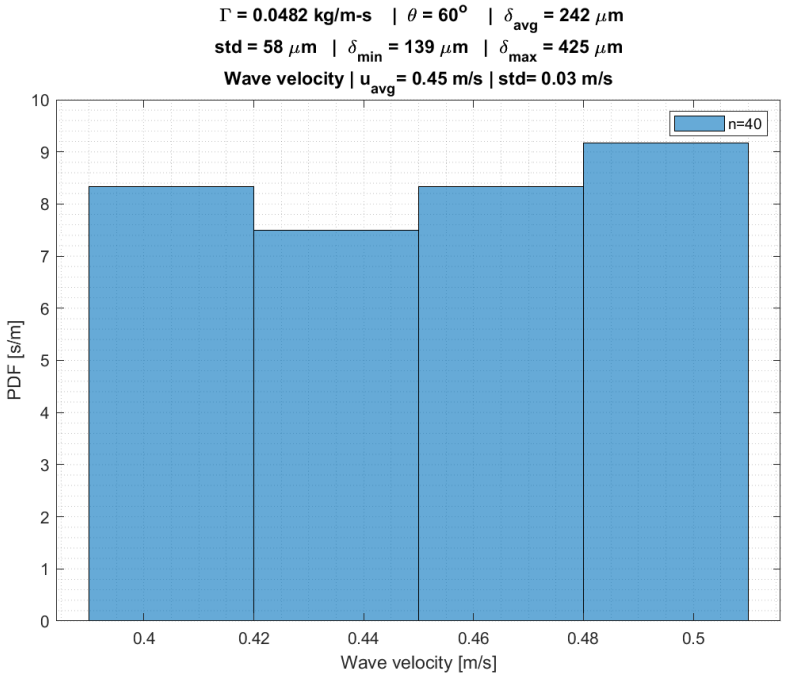

Wave velocity PDF for test condition No. 2.5

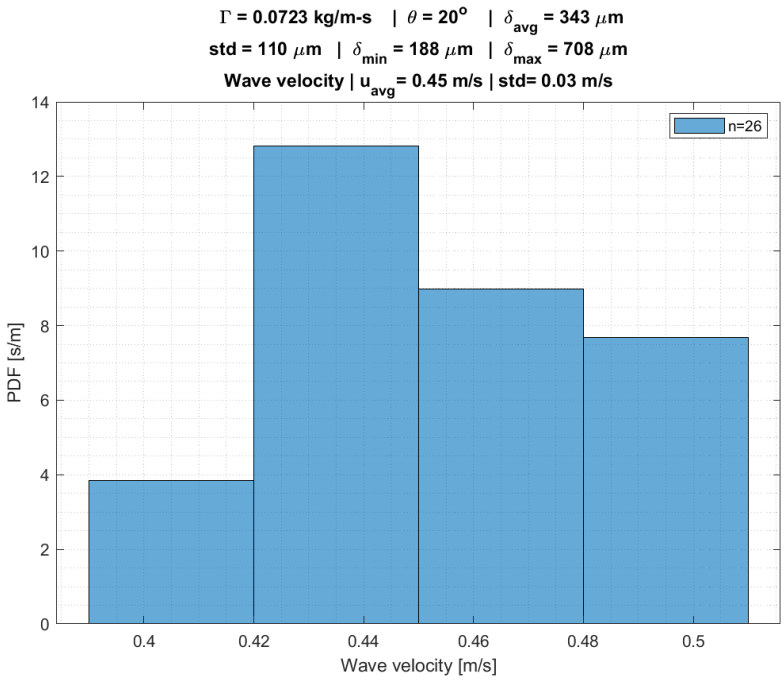

Wave velocity PDF for test condition No. 2.6

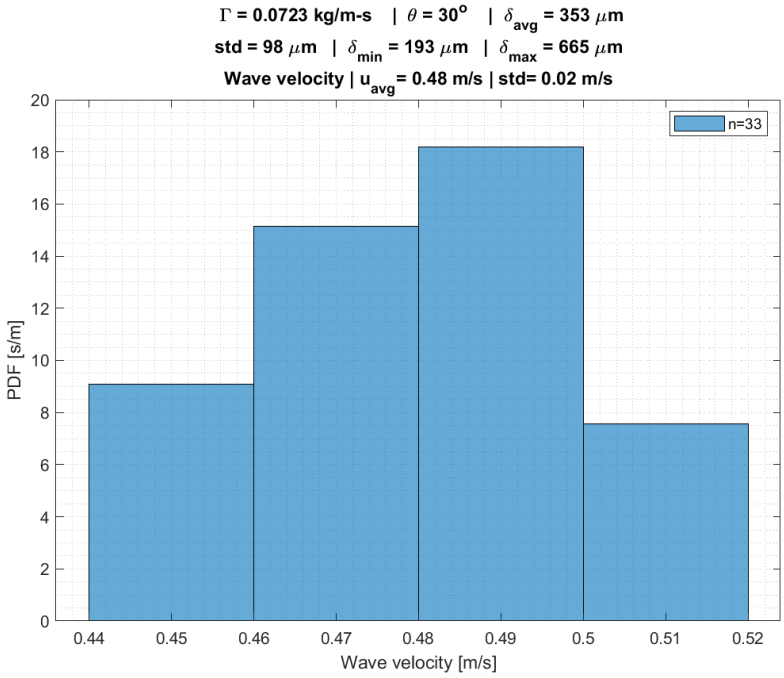

Wave velocity PDF for test condition No. 2.7

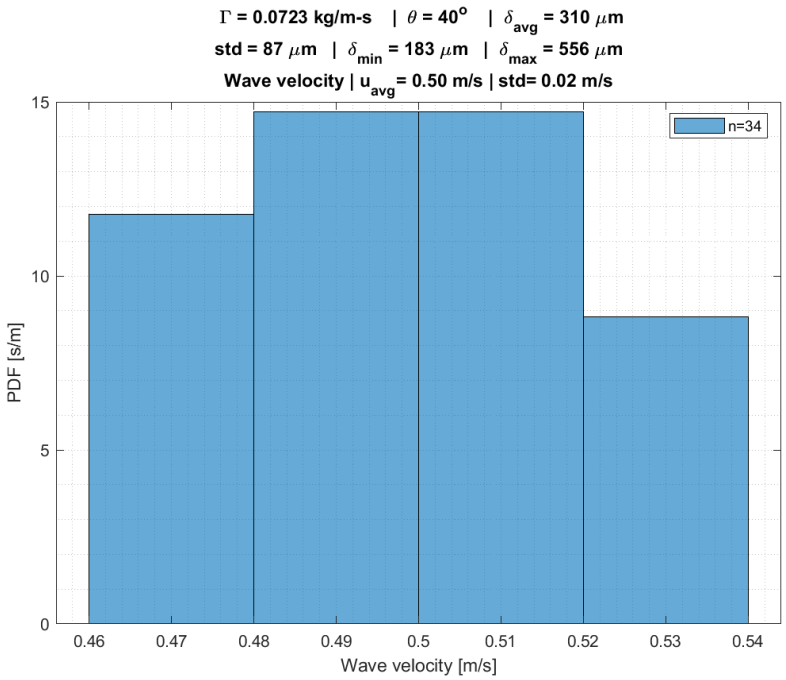

Wave velocity PDF for test condition No. 2.8

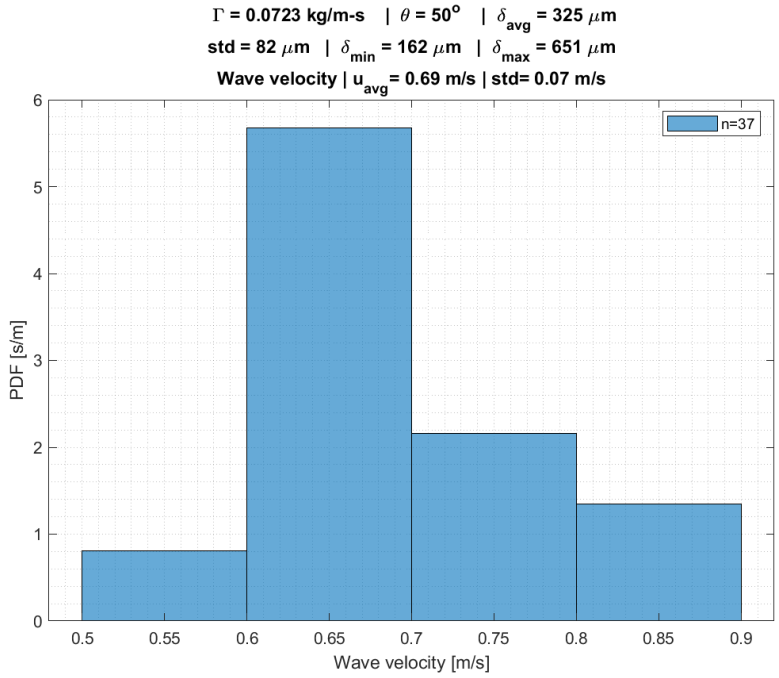

Wave velocity PDF for test condition No. 2.9

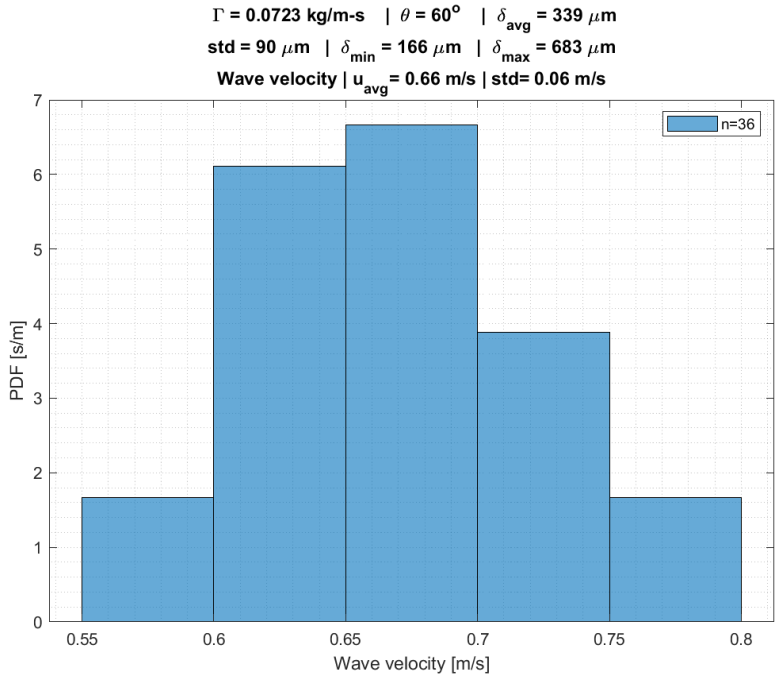

Wave velocity PDF for test condition No. 2.10

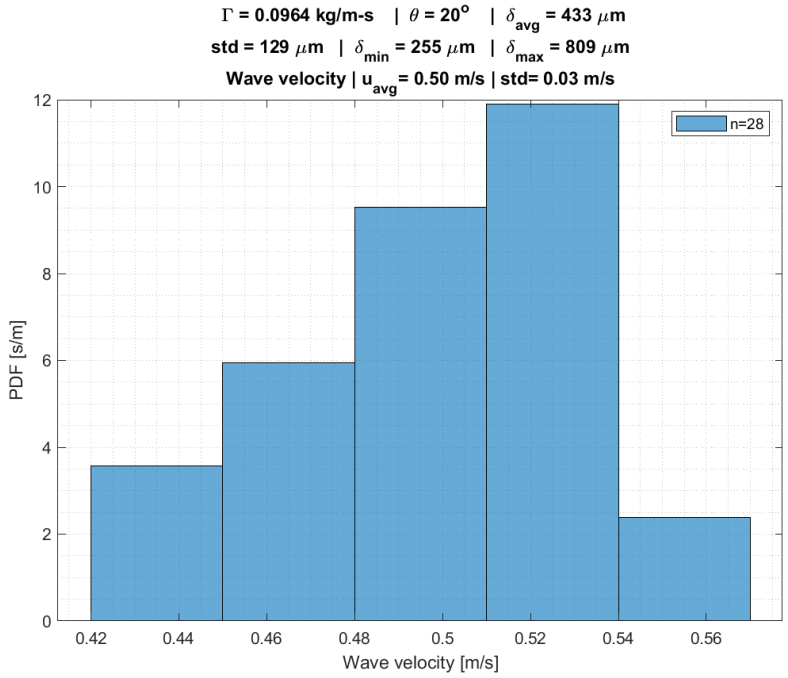

Wave velocity PDF for test condition No. 2.11

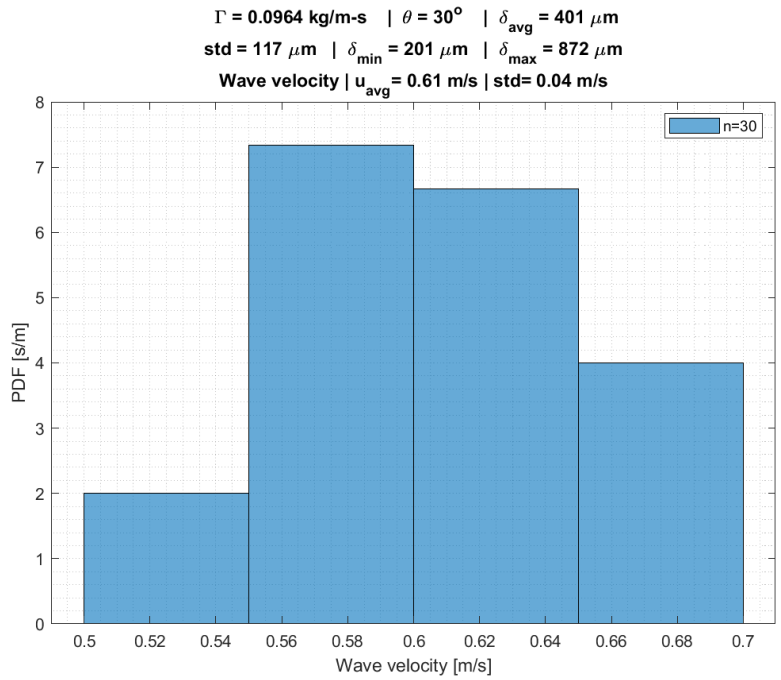

Wave velocity PDF for test condition No. 2.12

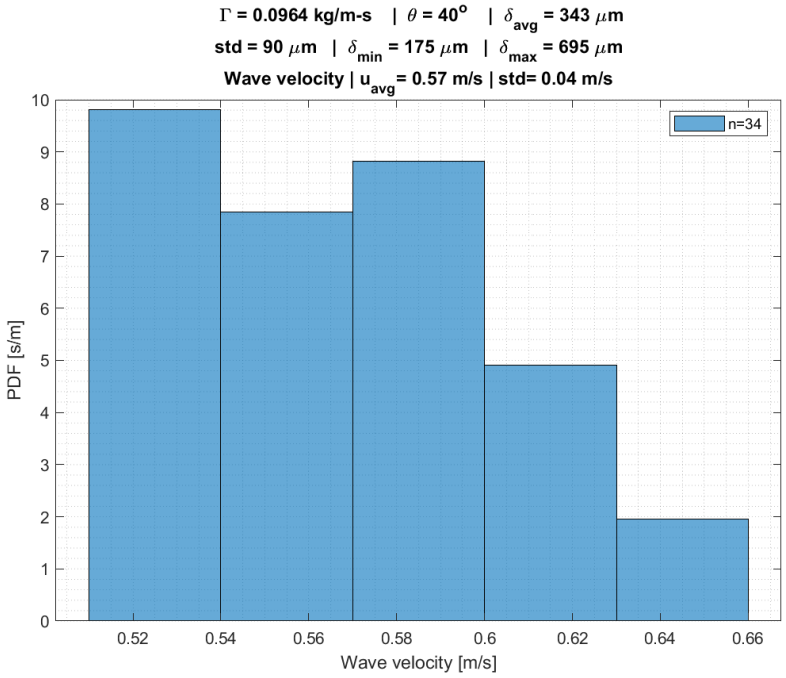

Wave velocity PDF for test condition No. 2.13

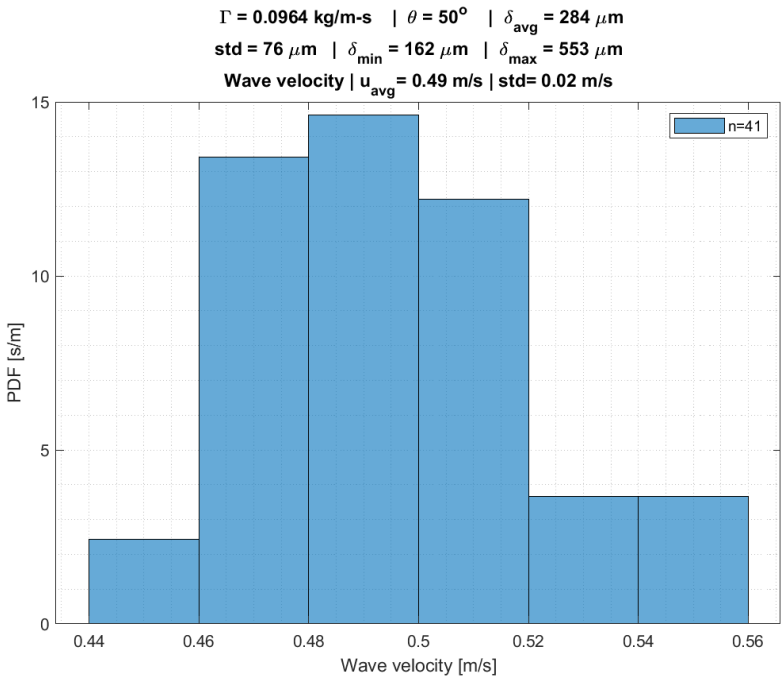

Wave velocity PDF for test condition No. 2.14

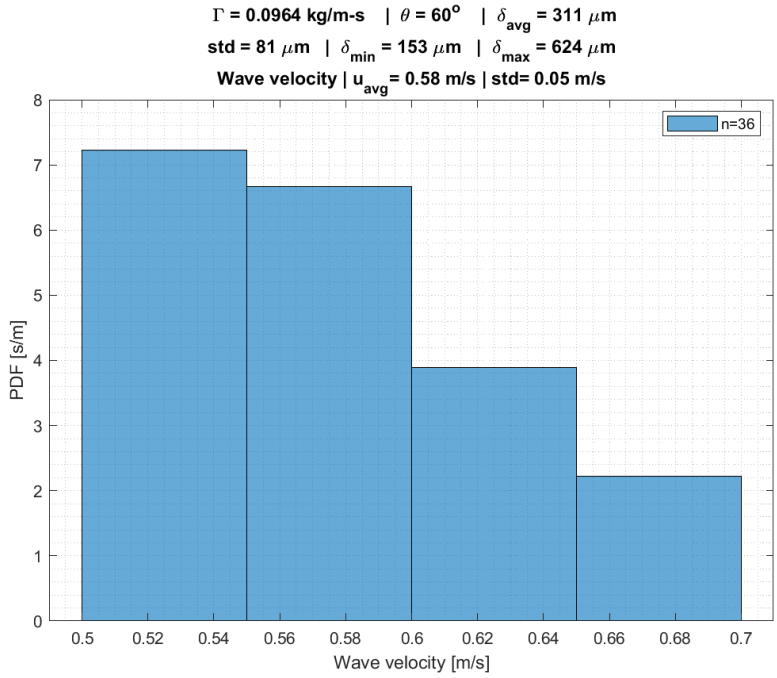

Wave velocity PDF for test condition No. 2.15

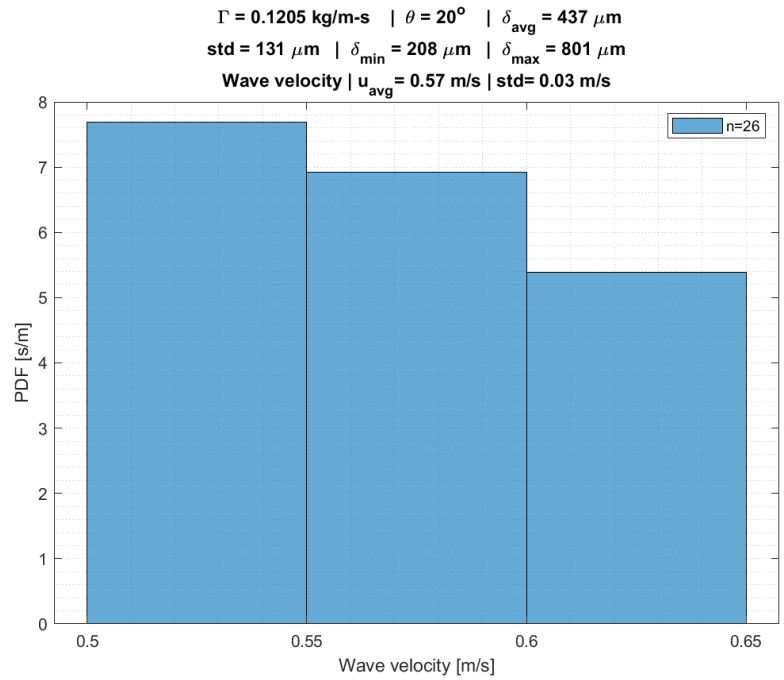

Wave velocity PDF for test condition No. 2.16

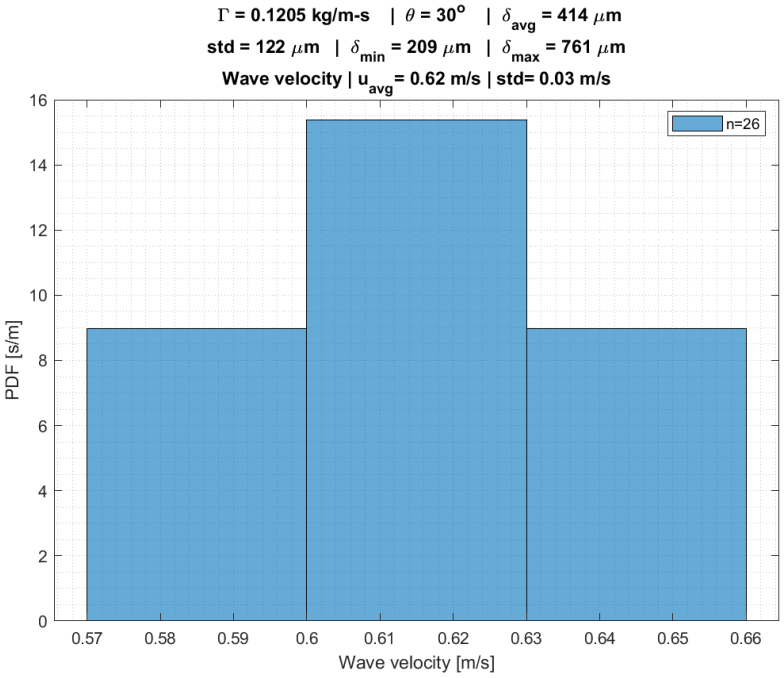

Wave velocity PDF for test condition No. 2.17

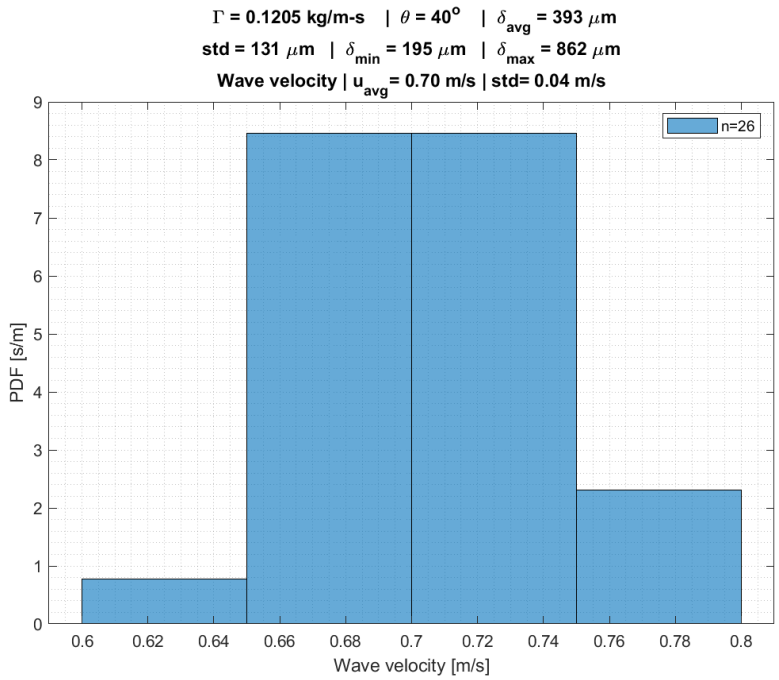

Wave velocity PDF for test condition No. 2.18

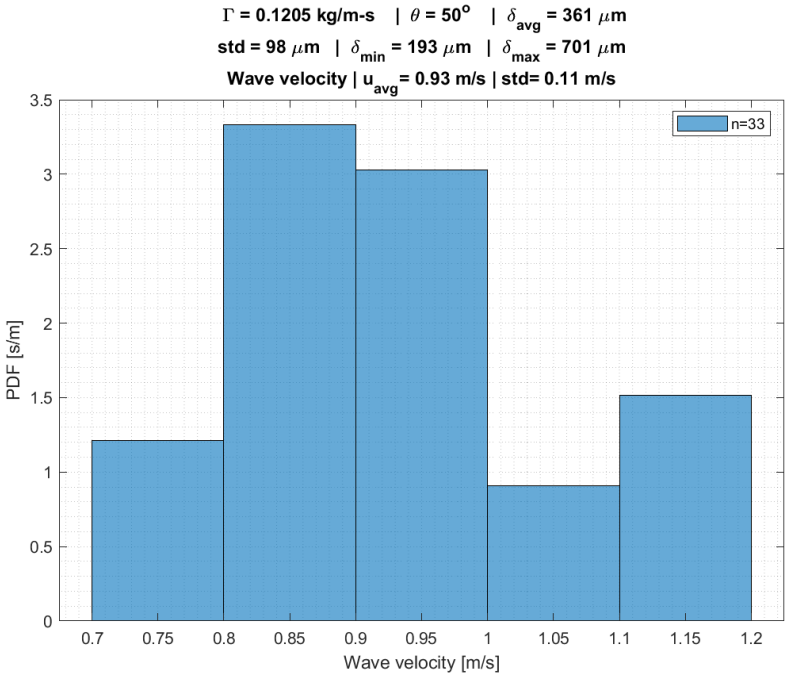

Wave velocity PDF for test condition No. 2.19

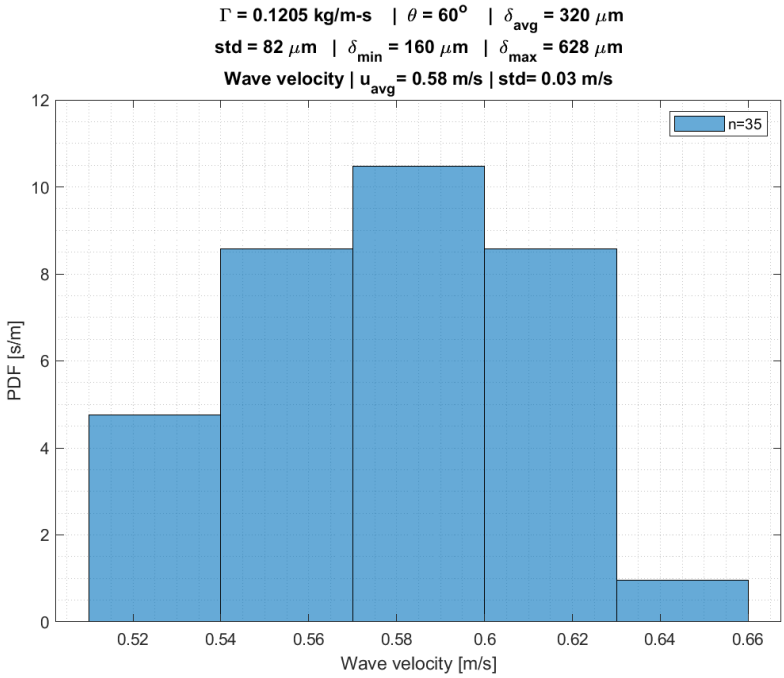

Wave velocity PDF for test condition No. 2.20

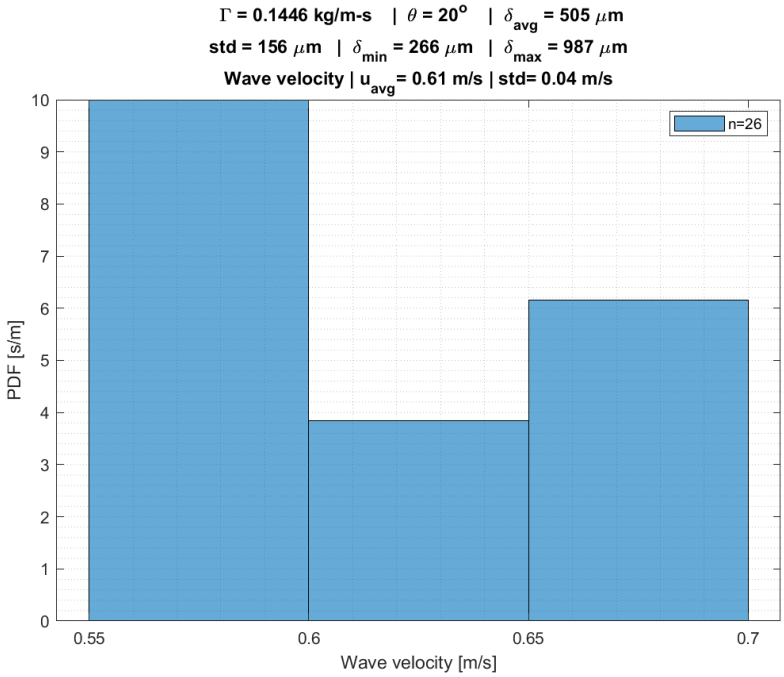

Wave velocity PDF for test condition No. 2.21

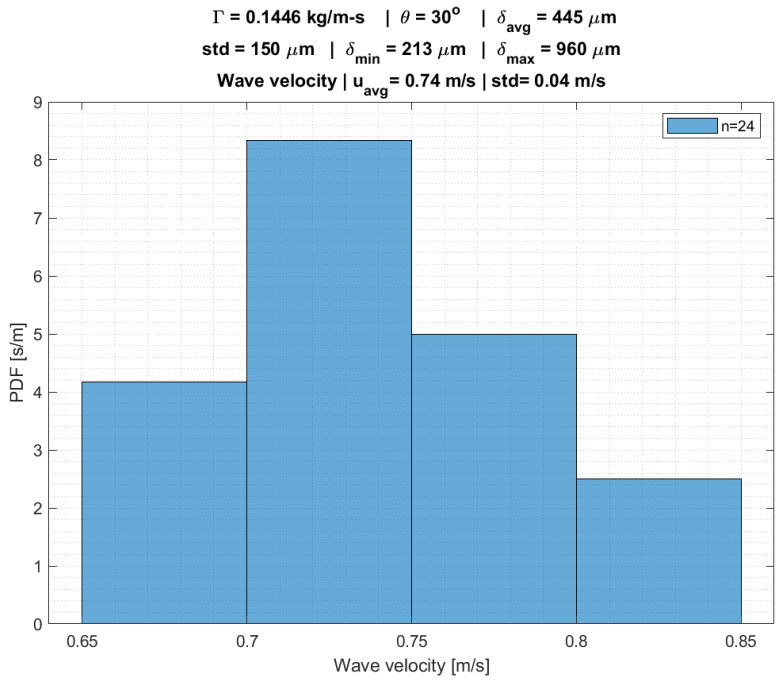

Wave velocity PDF for test condition No. 2.22

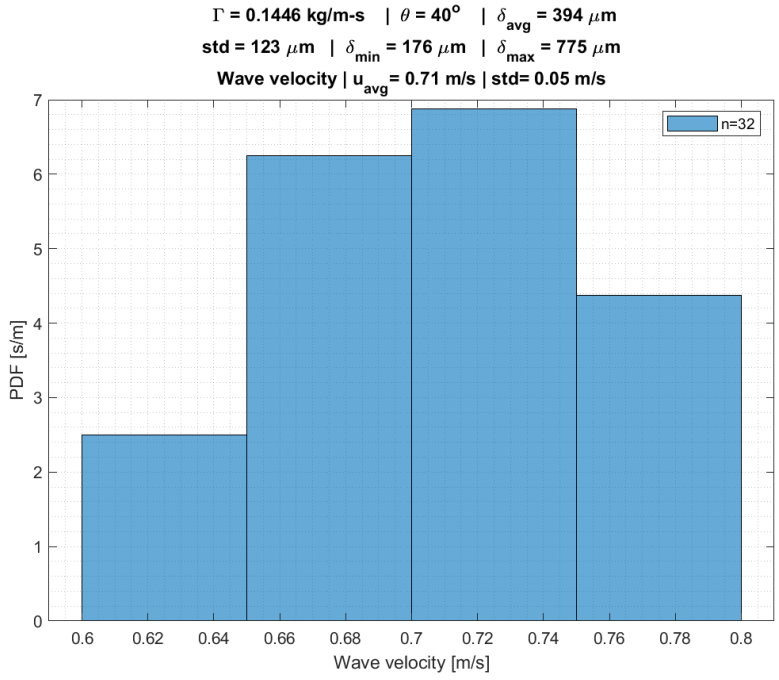

Wave velocity PDF for test condition No. 2.23

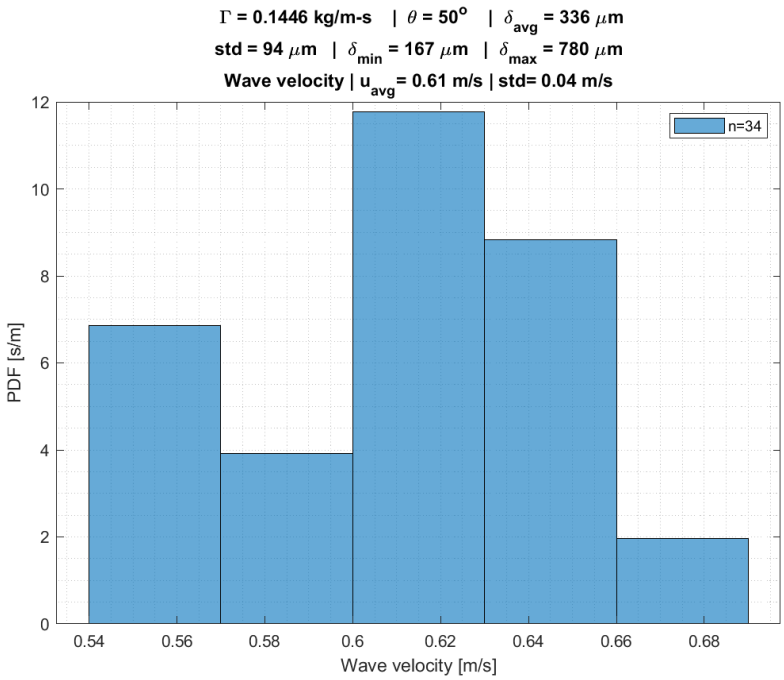

Wave velocity PDF for test condition No. 2.24

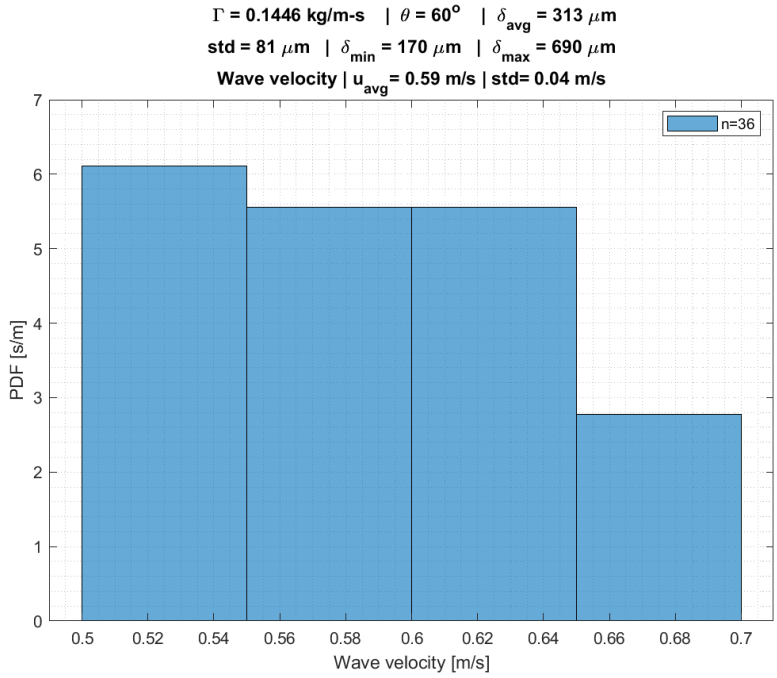

Wave velocity PDF for test condition No. 2.25

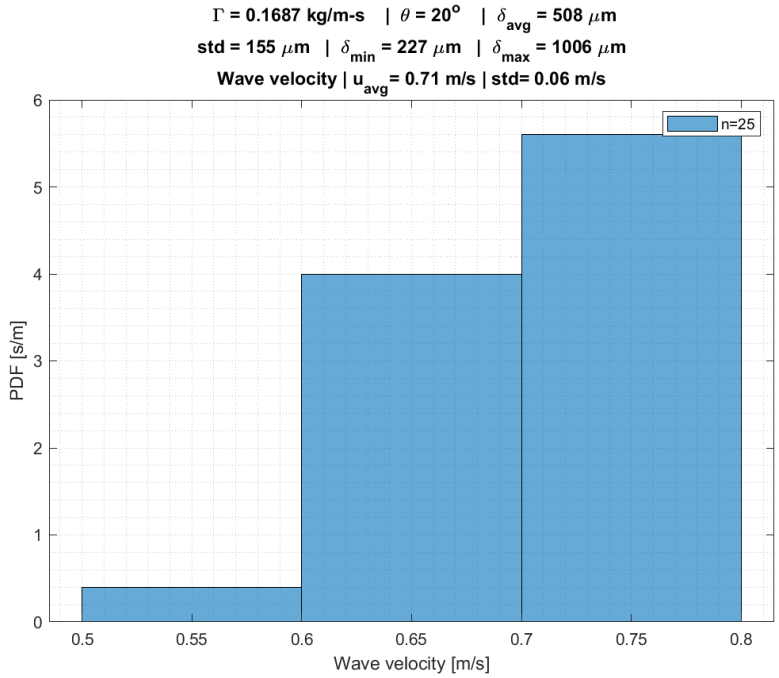

Wave velocity PDF for test condition No. 2.26

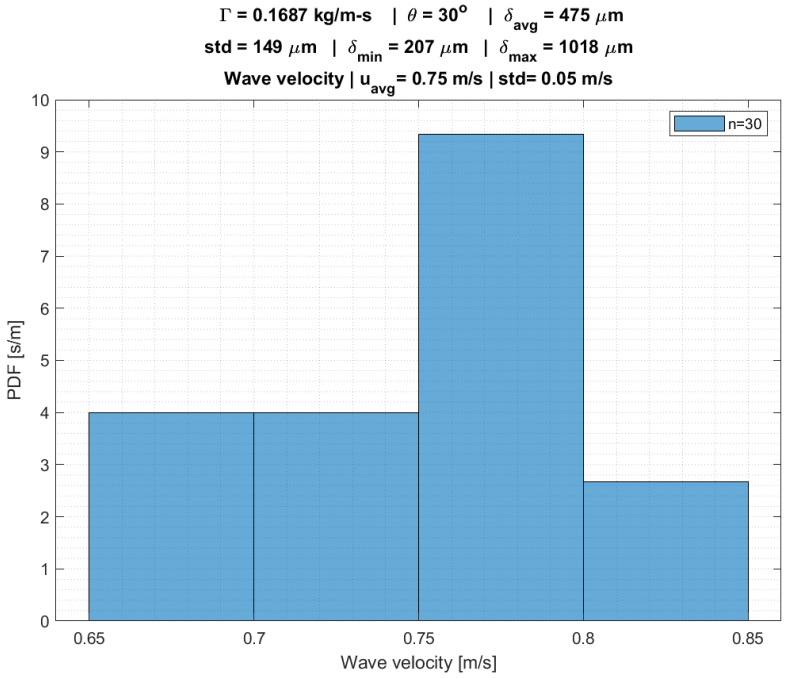

Wave velocity PDF for test condition No. 2.27

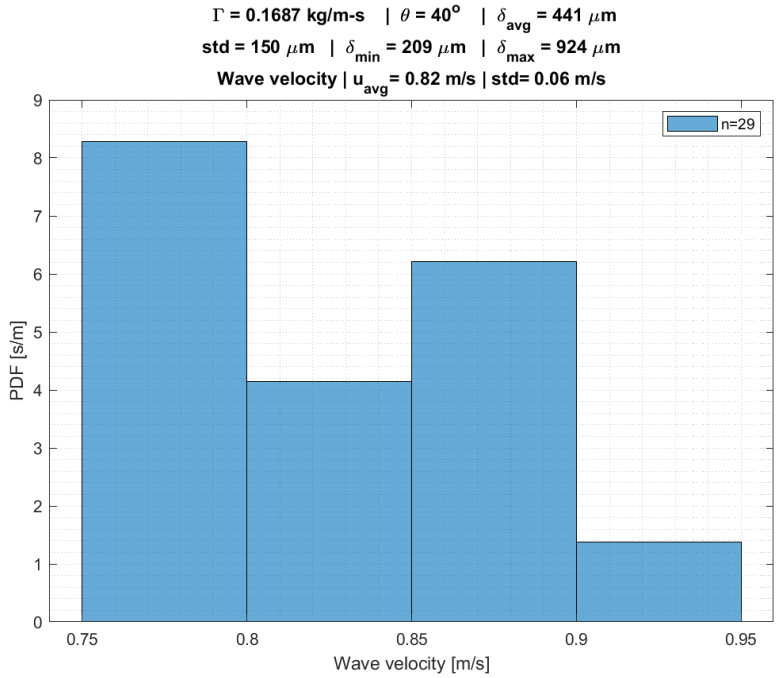

Wave velocity PDF for test condition No. 2.28

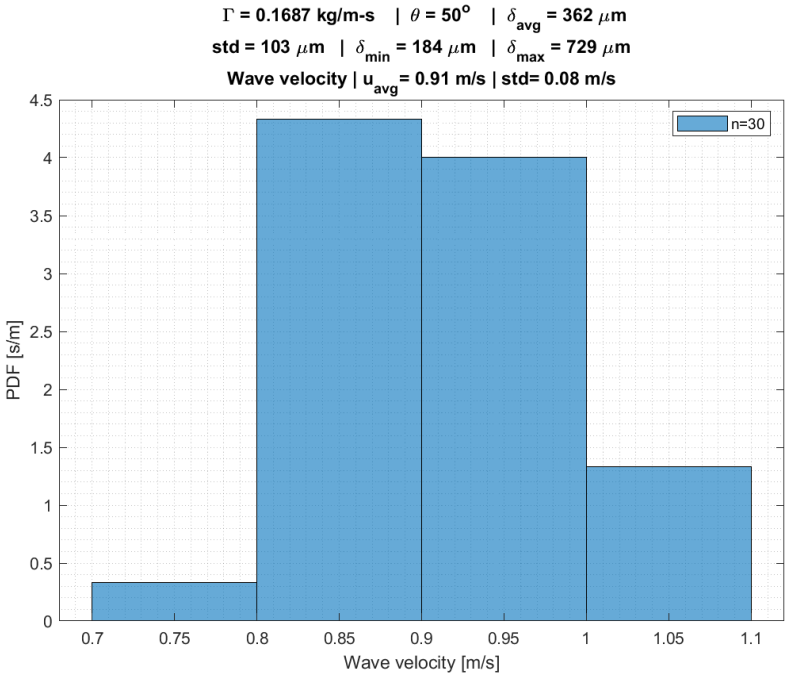

Wave velocity PDF for test condition No. 2.29

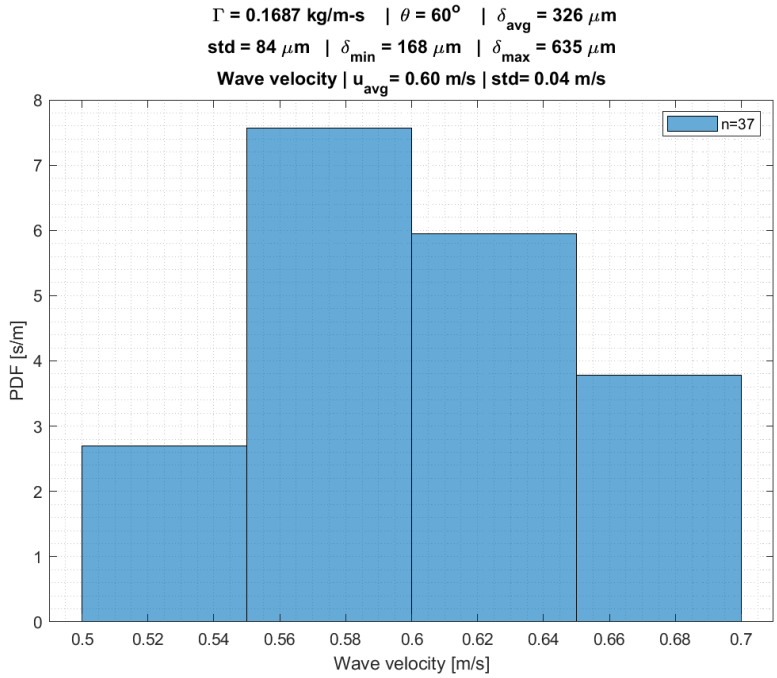

Wave velocity PDF for test condition No. 2.30

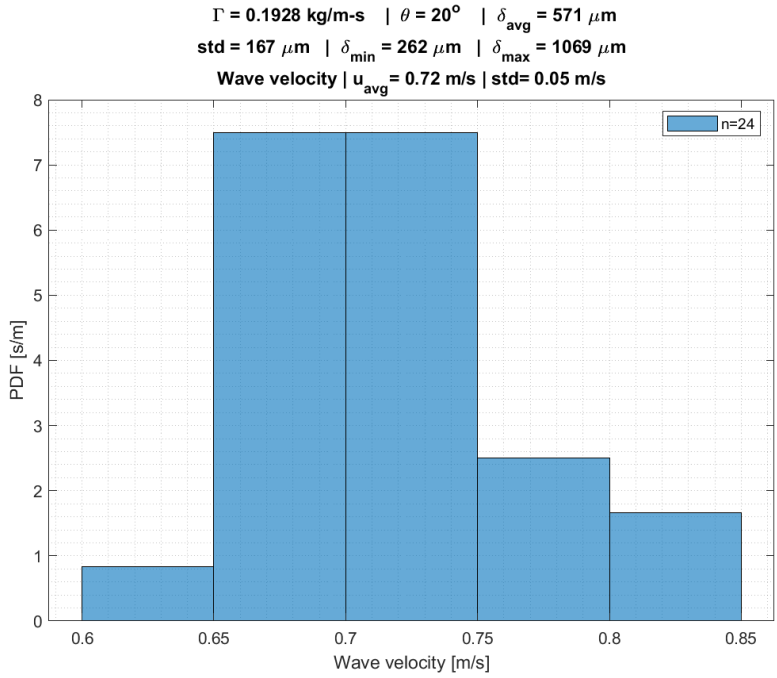

Wave velocity PDF for test condition No. 2.31

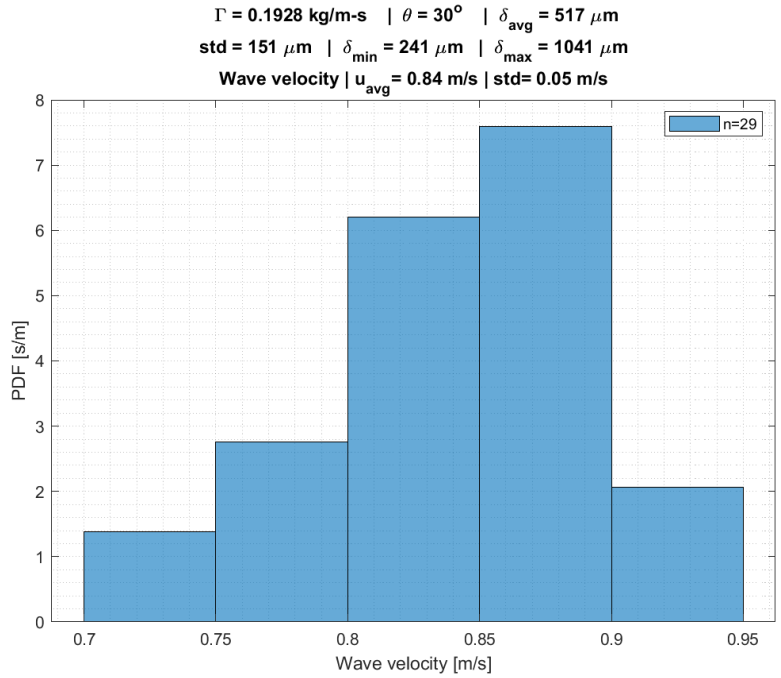

Wave velocity PDF for test condition No. 2.32

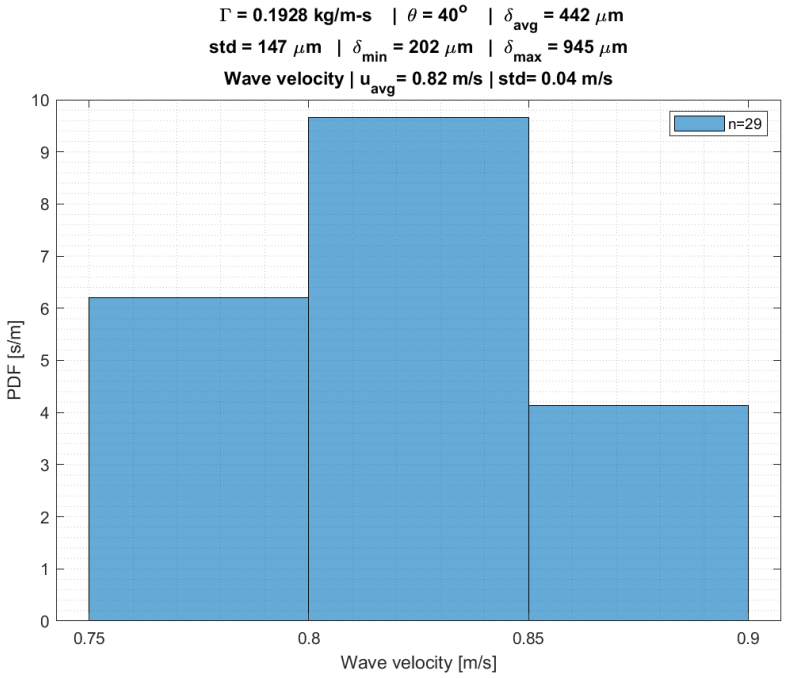

Wave velocity PDF for test condition No. 2.33

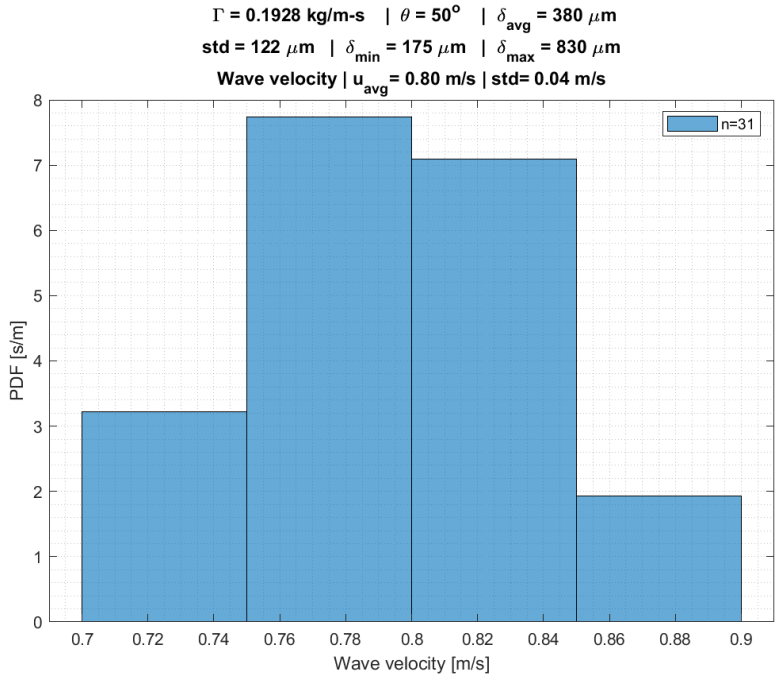

Wave velocity PDF for test condition No. 2.34

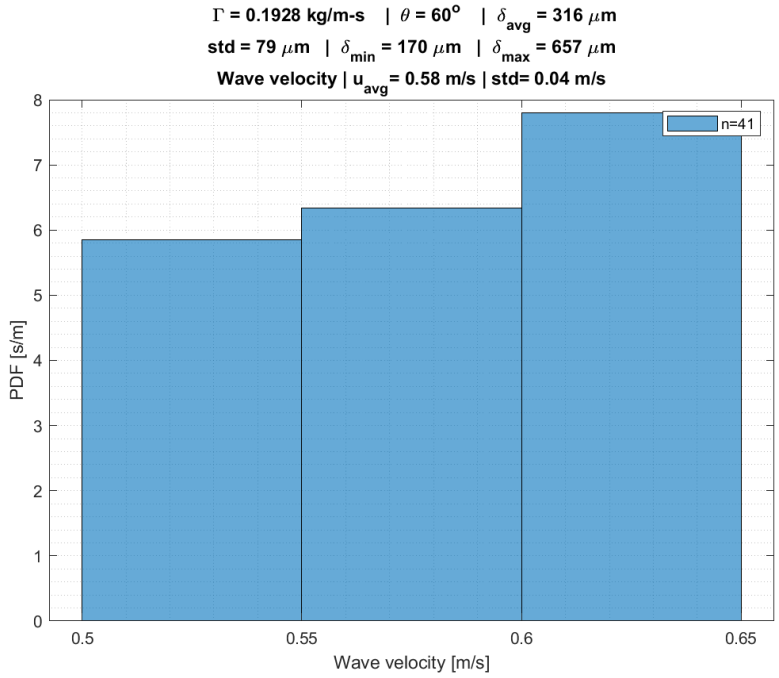

Wave velocity PDF for test condition No. 2.35

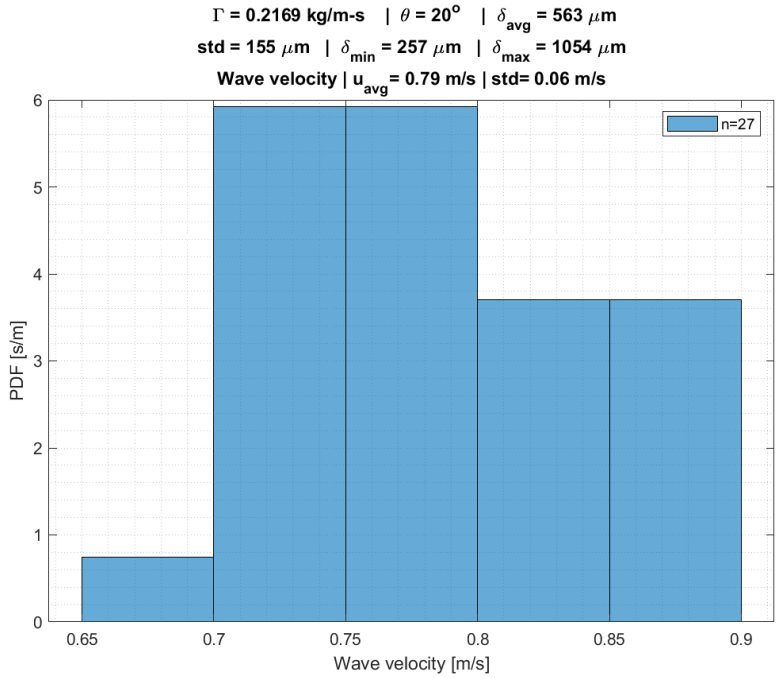

Wave velocity PDF for test condition No. 2.36

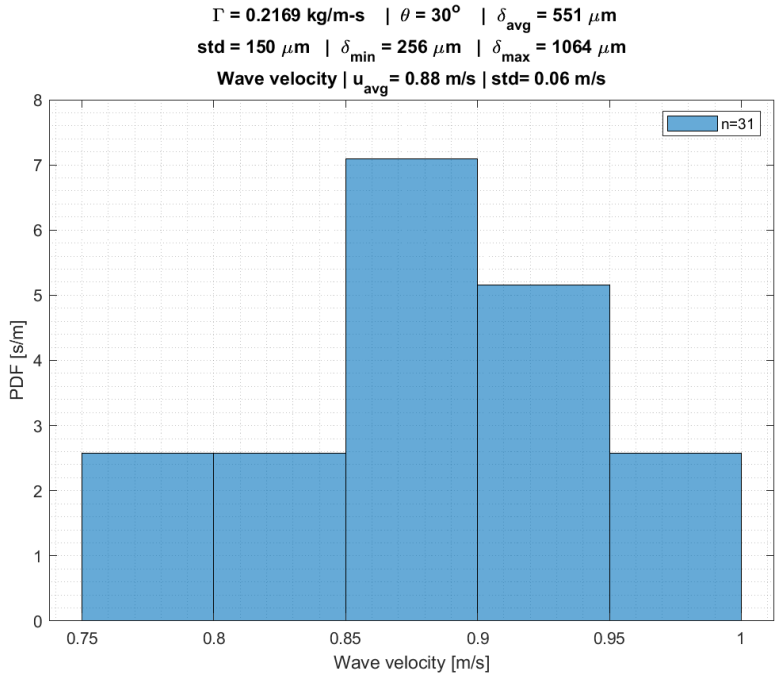

Wave velocity PDF for test condition No. 2.37

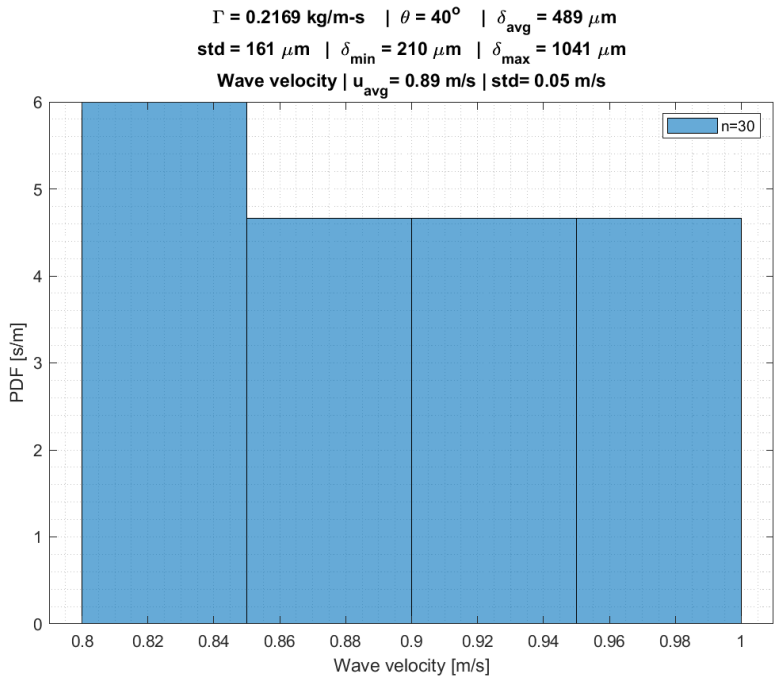

Wave velocity PDF for test condition No. 2.38

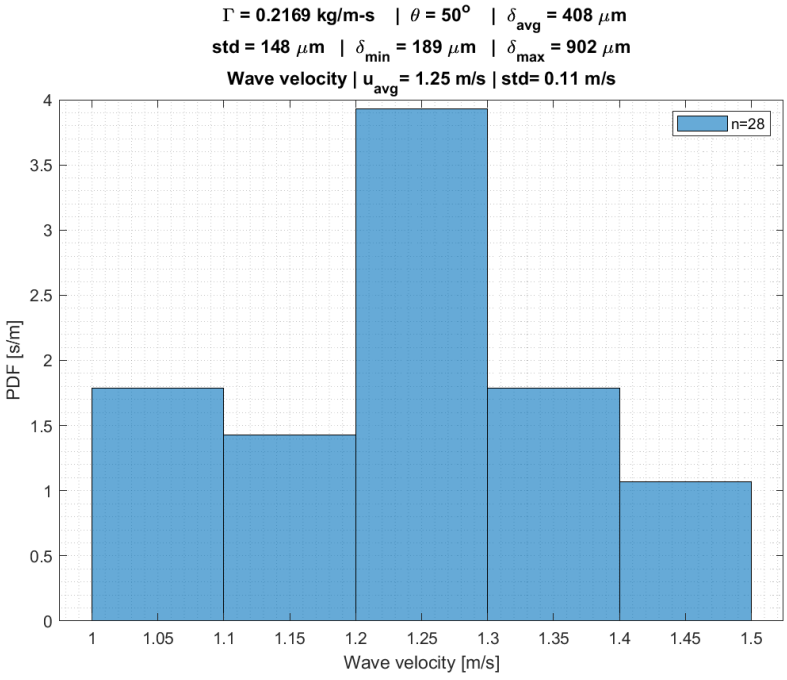

Wave velocity PDF for test condition No. 2.39

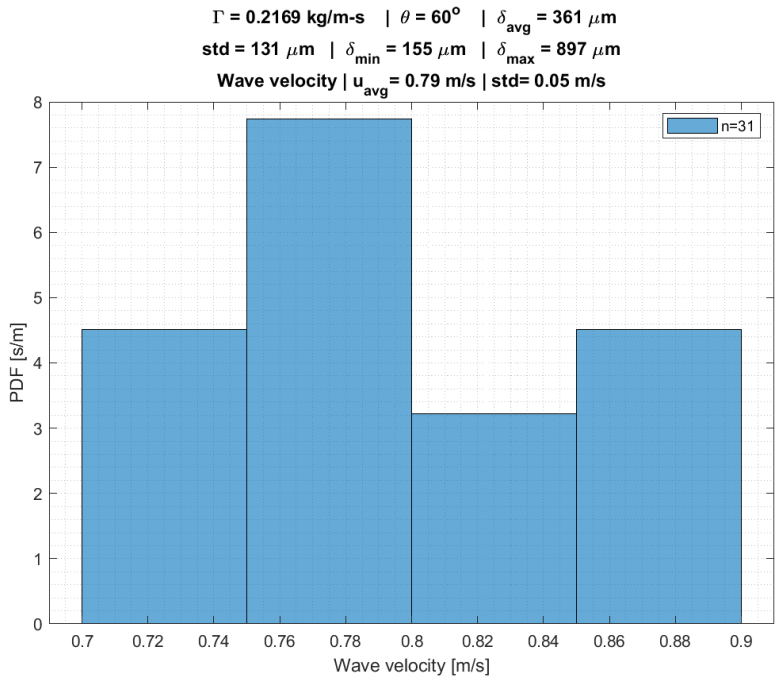

Wave velocity PDF for test condition No. 2.40

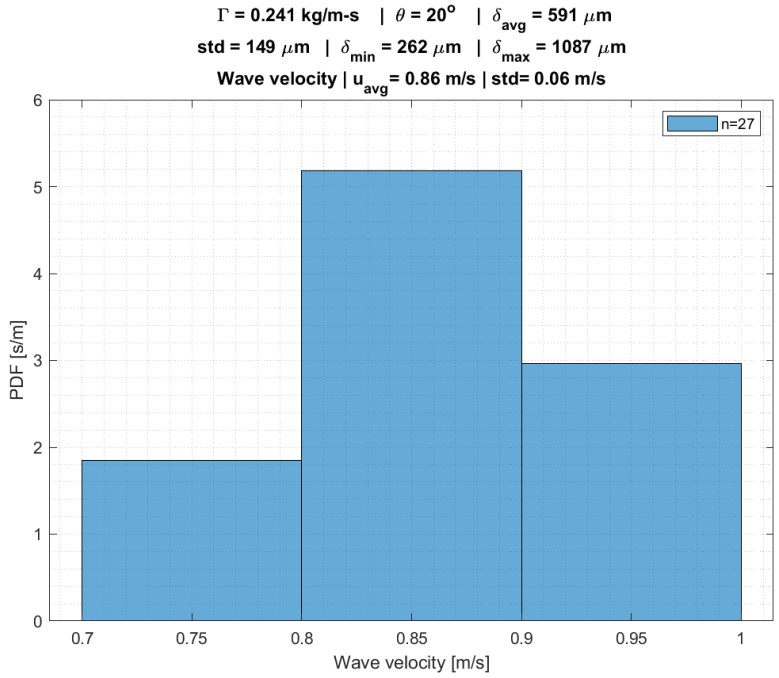

Wave velocity PDF for test condition No. 2.41

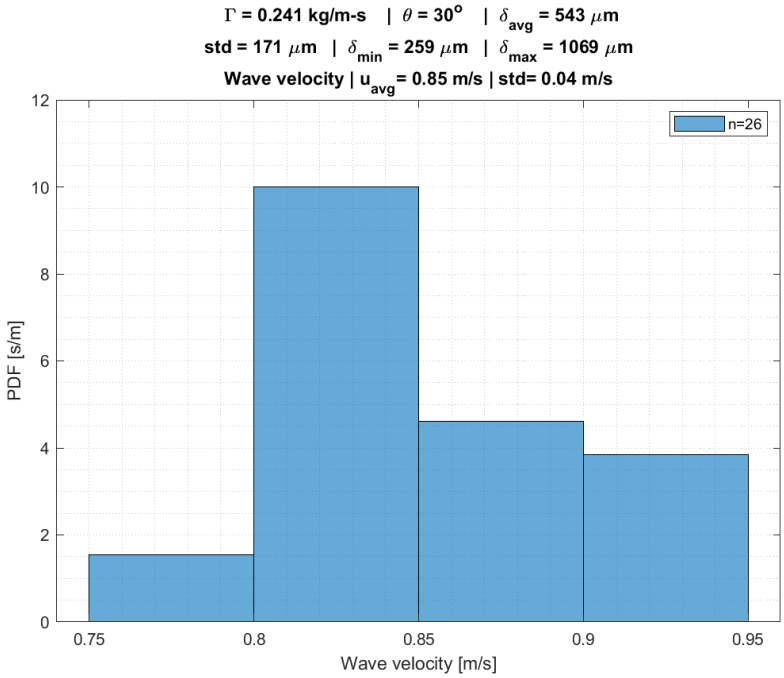

Wave velocity PDF for test condition No. 2.42

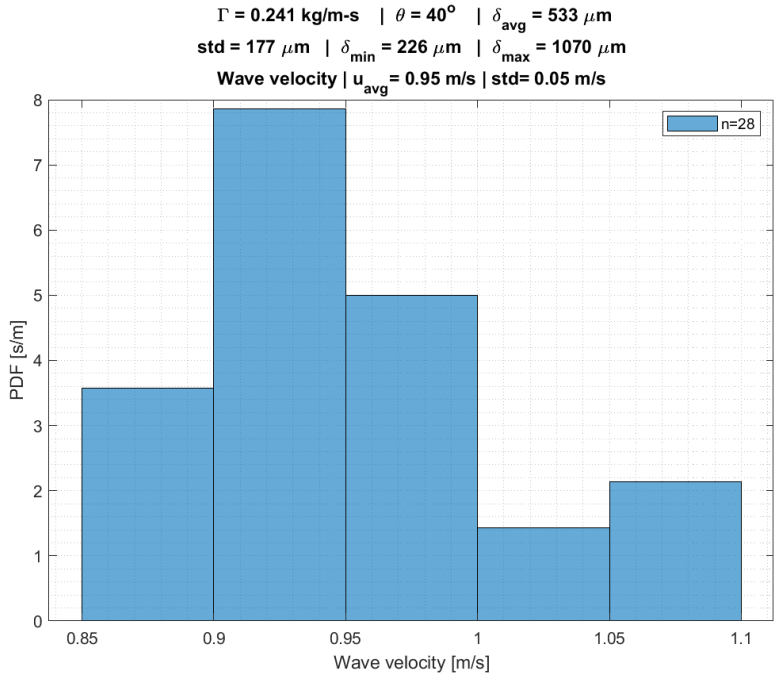

Wave velocity PDF for test condition No. 2.43

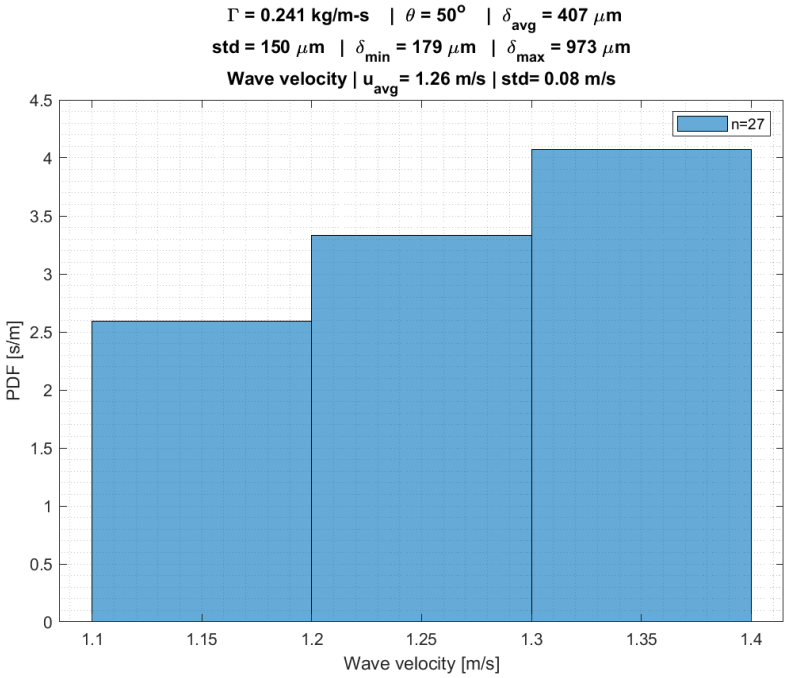

Wave velocity PDF for test condition No. 2.44

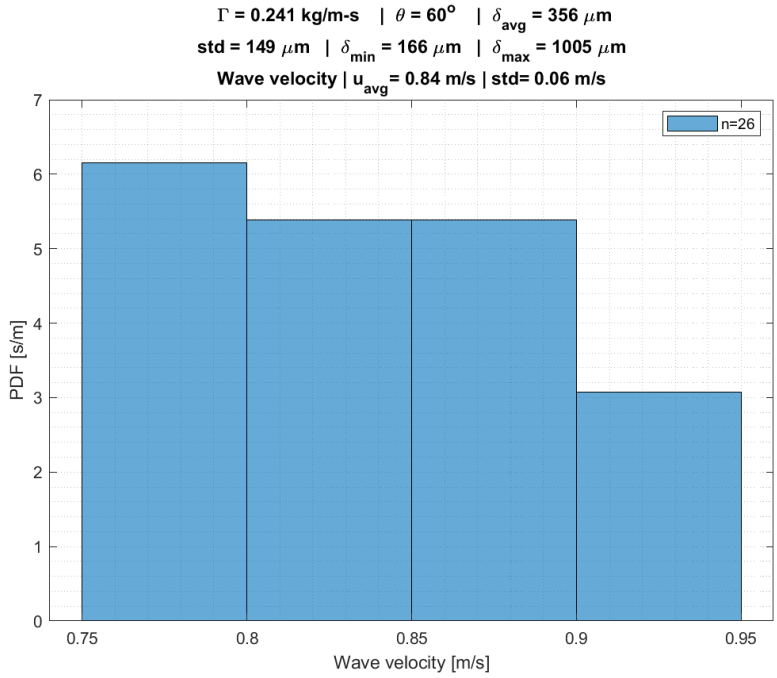

Wave velocity PDF for test condition No. 2.45

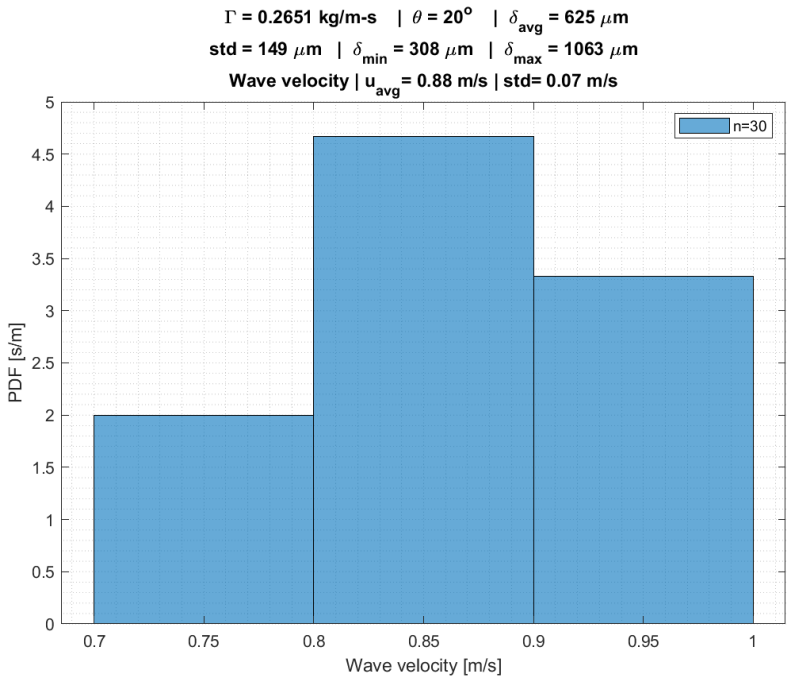

Wave velocity PDF for test condition No. 2.46

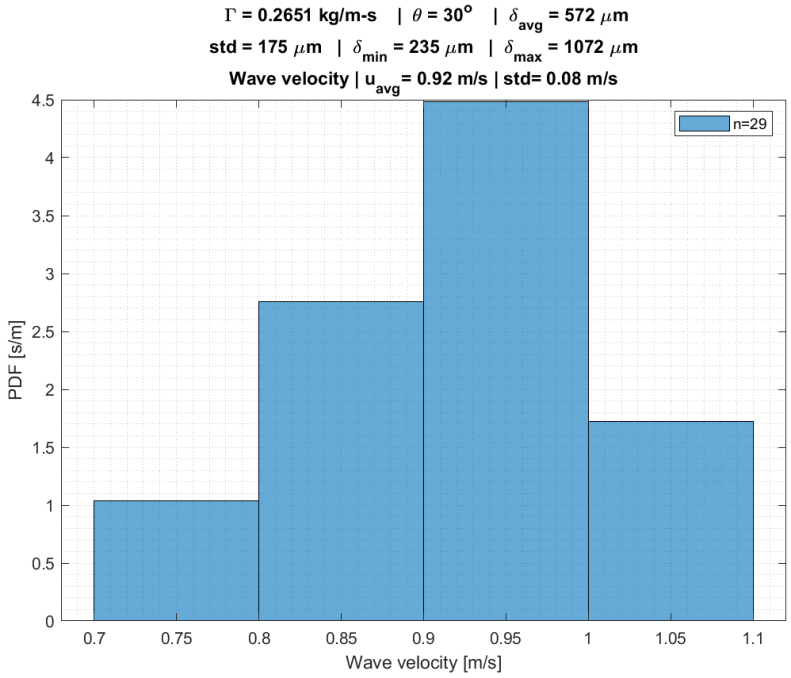

Wave velocity PDF for test condition No. 2.47

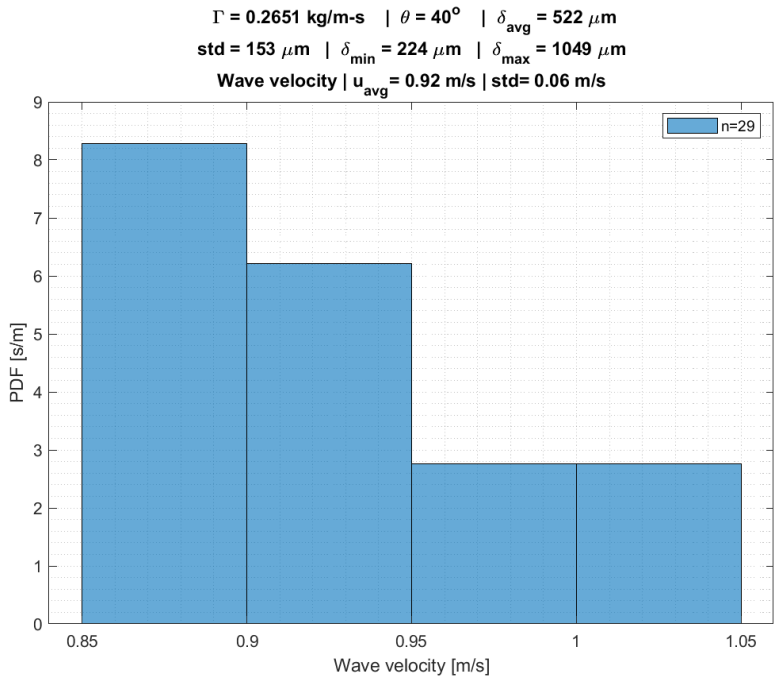

Wave velocity PDF for test condition No. 2.48

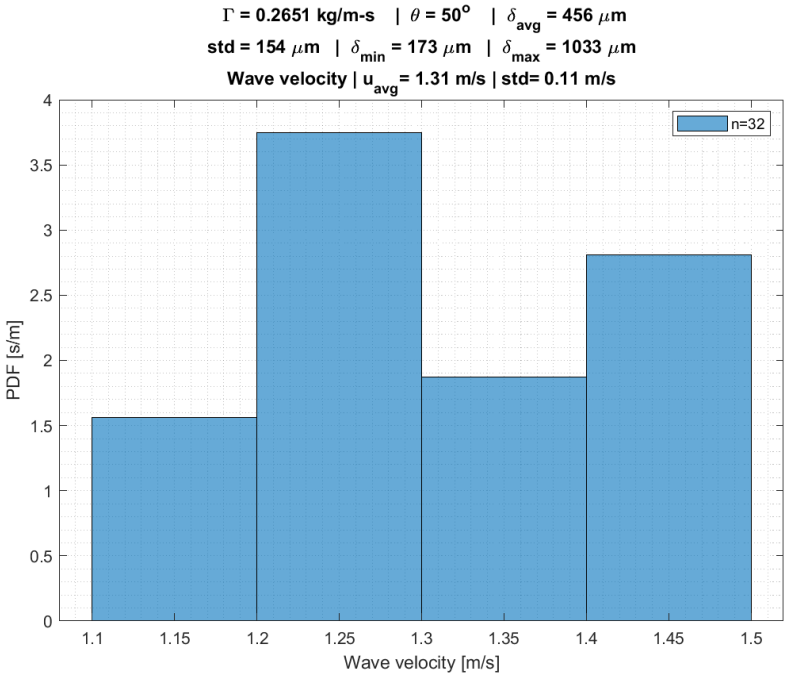

Wave velocity PDF for test condition No. 2.49

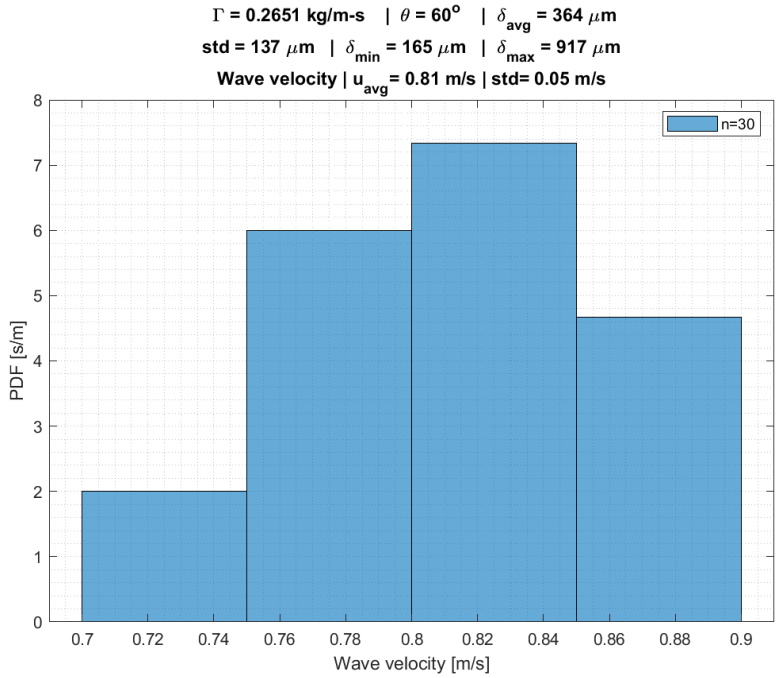

Wave velocity PDF for test condition No. 2.50

Appendix B

Appendix: Annular Flow

B.1 Film thickness measurements from parametric study

The film thickness measurements upstream and downstream of the flow obstruction are presented in this section.

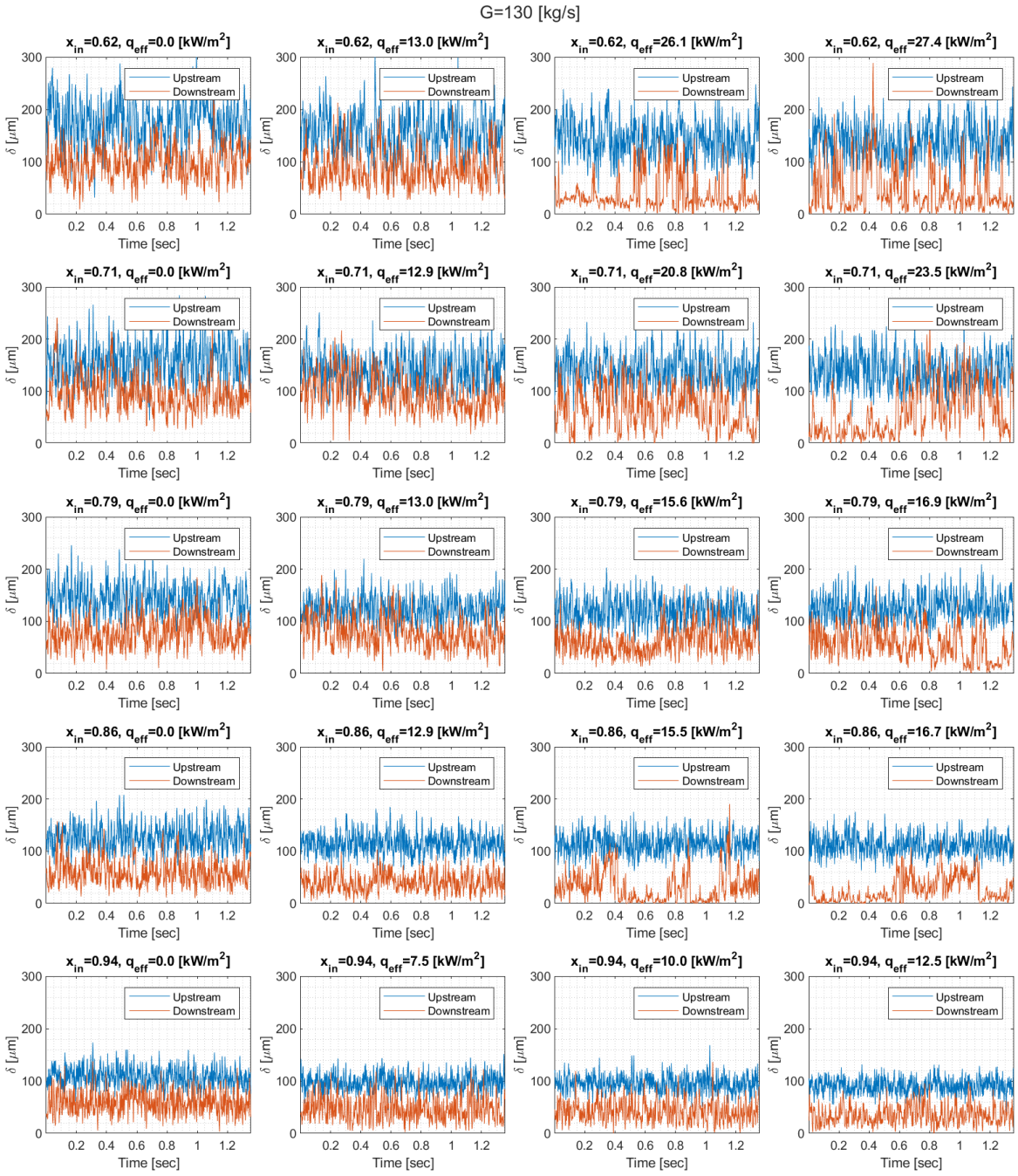

Film thickness measurements upstream and downstream of the flow obstruction. G=130 $[kg/m^2]$

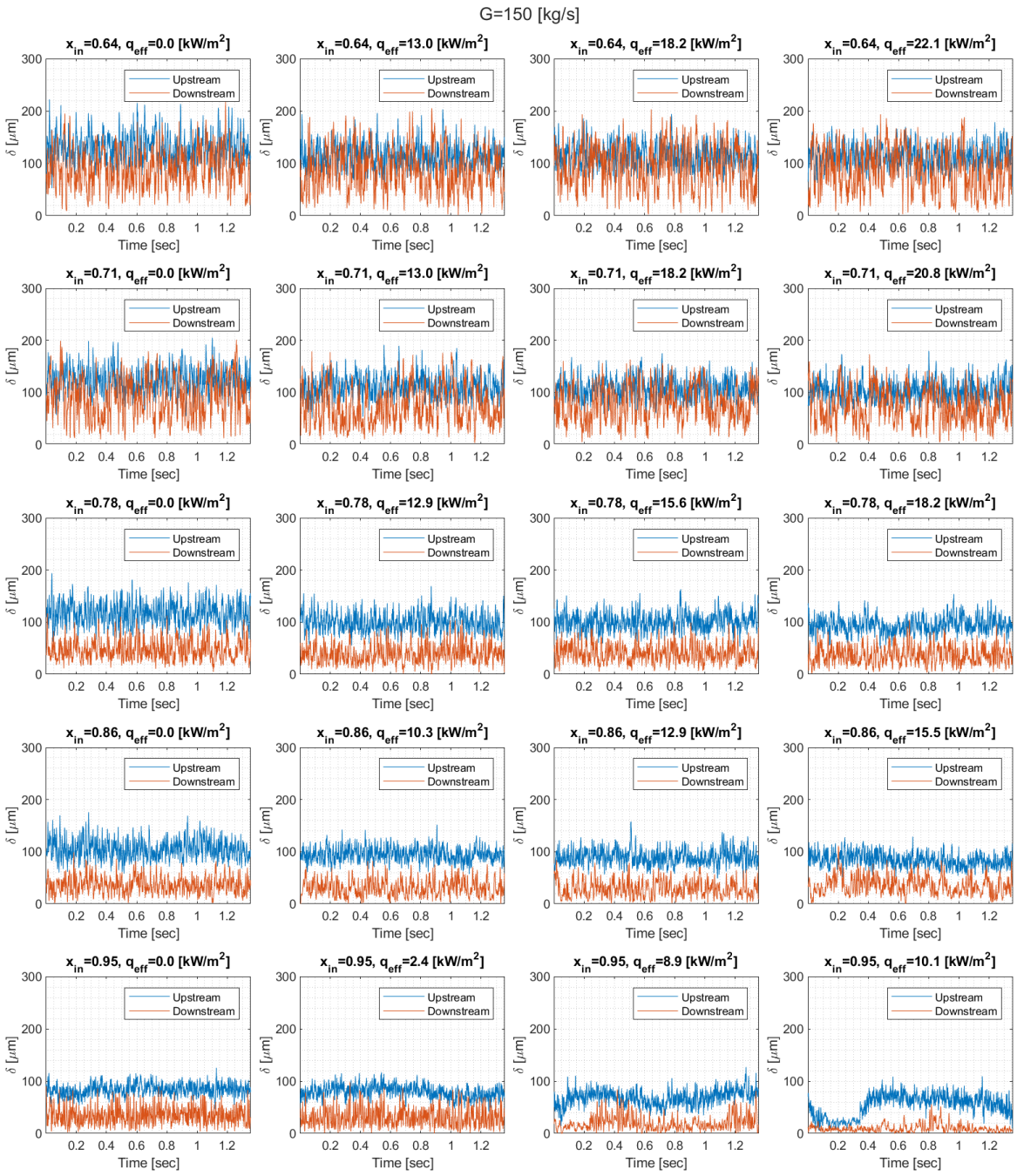

Film thickness measurements upstream and downstream of the flow obstruction. G=150 $[kg/m^2]$

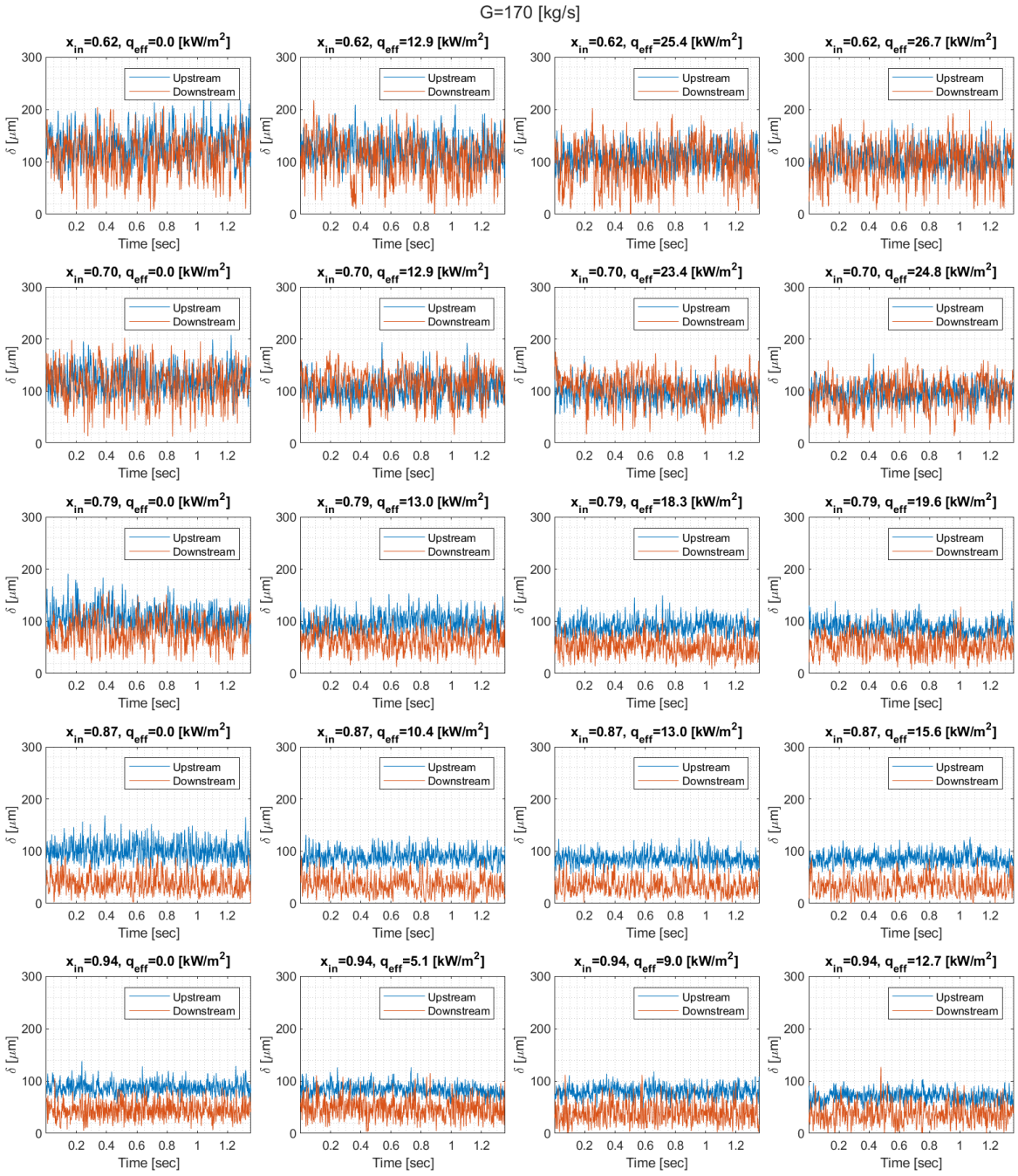

Film thickness measurements upstream and downstream of the flow obstruction. G=170 $[kg/m^2]$

B.2 Images of dry wake regions

Time-averaged high-speed images of the wake region downstream of the flow obstruction are shown in this section. The manually identified dry wake regions are highlighted in red. Images with no red highlights indicate no observable dry wake regions.

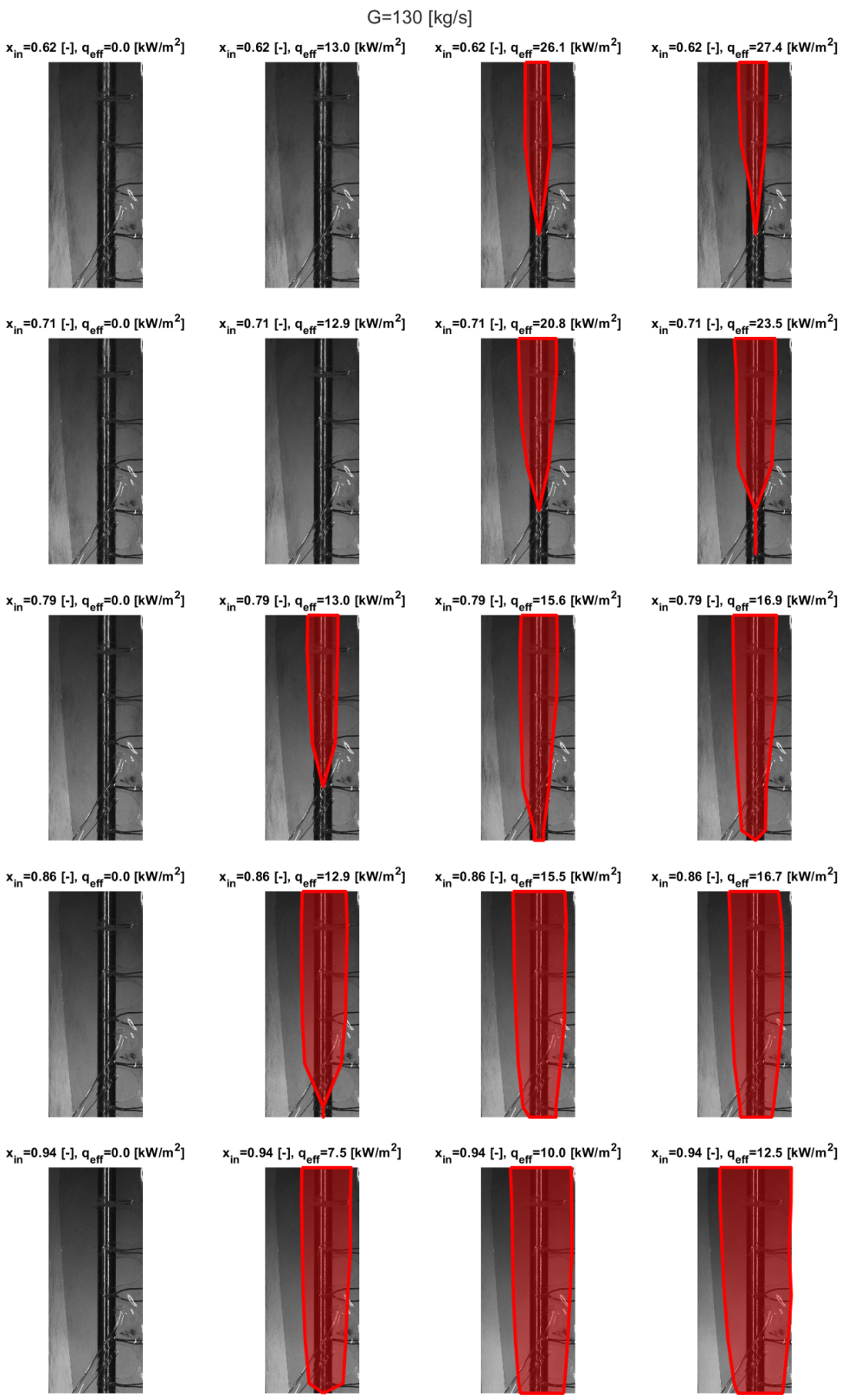

Time-averaged high-speed images of the wake region downstream of the flow obstruction. G=130 $[kg/m^2]$

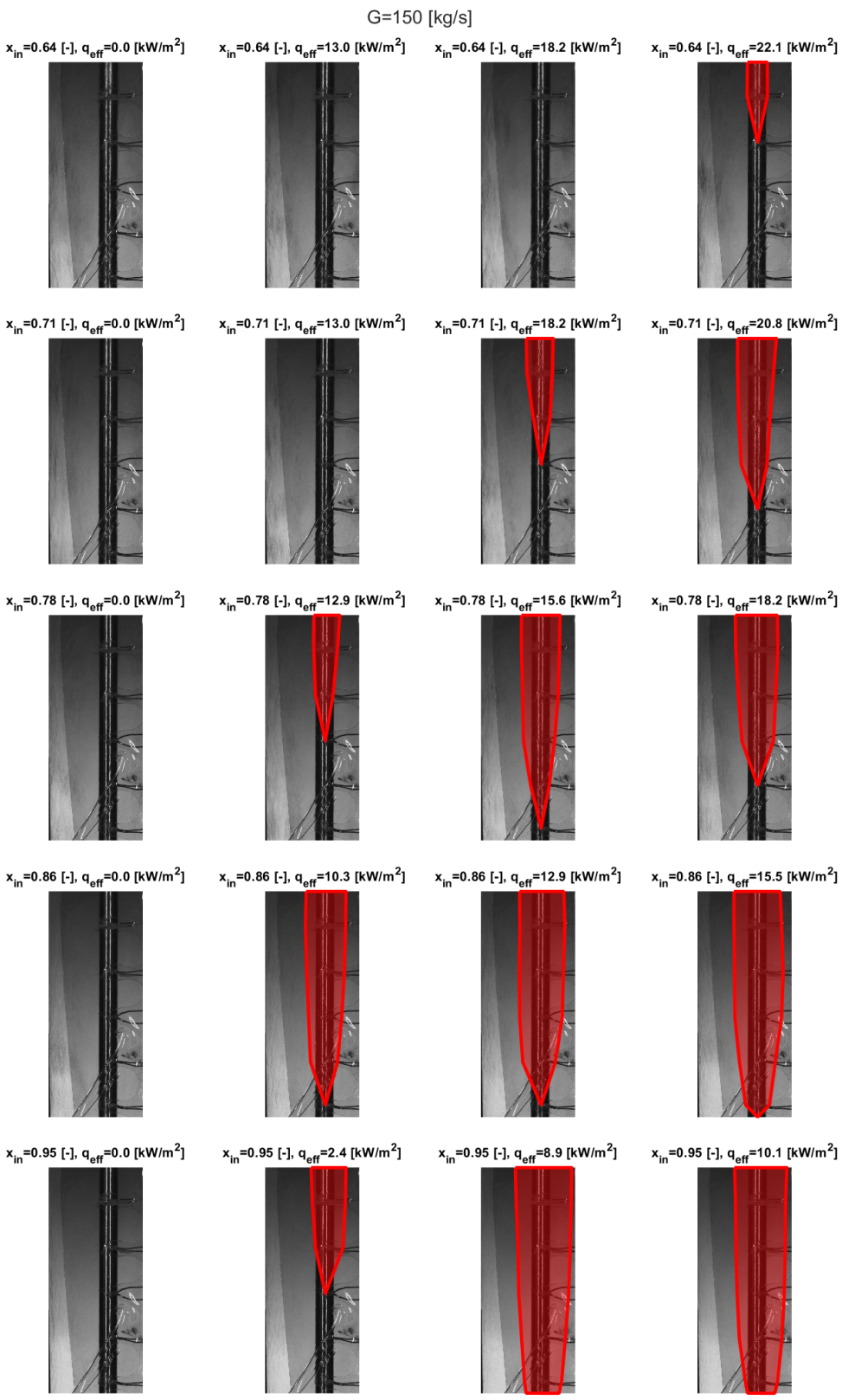

Time-averaged high-speed images of the wake region downstream of the flow obstruction. G=150 $[kg/m^2]$

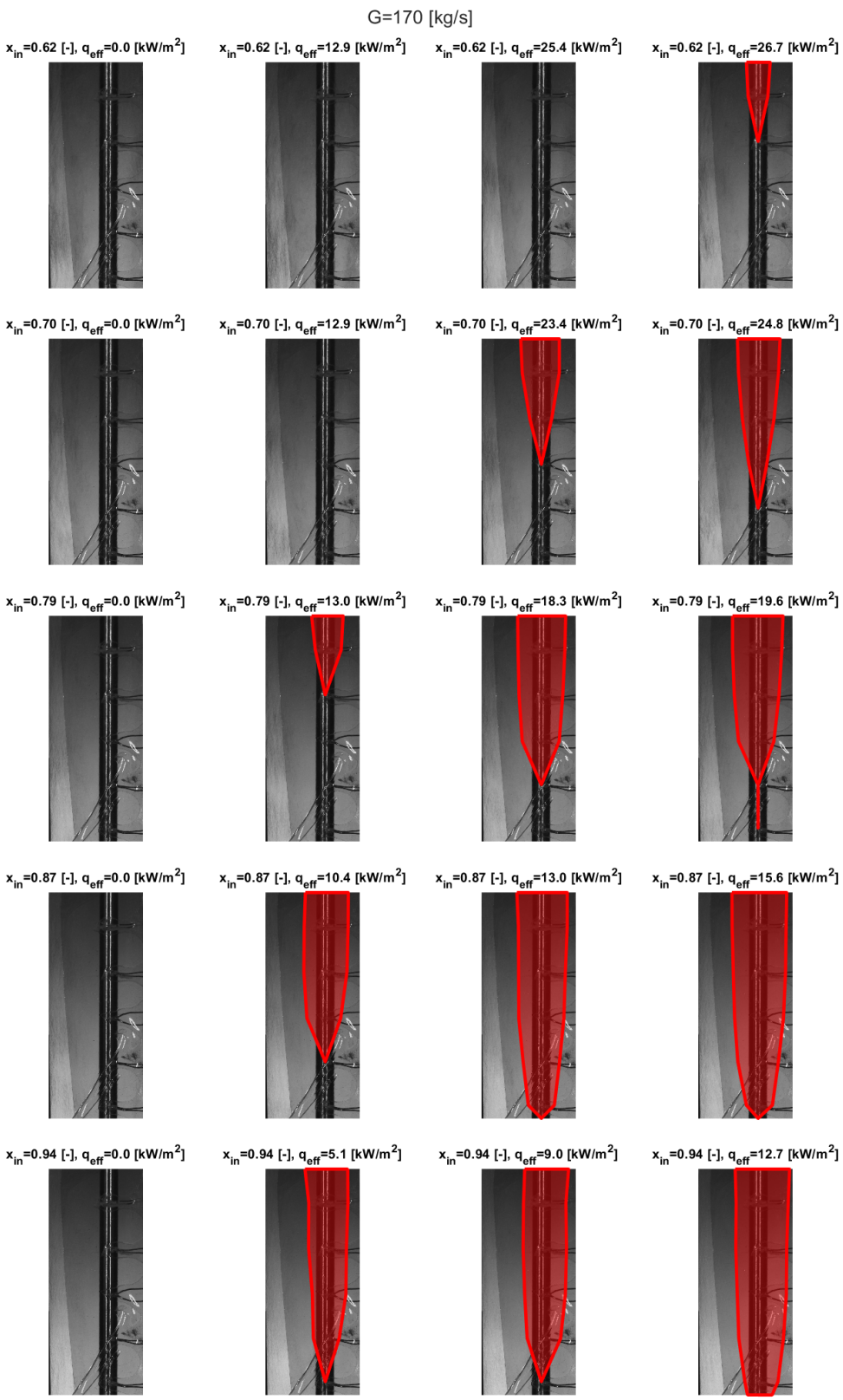

Time-averaged high-speed images of the wake region downstream of the flow obstruction. G=170 $[kg/m^2]$

B.3 Timetraces of external wall temperature in wake region

Timetraces of the external wall temperature measurement in the wake region are presented in this section. The numeric subscripts in the plot legends shown below correspond to the streamwise positions shown in Section 4.5, where 1 refers to the first thermocouple position downstream of the obstruction.

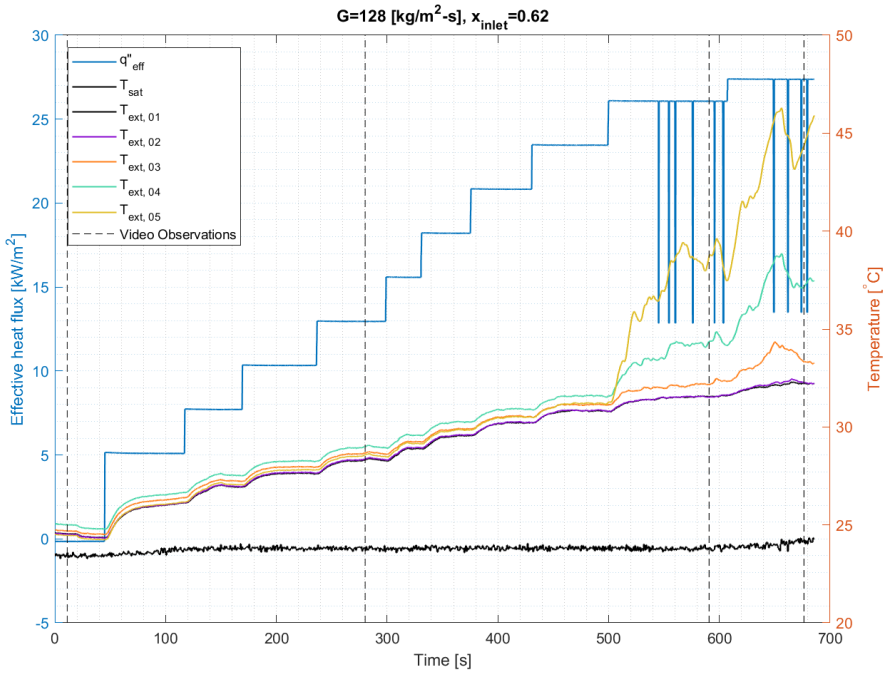

G=130 $[kg/m^2]$, $x_{in} = 0.62$

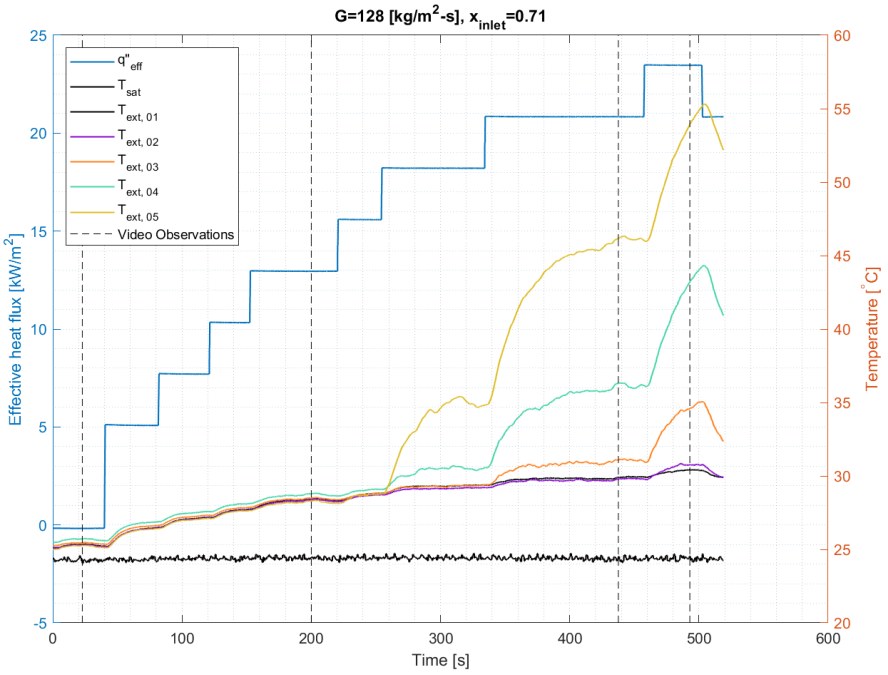

G=130 $[kg/m^2]$, $x_{in} = 0.70$

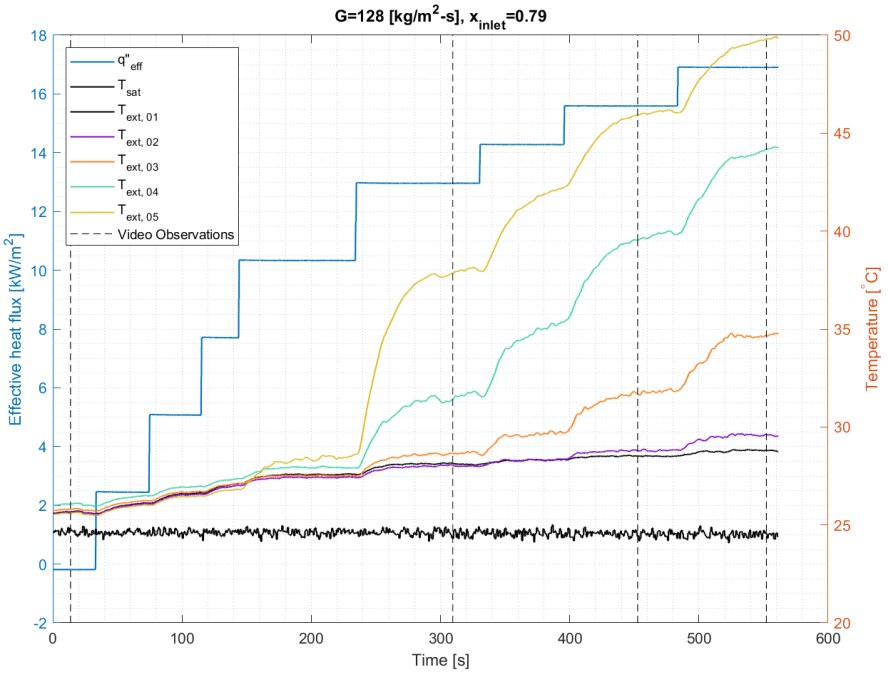

G=130 $[kg/m^2]$, $x_{in} = 0.79$

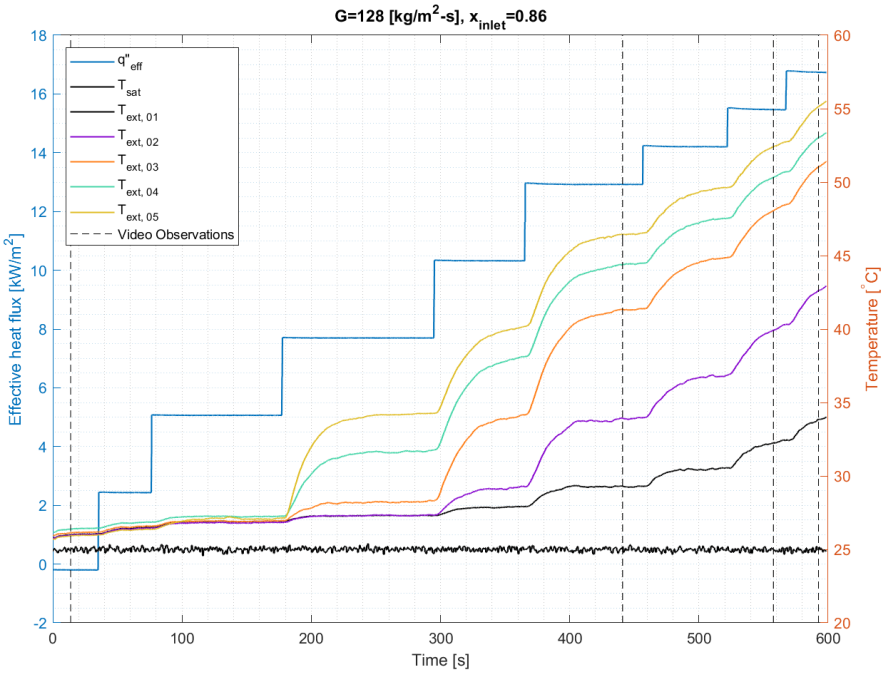

G=130 $[kg/m^2]$, $x_{in} = 0.87$

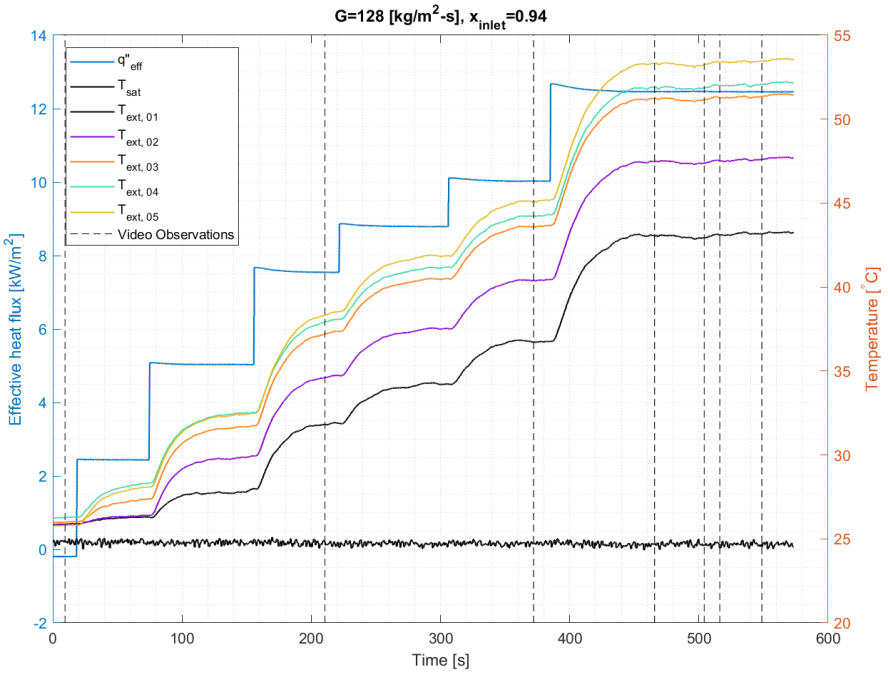

G=130 $[kg/m^2]$, $x_{in} = 0.94$

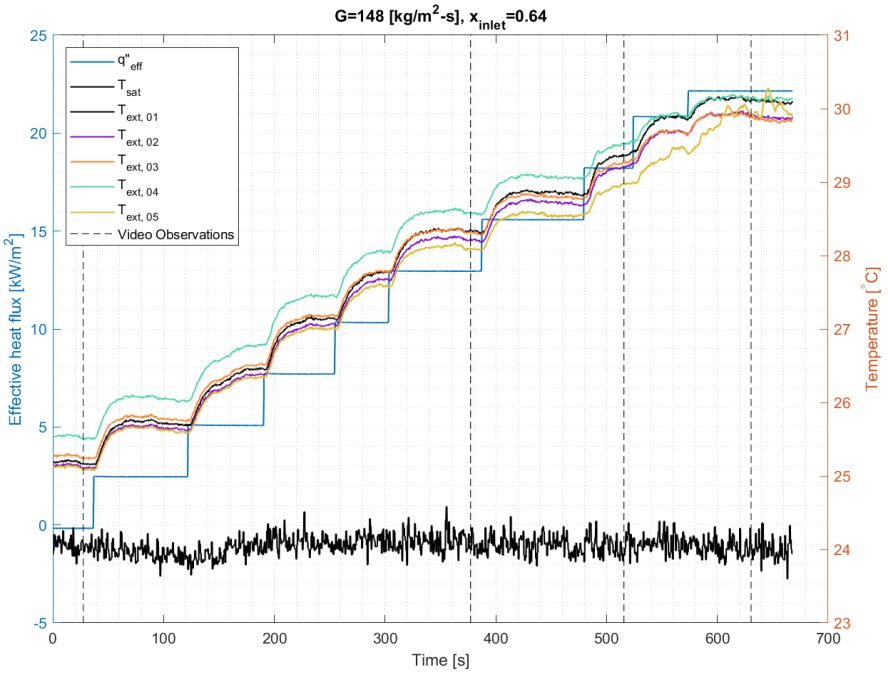

G=150 $[kg/m^2]$, $x_{in} = 0.62$

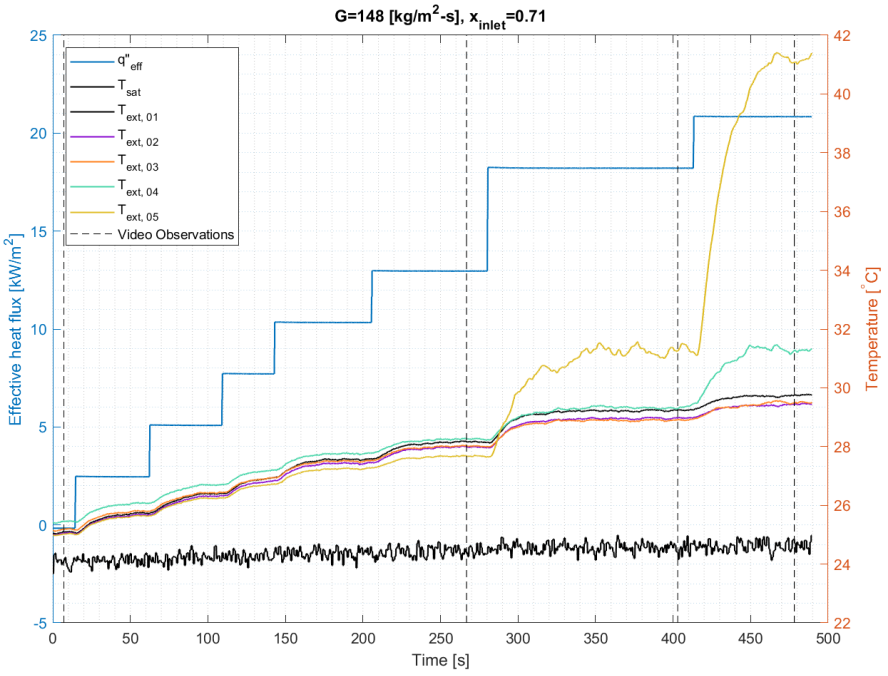

G=150 $[kg/m^2]$, $x_{in} = 0.70$

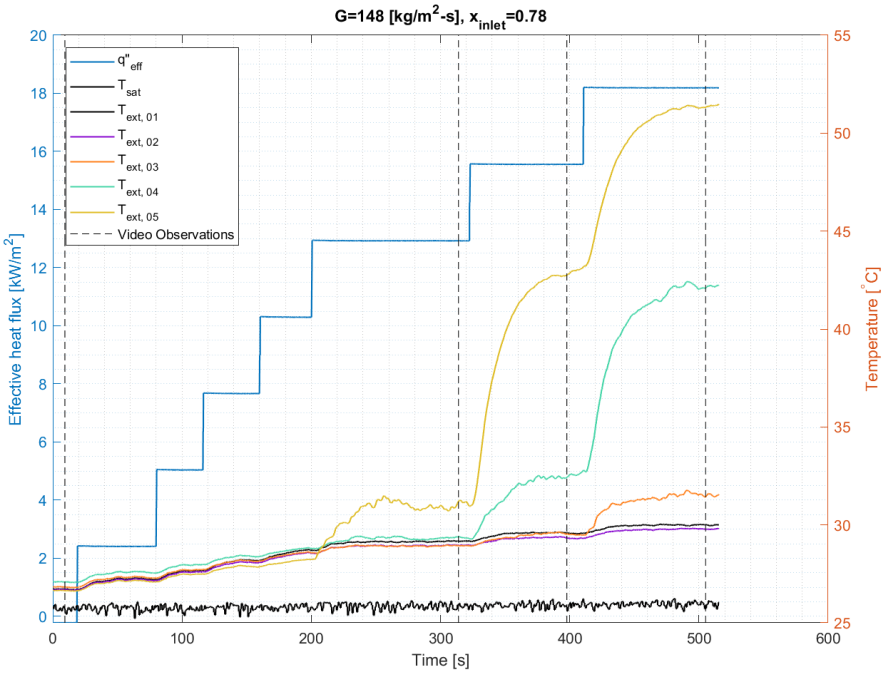

G=150 $[kg/m^2]$, $x_{in} = 0.79$

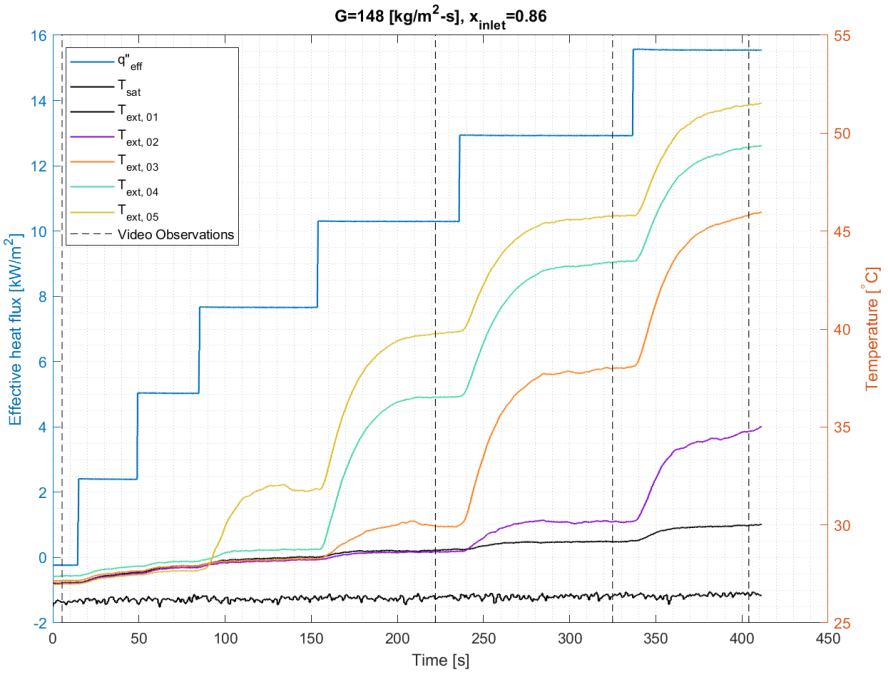

G=170 $[kg/m^2]$, $x_{in} = 0.87$

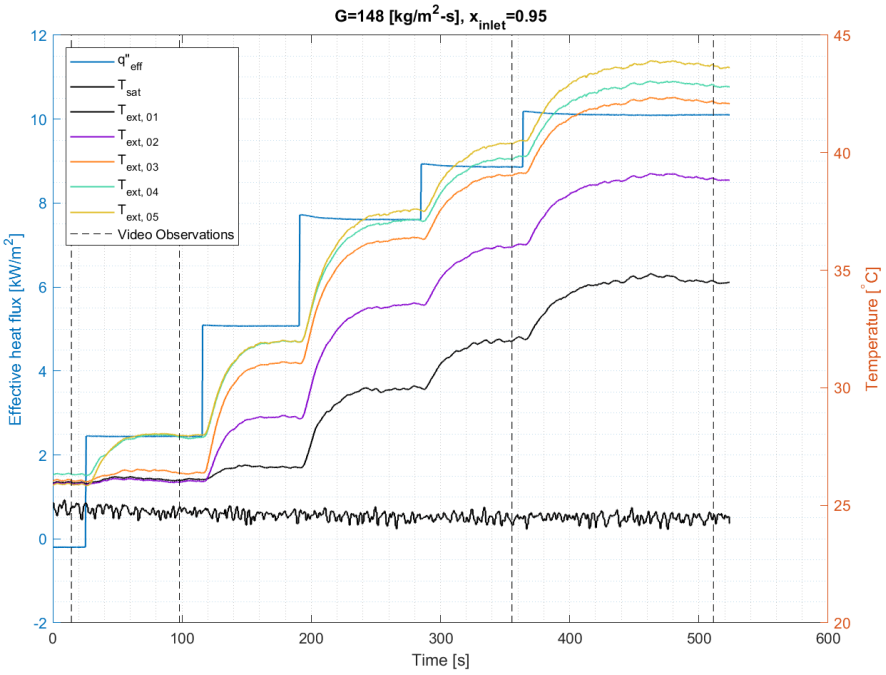

G=150 $[kg/m^2]$, $x_{in} = 0.94$

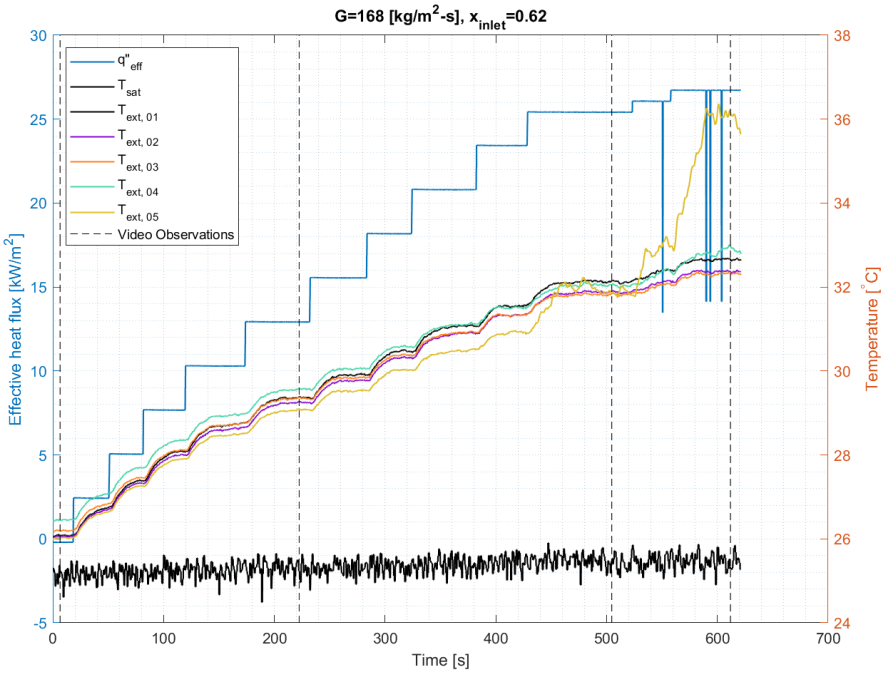

G=170 $[kg/m^2]$, $x_{in} = 0.62$

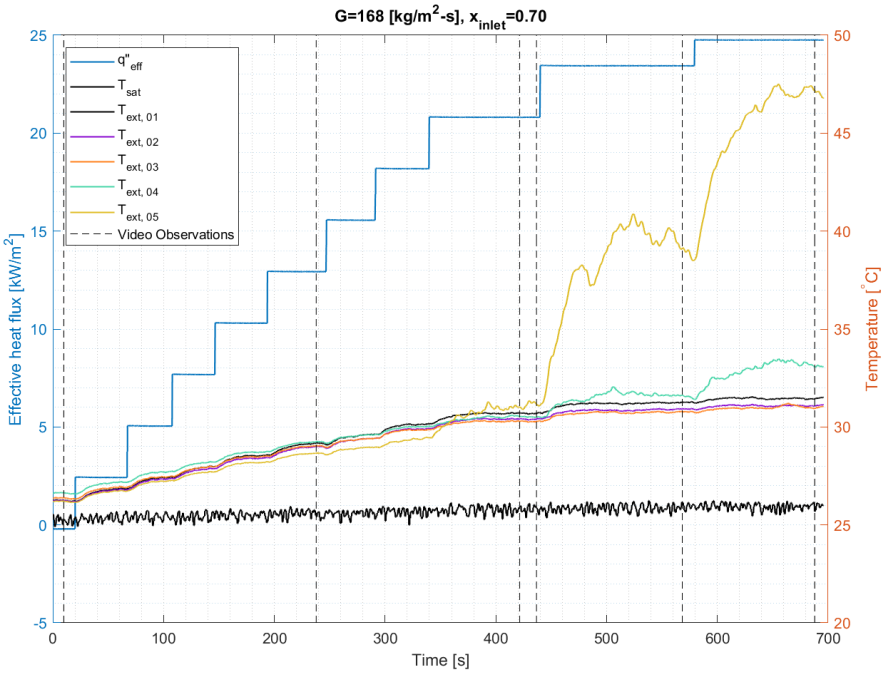

G=170 $[kg/m^2]$, $x_{in} = 0.70$

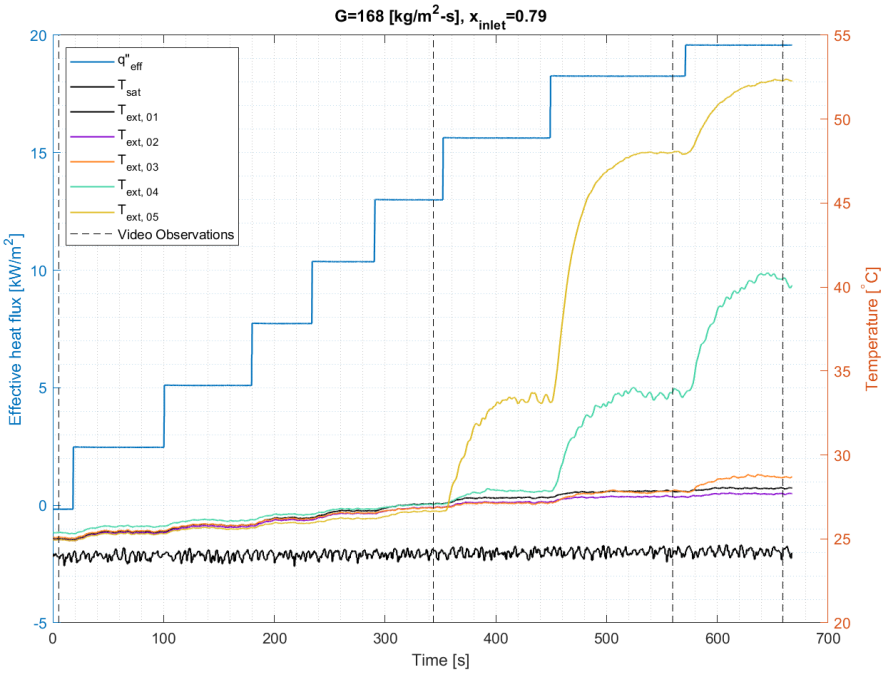

G=170 $[kg/m^2]$, $x_{in} = 0.79$

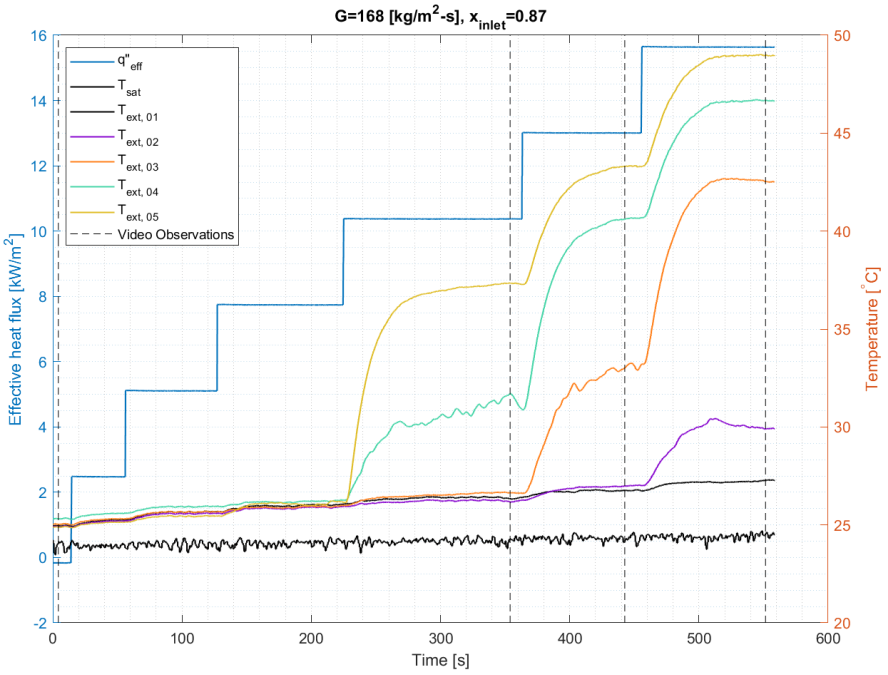

G=170 $[kg/m^2]$, $x_{in} = 0.87$

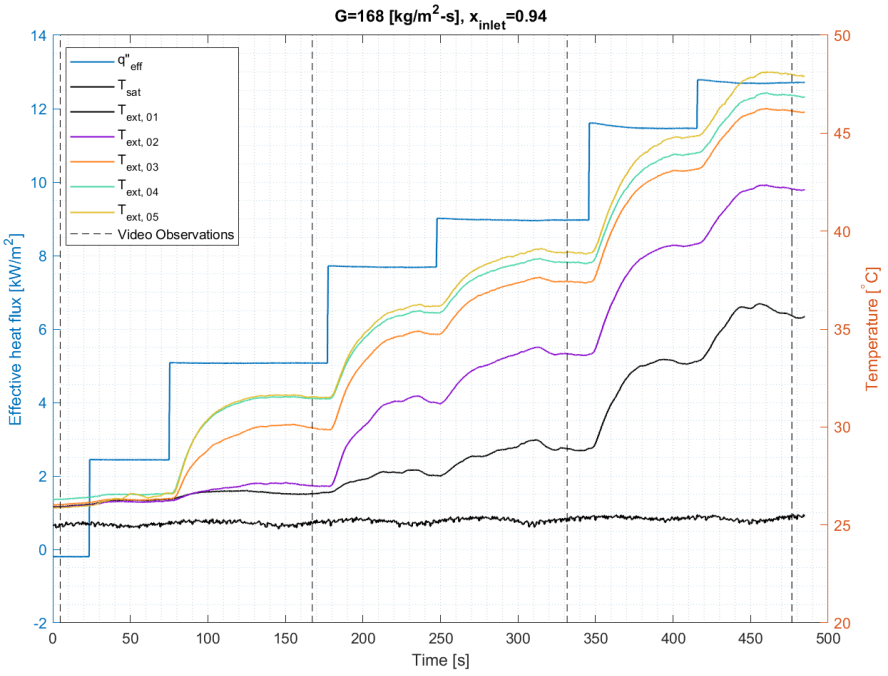

G=170 $[kg/m^2]$, $x_{in} = 0.94$